Subduction from top to bottom

Insights from linear and non-linear numerical geodynamic simulations

Sílvia Salvador Duarte

MSc. in Geophysical Sciences

A thesis submitted for the degree of

Doctor of Philosophy

at Monash University in 2019

School of Earth, Atmosphere & Environment

Copyright notice

Declaration

This thesis contains no material which has been accepted for the award of any other degree or diploma at any university or equivalent institution and that, to the best of my knowledge and belief, this thesis contains no material previously published or written by another person, except where due reference is made in the text of the thesis.

Signature: [redacted]

Print Name: Sílvia Salvador Duarte

Date: 04/10/2019

Acknowledgements

If you think you can do a thing or think you can't do a thing, you're right. – Henry Ford

In September 2015, I started my PhD with two supervisors and almost four years later, I am finishing it with four. Each of my supervisors played a different role, for which I am grateful for, during different stages of the project. Catherine A. Mériaux motivated me to purse a PhD degree during my Master's degree in Lisbon, and introduced me to Monash. Wouter P. Schellart continued to be involved in my project from the Netherlands and was constantly present in form of literature. Alexander R. Cruden suggested me to think about subduction 'non-linearly', which ended up developing into a big part of the project. And Peter G. Betts helped me developing the big picture ideas in the most optimistic and positive way possible.

In addition to my supervisors, my Panel members provided me with a lot of feedback and general advice related to the project. I am thankful to Roberto F. Weinberg for the discussions on linear versus non-linear flows and to Fabio A. Capitanio for the conversations about all things subduction related. I am particularly grateful to Oliver Nebel for taking interest in my results and contributing 'isotopically' to Chapter 4.

My research was supported by a Monash University Faculty of Science Dean's Postgraduate Research Scholarship and a Faculty of Science Dean's International Postgraduate Research Scholarship. My project was undertaken with the assistance of the resources and services from the National Computational Infrastructure (NCI), which is supported by the Australian Government. In addition, it was supported in part by the Monash eResearch Centre and eSolutions-Research Support Services through the use of the MonARCH HPC Cluster.

I would also like to acknowledge the invaluable help from Underworld2 Geodynamic Code developers John Mansour and Owen Kaluza for their contributions in building the numerical models, extracting all kinds of necessary outputs from them, and producing output images.

I am especially grateful to my family, who supported completely in my adventure to 'the other side of the world' and have always encouraged me to follow what I find most valuable. Finally, a very special thank you to Tobias for all the support given during this journey, and for teaching me on a regular basis that 'long-term planning' requires to look further than the next two weeks. More than our similarities, it is our differences that allow me to grow.

Abstract

For the past 60 years plate tectonics theory transformed our understanding of the processes and evolution of Earth's outermost layer, the lithosphere. More recently, the geodynamics community has started to address the dynamic link between tectonic processes and the behaviour of Earth's interior. This thesis uses simplified 2D models of subduction to address two poorly resolved aspects of Earth's dynamics: how does the geometry of the slab that initiates subduction impact the overall subduction process, and how does the mantle rheology control the interaction of a subducting slab with the 660 km mantle discontinuity.

Subduction is widely accepted to be the main driver for lithospheric plates motions and mantle convection. Both analogue and numerical modelling of subduction systems provide insights on how subducting slabs behave and evolve, and how they may impact neighbouring regions. Most often, geodynamic models are designed assuming an arbitrary initial instability that starts the subduction process, without considering the subduction initiation process, which is still a subject of major discussion. However, given that subduction is driven by negative buoyancy in a constrained medium (because Earth has finite dimensions), the following question arises: can different ways of starting subduction lead to variations in the evolution of subduction? Indeed, results of this thesis show that longer or steeper initial slabs lead to faster subduction. Moreover, the trench velocity is more sensitive to these variations than the slab sinking velocity.

Part of the constraints imposed on a subducting plate is the heterogeneity of the mantle. The mantle is primarily organised into layers, which resulted from differentiation, during Earth's formation. Upper mantle and lower mantle are characterised by contrasting density and viscosity. Consequently, a subducting plate will inevitably interact with the mantle discontinuity. Geophysical studies reveal that subducting slabs acquire diverse geometries upon reaching the mantle discontinuity. The mode of interaction between subducting plate and mantle discontinuity depends on plate characteristics, such as age, composition, strength, thickness. However, subducting plates are cold and stiff and, while sinking, induce high stresses on the surrounding mantle material. This phenomenon is explored by assessing how variations of the power-law rheology of the mantle and the upper-lower mantle density contrast influence the dynamics of subducting slab.

Results show that the rheology of the mantle is an additional key factor to determine the interaction between slab and mantle transition zone. A new subduction mode is proposed in

which the slab sinks straight into the lower mantle and accumulates by folding below the mantle discontinuity, opposing the common ‘slab-avalanche’ mode. Furthermore, the results imply that during subduction the slab folds trap upper mantle material, which can potentially reach the core-mantle boundary. Variations of the volume of subducted upper mantle material, caused by variations of the mantle rheology, could explain the global isotopic diversity of OIB.

Table of contents

Chapter 1 – Introduction

Chapter 2 – Slab initial geometry

Chapter 3 – Mantle stress dependent viscosity

Chapter 4 – Entrainment of upper mantle

Chapter 5 – Conclusions

List of figures

Chapter 1

Chapter 2

Chapter 3

Chapter 4

List of tables

Chapter 2

Chapter 3

Chapter 4

Table of abbreviations

CMB	Core-mantle boundary
EM-I	Enriched mantle I
EM-II	Enriched mantle II
FOZO	Focal zone (isotopic composition of OIB)
HIMU	High U/Pb mantle
HPC/HTC	High Performance Computer/High-Throughput Computer
INSZ	Induced nucleation of a subduction zone
LM	Lower mantle
MonARCH	Monash Advanced Research Computing Hybrid
MORB	Mid-ocean ridge basalt
MTZ	Mantle transition zone
NCI	National Computation Infrastructure
OIB	Ocean island basalt
SNSZ	Spontaneous nucleation of a subduction zone
TZ	Transition zone
UM	Upper mantle

Table of notations

Symbol	Meaning	SI units
L	Length of the domain	m
L_{sp}	Length of the subducting plate	m
l_{sp}	Length of the slab tip	m
l_0	Length of the initial slab tip	m
X_{sp}	Length of the ensemble trailing plate plus slab	m
e	Elongation of the ensemble trailing plate plus slab	–
H	Thickness of the domain/mantle	m
h_{UM}	Thickness of the upper mantle	m
h_{LM}	Thickness of the lower mantle	m
h_{sp}	Thickness of the slab and subducting plate	m
h_{sl}	Thickness of the 'sticky-layer'	m
h_c	Thickness of the crust	m
x	Position on the x-axis	m
x_{trench}	Horizontal position of the trench	m
x_{trench}^{660}	Horizontal position of the trench when $y_{slab} = 600$ km	m
x_{trench}^{C50}	Horizontal position of the trench when $C_{plate} \sim 50$ %	m
y	Position on the y-axis	m
y_{slab}	Vertical position of the slab tip	m
y_{trench}^{660}	Vertical position of the slab tip when $y_{slab} = 600$ km	m
y_{trench}^{C50}	Vertical position of the slab tip when $C_{plate} \sim 50$ %	m
$\boldsymbol{u}$ or $\boldsymbol{v}$	Velocity vector, $\boldsymbol{u} = u_x \boldsymbol{e}_x + u_y \boldsymbol{e}_y + u_z \boldsymbol{e}_z$ or $\boldsymbol{v} = v_x \boldsymbol{e}_x + v_y \boldsymbol{e}_y + v_z \boldsymbol{e}_z$	m/s
v_{Stokes}	Stokes velocity	m/s
v_x	Horizontal velocity at the surface	m/s
v_{slab} or v_s	Velocity of the slab (sinking velocity)	m/s
v_{trench} or v_t	Velocity of the trench	m/s
$v_{trailing\ edge}$ or v_{te} or v_{edge}	Velocity of the trailing edge of the surface plate	m/s
$v_{subduction}$	Velocity of subduction, $v_{subduction} = v_{edge} + v_{trench}$	m/s
t	Time	s
t^{660}	Time when $y_{slab} = 600$ km	s
t^{C50}	Time when $C_{plate} \sim 50$ %	s

Symbol	Meaning	SI units
C_{plate}	Percentage of the surface plate consumed by subduction	–
C_{plate}^{660}	Percentage of the surface plate consumed by subduction, when the slab tip reaches the 600 km mantle discontinuity	–
$M_i^{plate660}$	Amount of plate (surface plate and slab) below 600 km, at time i	m^2
M_{tot}^{plate}	Total amount of plate (surface plate and slab)	m^2
M_{plate}^{660}	Percentage of plate (surface plate and slab) below the 600 km	–
M_i^{UM660}	Amount of upper mantle that has sunk below the 600 km, at time i	
M_{tot}^{UM}	Total amount of upper mantle inside the domain	m^2
M_{UM}^{660}	Percentage of upper mantle that below the 600 km	–
R_i^{660}	Relative material contribution $R_i^{660} = M_i^{UM660}/M_i^{plate660}$	–
η	Dynamic viscosity	Pa·s
η_m	Dynamic viscosity of the sub-lithospheric mantle	Pa·s
η_{UM}	Dynamic viscosity of the upper mantle	Pa·s
η_{LM}	Dynamic viscosity of the lower mantle	Pa·s
η_{sp}	Dynamic viscosity of the slab and subducting plate	Pa·s
η_{sl}	Dynamic viscosity of the 'sticky-layer'	Pa·s
η_c	Dynamic viscosity of the crust	Pa·s
η_0	Dynamic reference viscosity (linear viscosity)	Pa·s
η_p	Power-law viscosity	Pa·s
η_{eff}	Effective viscosity	Pa·s
γ	Viscosity ratio between plate and mantle, $\gamma = \eta_{sp}/\eta_m$	–
γ_M	Viscosity ratio between lower mantle and upper mantle, $\gamma_M = \eta_{LM}/\eta_{UM}$	–
S	Stiffness, $S = \gamma\left(h_{sp}/l_{sp}\right)^3$	–
ρ	Density	kg/m^3
ρ_m	Density of the sub-lithospheric mantle	kg/m^3
ρ_{UM}	Density of the upper mantle	kg/m^3
ρ_{LM}	Density of the lower mantle	kg/m^3
ρ_{sp}	Density of the slab and subducting plate	kg/m^3
ρ_{sl}	Density of the 'sticky-layer'	kg/m^3
ρ_c	Density of the crust	kg/m^3
$\Delta\rho$	Density contrast, $\Delta\rho = \rho_{sp} - \rho_m$	kg/m^3
R	Slab density anomaly, $(\rho_{sp} - \rho_{LM})/(\rho_{sp} - \rho_{UM})$	
$\Delta\rho_M$	Density contrast between upper and lower mantle, $\Delta\rho_M = \rho_{LM} - \rho_{UM}$	kg/m^3
D_M	Mantle density contrast, $D_M = \Delta\rho_M/\rho_{UM}$	–

Symbol	Meaning	SI units
p	Dynamic pressure	Pa
$\boldsymbol{\tau}$	Deviatoric stress tensor	N/m^2
σ	Deviatoric stress	N/m^2
σ_{II}	Second invariant of the deviatoric stress	N/m^2
g	Gravity acceleration	m/s^2
$\boldsymbol{g}$	Gravity vector, $\boldsymbol{g} = g_x\boldsymbol{e}_x + g_y\boldsymbol{e}_y + g_z\boldsymbol{e}_z$	m/s^2
$\dot{\varepsilon}_{II}$	Second invariant of the strain rate	s^{-1}
$\dot{\varepsilon}_{II}^{T}$	Transition strain rate	s^{-1}
$(\dot{\varepsilon}_{II}^{T})_{UM}$	Upper mantle transition strain rate	s^{-1}
$(\dot{\varepsilon}_{II}^{T})_{LM}$	Lower mantle transition strain rate	s^{-1}
n	Power law exponent	–
n_{UM}	Power law exponent in the upper mantle	–
n_{LM}	Power law exponent in the lower manlte	–
θ	Slab dip angle	$\circ$
θ_0	Initial slab dip angle	$\circ$
Ra	Rayleigh number	–
F_b	Buoyancy force	N
F_{ext}	External viscous force acting on a bending portion of the plate	N
F_{int}	Internal viscous force acting on a bending portion of the plate	N

Chapter 1

Introduction

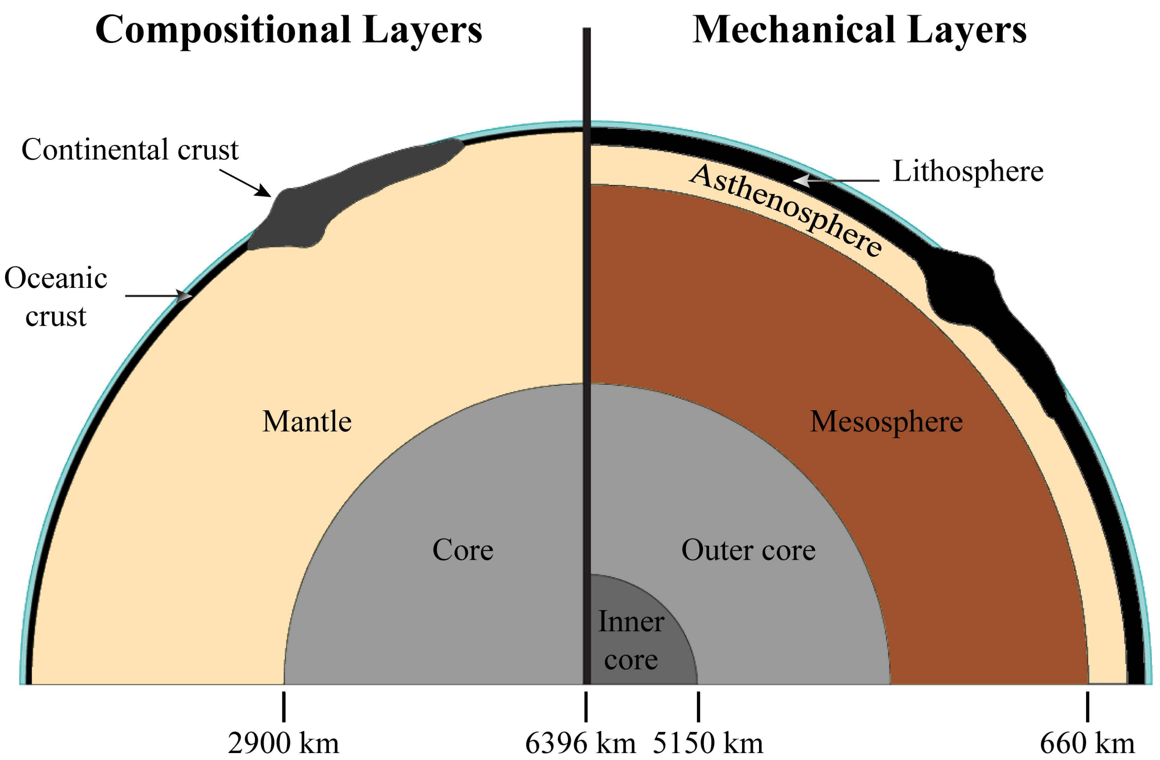

Cover image: Schematic illustration of compositional and mechanical layering of the Earth. Adapted from aashscience.weebly.com (2019).

1. Introduction

1.1. Earth's interior: structure and composition

With a radius just under 6,400 km, Earth is a complex system whose internal dynamics are inaccessible from direct observation. The current knowledge about the processes occurring deep beneath the surface is mostly derived through indirect methods of observation and results from a multidisciplinary effort that combines geology, geophysics and geochemistry. Geological phenomena and geodynamic processes are further investigated with geodynamic modelling, which relies on the constraints determined by the observational methods. Geoscientists organise Earth's interior into well-structured layers that can be described in terms of their composition, based on chemistry, or in terms of their mechanical attributes, based on the physical properties of the constituent materials.

Earth's composition is inferred from laboratory studies of the physical properties of minerals and rocks and field observations of exhumed rocks. Rocks that are thought to come from the inaccessible parts of the mantle have either been tectonically uplifted and exposed at the surface, or transported by magmas generated by partial melting of the mantle [Kushiro, 1968].

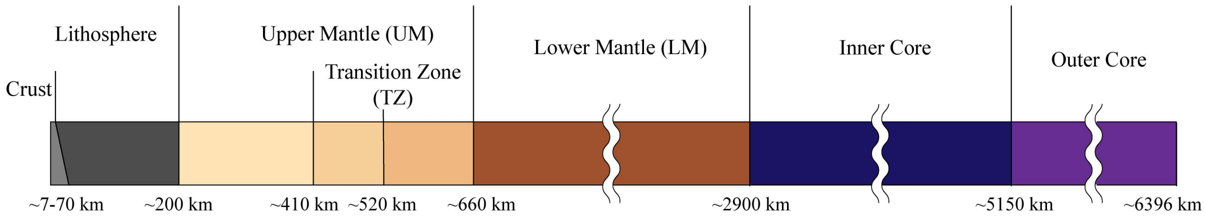

Figure 1. Illustration of Earth's layering from the surface to the centre, based on composition and mechanical properties.

Compositionally, Earth's interior can be divided into crust, mantle and core, whereas mechanically, Earth's interior can be divided into lithosphere, asthenosphere, mesosphere, outer core and inner core. The crust is the outermost layer of Earth and it comprises both oceanic crust and continental crust. With a thickness of ~ 7 km, oceanic crust is mainly composed of iron and magnesium silicate mineral-bearing mafic igneous rocks. Continental crust is between $\sim 0 - 70$ km thick and is composed mainly of sodium, potassium and aluminium silicate mineral-bearing felsic rocks.

The mantle extends between ~ 7 to ~ 2900 km depth and is usually differentiated between upper mantle (UM) and lower mantle (LM), based on a change in composition at a depth of

~ 660 km. The upper mantle is mainly composed of olivine, orthopyroxene, clinopyroxene, garnet, and high-pressure clinopyroxene, while the most abundant minerals in the lower mantle are ferropericlase and a magnesium silicate mineral in a perovskite structure [e.g., Karato, 2010 and references therein]. The core has a total radius of ~ 3500 km and mainly consists of iron and nickel [McDonough & Sun, 1995].

The mechanical layers of Earth are determined from seismological observations [e.g., Fowler, 2004] and experimental petrology studies [e.g., Wada & King, 2015 and references therein]. Seismological observations include the relocation of earthquake hypocentres, seismic tomography and shear wave splitting. These methods focus on the elastic propagation of seismic waves through the planet and provide a snapshot of the distribution of material properties, from which structural and thermal variations deep inside the planet are inferred. Additionally, the directional dependence of seismic wave velocity anomalies (seismic anisotropy) provides information on the formation and/or deformation of rocks, which is particularly useful in the lower mantle. Experimental petrology studies provide constraints on metamorphic and melting conditions by determining the stability and physical properties of high-pressure minerals phases as a function of pressure and temperature, focusing mainly on the mineral physics of the upper-mantle. Constraints on the densities of high pressure mineral phases in the lower mantle come from high pressure experimental synchrotron experiments, and due to their inherent inaccessibility, constraints on their elastic properties remain limited [Irifune & Tsuchiya, 2015].

The outer most mechanical layer of Earth is the lithosphere, which comprises the crust and the uppermost part of the upper mantle (lithospheric mantle), extending between the surface to depths of $\sim 70 - 200$ km. The lithosphere is considered to be mechanically strong, with a strong thermal gradient and a stress- and temperature-dependent rheology. It is synonymous with the term "tectonic plate".

The asthenosphere corresponds to the upper mantle below the lithospheric mantle. It extends from the base of the lithosphere to a depth of ~ 660 km and it is characterised by ductile behaviour. Between ~ 410 and ~ 660 km depth an extra layer is commonly defined as the mantle transition zone (TZ), where minerals undergo a phase transition due to increasing pressure and temperature. At 410 km olivine exhibits a phase transition to wadsleyite [e.g., Katsura & Ito, 1989; Ita & Stixrude, 1992; Vidale et al., 1995] and at 520 km wadsleyite transitions to ringwoodite [e.g., Akaogi et al., 1989; Shearer, 1990]. At 660 km ringwoodite transitions to calcium-silicate perovskite (bridgmanite), ferropericlase and a calcium ferrite-type phase [e.g., Anderson, 1967; Ito & Takahashi, 1989; Mitrovica & Forte, 1997]. These mineral phase transitions affect material strength and overall mantle flow, and the depths at which they occur can vary regionally [e.g., Shearer & Masters, 1992].

The mesosphere is equivalent to the lower mantle and it is characterised by a sharp increase in viscosity, relative to the asthenosphere. While most of the lower mantle is considered to be homogenous, the lowermost ~ 200 km, also referred to as the D'' layer (D double prime) is highly heterogeneous and anisotropic [e.g., Lay et al., 1998; Garnero, 2004].

The outer core is inferred to be liquid as it does not transmit seismic shear waves and the inner core is assumed to be solid [e.g., Kennett et al., 1995]. Both the outer and inner core are much denser and warmer than the mantle above and are separated from the mantle by the core-mantle boundary (CMB). The CMB is considered to be a thermal and chemical boundary, across which there is a strong heat flow. It contributes directly to planetary dynamic processes, such as providing the sources for some long-lived mantle plumes.

1.2. Mantle convection

Earth's mantle is a system which is heated from below through the cooling of the core and, to a lesser extent, from radioactive decay of isotopes (namely, uranium, thorium and potassium). From above, Earth is cooled by the oceans and atmosphere. In this type of system, heat transfer occurs mostly through a balance between conduction and convection. Conduction is the direct transfer of energy between two bodies in physical contact, whereas convection is the transfer of energy between a body and its environment due to fluid motion.

The balance between conduction and convection is described by the ratio of the timescale for thermal transport by diffusion over the timescale for thermal transport by convection, which defines the dimensionless Rayleigh number, Ra:

$$Ra = \frac{g\alpha\Delta T L^3}{\nu\kappa}, \tag{1}$$

where g is the gravitational acceleration, α is the thermal expansion coefficient, ΔT is the temperature contrast between top and bottom of the system, L is the characteristic length of the system, ν is the kinematic viscosity, and κ is the thermal diffusivity. Heat transfer occurs dominantly by convection when $Ra > 1000$ [Rayleigh, 1916; e.g., Turcotte & Schubert, 2014].

On Earth, Ra is estimated to be of the order of 10^7, implying that heat transfer occurs by vigorous convection. Consequently, there are regions of upwelling and downwelling of material in the mantle, which are identified through seismic tomography studies. Two broad-scale upwelling regions, referred to as Large Low-Shear-Velocity Provinces (LLSVP), are identified beneath the Central Pacific and Africa. Regions of downwelling are mostly located beneath the

Americas and Western Pacific. These regions exhibit long-term stability, which results in a long-term stability of the general mantle convection patterns [Dziewonski et al., 2010; Conrad et al., 2013].

The global convection system is complex, the degree of heterogeneity in the mantle it is not completely understood [e.g., Silver et al., 1988]. However, multidisciplinary studies have given rise to three proposed models for mantle convection: whole mantle convection, layered mantle convection and hybrid models [Turcotte & Schubert, 2014]. Given that some subducting plates (Section 1.4) sink below 660 km depth, whole mantle convection models assume that there must be also upwellings from the lower mantle that cross the 660 km discontinuity in order to maintain mass balance. In layered mantle convection models, convection takes place separately in the upper mantle and in the lower mantle, and convective motions induced by plate tectonics are restricted to the upper mantle. Lastly, in hybrid models it is assumed that convection is time dependent and that the 600 km discontinuity acts as a partial barrier, above which subducted lithosphere accumulates until there is enough material to sink into the lower mantle, resulting in whole mantle overturn.

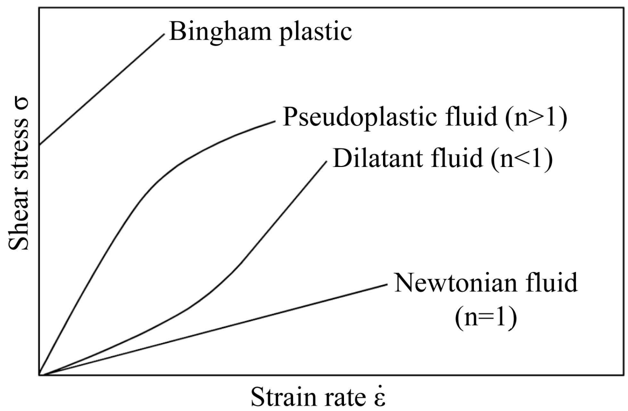

Figure 2. Stress and strain rate relationship for Newtonian and non-Newtonian fluids. Modified after Mehrabi & Setayeshi [2012].

1.3. Rheology

Rheology is the study of the deformation and flow of materials describing the relationship between applied stresses (applied forces per unit area) and strain or strain rate (rate of change of deformation). The constitutive behaviour (i.e., the way deformation occurs) varies for each material. Materials with complex types of flow are characterized by changing viscosity under changing applied stresses conditions (Figure 2). Viscosity is a measure of the resistance of a fluid or continuum to deformation, measured in terms of the strain rate in response to an applied stress.

Fluids that have constant viscosity independent of stress are considered to be Newtonian (e.g., water). Other types of fluids behave as rigid bodies at low stresses but flow with constant viscosity at high stress. These are called Bingham materials (plastic fluids; e.g., mayonnaise). Fluids characterised by changing viscosity, with a non-linear relation between stress and strain rate, are known as non-Newtonian or power law materials, categorized as either dilatant (strain rate hardening or shear thickening) or pseudo-plastic (strain rate softening or shear thinning or thixotropic) fluids. The viscosity of dilatant fluids (e.g., a mixture of corn-starch and water) increases with stress. Thus, it is harder to deform these materials at high stress. On the other hand, pseudo-plastic fluids (e.g., blood and ketchup) are characterized by decreasing viscosity with increasing stress. Consequently, it is easier to deform such materials at high stress.

Over geologic time-scales, solid Earth materials (minerals and rocks) exhibit flow at rates that depend on mineral composition, temperature, pressure, grain size, and water content. This deformation is achieved through the motion of atoms and defects inside (dislocation creep) and around (diffusion creep) the crystal lattice of natural minerals [e.g., Karato, 2008]. The relation between strain rate and stress in rocks and minerals is generally written as:

$$\dot{\varepsilon} = \mathrm{A}\left(\frac{\sigma}{\mu}\right)^{n}\left(\frac{b}{h}\right)^{m} e^{\left(-\frac{E+pV}{RT}\right)}, \tag{2}$$

where $\dot{\varepsilon}$ is the strain rate, σ is the deviatoric stress, and the relation depends on material properties: pre-exponential factor A, grain size h, length of Burgers vector, b, activation energy E and volume V, on the shear modulus μ and the temperature T. R is the universal gas constant and p is pressure, n and m are material dependent exponents [e.g., Turcotte & Schubert, 2014].

The parameters of the flow law defined in equation (2) vary for each mineral, and under different conditions, different deformation mechanisms dominate [Ashby, 1972]. For solid Earth materials, the important deformation mechanisms to consider are diffusion creep (also called Newtonian or linear flow), dislocation creep (also called non-Newtonian, non-linear or power-law flow) and Peierls creep. At low stress levels and at constant temperature and pressure, the deformation occurs by diffusion creep, where the strain rate increases linearly with stress, decreases with grain size and the exponent $n = 1$. At high stress levels and at constant temperature and pressure, the deformation occurs by dislocation creep, where the strain rate increases non-linearly with stress. However, it does not depend on the grain size and the exponents $m = 0$ and $n > 1$. The Peierls mechanism is a temperature-dependent mode of plastic deformation, which occurs instead of dislocation creep at elevated stresses.

The rheological parameters of minerals depend on temperature pressure, water content, the presence or absence of partial melting, deformation geometry and mineral phase transitions. These dependencies are studied through high temperature and pressure deformation experiments and experimental petrology. However, such methods have limitations because it is only possible to retrieve samples that come from depths above < 200 km in the uppermost part of upper mantle. Furthermore, laboratory studies of mineral deformation are limited to strain rates $\gtrsim 10^{-8}$ s^{-1}, which is > 5 orders of magnitude faster than strain rates associated with flow in the mantle ($\lesssim 10^{-13}$ s^{-1}). Hence, experimental studies require large extrapolations to determining the relationship between strain rate and variables such as stress, grain size, temperature and pressure, potentially leading to a considerable mismatch of the deformation mechanisms and rock rheological properties between laboratory results and nature.

Furthermore, there are no constraints on mineral grain size and water content in the mantle transition zone and in the lower mantle. Both properties strongly influence effective viscosity, hence the rheological parameters of the lowermost upper and lower mantle still remain poorly constrained.

Seismic anisotropy studies suggest that deformation in the upper mantle occurs by dislocation creep, indicating that in the vicinity of subducting slabs the viscosity of the mantle will be reduced due to higher stresses in such regions [e.g., Karato, 2008]. In the transition zone, the dominant mechanism of deformation is dislocation creep, although there are regional variations attributed to unmeasured changes in grain size and water content. It is suggested that most of the lower mantle deforms by diffusion creep, based on the absence of seismic anisotropy. However, some regions of the bottom boundary layer show seismic anisotropy [e.g., Kendall & Silver, 1996], and thus may have been deformed by dislocation creep.

The characterisation of the rheological law is crucial because, if dislocation creep is involved in deformation, the mantle viscosity is reduced in regions where applied stresses are higher. As a result, regions of cold downwelling can be localisation centres for dislocation creep, even in a lower mantle dominated by diffusion creep [McNamara et al., 2001].

1.4. Plate tectonics – the life cycle of lithosphere

In 1912, Alfred Wegener first published the theory of ‘continental drift’ based on multidisciplinary observations that suggested that North and South America were once connected to Europe and Africa [Wegener, 1912; Wegener, 2001 (Translation by W. R. Jacoby)]. The idea that the Americas were connected to Africa and Europe was only fully accepted and further developed in the 1960s. However, the theory of continental drift was replaced by plate tectonics theory, for lack of a mechanism to explain the continental drift.

Hess and Dietz [Dietz, 1961; Hess, 1962] pioneered the concept of ‘seafloor spreading’, which describes that new seafloor originates at mid-ocean ridges and pushes the surroundings in opposite directions, to either side of the ridge. This concept, which was eventually supported by newly available geological and geophysical data (e.g., radiometric dating, seafloor topography, seafloor magnetic striping, paleomagnetism and magnetic polar wander) revolutionised geology and geophysics, paving the way for the plate tectonics theory. However, the acceptance of seafloor spreading required a mechanism to justify why there is no ocean floor older than 200 Ma. Earthquake seismology provided evidence for seafloor destruction by showing that the ocean floor is thrusted or subducted underneath continents or island arcs along trenches [Plafker, 1965; Sykes, 1966] and that most of seismic activity in the Earth occurs along these regions [Isacks et al., 1968].

Plate tectonic theory gained traction after Wilson [1965] recognized a new class of faults (transform faults) along which motion is parallel and horizontal. This led to the proposition that the lithosphere is divided into several tectonic plates that move relatively to each other [Morgan, 1968; McKenzie & Parker, 1967]. The boundaries between the plates are classified as: (1) divergent, where plates move away from each other and new lithosphere is created; (2) convergent, where plates move towards each other leading to the recycling of lithosphere by subduction or the formation of mountain ranges by continental collision; and (3) transform, where the plates move laterally relative to each other. Accordingly, the opening and closing of ocean basins is described as the Wilson cycle. Continental breakup and rifting start in response to extensional tectonic forces. Eventual sea floor spreading opens a new ocean basin and subduction initiates at its passive margins. Old oceanic lithosphere is consumed by subduction leading to the closure of the ocean and subsequent continental collision.

Subduction is the process by which lithosphere is recycled. It driven by the negative buoyancy of the subducting plate, due to plate-mantle density contrast, and is the primary driving force for plate tectonics and mantle convection [e.g., Forsyth & Uyeda, 1975; Davies & Richards, 1992; Conrad & Lithgow-Bertelloni, 2002].

1.5. Subduction processes

1.5.1. Subduction initiation

The mechanisms by which subduction initiates are still highly debated [e.g., Stern & Gerya, 2018]. Two major driving mechanisms have been classified as induced nucleation of a subduction zone (INSZ) and spontaneous nucleation of a subduction zone (SNSZ) [Stern, 2004]. INSZ occurs by the continuous convergence of the plates, which causes subsidence of the denser plate. SNSZ results from local gravitational instabilities, in which pre-existing faults or zones of lithospheric weakness promote the collapse of oceanic lithosphere. These two general mechanisms can lead to various subduction initiation scenarios that can occur in different tectonic settings such as passive margins, transform boundaries between oceanic plates, or back-arc basins [Stern, 2004].

1.5.2. Subduction evolution

Once subduction has been initiated, the negative buoyancy of the slab (i.e., the portion of the plate that is dipping into the mantle) pulls the oceanic plate to greater depths. This slab acts as a stress guide, transmitting the negative buoyancy force to the surface plate, pulling it towards the trench [Elsasser, 1969], which leads to self-sustained subduction. As a result of the balance between driving and resisting forces acting on lithospheric plates, subduction evolves in three stages: (1) a transient stage when the slab begins to sink into the mantle, (2) an interaction stage, when the slab encounters a strong density/viscosity discontinuity in the mantle, and (3) a steady state stage, when subduction reaches an almost unvarying state [e.g., Funiciello et al., 2003a; Bellahsen et al., 2005].

The driving forces of subduction include ridge-push, slab-pull and negative buoyancy due to the olivine-to-wadsleyite phase transition at ∼410 km depth. Resisting forces include bending of the lithosphere, viscous shear resulting from viscous drag in the mantle and a positive buoyancy force that results from the ringwoodite-to-perovskite plus ferropericlase phase transition at ∼660 km depth. Ridge-push forces result from gravitational forces acting on the elevated and newly formed lithosphere at mid ocean ridges, which subsides as a consequence of cooling, while it moves away from the ridge. Conversely, slab-pull forces arise from gravitational forces acting on the cold and denser slab. The slab-pull force is estimated to be an order of magnitude stronger than the ridge-push force [e.g., Moberly, 1972; Forsyth & Uyeda, 1975].

Buoyancy forces related to mineral phase transitions depend on the Clausius-Clapeyron slope of the transition and the density contrast between mineral phases. The phase transition of olivine to wadsleyite is exothermic and has a positive Clausius-Clapeyron slope. Thus, in the cold subducting plate the denser mineral phase occurs at a shallower depth, causing the transition boundary to be elevated and increasing the slab negative buoyancy, enhancing mantle convection. In contrast, the phase transition of ringwoodite to calcium-silicate perovskite (bridgmanite) and ferropericlase is endothermic and has a negative Clausius-Clapeyron slope. This causes the transition boundary to be depressed, decreasing the plate negative buoyancy and weakening the vigour of mantle convection [e.g., Turcotte & Schubert, 2014].

Finally, in order to sink into the mantle, the lithosphere must bend downwards at the trench, which dissipates energy through elastic bending and subduction-induced mantle flow. The amount of energy dissipated solely by lithospheric bending during subduction is a topic of debate. Earlier studies estimated it to be ~ 60 % [Conrad & Hager, 1999], whereas other studies suggested an even higher percentage of ~ 95 % [Bellahsen et al., 2005]. However, more recent literature indicates that this percentage may be much lower, with estimates of ~ 10 % [e.g., Capitanio et al., 2007; Schellart, 2009; Irvine & Schellart, 2012; Chen et al., 2015].

As subduction evolves, the plates at the surface move towards the trench and, at the same time, the trench also migrates [e.g., Elsasser, 1971; Molnar & Atwater, 1978; Lallemand et al., 2005; Schellart et al., 2008]. Trench migration towards the subducting plate is called trench retreat or (slab) rollback, whereas migration away from the subducting plate is called trench advance. On Earth, most trenches are presently reported to be retreating independently of the reference frame used to describe the motion of plates and plate boundaries [e.g., Schellart et al., 2008]. Trench migration is controlled by parameters such as the width of the slab [Stegman et al., 2006; Schellart et al., 2007], the stiffness of the slab [Capitanio et al., 2007; Di Giuseppe et al., 2008; Ribe, 2010; Schellart, 2008] and the proximity to the lateral borders of the subducting plate [Schellart et al., 2011]. Trench retreat is always faster closer to the lateral borders of the plate and slow far away from the borders [Schellart et al., 2008]. Additionally, migration of the trench is controlled by the boundary conditions of the trailing edge of the subducting plate (i.e., whether the plate itself moves more rapidly or slowly with respect to the trench) [Funiciello et al., 2004; Schellart, 2005; Stegman et al., 2010b].

The behaviour of the sinking slab is impacted by trench migration [e.g., Jacoby, 1976; Schellart, 2004, 2005, 2008; Stegman et al., 2010a] and depends on the subducting plate velocity. Slowly subducting plates ($0 - 3$ cm/yr) show relatively fast trench retreat and the slab sinks at low angle, folding backwards. Rapidly subducting plates (≥ 13 cm/yr) experience trench advance and the slab folds forward. Moderate subducting plates ($\sim 4 - 11$ cm/yr) display low trench motion and the slab sinks sub-vertically [Schellart, 2005]. The dip of the sinking slab results from the bending of the slab at the trench and also depends on the slab-mantle viscosity contrast and the thickness of the plate itself [e.g., Bellahsen et al., 2005; Schellart, 2008]. Thus, the catalogue of present-day subducting plates is varied and there are different modes of subduction.

Schellart [2008] classified modes of subduction based on the mantle-plate thickness ratio as well as the plate-mantle viscosity ratio for narrow plates (Figure 3) and identified four

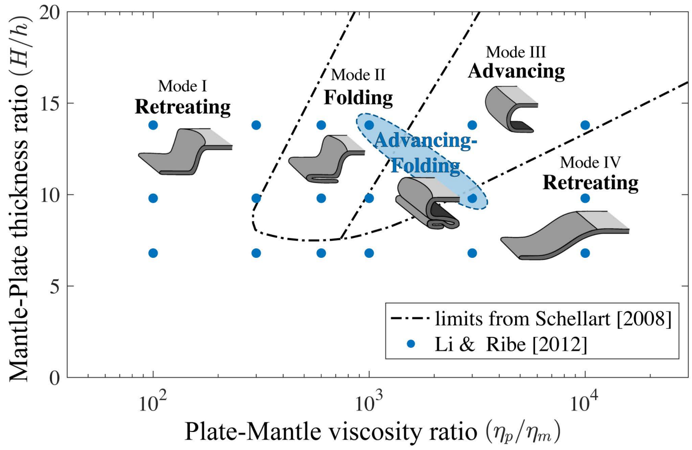

Figure 3. Subduction modes as function of plate-mantle viscosity ratio and mantle-plate thickness ratio as proposed by Schellart [2008]. Blue dots represent the numerical simulations by Li & Ribe [2012] and the region shaded in blue represents the transition mode they identified.

different modes. In mode I (retreating), subduction occurs via trench retreat, the trench is concave towards the mantle wedge, and the slab lies flat on the bottom boundary. In mode II (folding), subduction occurs by forward motion of the subducting plate, the trench motion is periodic, the trench curvature is reduced, and the slab initially folds against the bottom boundary. In mode III (advancing), subduction occurs via trench advance and forward plate motion, the trench curvature is reduced, and the slab is overturned against the bottom boundary. Lastly, in mode IV (retreating), subduction occurs by trench retreat, the trench is rectilinear, and the slab lies flat on the bottom boundary.

Similarly, Li & Ribe [2012] classified the same modes of subduction as function of the ratio between mantle thickness and initial slab length and the stiffness of the slab when subduction starts (see Chapter 2 for detailed description). These authors identified an intermediate mode between modes II and III, naming it ‘advancing-folding’ mode. In this case, trench advance is followed by trench retreat and the slab folds after being overturned against the bottom boundary. Overall, the mode of subduction is a function of the initial slab stiffness $S(0)$, the ratio between mantle thickness and initial slab length $H/l(0)$, the ratio between plate width and initial slab length $w/l(0)$, and initial slab dip angle $\theta_0(0)$. This implies that the limits of the subduction modes (Figure 3) also vary with the ratio between plate width and initial slab length [Li & Ribe, 2012].

In nature, subducting slabs have been imaged by seismicity and seismic tomography studies. A wide range of slab morphologies have been reported: from slabs trapped in the transition zone (e.g., Izu-Bonin slab, Tonga slab, North Japan slab) to slabs sinking deeply into the lower mantle (e.g., Mariana slab, Kermadec slab, Central America slab) [e.g., Fukao &

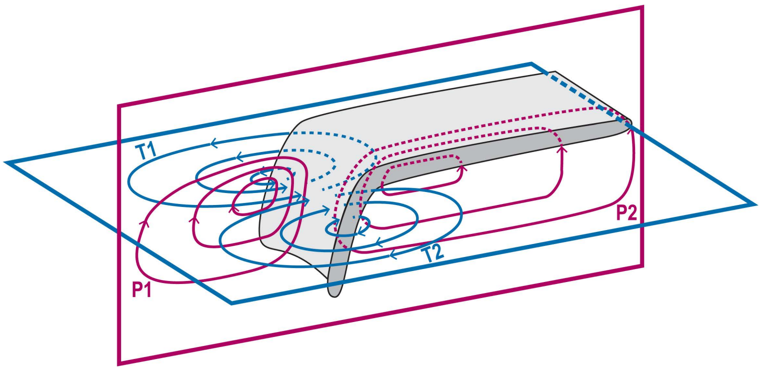

Figure 4. Schematic diagram of a subducting plate and its associated induced mantle flow [modified after Schellart, 2004]. The subduction induced mantle flow is composed by two poloidal cells and two toroidal cells. The poloidal cells are located in front of the slab (P1) and underneath the plate (P2). The toroidal cells are located around the lateral edges of the slab (T1 and T2).

Obayashi, 2013]. Most slabs that deflect horizontally upon reaching the transition zone deflect forwards, which corresponds to mode I. Moreover, there is no evidence from tomography that overturned slabs (mode III) occur in nature. The Tethys slab under the Himalayas may represent an exception, however, the mode of subduction remains inconclusive as this is a complex system involving continent-continent collision zone [Van der Voo et al., 1999]. Hence, these observations impose a limit on the slab-mantle viscosity ratio to $\sim 100 - 700$ in nature [Schellart, 2008].

As the slab sinks, subduction driven mantle flow develops, which is intrinsically three-dimensional (Figure 4). This flow is reported to have a poloidal component with a two-cell pattern. One cell is located under the plate and the other in in front of the slab. However, no mass transport occurs between the cells as the sinking slab induces rotation of the boundary between the two cells [Li & Ribe, 2012]. The flow also has a toroidal component, where the mantle material flows mainly sub-horizontally around the lateral edges of the slab [e.g., Schellart, 2008; Strak & Schellart, 2014].

During trench retreat type subduction (modes I and IV), material flows around the slab edges from underneath the subducting plate to the mantle wedge by toroidal flow [e.g., Kincaid & Griffiths, 2003; Schellart, 2004; Stegman et al., 2006], which is three to four times stronger than the poloidal flow [Stegman et al., 2006]. However, in nature, the toroidal component of the subduction induced mantle flow is significantly reduced at the centre of wide subduction zones [Schellart et al., 2007].

1.5.3. Subduction cessation and the fate of subducted plates

Subduction cessation can occur in several ways. Firstly, the negative buoyancy of the subducting plate can be lowered when features such as oceanic plateaus, seamounts, or fragments of continental crust, which are lighter than oceanic crust, subduct. As a result, the weight of the subducting slab overcomes its stretching strength, the slab becomes too weak to maintain its cohesion, and it breaks off from the surface plate [Andrews & Billen, 2009; Vogt & Gerya, 2014]. Secondly, subduction will also come to a halt once the oceanic lithosphere has been consumed and the trailing continental lithosphere reaches the trench, resulting in continent-continent collision. Lastly, subduction may also cease due to the collision of a large plateau, subduction of a ridge or transform fault, or major plate reorganization [Zeck, 1996; Wong A Ton & Wortel, 1997].

1.6. Subduction models

Since subduction is a large-scale process both in time and space, in which most of the activity takes place below the surface at inaccessible depths, the best way to study it is via indirect methods, such as geodynamic modelling. Geodynamics links together seismology, mineral physics, geochemistry, geodesy and geology. Using a continuum mechanics approach, geodynamics provides quantitative explanations (hypotheses and models) for forces and motions within Earth, focusing on ‘why’ and ‘how’ the structures inside the mantle develop. Moreover, geodynamics can provide predictions of the structural evolution of the planet.

Two main types of geodynamic models can be distinguished: 1) models focused on basic fluid dynamics that explain scaling and regimes of behaviour; and 2) models designed to match observations (seismological, geochemical, geological or geodetic). These types of models can also be classified relative to the time scale they focus on, be it instantaneous, short-term (over few hundreds of millions of years), or long term (over the 4.5 Ga of the age of the Earth).

1.6.1. Analogue and numerical models

Subduction systems are modelled to study the dynamics and kinematics of natural subduction systems at a small-scale and in relative short periods of time. One major advantage of modelling interior Earth systems is the opportunity to conduct parametric studies, i.e., investigate systematically the influence of very specific parameters thought to contribute to the geodynamic evolution of such systems.

There are two approaches to design subduction models: 1) analogue models, i.e., physical, scaled laboratory models that employ materials of scaled properties, and 2) numerical models, in which all the processes and materials have a mathematical description and the experiments are executed computationally. Although analogue and numerical modelling results can be complementary, only a small number of subduction studies published that have employed both approaches (e.g., Funiciello et al. [2003a], Schmeling et al. [2008] and Mériaux et al. [2018]).

Dimensional analysis is required to compare model and natural systems. Accordingly, the first step when modelling systems involving fluids is to identify the dimensionless numbers that characterise the processes. These numbers represent ratios that describe the behaviour of the system. Thus, both nature and model prototype will have similar dimensionless numbers. In geodynamic problems, the fluids are considered highly viscous, and the ratio between inertial forces and viscous forces, as defined by the Reynolds number, is very low. Other dimensionless numbers that are commonly used to characterised these systems are the Rayleigh number, and the Péclet number, which compares advection with conduction of heat [Turcotte & Schubert, 2014].

The main advantage of analogue models is that they are intrinsically three-dimensional. Thus, reproducing with relative ease 3D structures found in natural systems, and enabling the assessment of the effects of lateral changes in material properties. Analogue modelling of subduction is achieved using various materials to simulate both plates and mantle. The choice of materials depends on the studied system. For example, the behaviour of young oceanic lithosphere differs from old (and cold) oceanic lithosphere. As a result, the materials chosen to simulate both should reflected these differences. However, the materials must ensure proper geometric, kinematic and dynamic similarity between model and nature (see Schellart & Strak [2016] for a review on analogue modelling).

Conversely, numerical models have the advantage of facilitating the quantification of results, making it possible to track stresses, strain and strain-rates as experiments evolve. Another important advantage for this approach is the freedom and ease to implement different material properties, boundary conditions and initial geometry of the system. However, numerical models are often designed in a 2D geometry only, as the 3D geometry can be computationally demanding and requires a compromise between numerical accuracy and size of the computational domain.

1.6.2. Assumptions of numerical models

Despite the usefulness of models, there are two issues that result in uncertainties in how well the modelling results can be applied to Earth: uncertainties in physical properties and the effects of simplifying the complexity of the system being modelled. Some of the most important uncertainties relate to the density contrast between subducted oceanic lithosphere and the surrounding mantle [e.g., Kesson et al., 1998; Ono et al., 2005]. This may have significant implications regarding the ability of the plate to reach the CMB [e.g., Christensen & Hofmann, 1994; Xie & Tackley, 2004a, 2004b]. Another important uncertainty relates to the viscosity profile of the mantle, for which estimates vary greatly, especially for lower mantle depths [e.g., King, 1995; Forte & Mitrovica, 1996, 2001; Steinberger & Calderwood, 2006].

When designing models, simplifications of subduction related processes are necessary in order to isolate the effects of the parameters under investigation. This is essential due to limitations in numerical methods and available materials, as it is not possible to replicate all of the complexities associated with subduction in a single model. Thus, the geodynamic model setup highly depends on the problem being investigated.

Common assumptions focusing on subduction models include the choice of rheology of the lithospheric plates and the mantle, the thickness of the mantle and the density and viscosity layering of the mantle. In previous studies, the slab has been modelled as: viscous (with a constant viscosity) [Schellart, 2004; Funiciello et al., 2004; Enns et al., 2005]; stress-dependent, where the strain rate increases with the stress and the effective viscosity decreases non-linearly [Houseman & Gubbins, 1997]; visco-elastic, which allows the slab to maintain large deformation rates during bending and retain strength during unbending at depth [e.g., Farrington et al., 2014]; or with pseudo-plastic yielding, which approximates plate tectonics in viscous flow, but induces double-sided subduction [Moresi & Solomatov, 1998].

Moreover, the subducting lithospheric plate has also been modelled with two layers, in which the top half is visco-plastic and the bottom half is viscous [Schellart et al., 2007]; and three layers, in which during the plate bending plastic yielding occurs in the outer layers, where stresses are higher, and the centre is a strong layer that remains elastic [OzBench et al., 2008].

The rheology of the mantle is typically assumed either linear viscous, where viscosity is constant [Guillou-Frottier et al., 1995], temperature–dependent [King & Ita, 1995; Olbertz et al., 1997], visco-plastic [Burkett & Gurnis, 2013], or visco-plastic at shallow depths and linear viscous at great depths [Enns et al., 2005]. However, the lower mantle is consistently assumed to be linear viscous, due to the widely accepted suggestion that it is dominated by diffusion creep. Furthermore, the role of water is typically simplified and the grain size is neglected, despite its strong effect on viscosity during diffusion creep.

Because many subducting slabs stagnate on top on the mantle transition zone, some models assume a shallow mantle configuration, designing a domain that includes only the upper mantle or only the upper most layer of the lower mantle (the top ~ 340 km of the lower mantle). However, other studies have explored other mantle configurations and considered density and/or viscosity stratification. These configurations include: only a density contrast between the upper and lower mantle (of $\sim 10\%$) [e.g., Capitanio et al., 2009; Capitanio & Morra, 2012];

or only a viscosity ratio between the upper and lower mantle, with a range of $10 - 200$ [Faccenna et al., 2001; Funiciello et al., 2003b; Funiciello et al., 2003a; Enns et al., 2005; Quinquis et al., 2011; OzBench et al., 2008; Capitanio et al., 2011; Faccenda & Capitanio, 2013; Schellart, 2017]. Some studies have investigated subduction assuming both density and viscosity stratification, by either assuming a fixed density contrast and exploring range of viscosity ratios [Kincaid & Olson, 1987; Pusok & Kaus, 2015; Yamato et al., 2009; Capitanio & Faccenda, 2012; Capitanio, 2014], or by exploring a range of both density contrast ($0 - 90$ kg/m^3) and viscosity ratios ($1.4 - 100$) [Burkett & Gurnis, 2013].

Assumptions are also made when choosing of type of domain boundaries, which takes into account three criteria. The boundary can be: fixed or mobile and the motion can be driven internally or externally; permeable or impermeable, controlling the mass transport across the boundary; and separating two distinct materials. In analogue models, the boundaries of domain of the experiments are intuitively between a fluid and a rigid surface, i.e., the walls of the tank where the experiments are conducted, whose physical dimensions limit the processes being modelled. However, external drivers to the experiments can be put into place through the boundary walls, by using pistons that move one (or more) of the walls, by heating one (or more) walls to impose a density contrast in the system, and by including one (or more) source(s) of influx it is possible to impose a mass transport across boundaries.

In numerical models, given the flexibility in their design, there are additional choices for the type of boundaries of the considered domain, which can be defined as one of three types. If the boundaries are no-slip the fluid at the boundary has zero velocity. Domains with free-slip boundaries have zero shear stress at the walls. Free surface boundaries are characterised by zero normal and shear stress and, consequently the normal component of the velocity of the fluid equals the normal component of the velocity of the boundary. Free surface boundaries are usually defined for the top boundary to simulate the interaction between topography and the atmosphere or oceans. The lateral and bottom boundaries can introduce wall-related effects that can influence the dynamics of the processes being modelled. To work around such effects, some studies define open lateral boundaries as periodic, where the material flows in/out through one side of the models and flows out/in through the other side [Enns et al., 2005; Čížková et al., 2007; Kaus et al., 2010]. Other studies defined the domain as an infinite half space, in which the boundaries are open and infinite [Ribe, 2010; Li & Ribe, 2012].

2. Thesis aims and methods

2.1. Hypotheses

Geodynamic numerical models of subduction are tremendously useful to understand past, current and future tectonic settings. Therefore, it is important to continuously develop models and improve their accuracy. Furthermore, it is essential to clearly declare the simplifications assumed and the boundary conditions implemented in models in order to understand the full applicability of the results and the extent of the models' limitations. One way to improve the accuracy of numerical models is by systematically analysing the effects of the assumptions made on the dynamics of subduction.

For instance, geodynamic models of subduction mostly focus on 'self-sustained' subduction evolution, where subduction initiation processes are not taken into account. The instability that initiates subduction is imposed either manually or computationally assuming a slab of determined length and dip angle. In some studies, the slab initial geometry is only described as "sufficient to begin the process of subduction" [Faccenna et al., 2001; OzBench et al., 2008; Stegman et al., 2006]. However, the mode of subduction depends on the initial slab geometry and the angle at which the slab impinges on the bottom boundary [Ribe, 2010; Li & Ribe, 2012].

Additionally, in such models the whole mantle is usually assumed to be linear viscous or only the upper mantle is non-linear. The power-law rheology parameters are commonly presumed to be those of olivine, which is the most abundant mineral component in the upper mantle. However, since other mineral phases are present, the effective rheological flow law of the mantle can vary. This is typically not taken into to account in numerical models.

The dynamic evolution of a subducting plate, moreover, depends on the rheology of the mantle as well as on the upper to lower mantle density and viscosity contrasts. If subduction evolves quickly, it may induce high stress regions in the surrounding mantle. Thus, even in the linear flow dominated lower mantle, subducting slabs may localise power-law flow around them [McNamara et al., 2001].

Focusing on these two commonly overlooked model features – initial slab geometry and mantle rheology – the following hypotheses are proposed:

- The initial slab geometry, namely the slab tip length and angle, influence subduction dynamics. Their effects can be quantified.

- The addition of a power-law component to both the upper and lower mantle rheology changes trench and plate velocities.

- The interaction between a subducting slab and the mantle transition zone, with different upper to lower mantle density contrasts, varies with the addition of a power-law component to both the upper and lower mantle.

- The power-law component in the mantle rheology changes the amount of material subducted into the lower mantle over a given time.

2.2. Aims

The overarching goal of this thesis is to use numerical subduction models to assess how limiting parameters influence subduction dynamics. The parameters under investigation include the initial slab tip length and angle, power law rheology parameters, as well as the upper-lower mantle density and viscosity contrasts. The effects of such parameters are analysed and quantified relative to the i) geometric evolution of the slab, ii) sinking and trench velocities and the respective maximum velocities reached, iii) maximum subduction depth, iv) trench motion, and v) upper mantle material entrainment in the lower mantle. To this end, three objectives were defined, which form the following three research chapters of this thesis:

- Chapter 2 explores systematically how the initial slab geometry affects the subduction process dynamics.

- Chapter 3 examines how varying the power-law parameters of both upper and lower mantle rheology, and the upper-lower mantle density and viscosity contrasts effects the behaviour of a subducting plate.

- Chapter 4 evaluates the amount of material subducted into the lower mantle and the implications for recycling of material within the mantle.

These objectives contribute to a better understanding of the implications of common assumptions in numerical models of subduction. By quantifying the contribution of the slab initial geometry and the power-law mantle rheology, future models can be built with an increased confidence regarding their accuracy or relevance to nature.

2.3. Thesis structure

This thesis comprises an introduction chapter, three research chapters and a conclusion chapter. The research chapters are formatted as stand-alone manuscripts prepared for submission to peer-reviewed journals, which is an accepted thesis format structure at Monash University. This has inevitably resulted in the repetition of background information and methodology descriptions in several chapters.

Chapter 1: *Introduction*; presents the rationale behind this thesis and describes the background topics and methods related to subduction systems and subduction evolution.

Chapter 2: *The initial geometry of the slab and its effects on subduction evolution*; addresses the effects of the initial slab geometry on subduction evolution. The aim of this chapter is to highlight the importance of defining an appropriate initial slab geometry that drives subduction.

Chapter 3: *Exploring power-law rheology in the upper and lower mantle during subduction*; discusses the use of non-linear viscosity in both upper and lower mantle. As slabs induce high stresses, the way mantle deforms to accommodate subduction may be more complex than models in the current literature suggest. These results are also discussed from a surface tectonics perspective, quantifying trench migration and plate velocity in the context of variable upper to lower mantle density and viscosity contrasts.

Chapter 4: *Entrainment of upper mantle by subducted slabs*. The results of assuming a non-linear viscosity in both upper and lower mantle, and considering different mantle density profiles (as examined in Chapter 3), are discussed from a geochemical perspective. The amount of upper mantle entrainment into the lower mantle is quantified and the role of subduction in the global convection system and mantle material recycling is discussed.

Chapter 5: *Conclusions* synthesise the main outcomes and general findings of the research chapters. Future potential research topics are briefly described.

2.4. Methods

2.4.1. Numerical approach

In this thesis, the numerical models of subduction are two-dimensional and consist of a single lithospheric plate that initially lies on top of the mantle. The tip of the slab is initially kinked, dipping into the mantle and this acts as the instability that starts subduction. The overall subduction system is simplified by making the following assumptions (as described in detail in Chapters 2 and 3):

1. The lithospheric plate is linear viscous, because over geological timescales, subducting slabs behave like a fluid [Houseman & Gubbins, 1997].

2. The plate represents oceanic lithosphere, which is compositionally homogeneous. The negative buoyancy of the slab is the only force driving subduction and there are no external forces acting on the plate, such as ridge-push or pre-existing mantle convection.

3. Heat transfer in the mantle occurs primarily by convection, since in nature the Rayleigh number is high ($5 \times 10^5 - 5 \times 10^7$). It is also assumed that temperature dependent effects are confined to the top and bottom boundary layers (i.e., the lithosphere and the core-mantle boundary, respectively). Thus, thermal effects are not included in the system.

4. The overriding plate is passive. Interactions between subducting slabs and overriding plates are complex and beyond the scope of this study.

5. The subducting plate is infinitely wide and the 2D geometry corresponds to a cross-section at the centre of the subduction zone, where subduction induced mantle flow occurs mainly through poloidal flow.

6. The ~ 660 km mantle discontinuity is the only mantle discontinuity implemented. This discontinuity represents a resistance to the sinking of the slab due to the negative Clausius-Clapeyron slope of the ringwoodite phase transition.

2.4.2. Numerical code

To study the various components of interior Earth systems, a number of numerical codes have been previously developed. A list of examples includes: CITCOM [Zhong et al., 2000], DOUAR [Braun et al., 2008], FANTOM [Thieulot, 2011], IELVIS [Gerya & Yuen, 2007], LaMEM [Kaus et al., 2016], pTatin [May et al., 2014], SLIM3D [Popov & Sobolev, 2008], SOPALE [Fullsack, 1995], StaggYY [Tackley, 2008], SULEC[1] and Underworld2[2].

In this thesis, all numerical simulations of subduction were performed with Underworld2. This code was chosen as the developers were based at Monash University and at the University of Melbourne, facilitating numerical support in building and executing simulations. Underworld2 is a Python-friendly open-source code, tuned for large-scale geodynamic problems that can be run on a parallel High-Performing Computer (HPC). It is a hybrid, parallel particle-in-cell finite element code that solves the governing conservation equations on an

[1] http://www.geodynamics.no/buiter/sulec.html
[2] http://www.underworldcode.org/

Eulerian Finite Element mesh. Within each mesh element, a swarm of Lagrangian particles is employed to carry the material properties, such as density and viscosity [Moresi et al., 2003; Moresi et al., 2007; Moresi et al., 2002]. All simulations used a multigrid solver, with a total of 20 particles per element.

The subduction system is described by the equations of conservation of momentum and conservation of mass for an incompressible fluid:

$$\nabla \cdot \boldsymbol{\tau} - \nabla p = \Delta\rho \boldsymbol{g}, \tag{3}$$

$$\nabla \cdot \boldsymbol{u} = 0, \tag{4}$$

where $\boldsymbol{u}$ is the velocity, p is the dynamic pressure, $\Delta\rho$ is the density contrast, $\boldsymbol{g}$ is the gravitational acceleration and $\boldsymbol{\tau}$ is the deviatoric stress tensor,

$$\tau_{ij} = \eta\left(\frac{\partial u_i}{\partial x_j} + \frac{\partial u_j}{\partial x_i}\right), \tag{5}$$

where η is the dynamic viscosity and $\boldsymbol{x}$ is the position.

The numerical experiments were performed with a uniform Cartesian mesh, in which each element corresponds to $\sim 9 \times 9$ km^2 and contains a total of 20 Lagrangian particles.

2.4.3. Supercomputer usage and experimental analysis

The numerical experiments were executed by running of Python scripts in parallel, using resources available at Monash – MonARCH (Monash Advanced Research Computing Hybrid)[3], and at the NCI (National Computational Infrastructure[4]). MonARCH is a HPC/HTC (High Performance Computing/High-Throughput Computing) cluster provisioned through the Research Cloud at Monash e-solutions facilities. The NCI resources were made available under the National Computational Merit Allocation Scheme (NCMAS) during 2016-2019. NCI enabled access to the high-performance, distributed-memory cluster Raijin[5].

The following software was used:

- Underworld2 – numerical code to solve large-scale geodynamic problems
- Jupyter Notebook – to build and test models scripts using programming language Python
- LavaVu – a scientific visualisation tool, which is part of Underworld2

[3] https://docs.monarch.erc.monash.edu/

[4] http://nci.org.au/

[5] http://nci.org.au/systems-services/peak-system/raijin/

- MATLAB® – to plot slab vertical position, trench migration, calculate sinking velocities, calculate plate elongation and material entrainment
- Adobe Illustrator CC – for image processing

3. References

Akaogi, M., Ito, E. & Navrotsky, A. (1989), Olivine-modified spinel-spinel transitions in the system Mg_2SiO_4-Fe_2SiO_4: calorimetric measurements, thermochemical calculation, and geophysical application. *J. Geophys. Res. Solid Earth*, 94(B11), 15671-15685, doi: 10.1029/JB094iB11p15671.

Anderson, D. L. (1967), Phase changes in the upper mantle. *Science*, 157(3793), 1165-73, doi: 10.1126/science.157.3793.1165.

Andrews, E. R. & Billen, M. I. (2009), Rheologic controls on the dynamics of slab detachment. *Tectonophysics*, 464(1-4), 60-69, doi: 10.1016/j.tecto.2007.09.004.

Ashby, M. F. (1972), A first report on deformation-mechanism maps. *Acta Metallurgica*, 20(7), 887-897, doi: 10.1016/0001-6160(72)90082-x.

Bellahsen, N., Faccenna, C. & Funiciello, F. (2005), Dynamics of subduction and plate motion in laboratory experiments: Insights into the "plate tectonics" behavior of the Earth. *J. Geophys. Res.*, 110(B1), B01401, doi: 10.1029/2004jb002999.

Braun, J., Thieulot, C., Fullsack, P., DeKool, M., Beaumont, C. & Huismans, R. (2008), DOUAR: A new three-dimensional creeping flow numerical model for the solution of geological problems. *Phys. Earth Planet. Inter.*, 171(1-4), 76-91, doi: 10.1016/j.pepi.2008.05.003.

Burkett, E. & Gurnis, M. (2013), Stalled slab dynamics. *Lithosphere*, 5(1), 92-97, doi: 10.1130/L249.1.

Capitanio, F. A. (2014), The dynamics of extrusion tectonics: Insights from numerical modeling. *Tectonics*, 33(12), 2361-2381, doi: 10.1002/2014tc003688.

Capitanio, F. A. & Faccenda, M. (2012), Complex mantle flow around heterogeneous subducting oceanic plates. *Earth Planet. Sci. Lett.*, 353-354, 29-37, doi: 10.1016/j.epsl.2012.07.042.

Capitanio, F. A., Faccenna, C., Zlotnik, S. & Stegman, D. R. (2011), Subduction dynamics and the origin of Andean orogeny and the Bolivian orocline. *Nature*, 480(7375), 83-6, doi: 10.1038/nature10596.

Capitanio, F. A. & Morra, G. (2012), The bending mechanics in a dynamic subduction system: Constraints from numerical modelling and global compilation analysis. *Tectonophysics*, 522-523, 224-234, doi: 10.1016/j.tecto.2011.12.003.

Capitanio, F. A., Morra, G. & Goes, S. (2007), Dynamic models of downgoing plate-buoyancy driven subduction: Subduction motions and energy dissipation. *Earth Planet. Sci. Lett.*, 262(1-2), 284-297, doi: 10.1016/j.epsl.2007.07.039.

Capitanio, F. A., Morra, G. & Goes, S. (2009), Dynamics of plate bending at the trench and slab-plate coupling. *Geochem. Geophys. Geosyst.*, 10(4), Q04002, doi: 10.1029/2008gc002348.

Chen, Z. H., Schellart, W. P. & Duarte, J. C. (2015), Quantifying the energy dissipation of overriding plate deformation in three-dimensional subduction models. *J. Geophys. Res. Solid Earth*, 120(1), 519-536, doi: 10.1002/2014jb011419.

Christensen, U. R. & Hofmann, A. W. (1994), Segregation of subducted oceanic-crust in the convecting mantle. *J. Geophys. Res. Solid Earth*, 99(B10), 19867-19884, doi: 10.1029/93jb03403.

Čížková, H., van Hunen, J. & van den Berg, A. (2007), Stress distribution within subducting slabs and their deformation in the transition zone. *Phys. Earth Planet. Int.*, 161(3-4), 202-214, doi: 10.1016/j.pepi.2007.02.002.

Conrad, C. P. & Hager, B. H. (1999), Effects of plate bending and fault strength at subduction zones on plate dynamics. *J. Geophys. Res.*, 104(B8), 17551-17571, doi: 10.1029/1999jb900149.

Conrad, C. P. & Lithgow-Bertelloni, C. (2002), How mantle slabs drive plate tectonics. *Science*, 298(5591), 207-209, doi: 10.1126/science.1074161.

Conrad, C. P., Steinberger, B. & Torsvik, T. H. (2013), Stability of active mantle upwelling revealed by net characteristics of plate tectonics. *Nature*, 498(7455), 479-82, doi: 10.1038/nature12203.

Davies, G. F. & Richards, M. A. (1992), Mantle Convection. *Journal of Geology*, 100(2), 151-206, doi: 10.1086/629582.

Di Giuseppe, E., van Hunen, J., Funiciello, F., Faccenna, C. & Giardini, D. (2008), Slab stiffness control of trench motion: Insights from numerical models. *Geochem. Geophys. Geosyst.*, 9(2), Q02014, doi: 10.1029/2007gc001776.

Dietz, R. S. (1961), Continent and ocean basin evolution by spreading of the sea floor. *Nature*, 190(4779), 854-857, doi: 10.1038/190854a0.

Dziewonski, A. M., Lekic, V. & Romanowicz, B. A. (2010), Mantle Anchor Structure: An argument for bottom up tectonics. *Earth Planet. Sci. Lett.*, 299(1-2), 69-79, doi: 10.1016/j.epsl.2010.08.013.

Elsasser, W. M. (1969) *Convection and stress propagation in the upper mantle*. In The application of modern physics to the Earth and planetary interiors, edited by S. K. Runcorn, pp. 223-246, Wiley-Interscience, Lodon, 1969. doi: 10.1126/science.167.3924.1482

Elsasser, W. M. (1971), Sea-Floor Spreading as Thermal Convection. *J. Geophys. Res.*, 76(5), 1101-1112, doi: 10.1029/JB076i005p01101.

Enns, A., Becker, T. W. & Schmeling, H. (2005), The dynamics of subduction and trench migration for viscosity stratification. *Geophys. J. Int.*, 160(2), 761-775, doi: 10.1111/j.1365-246X.2005.02519.x.

Faccenda, M. & Capitanio, F. A. (2013), Seismic anisotropy around subduction zones: Insights from three-dimensional modeling of upper mantle deformation and SKS splitting calculations. *Geochem. Geophys. Geosyst.*, 14(1), 243-262, doi: 10.1029/2012gc004451.

Faccenna, C., Funiciello, F., Giardini, D. & Lucente, P. (2001), Episodic back-arc extension during restricted mantle convection in the Central Mediterranean. *Earth Planet. Sci. Lett.*, 187(1-2), 105-116, doi: 10.1016/S0012-821x(01)00280-1.

Farrington, R. J., Moresi, L. N. & Capitanio, F. A. (2014), The role of viscoelasticity in subducting plates. *Geochem. Geophys. Geosyst.*, 15(11), 4291-4304, doi: 10.1002/2014gc005507.

Forsyth, D. & Uyeda, S. (1975), On the Relative Importance of the Driving Forces of Plate Motion. *Geophys. J. Int.*, 43(1), 163-200, doi: 10.1111/j.1365-246X.1975.tb00631.x.

Forte, A. M. & Mitrovica, J. X. (1996), New inferences of mantle viscosity from joint inversion of long-wavelength mantle convection and post-glacial rebound data. *Geophys. Res. Lett.*, 23(10), 1147-1150, doi: 10.1029/96gl00964.

Forte, A. M. & Mitrovica, J. X. (2001), Deep-mantle high-viscosity flow and thermochemical structure inferred from seismic and geodynamic data. *Nature*, 410(6832), 1049-1056, doi: 10.1038/35074000.

Fowler, C. M. R. (2004) *The Solid Earth: An Introduction to Global Geophysics*. 2nd edition. Cambridge: Cambridge University Press. doi: 10.1017/CBO9780511819643

Fukao, Y. & Obayashi, M. (2013), Subducted slabs stagnant above, penetrating through, and trapped below the 660 km discontinuity. *J. Geophys. Res. Solid Earth*, 118(11), 5920-5938, doi: 10.1002/2013jb010466.

Fullsack, P. (1995), An arbitrary Lagrangian-Eulerian formulation for creeping flows and its application in tectonic models. *Geophys. J. Int.*, 120(1), 1-23, doi: 10.1111/j.1365-246X.1995.tb05908.x.

Funiciello, F., Faccenna, C. & Giardini, D. (2004), Role of lateral mantle flow in the evolution of subduction systems: insights from laboratory experiments. *Geophys. J. Int.*, 157(3), 1393-1406, doi: 10.1111/j.1365-246X.2004.02313.x.

Funiciello, F., Faccenna, C., Giardini, D. & Regenauer-Lieb, K. (2003a), Dynamics of retreating slabs: 2. Insights from three-dimensional laboratory experiments. *J. Geophys. Res.*, 108(B4), 2207, doi: 10.1029/2001jb000896.

Funiciello, F., Morra, G., Regenauer-Lieb, K. & Giardini, D. (2003b), Dynamics of retreating slabs: 1. Insights from two-dimensional numerical experiments. *J. Geophys. Res.*, 108(B4), 2206, doi: 10.1029/2001jb000898.

Garnero, E. J. (2004), A new paradigm for Earth's core-mantle boundary. *Science*, 304(5672), 834-6, doi: 10.1126/science.1097849.

Gerya, T. V. & Yuen, D. A. (2007), Robust characteristics method for modelling multiphase visco-elasto-plastic thermo-mechanical problems. *Phys. Earth Planet. Inter.*, 163(1-4), 83-105, doi: 10.1016/j.pepi.2007.04.015.

Guillou-Frottier, L., Buttles, J. & Olson, P. (1995), Laboratory Experiments on the Structure of Subducted Lithosphere. *Earth Planet. Sci. Lett.*, 133(1-2), 19-34, doi: 10.1016/0012-821x(95)00045-E.

Hess, H. H. (1962) History of Ocean Basins, in Engel, A. E. J., James, H. L. & Leonard, B. F. (eds), *Petrologic Studies*. Geological Society of America, 599-620. doi: 10.1130/Petrologic.1962.599

Houseman, G. A. & Gubbins, D. (1997), Deformation of subducted oceanic lithosphere. *Geophys. J. Int.*, 131(3), 535-551, doi: 10.1111/j.1365-246X.1997.tb06598.x.

Irifune, T. & Tsuchiya, T. (2015) Phase Transitions and Mineralogy of the Lower Mantle, *Treatise on Geophysics*. Elsevier, 33-60. doi: 10.1016/b978-0-444-53802-4.00030-0

Irvine, D. N. & Schellart, W. P. (2012), Effect of plate thickness on bending radius and energy dissipation at the subduction zone hinge. *J. Geophys. Res. Solid Earth*, 117, B06405, doi: 10.1029/2011jb009113.

Isacks, B., Oliver, J. & Sykes, L. R. (1968), Seismology and the new global tectonics. *J. Geophys. Res.*, 73(18), 5855-5899, doi: 10.1029/JB073i018p05855.

Ita, J. & Stixrude, L. (1992), Petrology, Elasticity, and Composition of the Mantle Transition Zone. *J. Geophys. Res. Solid Earth*, 97(B5), 6849-6866, doi: 10.1029/92jb00068.

Ito, E. & Takahashi, E. (1989), Postspinel transformations in the system Mg_2SiO_4-$Fe_2SiO_4$and some geophysical implications. *J. Geophys. Res. Solid Earth*, 94(B8), 10637-10646, doi: 10.1029/JB094iB08p10637.

Jacoby, W. R. (1976), Paraffin model experiment of plate tectonics. *Tectonophysics*, 35(1-3), 103-113, doi: 10.1016/0040-1951(76)90031-7.

Karato, S. (2008) *Deformation of earth materials: an introduction to the rheology of solid earth*. Cambridge: Cambridge : Cambridge University Press. doi: 10.1017/cbo9780511804892

Karato, S. (2010), Rheology of the Earth's mantle: A historical review. *Gondwana Research*, 18(1), 17-45, doi: 10.1016/j.gr.2010.03.004.

Katsura, T. & Ito, E. (1989), The system Mg_2SiO_4-Fe_2SiO_4 at high pressures and temperatures: Precise determination of stabilities of olivine, modified spinel, and spinel. *J. Geophys. Res. Solid Earth*, 94(B11), 15663-15670, doi: 10.1029/JB094iB11p15663.

Kaus, B. J. P., Mühlhaus, H. & May, D. A. (2010), A stabilization algorithm for geodynamic numerical simulations with a free surface. *Phys. Earth Planet. Inter.*, 181(1-2), 12-20, doi: 10.1016/j.pepi.2010.04.007.

Kaus, B. J. P., Popov, A. A., Baumann, T. S., Püsök, A. E., Bauville, A., Fernandez, N. & Collignon, M. (2016), Forward and inversemodeling of lithospheric deformation on geological timescales. *NIC Symposium 2016—Proceedings*, 48, 299-307, doi:

Kendall, J. M. & Silver, P. G. (1996), Constraints from seismic anisotropy on the nature of the lowermost mantle. *Nature*, 381(6581), 409-412, doi: 10.1038/381409a0.

Kennett, B. L. N., Engdahl, E. R. & Buland, R. (1995), Constraints on seismic velocities in the Earth from traveltimes. *Geophys. J. Int.*, 122(1), 108-124, doi: 10.1111/j.1365-246X.1995.tb03540.x.

Kesson, S. E., Fitz Gerald, J. D. & Shelley, J. M. (1998), Mineralogy and dynamics of a pyrolite lower mantle. *Nature*, 393(6682), 252-255, doi: 10.1038/30466.

Kincaid, C. & Griffiths, R. W. (2003), Laboratory models of the thermal evolution of the mantle during rollback subduction. *Nature*, 425(6953), 58-62, doi: 10.1038/nature01923.

Kincaid, C. & Olson, P. (1987), An Experimental Study of Subduction and Slab Migration. *J. Geophys. Res.*, 92(B13), 13832-13840, doi: 10.1029/JB092iB13p13832.

King, S. D. (1995), The viscosity structure of the mantle. *Reviews of Geophysics*, 33, 11-17, doi: 10.1029/95rg00279.

King, S. D. & Ita, J. (1995), Effect of slab rheology on mass transport across a phase transition boundary. *J. Geophys. Res.*, 100(B10), 20211-20222, doi: 10.1029/95jb01964.

Kushiro, I. (1968), Compositions of magmas formed by partial zone melting of the Earth's upper mantle. *J. Geophys. Res.*, 73(2), 619-634, doi: 10.1029/JB073i002p00619.

Lallemand, S., Heuret, A. & Boutelier, D. (2005), On the relationships between slab dip, back-arc stress, upper plate absolute motion, and crustal nature in subduction zones. *Geochem. Geophys. Geosyst.*, 6, Q09006, doi: 10.1029/2005gc000917.

Lay, T., Williams, Q. & Garnero, E. J. (1998), The core–mantle boundary layer and deep Earth dynamics. *Nature*, 392(6675), 461-468, doi: 10.1038/33083.

Li, Z. H. & Ribe, N. M. (2012), Dynamics of free subduction from 3-D boundary element modeling. *J. Geophys. Res.*, 117, B06408, doi: 10.1029/2012jb009165.

May, D. A., Brown, J. & Le Pourhiet, L. (2014), pTatin3D: High-Performance Methods for Long-Term Lithospheric Dynamics. *Sc14: International Conference for High Performance Computing, Networking, Storage and Analysis*, 274-284, doi: 10.1109/Sc.2014.28.

McDonough, W. F. & Sun, S. (1995), The composition of the Earth. *Chemical Geology*, 120(3-4), 223-253, doi: 10.1016/0009-2541(94)00140-4.

McKenzie, D. P. & Parker, R. L. (1967), The North Pacific: an Example of Tectonics on a Sphere. *Nature*, 216(5122), 1276-1280, doi: 10.1038/2161276a0.

McNamara, A. K., Karato, S.-I. & van Keken, P. E. (2001), Localization of dislocation creep in the lower mantle: implications for the origin of seismic anisotropy. *Earth Planet. Sci. Lett.*, 191(1-2), 85-99, doi: 10.1016/s0012-821x(01)00405-8.

Mehrabi, M. & Setayeshi, S. (2012), Computational Fluid Dynamics Analysis of Pulsatile Blood Flow Behavior in Modelled Stenosed Vessels with Different Severities. *Mathematical Problems in Engineering*, 2012, 1-13, doi: 10.1155/2012/804765.

Mériaux, C. A., May, D. A., Mansour, J., Chen, Z. & Kaluza, O. (2018), Benchmark of three-dimensional numerical models of subduction against a laboratory experiment. *Phys. Earth Planet. Inter.*, 283, 110-121, doi: 10.1016/j.pepi.2018.07.009.

Mitrovica, J. X. & Forte, A. M. (1997), Radial profile of mantle viscosity: Results from the joint inversion of convection and postglacial rebound observables. *J. Geophys. Res. Solid Earth*, 102(B2), 2751-2769, doi: 10.1029/96jb03175.

Moberly, R. (1972) Origin of Lithosphere behind Island Arcs, with Reference to the Western Pacific, *Studies in Earth and Space Sciences*. Geological Society of America Memoirs, 35-56. doi: 10.1130/MEM132-p35

Molnar, P. & Atwater, T. (1978), Interarc spreading and Cordilleran tectonics as alternates related to the age of subducted oceanic lithosphere. *Earth Planet. Sci. Lett.*, 41(3), 330-340, doi: 10.1016/0012-821x(78)90187-5.

Moresi, L., Dufour, F. & Mühlhaus, H. B. (2002), Mantle convection modeling with viscoelastic/brittle lithosphere: Numerical methodology and plate tectonic modeling. *Pure and Applied Geophysics*, 159(10), 2335-2356, doi: 10.1007/s00024-002-8738-3.

Moresi, L., Dufour, F. & Mühlhaus, H. B. (2003), A Lagrangian integration point finite element method for large deformation modeling of viscoelastic geomaterials. *J. Comput. Phys.*, 184(2), 476-497, doi: 10.1016/S0021-9991(02)00031-1.

Moresi, L., Quenette, S., Lemiale, V., Mériaux, C., Appelbe, B. & Mühlhaus, H. B. (2007), Computational approaches to studying non-linear dynamics of the crust and mantle. *Phys. Earth Planet. Inter.*, 163(1-4), 69-82, doi: 10.1016/j.pepi.2007.06.009.

Moresi, L. & Solomatov, V. (1998), Mantle convection with a brittle lithosphere: thoughts on the global tectonic styles of the Earth and Venus. *Geophys. J. Int.*, 133(3), 669-682, doi: 10.1046/j.1365-246X.1998.00521.x.

Morgan, W. J. (1968), Rises, trenches, great faults, and crustal blocks. *J. Geophys. Res.*, 73(6), 1959-1982, doi: 10.1029/JB073i006p01959.

Olbertz, D., Wortel, M. J. R. & Hansen, U. (1997), Trench migration and subduction zone geometry. *Geophys. Res. Lett.*, 24(3), 221-224, doi: 10.1029/96gl03971.

Ono, S., Ohishi, Y., Isshiki, M. & Watanuki, T. (2005), In situ X-ray observations of phase assemblages in peridotite and basalt compositions at lower mantle conditions: Implications for density of subducted oceanic plate. *J. Geophys. Res. Solid Earth*, 110, B02208, doi: 10.1029/2004jb003196.

OzBench, M., Regenauer-Lieb, K., Stegman, D. R., Morra, G., Farrington, R., Hale, A., May, D. A., Freeman, J., Bourgouin, L., Mühlhaus, H. & Moresi, L. (2008), A model comparison study of large-scale mantle-lithosphere dynamics driven by subduction. *Phys. Earth Planet. Inter.*, 171(1-4), 224-234, doi: 10.1016/j.pepi.2008.08.011.

Plafker, G. (1965), Tectonic Deformation Associated with the 1964 Alaska Earthquake: The earthquake of 27 March 1964 resulted in observable crustal deformation of unprecedented areal extent. *Science*, 148(3678), 1675-87, doi: 10.1126/science.148.3678.1675.

Popov, A. A. & Sobolev, S. V. (2008), SLIM3D: A tool for three-dimensional thermomechanical modeling of lithospheric deformation with elasto-visco-plastic rheology. *Phys. Earth Planet. Inter.*, 171(1-4), 55-75, doi: 10.1016/j.pepi.2008.03.007.

Pusok, A. E. & Kaus, B. J. P. (2015), Development of topography in 3-D continental-collision models. *Geochem. Geophys. Geosyst.*, 16(5), 1378-1400, doi: 10.1002/2015gc005732.

Quinquis, M. E. T., Buiter, S. J. H. & Ellis, S. (2011), The role of boundary conditions in numerical models of subduction zone dynamics. *Tectonophysics*, 497(1-4), 57-70, doi: 10.1016/j.tecto.2010.11.001.

Rayleigh (1916), LIX. On convection currents in a horizontal layer of fluid, when the higher temperature is on the under side. *The London, Edinburgh, and Dublin Philosophical Magazine and Journal of Science*, 32(192), 529-546, doi: 10.1080/14786441608635602.

Ribe, N. M. (2010), Bending mechanics and mode selection in free subduction: a thin-sheet analysis. *Geophys. J. Int.*, 180(2), 559-576, doi: 10.1111/j.1365-246X.2009.04460.x.

Schellart, W. P. (2004), Kinematics of subduction and subduction-induced flow in the upper mantle. *J. Geophys. Res.*, 109, B07401, doi: 10.1029/2004jb002970.

Schellart, W. P. (2005), Influence of the subducting plate velocity on the geometry of the slab and migration of the subduction hinge. *Earth Planet. Sci. Lett.*, 231(3-4), 197-219, doi: 10.1016/j.epsl.2004.12.019.

Schellart, W. P. (2008), Kinematics and flow patterns in deep mantle and upper mantle subduction models: Influence of the mantle depth and slab to mantle viscosity ratio. *Geochem. Geophys. Geosyst.*, 9, Q03014, doi: 10.1029/2007gc001656.

Schellart, W. P. (2009), Evolution of the slab bending radius and the bending dissipation in three-dimensional subduction models with a variable slab to upper mantle viscosity ratio. *Earth Planet. Sci. Lett.*, 288(1-2), 309-319, doi: 10.1016/j.epsl.2009.09.034.

Schellart, W. P. (2017), A geodynamic model of subduction evolution and slab detachment to explain Australian plate acceleration and deceleration during the latest Cretaceous–early Cenozoic. *Lithosphere*, 9(6), 976-986, doi: 10.1130/l675.1.

Schellart, W. P., Freeman, J., Stegman, D. R., Moresi, L. & May, D. (2007), Evolution and diversity of subduction zones controlled by slab width. *Nature*, 446(7133), 308-311, doi: 10.1038/nature05615.

Schellart, W. P., Stegman, D. R., Farrington, R. J. & Moresi, L. (2011), Influence of lateral slab edge distance on plate velocity, trench velocity, and subduction partitioning. *J. Geophys. Res.*, 116, B10408, doi: 10.1029/2011jb008535.

Schellart, W. P., Stegman, D. R. & Freeman, J. (2008), Global trench migration velocities and slab migration induced upper mantle volume fluxes: Constraints to find an Earth reference frame based on minimizing viscous dissipation. *Earth Sci. Rev.*, 88(1-2), 118-144, doi: 10.1016/j.earscirev.2008.01.005.

Schellart, W. P. & Strak, V. (2016), A review of analogue modelling of geodynamic processes: Approaches, scaling, materials and quantification, with an application to subduction experiments. *Journal of Geodynamics*, 100, 7-32, doi: 10.1016/j.jog.2016.03.009.

Schmeling, H., Babeyko, A. Y., Enns, A., Faccenna, C., Funiciello, F., Gerya, T., Golabek, G. J., Grigull, S., Kaus, B. J. P., Morra, G., Schmalholz, S. M. & van Hunen, J. (2008), A benchmark comparison of spontaneous subduction models – Towards a free surface. *Phys. Earth Planet. Inter.*, 171(1-4), 198-223, doi: 10.1016/j.pepi.2008.06.028.

Shearer, P. M. (1990), Seismic imaging of upper-mantle structure with new evidence for a 520-km discontinuity. *Nature*, 344(6262), 121-126, doi: 10.1038/344121a0.

Shearer, P. M. & Masters, T. G. (1992), Global Mapping of Topography on the 660-Km Discontinuity. *Nature*, 355(6363), 791-796, doi: 10.1038/355791a0.

Silver, P. G., Carlson, R. W. & Olson, P. (1988), Deep slabs, geochemical heterogeneity, and the large-scale structure of mantle convection: investigation of an enduring paradox. *Annu. Rev. Earth Planet Sci.*, 16(1), 477-541, doi: 10.1146/annurev.ea.16.050188.002401.

Stegman, D. R., Farrington, R., Capitanio, F. A. & Schellart, W. P. (2010a), A regime diagram for subduction styles from 3-D numerical models of free subduction. *Tectonophysics*, 483(1-2), 29-45, doi: 10.1016/j.tecto.2009.08.041.

Stegman, D. R., Freeman, J., Schellart, W. P., Moresi, L. & May, D. (2006), Influence of trench width on subduction hinge retreat rates in 3-D models of slab rollback. *Geochem. Geophys. Geosyst.*, 7, Q03012, doi: 10.1029/2005gc001056.

Stegman, D. R., Schellart, W. P. & Freeman, J. (2010b), Competing influences of plate width and far-field boundary conditions on trench migration and morphology of subducted slabs in the upper mantle. *Tectonophysics*, 483(1-2), 46-57, doi: 10.1016/j.tecto.2009.08.026.

Steinberger, B. & Calderwood, A. R. (2006), Models of large-scale viscous flow in the Earth's mantle with constraints from mineral physics and surface observations. *Geophys. J. Int.*, 167(3), 1461-1481, doi: 10.1111/j.1365-246X.2006.03131.x.

Stern, R. J. (2004), Subduction initiation: spontaneous and induced. *Earth Planet. Sci. Lett.*, 226(3-4), 275-292, doi: 10.1016/j.epsl.2004.08.007.

Stern, R. J. & Gerya, T. (2018), Subduction initiation in nature and models: A review. *Tectonophysics*, 746, 173-198, doi: 10.1016/j.tecto.2017.10.014.

Strak, V. & Schellart, W. P. (2014), Evolution of 3-D subduction-induced mantle flow around lateral slab edges in analogue models of free subduction analysed by stereoscopic particle image velocimetry technique. *Earth Planet. Sci. Lett.*, 403, 368-379, doi: 10.1016/j.epsl.2014.07.007.

Sykes, L. R. (1966), The seismicity and deep structure of Island arcs. *J. Geophys. Res.*, 71(12), 2981-3006, doi: 10.1029/JZ071i012p02981.

Tackley, P. J. (2008), Modelling compressible mantle convection with large viscosity contrasts in a three-dimensional spherical shell using the yin-yang grid. *Phys. Earth Planet. Inter.*, 171(1-4), 7-18, doi: 10.1016/j.pepi.2008.08.005.

Thieulot, C. (2011), FANTOM: Two- and three-dimensional numerical modelling of creeping flows for the solution of geological problems. *Phys. Earth Planet. Inter.*, 188(1-2), 47-68, doi: 10.1016/j.pepi.2011.06.011.

Turcotte, D. L. & Schubert, G. (2014) *Geodynamics*. Cambridge: Cambridge University Press. doi: 10.1017/CBO9780511843877

Van der Voo, R., Spakman, W. & Bijwaard, H. (1999), Tethyan subducted slabs under India. *Earth Planet. Sci. Lett.*, 171(1), 7-20, doi: 10.1016/s0012-821x(99)00131-4.

Vidale, J. E., Ding, X.-Y. & Grand, S. P. (1995), The 410-km-depth discontinuity: A sharpness estimate from near-critical reflections. *Geophys. Res. Lett.*, 22(19), 2557-2560, doi: 10.1029/95gl02663.

Vogt, K. & Gerya, T. V. (2014), From oceanic plateaus to allochthonous terranes: Numerical modelling. *Gondwana Research*, 25(2), 494-508, doi: 10.1016/j.gr.2012.11.002.

Wada, I. & King, S. (2015) Dynamics of Subducting Slabs: Numerical Modeling and Constraints from Seismology, Geoid, Topography, Geochemistry, and Petrology, *Treatise on Geophysics*. Elsevier, 339-391. doi: 10.1016/b978-0-444-53802-4.00132-9

Wegener, A. (1912), Die Entstehung der Kontinente. *Geologische Rundschau*, 3(4), 276-292, doi: 10.1007/bf02202896.

Wegener, A. (2001), The origins of the continents, Translation of Die Entstehung der Kontinente Dr Alfred Wegener Petermanns Geographische Mitteilungen, 58 I, 185–195, 253–256, 305–309, 1912. *Journal of Geodynamics*, 32(1-2), 31-63, doi: 10.1016/s0264-3707(01)00027-8.

Wilson, J. T. (1965), A New Class of Faults and Their Bearing on Continental Drift. *Nature*, 207(4995), 343-347, doi: 10.1038/207343a0.

Wong A Ton, S. Y. M. & Wortel, M. J. R. (1997), Slab detachment in continental collision zones: An analysis of controlling parameters. *Geophys. Res. Lett.*, 24(16), 2095-2098, doi: 10.1029/97gl01939.

Xie, S. X. & Tackley, P. J. (2004a), Evolution of helium and argon isotopes in a convecting mantle. *Phys. Earth Planet. Inter.*, 146(3-4), 417-439, doi: 10.1016/j.pepi.2004.04.003.

Xie, S. X. & Tackley, P. J. (2004b), Evolution of U-Pb and Sm-Nd systems in numerical models of mantle convection and plate tectonics. *J. Geophys. Res. Solid Earth*, 109(B11), B11204, doi: 10.1029/2004jb003176.

Yamato, P., Husson, L., Braun, J., Loiselet, C. & Thieulot, C. (2009), Influence of surrounding plates on 3D subduction dynamics. *Geophys. Res. Lett.*, 36(7), L07303, doi: 10.1029/2008gl036942.

Zeck, H. P. (1996), Betic-Rif orogeny: subduction of Mesozoic Tethys lithosphere under eastward drifting Iberia, slab detachment shortly before 22 Ma, and subsequent uplift and extensional tectonics. *Tectonophysics*, 254(1-2), 1-16, doi: 10.1016/0040-1951(95)00206-5.

Zhong, S. J., Zuber, M. T., Moresi, L. & Gurnis, M. (2000), Role of temperature-dependent viscosity and surface plates in spherical shell models of mantle convection. *J. Geophys. Res. Solid Earth*, 105(B5), 11063-11082, doi: 10.1029/2000jb900003.

Websites

aashscience.weebly.com (2019), Layering of the Earth.
http://aashscience.weebly.com/uploads/1/3/5/7/13577302/995717806_orig.gif
Accessed 30-05-2019.

Chapter 2

The initial geometry of the slab and its effects on subduction evolution

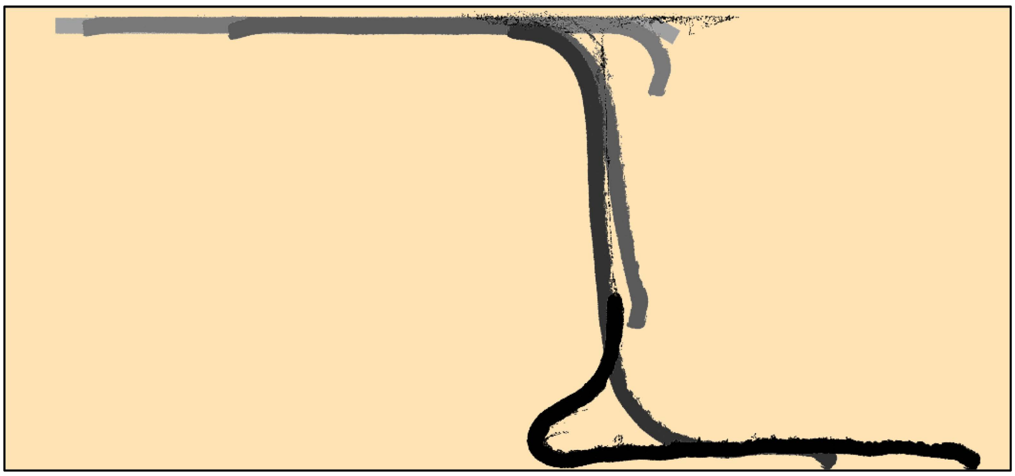

Cover image: Five sequential stages of subduction of experiment DF1, which started with a short slab tip of 125 km dipping at 30° into the mantle.

Abstract

Geodynamic models of subduction systems often focus on ‘self-sustained’ subduction evolution, where the subduction process is solely due to the negative buoyancy of a slab, with an imposed geometry, penetrating into the mantle. However, these models do not account for the diversity of geometries of the initial slab that may occur in nature due to different subduction initiation processes. Understanding how the initial slab geometry impacts subduction is important since it potentially impacts subduction evolution. This study uses two-dimensional numerical models to evaluate how different slab geometries influence the early evolution of subduction. The effects of changes in the initial slab length and dip angle are examined on the down-going plate geometry as well as on the plate sinking and trench migration velocities. These effects are explored for both a deep mantle (down to 2280 km depth) and a shallow mantle (down to 660 km depth). Furthermore, these effects are compared by varying the boundary condition of the trailing edge of the plate, which is either fixed or free to move as the plate is subducted. In these end-member cases, the plate either moves very slowly relative to the trench, or its velocity relatively fast due to mid-ocean ridge push, respectively. Results show that a longer initial slab and a steeper dip angle lead to a more rapid subduction evolution. Increasing the dip angle has a larger impact on the maximum slab sinking velocity than lengthening the initial slab. The trench velocity is also more susceptible to changes in the initial dip angle. These results provide insights into slab sinking velocities and trench migration rates, with implications for how fast subducting plates are recycled into the mantle, and on the behaviour of trenches. Both of these parameters impact crustal deformation patterns at convergent margins. The conclusions of this study suggest that the dynamics of ‘self-sustained’ subduction is strongly influence by the initial conditions of subduction, as well as the boundary condition at the trailing edge of the plate.

Keywords: Subduction models, geodynamics, numerical modelling, sinking velocity, initial slab geometry

1. Introduction

The concept of the Wilson Cycle has underpinned the manner in which geoscientists understand the evolution of Earth, how new continents are created and dispersed around the planet, and how continents converge and collide to form supercontinents [Wilson, 1965]. The Wilson cycle appears to have been operating since the advent of plate tectonics on Earth with multiple cycles of supercontinent formation dating back to the Neo-Archean [Cawood et al., 2006; Shirey & Richardson, 2011]. The cycle requires fundamental transformations in plate boundary behaviours and a transition from divergent tectonic processes, involving continental rifting and ocean creation, to convergent plate boundaries, where a tectonic plate sinks under another into the mantle, during a process termed subduction which drives mantle convection [Forsyth & Uyeda, 1975; Davies & Richards, 1992; Conrad & Lithgow-Bertelloni, 2002]. How this transition occurs remains one of the least understood aspects of plate tectonics as is it clear how the initial slab geometry influences subduction dynamics once initiated and the subduction initiation process is poorly resolved.

Stern [2004] proposes two general mechanisms for subduction initiation: induced nucleation of a subduction zone (INSZ), where the continuous convergence of the plates is responsible for the subsidence of the denser plate, and spontaneous nucleation of a subduction zone (SNSZ), which results from local gravitational instabilities (old and dense lithosphere collapses into the mantle at pre-existing faults or zones of lithospheric weakness). These two mechanisms can lead to various subduction initiation scenarios that can occur in different tectonic settings, such as passive margins, transform boundaries between oceanic plates, or back-arc basins. Different subduction initiation scenarios in diverse tectonic settings can lead to variations in the initial slab geometry (slab length and dip angle) that drives subduction [Nikolaeva et al., 2010]. This study addresses how the initial slab geometry influences the dynamics of subduction during the period immediately after initiation.

The subduction process has been extensively studied through both analogue and numerical modelling. These models are used to reconstruct and understand the past, present and future evolution of tectonic settings. Through such studies it is possible to identify and quantify the forces that drive plate tectonics, analyse mantle convection processes, understand the surface expression and morphology of Earth surface and quantify the rates of motion of plate tectonics. How subduction shapes the tectonic processes of Earth is also influenced by the range of different plate and plate boundary scales (length, width and thickness), as well as different slab-mantle density contrasts and viscosity ratios in the interior of the planet. The role of such parameters has been widely quantified and related to subduction style, sinking velocity and trench migration [Bellahsen et al., 2005; Funiciello et al., 2006; Funiciello et al., 2003b; Schellart, 2008, 2010; Li & Ribe, 2012]. However, in these types of studies, the instability that initiates subduction (i.e., the initial slab, which represents the tip of the plate that bends downwards into the mantle) is imposed either manually or computationally by making assumptions about the initial dip angle or slab length and therefore the subduction initiation processes are not considered.

Ribe [2010] and Li & Ribe [2012] showed that the style of subduction also depends on the initial slab geometry, and that there is a strong relation between the depth at which the subducting slab will acquire a vertical dip and the slab initial conditions, which also depends on the slab-mantle viscosity ratio. Furthermore, Li & Ribe [2012] determined that the mode of subduction is also controlled by the angle at which the slab impinges on the bottom boundary. But these scaling laws have been determined considering an infinite deep mantle or only considering the upper mantle. These studies also did not examine how the effects of different initial slabs vary considering different trailing edge conditions.

In this study, it is tested if the initial slab geometry affects the style and dynamics of subduction during the transition to "self-sustained" subduction. These effects are quantified using a 2D numerical modelling approach in which experiments simulate a plate sinking in a homogeneous mantle (i.e. a mantle with no viscosity or density contrasts at depth), driven only by its negative buoyancy and without considering temperature and mineral phase changes. The experiments include a free surface approximation that comprises a low density and low viscosity layer at the top of the model domain, which decouples the plate from the top boundary and allows the growth of topography [Schmeling et al., 2008; Crameri et al., 2012]. The effects of varying the mantle thickness were also analysed for end-member scenarios where the plate is either fixed at one end or free to move, representing cases where the plate moves very slowly relative to the trench or when the plate velocity is relatively rapid due to mid-ocean ridge push, respectively.

2. Methodology

2.1. Model setup

Figure 1 illustrates the general model set-up in a Cartesian coordinate system. The mantle is represented by a 'box' of dimensions $L \times H$ and has density ρ_m and dynamic shear viscosity η_m. The plate is homogeneous of length L_{sp}, thickness h_{sp}, density ρ_{sp} and viscosity η_{sp}.

Initially, the plate is lying on top of the mantle and is overlain by a low density and low viscosity layer of thickness h_{sl}, density ρ_{sl} and viscosity η_{sl}. This layer (hereon 'sticky-layer') represents an air or soft-sediment cover. The trailing edge of the plate is located at a distance $x^0{}_{sp}$ from the domain boundary and, on the opposite end, the plate has a kinked tip with an initial slab length $l_0 = l_{sp}(0)$, dipping at an angle θ_0 into the mantle.

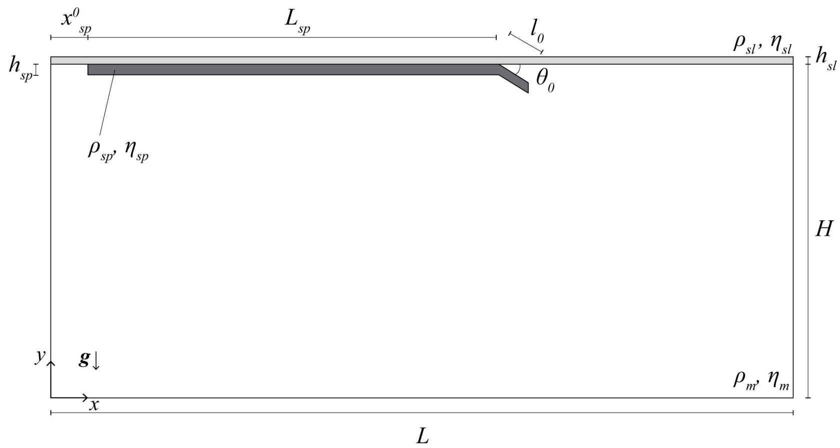

Figure 1. 2D model setup: a plate of length L_{sp} and thickness h_{sp}, is located at a distance $x^0{}_{sp}$ from the domain boundary and, on the opposite end, has a kinked tip with an initial slab length $l_0 = l_{sp}(0)$, dipping at θ_0. The plate has density ρ_{sp} and viscosity η_{sp}, is initially lying on top of the mantle and is overlain by a layer of thickness h_{sl}, density ρ_{sl} and viscosity η_{sl}. The mantle has length L, total thickness H, density ρ_m and viscosity η_m. The gravitational acceleration is represented by $\boldsymbol{g}$.

The system is simplified based on the following assumptions:

1. The rheology is linear viscous, since over geological timescales subducting lithosphere behaves on first approximation like a fluid [Houseman & Gubbins, 1997]. Furthermore, only oceanic lithosphere is simulated, which is compositionally more homogeneous than continental lithosphere.
2. The driving force of the system is the negative buoyancy of the subducting plate. It is assumed that there are no external forces acting on the system, such as ridge-push or pre-existing mantle convection. The focus is solely on the subduction dynamics without considering global convection.
3. Thermal effects are not included. In nature, the Rayleigh number is assumed to be sufficiently high ($5 \times 10^5 - 5 \times 10^7$) to consider that the heat transfer across the mantle occurs primarily by convection. It is assumed that convection occurs in the whole mantle and that the temperature dependent effects are confined to the boundary layers (i.e., the lithosphere at the top and the core-mantle boundary at the bottom).
4. The system does not include an overriding plate, assuming that it moves passively with the trench. The complex interplay between subducting and overriding plates is beyond

the scope of this study.

5. The subduction zone is infinitely wide. This is a consequence of the 2D space, in which the subduction induced mantle flow occurs through poloidal flow and the 3D intrinsic toroidal flow is absent.

2.2. Numerical description

The system is described by the equations of conservation of momentum and conservation of mass for an incompressible fluid:

$$\nabla \cdot \boldsymbol{\tau} - \nabla p = \Delta\rho \boldsymbol{g}, \tag{1}$$

$$\nabla \cdot \boldsymbol{u} = 0, \tag{2}$$

where $\boldsymbol{u}$ is the velocity, p is the dynamic pressure, $\Delta\rho$ is the density contrast, $\boldsymbol{g}$ is the gravitational acceleration and τ is the deviatoric stress tensor,

$$\tau_{ij} = \eta \left(\frac{\partial u_i}{\partial x_j} + \frac{\partial u_j}{\partial x_i} \right), \tag{3}$$

where η is the dynamic shear viscosity.

The numerical experiments were performed with the Underworld2 Geodynamic code[1], which is a parallel hybrid particle-in-cell finite element method. Using a multigrid solver, a standard Eulerian Finite Element mesh is utilised to discretise the domain of the problem and solve the governing equations. Within each mesh element, a total of 20 Lagrangian particles are employed to carry the material properties, such as density and viscosity [Moresi et al., 2003; Moresi et al., 2007]. The resolution of the mesh used in the models depends on the depth on the mantle (see Section 3).

2.3. Model scaling

In nature, subductions systems are described by very high values (e.g., the total mantle thickness considered here is ~ 2,280 km and the mantle viscosity is ~ 10^{21} Pa.s). The general model is scaled down taking the time it takes for a slab element of thickness h_{sp} to sink through a mantle of thickness H, at the velocity scale $v^* = \Delta\rho g h_{sp}^2/\eta_m$, where $\Delta\rho$ is the density contrast between the plate and the mantle, η_m is the mantle viscosity and g is the gravitational acceleration. Given that velocity is length divided by time ($v = H/t$), time is scaled as

$$\frac{t^N}{t^M} = \frac{H^N}{H^M} \frac{\left(\Delta\rho g h_{sp}^2/\eta_m\right)^M}{\left(\Delta\rho g h_{sp}^2/\eta_m\right)^N}, \tag{4}$$

where the superscripts M and N refer to model and nature, respectively.

[1] http://www.underworldcode.org/

Considering the subduction process as a sequence of quasi-static states, a characteristic velocity can be estimated for any arbitrary instant in time. The system is driven only by the plate negative buoyancy, and assuming negligible bending resistance of the slab, the effective buoyancy of the slab tip per plate width unit ($F_b = l_{sp} h_{sp} g \Delta\rho$, where l_{sp} is the subducted length) is approximately equal to the traction applied by the mantle fluid integrated over the slab length (i.e., the external force acting on the slab per plate width unit $F_{ext} = \eta_m V$) [Ribe, 2010; Li & Ribe, 2012]. Accordingly, an approximation of Stokes velocity can be computed as

$$V \sim \frac{\Delta\rho g h_{sp} l_{sp}}{\eta_m} \equiv v_{Stokes}. \tag{5}$$

Ribe [2010] defines the ratio of internal and external viscous forces acting on the slab as a measure for the stiffness of the plate:

$$S \sim \gamma \left(\frac{h_{sp}}{l_{sp}}\right)^3, \tag{6}$$

where γ is the viscosity ratio between plate and mantle. The dimensionless quantity S defines if the sinking velocity is controlled by mantle viscosity ($S < 1$), by the viscosity of the plate ($S > 10$), or both ($1 < S < 10$). In the stiffness definition Ribe [2010] uses a bending length l_b, which consists of the slab length, l_{sp}, plus a seaward flexural bulge, calculated through the analysis of the rate of change of the plate curvature in the trench area. The initial bending length depends on the viscosity ratio γ (higher ratio results in a longer bending length), at the start of Ribe's simulations with $l_{sp} = 4h_{sp}$, the difference $l_b - l_{sp} \approx 0.5h_{sp}$ if $\gamma = 100$ and $\sim 1.75h_{sp}$ if $\gamma = 1000$. In this study, this definition of plate stiffness is used, but for simplicity, assumed as $l_b \sim l_{sp}$, which overestimates the stiffness. The assumption arises from the initial slab geometry definition, which in this study is kinked. Thus, at the start of the experiments the bending length is nil and the curvature of the plate near the trench only develops as the slab subducts.

2.4. Boundary conditions

The domain boundaries are free-slip and a sticky-layer is included at the top of the domain to simulate a free surface [e.g., Schmeling et al., 2008]. This layer has low viscosity and low density to simulated air (or water/soft sediments) and allows for the development of topography without exerting stress on it. The sticky-layer viscosity and thickness parameters are chosen to ensure that the interface between plate and stick-layer remains traction free for both short (isostatic relaxation) and long (geologic) timescales [Crameri et al., 2012] and are defined in equations 7 and 8, respectively:

$$C_{isos} = \frac{3}{16\pi^3}\left(\frac{L}{h_{sl}}\right)^3 \frac{\eta_{sl}}{\eta_m}, \tag{7}$$

$$C_{Stokes} = \frac{3}{16}\frac{\Delta\rho}{\rho}\left(\frac{H}{h_{sl}}\right)^3 \frac{\eta_{sl}}{\eta_m}, \tag{8}$$

which are satisfied when $C_{isos} \ll 1$ and $C_{Stokes} \ll 1$.

2.5. Viscosity interfaces

The general model setup (Figure 1) comprises three different fluids in the trench area: viscous plate, mantle, and sticky-layer. In nature, the plate-air viscosity ratio is very high ($\sim 10^{25}$) and the plate-mantle viscosity ratio is of the order of $\sim 10^2$ [Moresi & Gurnis, 1996; Schellart, 2008]. The Underworld 2.0 code maps the viscosity advected by the Lagrangian particles to the Finite Element (FE) mesh, and to handle such contrasts numerically, an averaging law has to be applied on the mesh elements at the viscosity interfaces. Schmeling et al. [2008] demonstrated that applying a harmonic averaging scheme facilitates the decoupling of the subducting plate from the top surface and improves the convergence between numerical and laboratory analogue models results. The harmonic average effectively reduces the viscosity of the high contrasting materials at the interfaces. A harmonic averaging scheme is implemented, as:

$$\frac{1}{\eta_{ave}} = \sum_i \frac{C_i}{\eta_i}, \tag{9}$$

where η_i is the viscosity of the i material and C_i is the relative volumetric fraction of the i material in the vicinity of the FE-node for which the average viscosity η_{ave} is being calculated. This implementation is a distinct feature of this study's numerical models compared to other numerical models.

3. Results

A total of 48 experiments were performed using the 2D model set-up (Figure 1). Half of the experiments were executed for the case where the plate is fixed at the boundary at one end (hereinafter 'Fixed case'), with ${x^0}_{sp} = 0$ m. In the other half of the experiments, the plate was free to move (hereinafter 'Free case'). Each group is divided into three experiment sets: 10 experiments in a deep mantle configuration, 10 experiments in a shallow mantle configuration, and 4 experiments in which the mantle depth is varied. The deep mantle experiments assume a homogeneous mantle of thickness 2280 km. The shallow mantle experiments assume a homogeneous mantle of thickness 660 km, corresponding to the bottom of the mantle transition zone (MTZ). In the models varying the mantle depth, the values explored also include the 410 km depth, which is associated with the mineral phase transition olivine to wadsleyite and ringwoodite [Ringwood, 1956; Ringwood & Major, 1966], as well as 1100 km and 1720 km depths. The latter depths were arbitrarily chosen between the MTZ and the core-mantle boundary (CMB).

Table 1. Model parameters common to all experiments.

Parameter	Symbol	Value	Units
Gravitational acceleration	g	9.8	m/s2
Domain length	L	5067×10^3	m
Domain height (deep mantle experiments)	$H + h_{sl}$	2280×10^3	m
Trailing plate length at $t = 0$ s	$L_{sp}(0)$	2800×10^3	m
Plate thickness	h_{sp}	75×10^3	m
Sticky-layer thickness	h_{sl}	50×10^3	m
Distance of plate trailing edge to boundary (free plate experiments)	$x^0{}_{sp}$	250×10^3	m
Plate and slab density	ρ_{sp}	3300	kg/m3
Mantle density	ρ_m	3200	kg/m3
Sticky-layer density	ρ_{sl}	0	kg/m3
Density contrast between plate and mantle	$\Delta\rho = \rho_{sp} - \rho_m$	100	kg/m3
Plate and slab viscosity	η_{sp}	6.4×10^{23}	Pa·s
Mantle viscosity	η_m	1×10^{21}	Pa·s
Sticky-layer viscosity[2]	η_{sl}	$10^{-2}\ \eta_m$	Pa·s
Viscosity ratio between plate and mantle	$\gamma = \eta_{sp}/\eta_m$	640	–

In each subset of 10 experiments (Fixed/Free case and Deep/Shallow mantle), there are five experiments in which only the initial slab length is varied (experiments 1 to 5) and five experiments in which only the initial slab dip angle is varied (experiments 6 to 10). The initial slab tip length is varied from 125 to 250 km, whereas the initial slab tip angle is varied from 15 to 90°. Experiment 5 (all cases) is used as reference and included in analysis of results for all sets. The parameters kept constant between all experiments are summarised in Table 1 and the parameters varied are presented in Table 2. For all other experiments, the vertical resolution of the mesh was adapted in order to keep the same vertical resolution of the plate (~8-9 mesh elements).

[2] The viscosity of the sticky-layer used is significantly higher than the nature value (10^{-5} Pa.s). The value used was chosen based on equations (7) and (8) and is low enough to consider a high contrast between sticky-layer and mantle, but sufficiently high to allow numerical efficiency.

Table 2. Model parameters varied between the experiments: initial slab length, initial slab dip angle, and mantle thickness. Deep mantle experiments in the Fixed case are represented by D and in the Free case by DF. Shallow mantle experiments in the Fixed case are represented by S and in the Free case by SF. Variable mantle thickness experiments in the Fixed case are represented by H and in the Free case by HF.

<table>
<tr><th></th><th>Experiment</th><th>l_0 [km]</th><th>θ_0 [°]</th><th>H [km]</th></tr>
<tr><td rowspan="10">Deep mantle</td><td>D1, DF1</td><td>125</td><td rowspan="5">30</td><td rowspan="10">2280</td></tr>
<tr><td>D2, DF2</td><td>150</td></tr>
<tr><td>D3, DF3</td><td>175</td></tr>
<tr><td>D4, DF4</td><td>200</td></tr>
<tr><td>D5, DF5</td><td rowspan="6">250</td></tr>
<tr><td>D6, DF6</td><td>15</td></tr>
<tr><td>D7, DF7</td><td>45</td></tr>
<tr><td>D8, DF8</td><td>60</td></tr>
<tr><td>D9, DF9</td><td>75</td></tr>
<tr><td>D10, DF10</td><td>90</td></tr>
<tr><td rowspan="10">Shallow mantle</td><td>S1, SF1</td><td>125</td><td rowspan="5">30</td><td rowspan="10">660</td></tr>
<tr><td>S2, SF2</td><td>150</td></tr>
<tr><td>S3, SF3</td><td>175</td></tr>
<tr><td>S4, SF4</td><td>200</td></tr>
<tr><td>S5, SF5</td><td rowspan="6">250</td></tr>
<tr><td>S6, SF6</td><td>15</td></tr>
<tr><td>S7, SF7</td><td>45</td></tr>
<tr><td>S8, SF8</td><td>60</td></tr>
<tr><td>S9, SF9</td><td>75</td></tr>
<tr><td>S10, SF10</td><td>90</td></tr>
<tr><td rowspan="3"></td><td>H11, HF11</td><td rowspan="3">250</td><td rowspan="3">30</td><td>410</td></tr>
<tr><td>H13, HF13</td><td>1100</td></tr>
<tr><td>H14, HF14</td><td>1720</td></tr>
</table>

Subduction does not evolve as a steady state process after initiation [Bellahsen et al., 2005; Funiciello et al., 2003a], but goes through three main phases: (1) slab sinking into the upper mantle in a transient way, (2) interaction with a deep viscosity discontinuity, and (3) steady state subduction. In this study, the focus is on stage 1 only, and the experiments were carefully analysed until the slab reaches the bottom boundary. All results are presented in nature units.

3.1. Deep mantle models

3.1.1. Plate geometry

Figure 2 shows the plate geometry evolution for end-member experiments of the deep mantle model, for both Fixed and Free cases – D1, DF1, D5, DF5, D8 and DF8. Four times are depicted for each experiment, corresponding to the start, $t = 0$ s, the end, and two intermediate

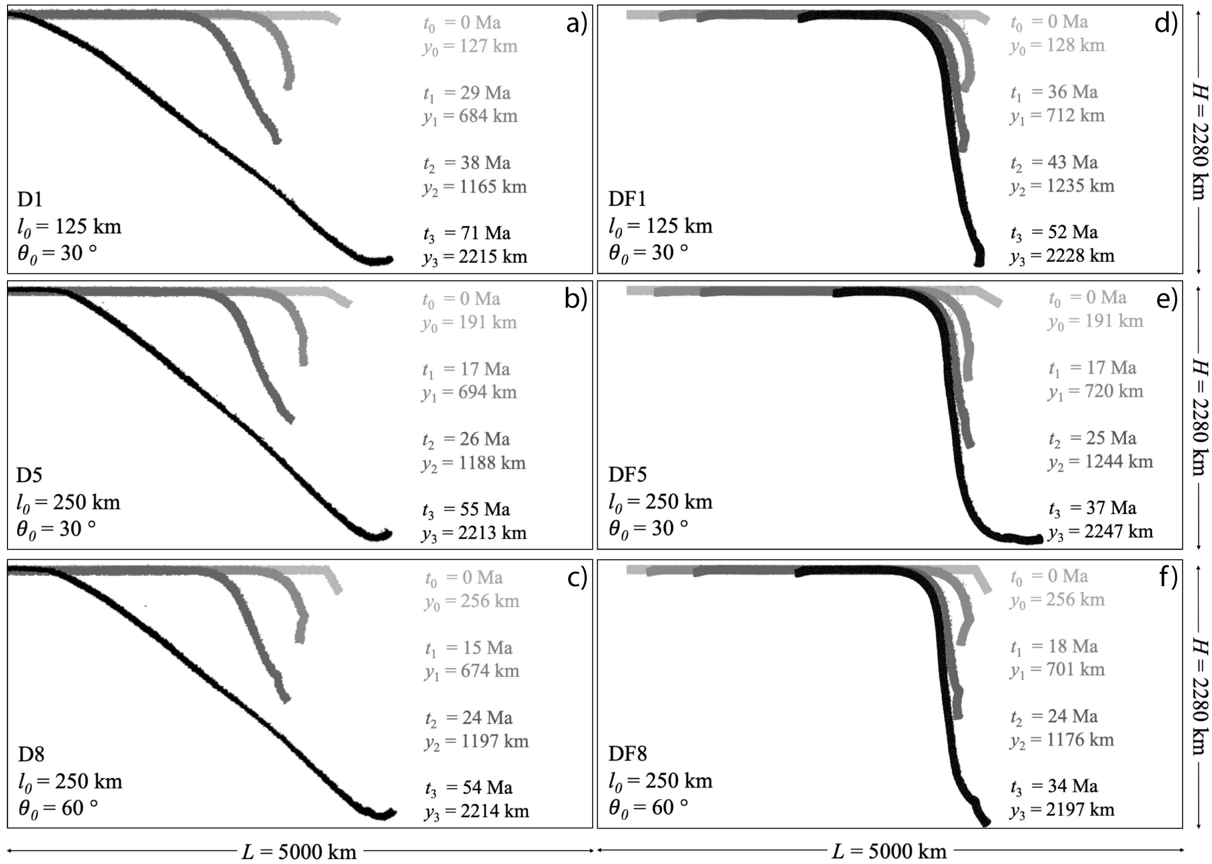

Figure 2. Slab geometric evolution of experiments D1, D5 and D8 (a-c) and DF1, DF5 and DF8 (d-f). Four times are depicted, corresponding to the start, t = 0 s (light grey), the end (in black) and two intermediate times (Table A1).

times when the slab tip reaches a depth of $\sim 707 \pm 18$ km and a depth of $\sim 1185 \pm 39$ km, respectively (Table A1). The variations between the experiments are due to small variations in the numerical time-step, which is case-dependent.

In all experiments, the observed subduction process can be described by a sequence of 3 stages: (1) a transient stage, while the initially imposed slab bends downwards, (2) a quasi-steady state subduction, while the slab sinks in a concave downward shape, and (3) a sinking decelerating stage, in which the curvature of the slab tip inverts (i.e., the tip initially is bending oceanwards and after reaching about half the mantle thickness bends in the direction of the mantle wedge). Doubling the initial slab length (D1 to D5, and DF1 to DF5; Figure 2) results in different times for the slab to reach the bottom. The slab in experiments D5 and DF5 reaches the bottom ~ 15 Ma before D1 and DF1, and increasing the dip angle (D5 to D8, and DF5 to DF8; Figure 2), the slab reaches the bottom only $\sim 1 - 3$ Ma earlier.

In the experiments with higher initial slab dip angle (e.g., D8 and DF8; Figure 2), the kink initially imposed on the slab gets less smoothed by the end of the experiment. The slab retains the sharp angular shape between the initial slab and the trailing plate, resulting from the high resistance of the plate bending/unbending due to the high plate-mantle viscosity ratio.

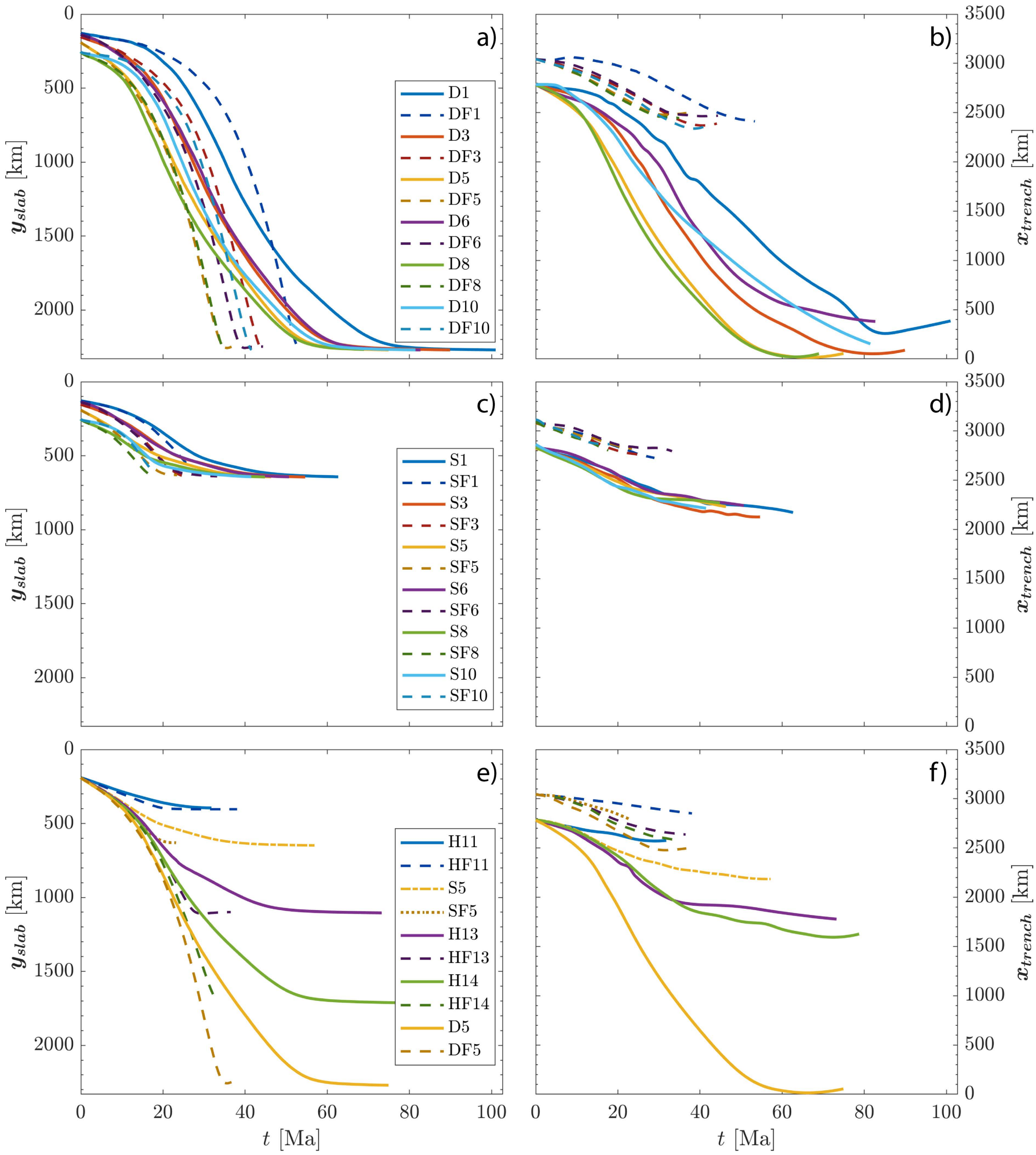

Figure 3. Slab tip vertical position y_{slab} plotted against time for a) Deep mantle experiments, c) Shallow mantle experiments and e) changing mantle depth experiments. Trench horizontal position x_{trench} plotted against time for b) Deep mantle experiments, d) Shallow mantle experiments and f) changing mantle depth experiments. Solid lines refer to Fixed experiments and dashed lines refer to Free experiments.

3.1.2. Slab sinking and trench retreat

The slab tip vertical position and the trench horizontal position were tracked during each experiment. Figure 3a-b shows these displacements over time for end-member cases of the deep mantle experiments, and for both Fixed and Free cases. The slab vertical displacement curves (Figure 3a) show two different patterns if the plate is either fixed or free. In the Fixed case, the curves (solid lines) have a concave downward shape until the tip reaches about half the mantle depth, after which they acquire a convex shape. Whereas in the Free case (dashed lines), the curves retain the concave shape almost until the slab tip reaches the bottom.

Changes in the initial slab geometry do not change the overall curve shapes. The main differences are in the duration of the initial bending stage until the slab tip reaches ~ 500 km depth. Increasing the initial slab length (D1, D3 and D5 and DF1, DF3 and DF5) results in a progressively shorter bending stage. Increasing the initial slab dip angle (D6, D5, D8 and D10 and DF6, DF5, DF8 and DF10) also results in a progressively shorter bending stage (stage 1). However, for $\theta_0 = 90°$ (D10 and DF10), the initial bending stage is longer than compared to $\theta_0 = 60°$ (D8 and DF8). In the Free case, the slab tip depth curves of experiments DF5 ($\theta_0 = 30°$) and DF8 ($\theta_0 = 60°$) overlap after the initial bending stage. After the initial slab bending stage, when $y_{slab} > 500$ km depth, the curves evolve with similar slopes, indicating that the slab will sink with similar velocities for both the Fixed and Free setting. The experiments that show longer initial bending stages also require more time to reach the bottom.

The trench displacement curves (Figure 3b) also show two different patterns depending on whether the plate is either fixed or free. In the Fixed case (solid lines), the trench retreats from its starting position until the domain boundary, covering about 2700 km. The trench position curves have similar shape, however, the slopes of the curves vary between cases. In the Free case (dashed lines), the trench retreat is limited to a maximum of ~ 650 km distance away the starting position. With the exception of experiment DF1, which has the shortest initial slab, the trench migration curves are very similar, almost overlapping.

During the first 20 Ma, experiments D1 and DF1, both experiments with the shortest initial slab ($l_0 = 125$ km), have a low trench retreat rate, compared to the other cases, and only after this initial period the trench retreats significantly.

Generally, the curves in Figure 3 are characterized by continuously changing rates, which means that the slab vertical velocity and the trench horizontal velocity vary in time. In order to understand the role of the slab initial geometry in the variations of these velocities over time, a finite centred difference scheme is applied to the position curves as:

$$\begin{cases} v_s^i = \dfrac{y^{i+1} - y^{i-1}}{t^{i+1} - t^{i-1}}, \\ v_t^i = \dfrac{x^{i+1} - x^{i-1}}{t^{i+1} - t^{i-1}}, \end{cases} \tag{10}$$

where v_s^i and v_t^i are the slab and trench velocities, calculated for the time t_i, y^{i+1} and y^{i-1} are the slab vertical positions at times t^{i+1} and t^{i-1}. Similarly, x^{i+1} and x^{i-1} are the trench horizontal positions at times t^{i+1} and t^{i-1}, respectively.

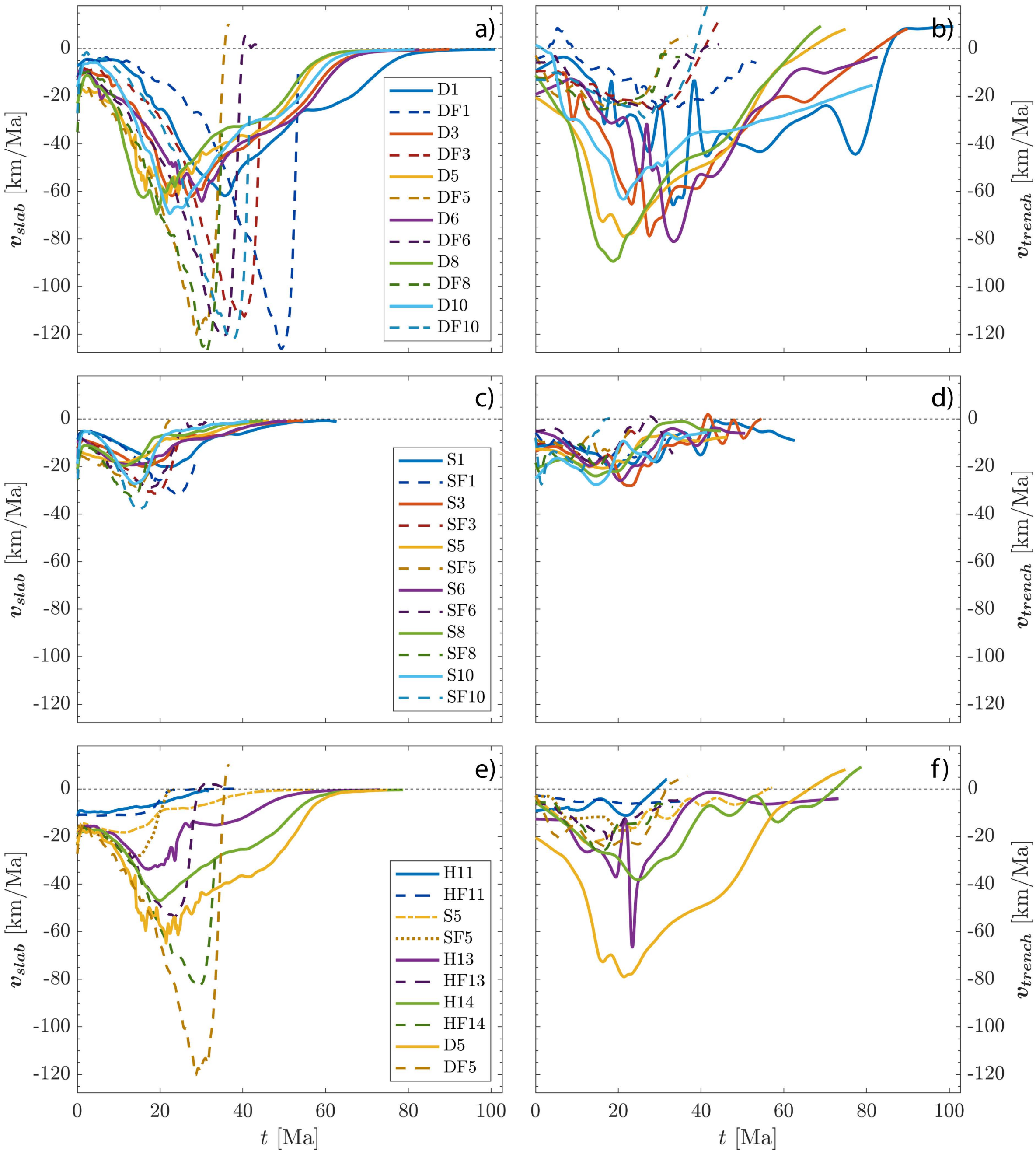

Figure 4. Slab tip sinking velocity v_{slab} plotted against time for a) Deep mantle experiments, c) Shallow mantle experiments and e) changing mantle depth experiments. Trench velocity v_{trench} plotted against time for b) Deep mantle experiments, d) Shallow mantle experiments and f) changing mantle depth experiments. Solid lines refer to Fixed experiments and dashed lines refer to Free experiments.

Figures 4a and 4b show the slab sinking velocity and trench velocity over time for the same end-member cases of the deep mantle experiments presented in Figures 3a and b. All curves exhibit an increase in absolute value, followed by a decrease. The Fixed case experiments reach lower absolute sinking velocities ~65 km/Ma and higher trench retreat velocities ~70 km/Ma than the Free case experiments, which reach absolute sinking velocities of the order of ~120 km/Ma and trench retreat velocities of the order of ~25 km/Ma.

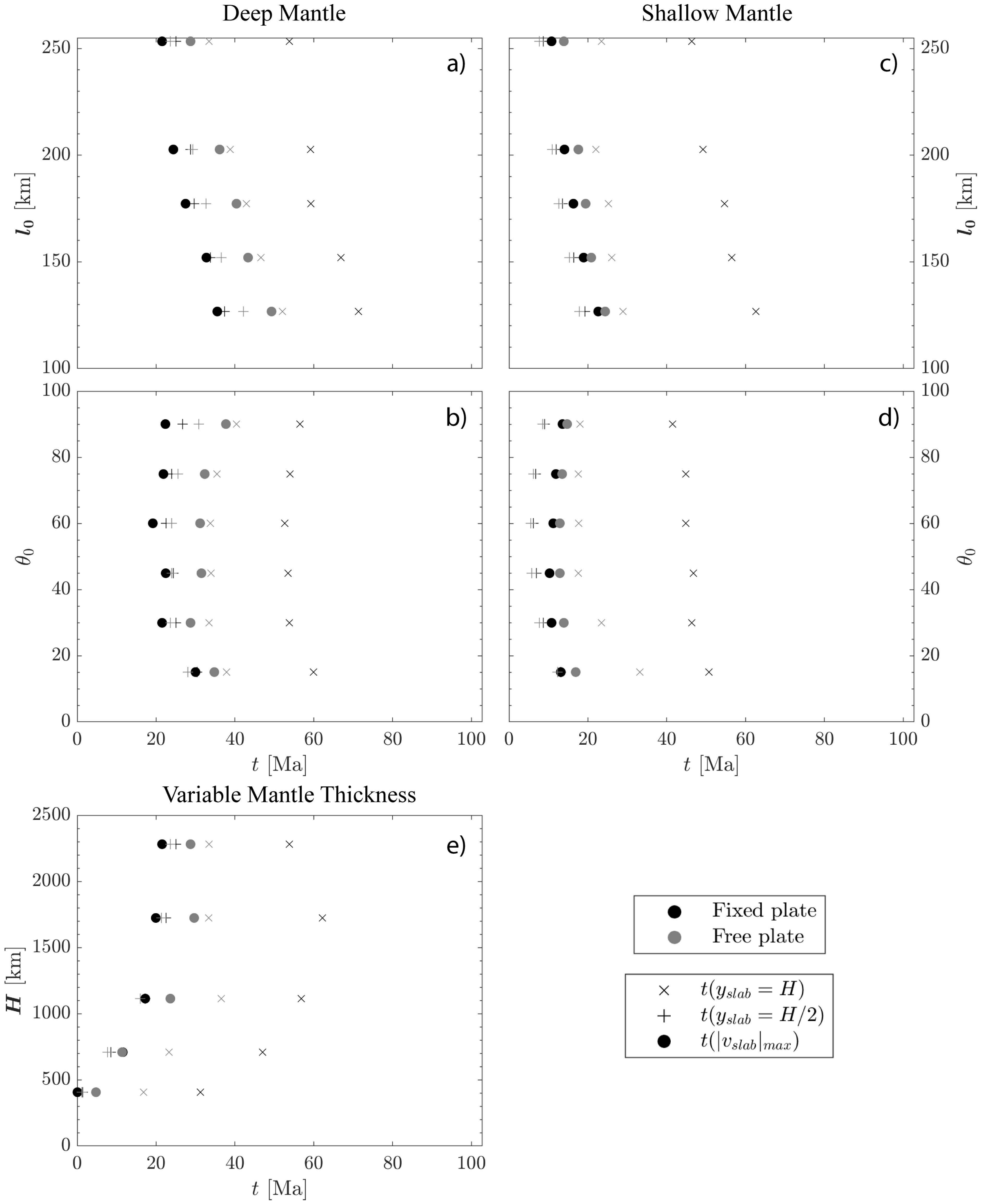

Figure 5. Times at which the slab reaches half of the mantle thickness depth ('+'), first touches the bottom ('x') and reaches the maximum sinking velocity (black circles for the Fixed case and grey circles for the Fixed case experiments). a) Deep mantle experiments varying the initial slab length, b) Deep mantle experiments varying the initial slab angle, c) Shallow mantle experiments varying the initial slab length, d) Shallow mantle experiments varying the initial slab angle, e) experiments varying the mantle thickness.

The times at which these absolutes maximums are reached vary with the initial slab geometry. The times at which the maximum absolute sinking velocity $|v_s|_{max}$ occur, $t(|v_s|_{max})$, are depicted in Figure 5, and compared to the times when the slab tip depth equals the half of the mantle thickness $t(y_{slab} = H/2)$ and the bottom of the mantle $t(y_{slab} = H)$ (Table A2). In the Fixed case (Figures 5 a and 5b), $|v_s|_{max}$ (black circles) occurs ~4 Ma before $t(y_{slab} = H/2)$, represented by the black plus signs. In the Free case, $|v_s|_{max}$ (grey circles) occurs ~7 Ma after $t(y_{slab} = H/2)$, represented by the grey plus signs. Changing the initial slab length (Figure 5a), $t(|v_s|_{max})$ is inversely proportional to the initial slab length (i.e., the longer the initial slab is, the earlier $|v_s|_{max}$ is reached). Changing the initial slab dip angle (Figure 5b) has a two-branch behaviour, for $15° < \theta_0 < 40°$, $|v_s|_{max}$ is reached up to 9 Ma earlier than for $60° < \theta_0 < 90°$, where $|v_s|_{max}$ is reached up to 6 Ma later. Independently from initial slab geometry, the slab in the Fixed cases reaches the bottom $\sim 30 - 36$ Ma after $|v_s|_{max}$ is reached, whereas the slab in the Free cases reaches the bottom $\sim 3 - 8$ Ma after $|v_s|_{max}$ is reached.

Table 3. Summary of maximum absolute velocities mean values and standard deviations.

		Experiments	$\lvert v_s\rvert_{max}^{mean} \pm \sigma$ [km/Ma]	$\lvert v_t\rvert_{max}^{mean} \pm \sigma$ [km/Ma]	$\lvert v_{te}\rvert_{max}^{mean} \pm \sigma$ [km/Ma]
Deep mantle	**Fixe**	D1–D5	62.3 ± 2.9	72.6 ± 8.0	–
		D5–D10	67.9 ± 2.5	76.1 ± 11.9	–
	Free	DF1–DF5	120.3 ± 5.0	24.8 ± 1.6	111.4 ± 7.4
		DF5–DF10	121.3 ± 4.8	27.5 ± 2.3	108.9 ± 4.8
Shallow mantle	**Fixed**	S1 – S5	19.8 ± 0.9	24.5 ± 4.4	-
		S5 – S10	21.2 ± 3.4	25.1 ± 2.7	-
	Free	SF1 – SF5	31.0 ± 1.5	19.7 ± 3.5	32.9 ± 4.0
		SF5 – SF10	32.4 ± 4.2	21.8 ± 4.9	32.0 ± 4.1
H	**Fixed**	D5, S5 & H11–H14	35.0 ± 21.8	46.3 ± 29.5	–
	Free	DF5, SF5 & HF11–HF14	59.2 ± 43.4	18.4 ± 7.9	56.6 ± 35.8

The mean values of the maximum absolute sinking velocity and the maximum absolute trench velocity ($|v_s|_{max}$ and $|v_t|_{max}$, respectively) for all sets of experiments, as well as the respective standard deviations are summarised in Table 3. For the Fixed case Deep mantle experiments, changing the slab length (D1 – D5) and changing the initial dip angle (D5 – D10) results in a comparable mean and standard deviation of $|v_s|_{max}$, with only 5.6 km/Ma difference between means and 0.4 km/Ma difference between standard deviations, indicating that changes in l_0 or θ_0 affect $|v_s|_{max}$ similarly. However, changing the initial dip angle (D5 – D10) results in a similar mean but a higher dispersion of $|v_t|_{max}$ (3.5 km/Ma difference between means and 3.9 km/Ma difference between standard deviations), compared to changing the slab length (D1 – D5). A higher standard deviation indicates that the absolute maximum velocities of that set are spread over a wider range of values around the mean value, implying the initial dip angle has a higher effect on $|v_t|_{max}$.

For the Free case experiments, changing the slab length (DF1 – DF5) and the initial dip angle (DF5 – DF10) results in a comparable mean and standard deviation of $|v_s|_{max}$, with only 1.0 km/Ma difference between means and 0.2 km/Ma difference between standard deviations. It also results in a comparable mean and standard deviation of $|v_t|_{max}$, with only 2.7 km/Ma difference between means and 0.7 km/Ma difference between standard deviations.

Additionally, in the Free case experiment it is possible to evaluate the effects of changing the initial slab geometry on the motion of the trailing edge of the plate. The trailing edge velocity $|v_{te}|_{max}$ is the velocity at which the free edge of the surface plate moves trenchward. The plate trailing edge position over time curves and plate trailing edge velocity over time in Figure A1. Changing the slab length (DF1 – DF5) and the initial dip angle (DF5 – DF10) results in lower mean and standard deviation of the maximum absolute trailing edge velocity, $|v_{te}|_{max}$ (-2.5 km/Ma difference between means and -2.6 km/Ma difference between standard deviations), indicating the initial slab length has a higher effect on $|v_{te}|_{max}$.

3.1.3. Elongation

In the Fixed cases (Figures 2a-c), stretching of the plate and slab is accentuated during subduction, which becomes more pronounced as the slab tip approaches the bottom. In the Free cases (Figures 2d-f) little stretching is observed. In order to quantify the effects of the initial slab geometry on the total stretching, the elongation of the plate and slab was estimated over time. The total length of the plate and slab X_{sp} is defined as the length of the trailing plate plus the length of the slab ($X_{sp} = L_{sp} + l_{sp}$). At the start of each experiment $X_{sp}(0) = L_{sp}(0) + l_0$ and the elongation e is defined by:

$$e = \frac{X_{sp} - X_{sp}(0)}{X_{sp}(0)}. \tag{11}$$

The total plate and slab elongation is plotted as function of time in Figure 6, representing how much the ensemble plate plus slab grows relative to its initial length. The maximum elongation for each experiment is shown in brackets in the legend of Figure 6. For the Fixed case Deep mantle experiments (solid lines; Figure 3a), the total elongation increases continuously, reaching maximum of $\sim 58 - 113$ %. Changing the initial slab length (D1, D3 and D5), for $t < 20$ Ma the curves collapse into one. At $t > 20$ Ma, as the slab tip approaches approximately half of the mantle thickness depths, the elongation curves have different slopes,

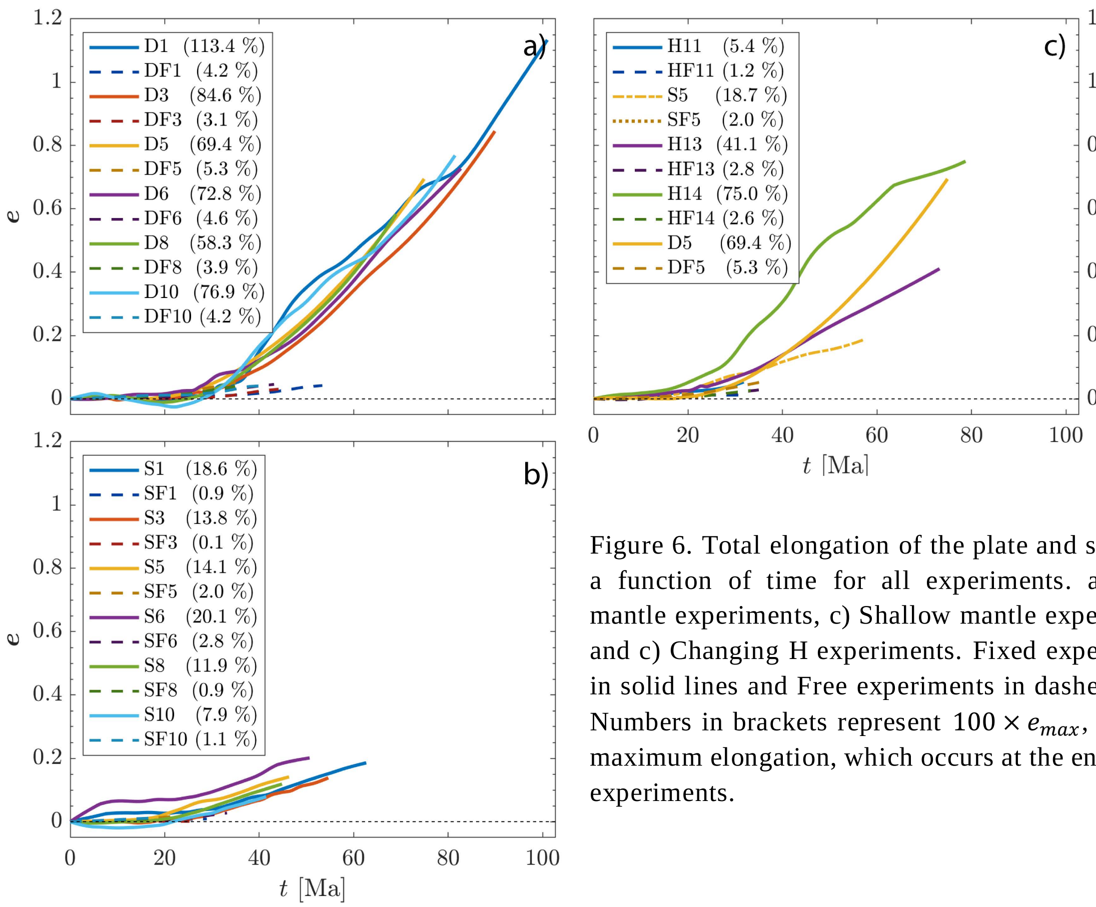

Figure 6. Total elongation of the plate and slab e as a function of time for all experiments. a) Deep mantle experiments, c) Shallow mantle experiments and c) Changing H experiments. Fixed experiments in solid lines and Free experiments in dashed lines. Numbers in brackets represent $100 \times e_{max}$, i.e., the maximum elongation, which occurs at the end of the experiments.

indicating that the plate and the slab stretch at different rates. The stretching occurs at a progressively higher rate after ~50 Ma for experiments with higher l_0 (D5). When the initial slab dip angle is increased (D6, D5, D8 and D10), the elongation curves overlap when $t < 20$ Ma. At $t > 20$ Ma, the elongation curves have similar slopes, indicating the plate and slab stretch at similar rates. In the Free case (dashed curves in Figure 3a), the total elongation is minimum for all experiments, between ~$3.1 - 5.3$ %.

3.1.4. Instantaneous dimensionless sinking velocity

The velocity curves shown in Figure 3 were normalized by the Stokes velocity approximation (equation 5) and plotted as function of the plate stiffness S (equation 6) in Figure 7. The beginning of each experiment ($t = 0$ s) corresponds to the highest value of S, and as the slab sinks, the stiffness decreases as a response to the increase of the slab length l_{sp}. The change in plate thickness h_{sp} is not accounted for, even though the plate stretches and thins during the experiments. Consequently, with the exception of the start of the experiments (when $t = 0$ s), the plate stiffness is increasingly overestimated towards a maximum at the end of the experiments. The maximum overestimation can be assessed by analysing the plate and slab elongation. The Fixed case Deep mantle experiments have the maximum total elongation

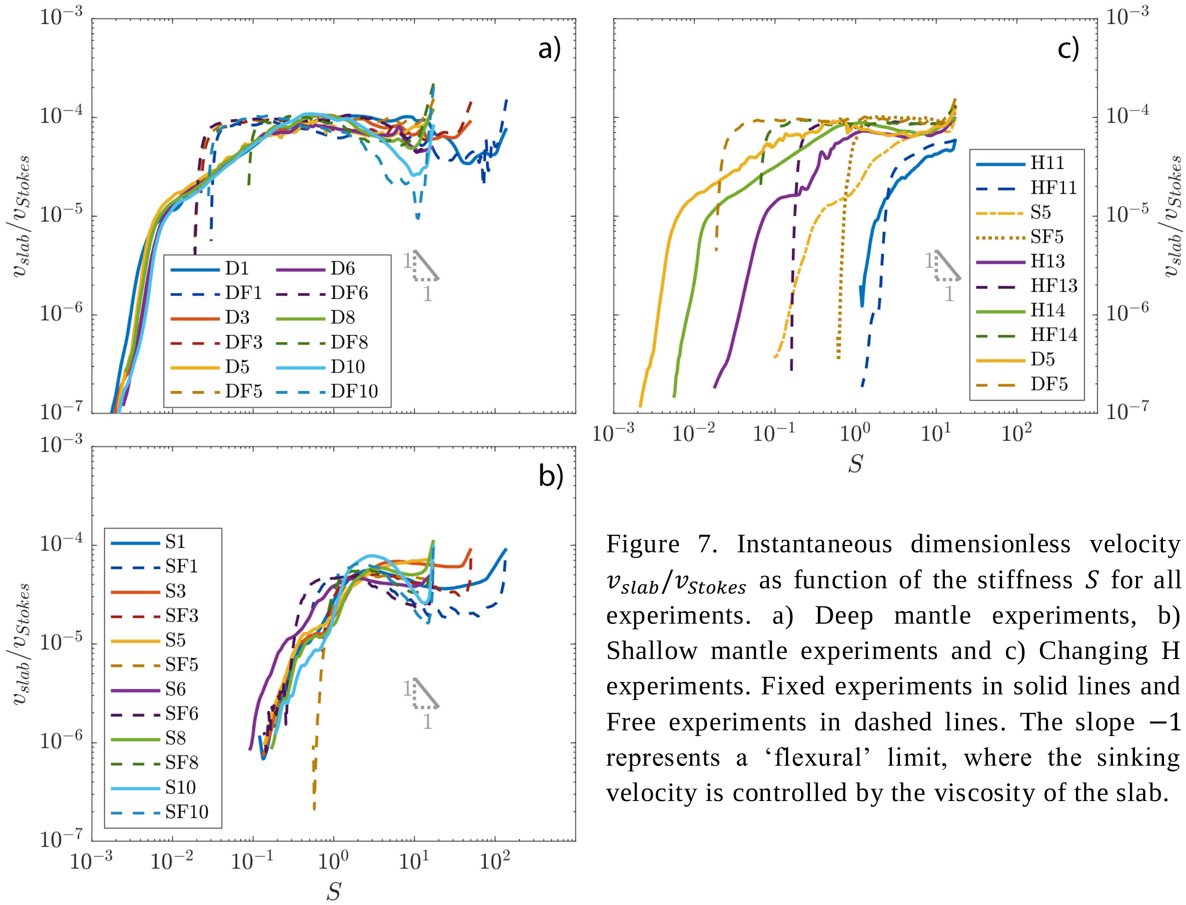

Figure 7. Instantaneous dimensionless velocity v_{slab}/v_{Stokes} as function of the stiffness S for all experiments. a) Deep mantle experiments, b) Shallow mantle experiments and c) Changing H experiments. Fixed experiments in solid lines and Free experiments in dashed lines. The slope -1 represents a 'flexural' limit, where the sinking velocity is controlled by the viscosity of the slab.

(Figure 7). The largest elongation occurred in experiment D1 (113.4 %, Figure 7a), where the combined plate and slab length increased from 2,925 km, at the start of the experiment, and reached a length of ~6,242 km at the end, which implies that the thickness of the plate has been reduced by a factor of ~2. In this scenario, the stiffness of the plate was overestimated by a factor ~2^3 by the end of the experiment (equation 6). Only the Fixed case experiments exhibit very high maximum elongation, which explains why the curves in Figure 7 differ between Fixed and Free cases at $S < 0.1$. Because the plate and the slab stretch the most only after the slab tip has sank below half the mantle thickness depth, it presumed that for $S > 0.1$ the values of stiffness are reasonably estimated.

In Figure 7a, the Deep mantle experiments in which the slab is initially shorter (D1, DF1, D3 and DF3) start with larger stiffness. All experiments show the same pattern of decreasing instantaneous velocity while the slab lengthens until a critical stiffness value is attained. The critical stiffness value varies with the initial slab length ($S \sim 10 - 70$) but not with the initial angle ($S \sim 10$). This behaviour corresponds to the initial bending stage while the slab tip bends downwards without significant subduction, during which the slab kinked tip adjusts to a smoother geometry. Following this stage, the instantaneous velocity increases until $S \sim 1$ at different rates. When the initial slab dip angle is increased (D6, DF6, D5, DF5, D8, DF8, D10 and DF10), for $1 < S < 10$, higher values of θ_0 results in a slope of the curve progressively closer to -1, implying that the sinking velocity is further controlled by the viscosity of the plate [Ribe, 2010; Li & Ribe, 2012] for higher initial slab angle.

The Fixed case curves reach a local maximum of the instantaneous velocity (between $\sim 8 \times 10^{-5}$ and $\sim 10^{-4}$) at $S \sim 0.4$, followed by a decrease as the slab grows further and the stiffness decreases. This maximum occurs at lower values of S for the Free case experiments ($S \sim 0.2$) but with similar instantaneous velocity maximum values. After the maximum instantaneous velocity is reached, results from experiments with the same initial slab length collapse into a single curve, in both Fixed and Free cases.

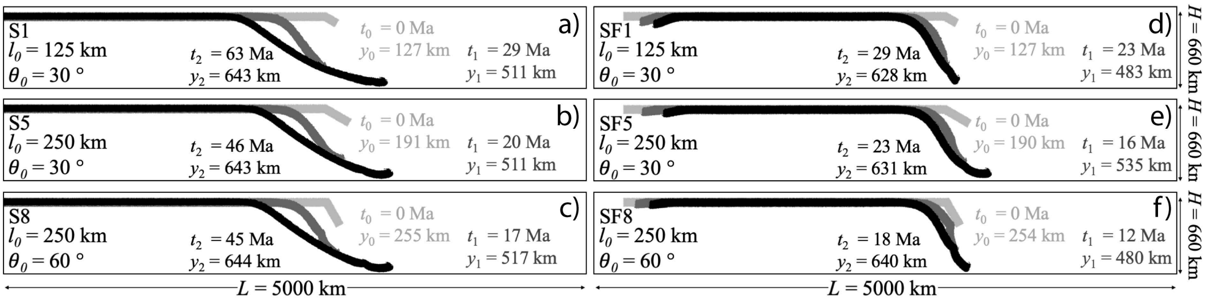

Figure 8. Slab geometric evolution of experiments S1, S5 and S8 (a-c) and SF1, SF5 and SF8 (d-f). Four times are depicted, corresponding to the start, t = 0 s (light grey), the end (in black) and two intermediate times (Table A1).

3.2. Shallow mantle models

3.2.1. Plate geometry

Figure 8 shows the plate geometric evolution for experiments S1, SF1, S5, SF5, S8 and SF8. Four times are depicted for each experiment, corresponding to the start, t = 0 s, the end and two intermediate times when the slab tip reaches a depth of $\sim 310 \pm 18$ km and a depth of $\sim 515 \pm 27$ km (Table A1). Two stages of subduction are identified in all experiments: (1) a transient stage, when the slab tip bends downwards; and (2) a decelerating stage, where the curvature of the slab tip inverts.

Overall, the initial slab geometry has little effect on the evolving plate geometry, mainly due to shallow thickness of the mantle, which results in constant interaction between the slab and the bottom boundary. Changes in the slab initial geometry results in different times for the slab to reach the bottom. Doubling the initial slab length in the Fixed case (S1 to S5; Figure 8) results in the slab reaching the bottom ~ 17 Ma earlier, whereas in the Free case (SF1 to SF5; Figure 8), a ~ 6 Ma difference is observed. However, increasing the initial slab dip angle (S5 to S8, and SF5 to SF8), results in the slab reaching the bottom only $\sim 1 - 5$ Ma earlier.

3.2.2. Slab sinking and trench retreat

The slab tip vertical position and the trench horizontal position of end-member cases for Fixed and Free Shallow mantle experiments, are presented in Figure 3c and d. The slab vertical displacement curves (Figure 3c) display two different patterns if the plate is either fixed or free. In the Fixed case, the curves (solid lines) have a concave shape until the tip reaches around 500 km depth, after which they acquire a convex shape. In the Free case, the curves (dashed lines) retain the concave shape almost until the slab reaches the bottom. The main differences between these curves are in the initial stage, where the slab initial depth is varied as result of the slab geometry. Experiments with a longer initial slab length have a shorter bending stage, similar to experiments with a steeper initial slab dip angle. However, for $\theta_0 = 90°$, the initial bending stage is longer as the plate bending/unbending is hindered at the trench region delaying the subduction process. The experiments that shows longer initial bending stages also take longer to reach the bottom. In the Fixed case, the trench displacement curves (Figure 3d), show almost constant trench retreat until around the time when the slab tip reached about 500 km depth, after which the slope of the curves is reduced. In the Fixed case, the trench (solid lines in Figure 3d) retreats from its starting position a maximum of ~ 700 km oceanwards. In the Free case, the trench (dashed lines in Figure 3d) retreat is limited to a maximum of ~ 360 km oceanwards.

The slab sinking velocity and trench velocity (Figure 4c-d) were also calculated by centered finite differences (equation 11). All curves show an increase in absolute velocity followed by a decrease. Free case experiments reach higher absolute sinking velocities and lower trench retreat velocities. The times at which these absolutes maximums are reached vary with the initial slab geometry. The times at which the maximum absolute sinking velocity $|v_s|_{max}$ occur, $t(|v_s|_{max})$, are compared to the times when the slab tip depth equals the half of the mantle thickness $t(y_{slab} = H/2)$, and the bottom of the mantle $t(y_{slab} = H)$ (Figure 5c-d, and Table A2). In the Fixed case, $|v_s|_{max}$ occurs ~ 3 Ma after $t(y_{slab} = H/2)$, while in the Free case, $|v_s|_{max}$ occurs ~ 6 Ma after $t(y_{slab} = H/2)$. Changing the initial slab length (Figure 5c), $t(|v_s|_{max})$ is inversely proportional to the initial slab length (i.e., the longer the initial slab is, the earlier $|v_s|_{max}$ is reached). Varying the initial slab dip angle $t(|v_s|_{max})$ occurs within a 4 Ma variation. Independently of the initial slab geometry, the slab in the Fixed cases reaches the bottom $\sim 27 - 39$ Ma after $t(|v_s|_{max})$ and the slab in the Free cases reaches the bottom $\sim 3 - 16$ Ma after $t(|v_s|_{max})$.

The mean values of the maximum absolute sinking velocity and the maximum absolute trench velocity ($|v_s|_{max}$ and $|v_t|_{max}$, respectively) for all sets of experiments and the respective standard deviations are summarised in Table 3. For the Fixed Shallow mantle experiments, changing the slab length (S1 – S5) and changing the initial dip angle (S5 – S10) results in a comparable mean and but distinct standard deviation of $|v_s|_{max}$, with 1.4 km/Ma difference between means and 2.5 km/Ma difference between standard deviations. This indicates that changes in θ_0 affect $|v_s|_{max}$ more than changes in l_0. Changing the initial dip angle (S5 – S10) results in a similar mean but a lower dispersion of $|v_t|_{max}$, with 0.6 km/Ma difference between means and -1.7 km/Ma difference between standard deviations, compared to changing the slab length (S1 – S5), implying that the initial slab length has a higher effect on $|v_t|_{max}$.

For the Free case experiments, changing the slab length (SF1 – SF5) and the initial dip angle (SF5 – SF10) results in a comparable mean and dissimilar standard deviation of $|v_s|_{max}$, with only 1.4 km/Ma difference between means and 2.7 km/Ma difference between standard deviations. It also results in a different mean and standard deviation of $|v_t|_{max}$, with 2.1 km/Ma difference between means and 1.4 km/Ma difference between standard deviations. Indicating that in the Free case the initial slab dip angle has higher effect on both$|v_s|_{max}$ and $|v_t|_{max}$, than the initial slab length.

Additionally, in the Free case experiments it is possible to evaluate the effects of changing the initial slab geometry on the motion of the trailing edge of the plate (Figure A1). Changing the slab length (SF1 – SF5) and the initial dip angle (SF5 – SF10) results in comparable mean and standard deviation of $|v_{te}|_{max}$, with -0.9 km/Ma difference between means and 0.1 km/Ma difference between standard deviations. This demonstrates that the initial slab length and initial slab dip angle affect $|v_{te}|_{max}$.

3.2.3. Elongation

In Figure 6b the plate and slab elongation is plotted as function of time for the Shallow mantle experiments. In Fixed case (solid lines), the total elongation increases continuously, reaching maximum of $\sim 8-20$ %. For $t < 20$ Ma the elongation curves have different slopes, indicating that the plate and the slab stretch at different rates. And at $t > 20$ Ma, the slopes of the elongation curves slopes are similar, implying that the plate and the slab stretch at similar rates. When the initial slab dip angle is increased (D6, D5, D8 and D10), the elongation curves overlap and the total elongation is minimum for all experiments, between $\sim 0.1-2.8$ %.

3.2.4. Instantaneous dimensionless sinking velocity

The dimensionless sinking velocity is plotted as function of the plate stiffness S (equation 6) in Figure 7b for the Shallow mantle experiments. In the Shallow mantle experiments the plate and slab also stretch during subduction. The largest elongation occurred in experiment S8 (20.1 %, Figure 7b), where the combined plate and slab length increased from $2{,}925$ km, at the start of the experiment, and reached a length of ~ 3513 km at the end. This implies that the thickness of the plate has been reduced by a factor of ~ 1.2. In this scenario, the stiffness of the plate was overestimated by a factor $\sim 1.2^3$ (~1.7) by the end of the experiment (equation 6). Thus, the overestimation of plate stiffness is much smaller for these experiments.

The experiments in which the slab is initially shorter (S1, SF1, S3 and SF3) start with larger stiffness (Figure 7b). All experiments show the same pattern of decreasing instantaneous velocity while the slab lengthens until a critical stiffness value is attained. The critical stiffness value varies with the initial slab length ($S \sim 10 - 70$) but not with the initial angle ($S \sim 10$). This behaviour corresponds to the initial bending stage while the slab tip dips bend downwards without significant subduction, during which the slab kinked tip adjusts to a smoother geometry. After this stage, the instantaneous velocity increases until $S \sim 3$ at different rates. When the initial slab dip angle is increased (S6, SF6, S5, SF5, S8, SF8, S10 and SF10), for $1 < S < 10$, higher values of θ_0 results in a slope of the curve progressively closer to -1, implying the sinking velocity is further controlled by the viscosity of the plate [Ribe, 2010; Li & Ribe, 2012] for higher initial slab angle.

The Fixed case curves reach a local maximum of the instantaneous velocity (between $\sim 5 \times 10^{-5}$ and ~8×10^{-5}) at $S \sim 0.4$, followed by a decrease as the slab grows further and the stiffness decreases. This maximum occurs at lower values of S for the Free case experiments ($S \sim 0.2$) and lower instantaneous velocity maximum values (between $\sim 5 \times 10^{-5}$ and $\sim 7 \times 10^{-5}$).

3.3. Varying mantle depth models

The geometric evolution of experiments H11, HF11, S5, SF5, H13, HF13, H14, HF14, D5 and DF5 (Figure 9) shows an incremental sequence of the previously described subduction stages for Deep mantle (Figure 2) and Shallow mantle experiments (Figure 8). The boundary effects are exerted on the slab at a later stage into the subduction process if the mantle is thicker. Thus, for an increasingly thicker mantle, the geometric evolution of the slab is closer to that in the Deep mantle experiments. Changing the mantle thickness from 410 km to 2280 km, in the Fixed case (H11 to D5; Figure 9), results in the slab reaching the bottom ~ 33 Ma later, and in the Free case (HF11 to DF5; Figure 9), results in a ~ 18 Ma difference (Table A1).

The slab tip vertical position curves (Figure 3e) display two different patterns when the plate is either fixed or free. In the Fixed case, the curves (solid lines) have a concave shape until

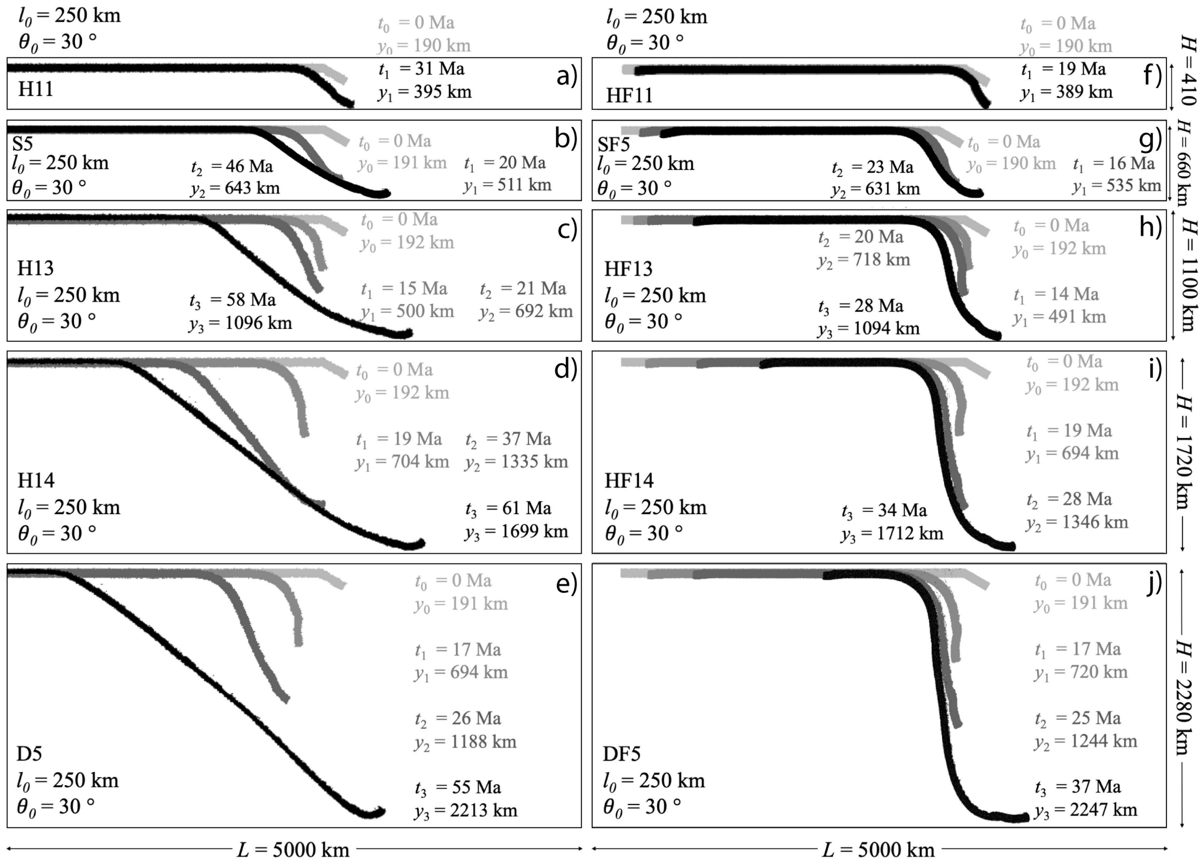

Figure 9. Slab geometric evolution of experiments H11, S5, H13, H14 and D5 (a-e) and HF11, SF5, HF13, HF14 and DF5 (f-j). Four times are depicted, corresponding to the start, t = 0 s (light grey), the end (in black) and two intermediate times (Table A1).

the tip reaches around half the mantle thickness depth, after which they acquire a convex shape. In the Free case, the curves (dashed lines) retain the concave shape almost until the slab reaches the bottom. The total trench retreat also increases with the mantle thickness (Figure 3f), varying between $\sim 210 - 2700$ km in the Fixed case, and $\sim 80 - 550$ km in the Free case.

The slab sinking velocity curves (Figure 4e) exhibit an absolute maximum, with the exception of experiments H11 and HF11 (in which $H = 410$ km). In both Fixed and Free cases, the slab the absolute maximum is higher with increasing mantle thickness, and the absolute maximums are reached later, as the plate interaction with the bottom also occurs later (Figure 5e). In the Fixed case, the slab reaches the bottom $\sim 31 - 41$ Ma after $t(|v_s|_{max})$ and in the Free cases the slab reaches the bottom $\sim 4 - 14$ Ma after $t(|v_s|_{max})$, depending on the mantle thickness. The slab in Experiments H11 and HF11 reaches $|v_s|_{max}$ the beginning of subduction, because the mantle is so shallow that the slab is in strong interaction with the bottom from the start. In addition, Experiment HF11 has a sinking velocity almost constant until ~ 15 Ma.

Both in the Fixed and Free cases the change in mantle thickness results in a large dispersion of the absolute maximum sinking velocity (see Table 3, $|v_s|_{max}^{mean} = 35.0 \pm 21.8$ km/Ma in the Free case and $|v_s|_{max}^{mean} = 59.2 \pm 43.4$ km/Ma in the Free case) and of the maximum trench velocity ($|v_t|_{max}^{mean} = 46.3 \pm 29.5$ km/Ma in the Free case and $|v_t|_{max}^{mean} = 18.4 \pm 7.9$ km/Ma in the Free case), indicating that the mantle thickness strongly affects the maximum velocities reaches. In the Free case experiments, the trailing edge motion (Figure A1) is also strongly affected by the mantle thickness with $|v_{te}|_{max}^{mean} = 56.6 \pm 35.8$ km/Ma.

The plate and slab elongation (Figure 6c) is also progressively higher with increasing mantle thickness. The dimensionless velocity (Figure 7c) also shows strong dependence on the mantle thickness. In the extreme case of $H = 410$ km (H11 and HF11), at $S > 10$ there is no inflection of the curve related with the initial stages of subduction and the instantaneous sinking velocity is lower.

4. Discussion

Subduction is the process responsible for the closing of ocean basins, and its implications for the global tectonics and mantle convection are commonly investigated through dynamic numerical and analogue experiments. However, models of subduction seldom take into account the mechanisms by which subduction initiates, of which many have been proposed [e.g., Stern & Gerya, 2018]. Different initiation processes yield different initial slab geometries that drive subduction [Nikolaeva et al., 2010]. How this initial slab geometry impacts the subduction dynamic evolution is not yet fully understood. The main aim of this study was to evaluate how variations in the initial slab geometry influence subduction evolution.

4.1. Effect of initial slab length, initial dip angle and mantle thickness on slab geometry evolution

Subduction dynamics was investigated using isothermal 2D numerical experiments assuming linear and homogeneous rheologies. Three parameters were varied: the length and the dip angle of the initially imposed kinked slab and the mantle thickness. The results show that different initial slab geometries impact mostly the duration of the subduction stages, between initiation to the moment the slab reaches the bottom boundary. The main differences are in the duration of the initial bending stage, until the slab tip reaches ~ 500 km depth, which is due to changes in the initial depth of the slab as result of the imposed slab geometry. These time variations are reflected in variations in the sinking and trench retreat rates, especially in the absolute maximum velocities reached.

The predominant difference in the observed slab geometry evolution relates to the dip angle of the initially kinked slab: a sharper kink due to a steeper initial slab angle is better preserved at the end of the experiment. The high resistance to bending/unbending is explained by the viscosity ratio between plate and the underlying mantle used in this study ($\gamma = 640$). This results in a high ratio between the slab radius of curvature and its thickness [Schellart, 2008; Ribe, 2010], such that the slab is stronger and bends less than in cases with lower values of γ.

Generally, in the Fixed case, sinking velocities are lower and trench retreat velocities are higher compared to the Free case. The difference results from the change in plate trailing edge boundary condition, which also impacts the total amount of stretching of both the plate and the slab. This is most evident in the deep mantle experiments, where the bottom boundary effects are delayed.

The Fixed case experiments exhibit accentuated stretching of the plate and slab, whereas in the Free case the total elongation is minimum for all experiments. In the Deep mantle configuration, the Fixed case experiments are, on average, 35 Ma slower to reach the bottom than in the Free case. These experiments also show a similar geometric evolution, with slabs dipping $30 - 40°$ when the tip of the slab reaches the bottom boundary in the Fixed cases, and very steep slabs ($\sim 80°$) in the Free cases. In the shallow mantle experiments, the Fixed case experiments are, on average, 29 Ma slower to reach the bottom than the Free case ones. The shallow mantle experiments also show a similar geometric evolution, with slabs dipping 30 – 40° when the tip of the slab reaches the bottom boundary in the Fixed cases and steeper slabs (60 – 70°) in the Free cases. All differences between Fixed and Free case result from the trailing edge boundary condition: when the plate is fixed there is an extra resisting force to slab pull. Thus, slab sinking is reduced while subduction is mostly accommodated by trench retreat through plate stretching.

The changes in the initial slab length result in variations of the time the slab takes to reach the bottom boundary. In the deep mantle experiments, an increase of the initial slab length from 125 to 250 km results in the slab reaching the bottom 16 Ma earlier in Fixed case, and 15 Ma earlier in the Free case. In the shallow mantle experiments, the same increase of the initial slab length results in the slab reaching the bottom 17 Ma earlier in the Fixed case, and 6 Ma earlier in the Free case. The faster subduction can be explained due to the increased buoyancy of the longer slab driving subduction. A shorter initial slab leads to a longer initial bending stage, until the slab is sufficiently negatively buoyant to drive subduction.

In the first 20 Ma of the deep mantle experiments, before the slab reaches half the mantle depth, it is possible to differentiate that initial slab dip angles of $15°$ and $90°$ result in lower sinking velocities, both if the plate is fixed or free. The same applies in shallow mantle experiments but over a shorter initial period (the first 15 Ma). These observations suggest that there is a critical angle for the slab dynamics effects, which can be explained in cases of very low initial dip angle by the fact that the slab must rotate downwards more before the slab tip sinks to ~ 500 km, when the sinking velocity increases. In cases of a very steep initial dip angle sinking velocities are lower because there is a very sharp kink between the plate and slab, which hinders plate bending/unbending in the trench region, delaying the subduction process.

Increasing the mantle thickness from 410 to 2280 km in the Fixed case results in a difference of ~30 Ma for the slab to reach the bottom. In the Free case experiments, the same mantle thickness increase results in ~20 Ma difference. The Fixed case experiments are, on average, 22 Ma slower to reach the bottom than the Free case ones, because (again) the plate motion is constrained and subduction occurs mostly by trench retreat. The plate and slab elongation (Figure 6c) becomes progressively higher with increasing mantle thickness. Thus, the entire plate is more elongated, since it takes longer for the slab to reach the bottom. The value of v_{Stokes} (equation 6) varies only with the slab length and assumes an infinite volume of viscous fluid, however the sinking velocity is strongly affected by the depth of the mantle. Thus, the dimensionless sinking velocity increases with H/l, (see Figure 7 of Li & Ribe [2012]). In the extreme case of $H = 410$ km (H11 and HF11) the plate is always under strong boundary effects and the plate viscosity controls the sinking velocity.

4.2. Comparison with previous models

Previous models of subduction did not systematically explore differences in subduction dynamics caused by the initial imposed slab geometry. Most analogue modelling studies start subduction by manually forcing the tip of the plate downwards to an arbitrary depth, so that it is enough to drive subduction [Funiciello et al., 2006; Bellahsen et al., 2005; e.g. Funiciello et al., 2003a], or until a pre-determined length of the slab is bent between 15 to 30° [e.g., Schellart, 2004a, 2004b, 2010]. In numerical models, the geometry of the slab is defined considering either a certain maximum depth or a minimum slab length dipping into the mantle [Schmeling et al., 2008; Capitanio et al., 2010; Quinquis et al., 2011; Stegman et al., 2010]. In some cases, in both analogue and numerical studies, the geometry is not clearly specified and subduction in the models starts with a perturbation that is described as “sufficient to begin the process of subduction” [Faccenna et al., 2001; OzBench et al., 2008; Stegman et al., 2006].

In a wide variety of subduction models the range of initial slab length is usually between 100 and 200 km. Ribe [2010] explores how the mode of subduction depends on the slab length and the initial dip angle. He tests ratios of $l_0/h \in [4;6]$ and in the experiments of this study, h is constant and the ratio $l_0/h \in [1.7;3.3]$. However, the initial slab he defines is curved and the initial slab used here is kinked, therefore, the l_0/h ratio of the experiments is underestimated by comparison. Nonetheless, Ribe [2010] concluded that the plate stiffness S, which decreases during subduction due to the growth of the slab, determines whether plate deformation is controlled by the viscosity of the plate or the mantle. As the slab lengthens and $S \leq 1$, the viscosity of the plate becomes less important for both plate deformation and sinking velocity. The experiments in this study do not show the same distinct limit (Figure 7), as the model domain is constrained by free-slip boundaries, whereas the models of Ribe [2010] are defined in an infinite half-space. However, it is still possible to identify a 'flexural' limit that determines if the sinking velocity is controlled by the plate viscosity or by the mantle viscosity, which varies with the initial slab geometry. Despite the initial slab being shorter in the experiments presented here, the mantle viscosity controls the subduction dynamics when the slab is not influenced by boundaries effects, which is a very short period. This explains why in Figure 7 the instantaneous velocity decreases again at low values of the plate stiffness.

The mode of subduction is a function of the initial plate stiffness, the ratio between mantle thickness and initial slab length, the ratio between plate width and initial slab length and initial slab dip angle [Li & Ribe, 2012]. The range of mantle thickness to initial slab length ratios in this study is $1.64 - 18.24$, which overlaps with the lower end of the range $1.13 - 2.27$ presented by Li & Ribe [2012]. In their 3D study, the trailing plate is free to move as the slab subducts. Their model with a plate-mantle viscosity ratio $\gamma = 600$, and the Free case experiments here with $\gamma = 640$ display different slab geometries. In this study, the slab tip tends to slide along the bottom boundary in all mantle conditions, whereas in the models of Li

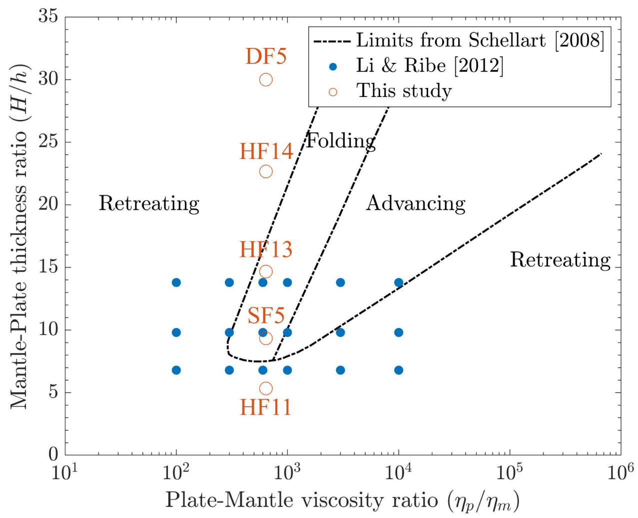

Figure 10. Subduction regime diagram with limits defined by Schellart [2008]. Also plotted are the range of plate to mantle thickness ratio and plate to mantle viscosity ratio used in Li & Ribe [2012] and used in this study (experiments in which only the mantle thickness was varied).

& Ribe [2012], some folding occurs for deeper mantle conditions. This difference could be explained by the fact that Li & Ribe [2012] models are 3D and the mantle is laterally unconstrained, thus there are no lateral wall effects influencing subduction induced mantle flow. In a 2D model set-up subduction induced mantle flow is restricted to poloidal flow around the slab tip, from the sub-slab region towards the mantle wedge region. In a 3D model, the mantle flow has a toroidal flow component around the plate edges, which for narrow plates (of width $\leq$ 1500 km) is three to four times stronger than the poloidal flow [Stegman et al., 2006]. Subduction induced mantle flow occurs mainly around lateral slab edges [Schellart, 2004a, 2008; Li & Ribe, 2012]. Toroidal flow facilitates the slab to retain a steeper dip angle as it approaches the bottom, promoting slab folding.

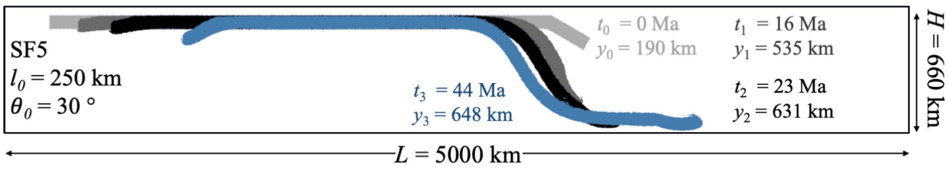

Figure 11. Slab geometric evolution of experiment SF5. Five times are depicted, corresponding to the start, t = 0 s (light grey), the end (in black), two intermediate times and 11 Ma times after the end of the experiment (blue).

Although the mantle-plate thickness ratio and the plate-mantle viscosity ratios used in this study predict that experiments SF5 and HF13 should follow a slab folding mode of subduction [e.g., Schellart, 2008; Li & Ribe, 2012] (Figure 10), no such folding is observed (Figure 9). Analysis of the experiments presented here applies until the moment the slab tip touched the bottom boundary and does not consider slab geometric evolution during the subsequent steady-state stage of subduction. However, even 11 Ma after reaching the bottom, the slab in experiment SF5 (Figure 11) did not develop folding. A similar geometric evolution after slab interaction with the bottom boundary was observed in other experiments.

The folding regime is also characterized by episodic trench migration [Schellart, 2008], which is also not found in the present study, although trench migration is reduced. The geometric evolution of slabs in the Deep mantle experiments in the Free case experiments is consistent with the retreating regime, as predicted, with comparable trench migration (dashed lines in Figure 3a and b).

Schellart [2008] investigated both deep and shallow mantle models, varying the plate-mantle viscosity contrast γ and summarised the maximum trench and subducting plate velocities in analogue experimental units. It is possible to compare the maximum velocities reported in Schellart [2008] with results of this study by conversion to units in nature using the appropriate scaling factors (Table 4). Model DM4 in Schellart [2008] has $\gamma = 798$. In this study, the mantle viscosity is slightly higher, resulting in lower maximum trench and trailing edge velocities (which is a good proxy for the subducting plate velocity). Nevertheless, the maximum velocities in the Free case are in good agreement with the results of Schellart [2008]

Table 4. Average maximum trench and trailing edge velocities in model units to compare with results from Schellart [2008]. The model-nature timescale for the experiments in this study is $t^N/t^M = 0.064221$, and the length scale is L^N/L^M =5066.7, where the superscripts M and N refer to model and nature, respectively.

Deep Mantle		This study $\gamma = 640$	Schellart [2008] $\gamma = 798$
$\lvert v_t \rvert_{max}$ [cm/h]	changing l_i	112.6 $\pm$ 7.1	203.0
	changing θ_i	123.2 $\pm$ 11.6	
$\lvert v_{te} \rvert_{max}$ [cm/h]	changing l_i	480.4 $\pm$ 19.6	759.8
	changing θ_i	477.0 $\pm$ 35.7	
Shallow Mantle		**This study $\gamma = 640$**	**Schellart [2008] $\gamma = 706$**
$\lvert v_t \rvert_{max}$ [cm/h]	changing l_i	79.7 $\pm$ 7.2	158.6
	changing θ_i	99.1 $\pm$ 22.8	
$\lvert v_{te} \rvert_{max}$ [cm/h]	changing l_i	184.3 $\pm$ 10.4	172.4
	changing θ_i	160.8 $\pm$ 63.9	

4.3. Implications for nature

The geometric variations observed between all experiments are too subtle to compare with natural systems, since the spatial resolution of the slab tips in nature is beyond the resolution of tomography imaging. Experiments with initial short slab lengths, or very low and very high initial slab dip angles, show a longer initial stage in early subduction associated with the slab tip bending before self-sustained subduction starts. Slowly evolving subduction would extend the periods of time over which a slab could equilibrate thermally (i.e., get warmer, and thus reducing its density), which ultimately can hamper self-sustained subduction [Marques et al., 2014]. Even though the experiments in this study did not account for the thermal effects and mineral phase changes, it is plausible to conclude that initiation with short slab lengths and extreme dip angles will be lead to short-lived subduction.

Present-day slab configurations do not provide enough information to infer the starting conditions of subduction, and there are only a few examples of incipient subduction in nature. Furthermore, these examples are at such an early stage it cannot be predicted how will they evolve. For example, in the Puysegur trench at least 350 km of the Australian plate has been subducted at an highly oblique angle, reaching ~ 150 km depth, for the past $12 - 15$ Ma

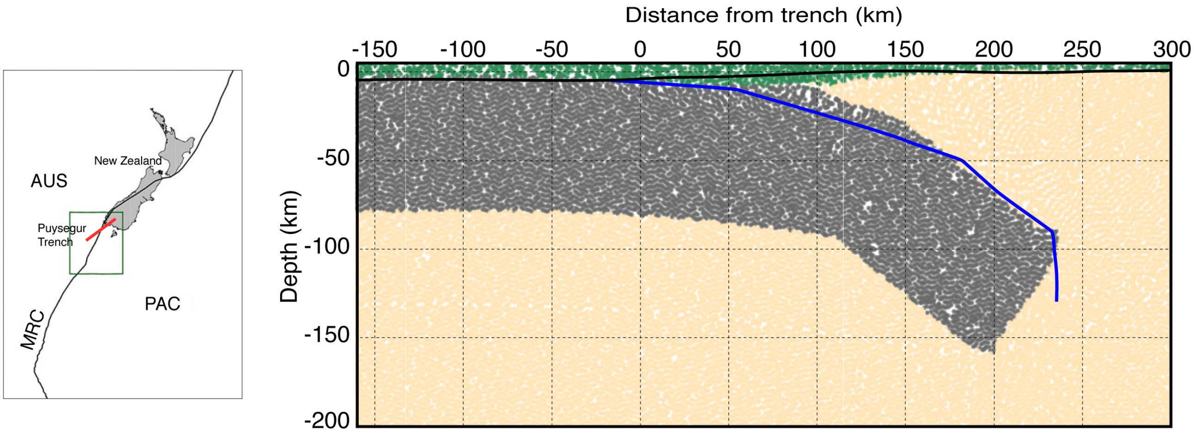

Figure 12. a) Plate boundary of New Zealand region (modified after Mao et al. [2017]) and b) early stage subduction of experiment S1 ($l_0 = 125$ km and $\theta_o = 30°$) overlapped with the Wadati-Benioff zone derived by Hayes & Furlong [2010] in blue and the topography contour in black, at the profile indicated by the red line on the left panel.

[Lamarche & Lebrun, 2000] (Figure 12). The Puysegur margin resulted from convergence across a pre-existing transform fault [Toth & Gurnis, 1998; Lebrun et al., 2000; Lebrun et al., 2003] and the present Wadati-Benioff zone dips steeply [Lamarche & Lebrun, 2000]. Thus, the slab is inferred to be short and steep (blue line in Figure 12). In this example, the slab dips into the mantle, but has not yet descended deep enough to be considered as a self-sustained subduction zone [Mao et al., 2017].

The starting stage of the experiments reported here is compared with the present-day Puysegur slab geometry. Experiment S1 starts with a slab dipping at $30°$ and reaching a depth of ~ 125 km. After 5 Ma, the slab tip has reached a depth of 155 km, equivalent to the present depth of the Puysegur slab. This suggests that it would have taken $7 - 10$ Ma for the Puysegur slab to initiate descent into the mantle to its present position. Following the evolution of experiment S1, the Puysegur slab is presently at the end of the bending stage and over the next ~ 20 Ma the sinking velocity will increase, leading to an increase in trench retreat velocity before it will eventually slow down.

In Figure 12, the slab geometry of experiment S1 at 5 Ma is compared to the Wadati-Benioff of the Puysegur subduction zone [Hayes & Furlong, 2010]. Overall, the slab geometry correlates reasonably well with the Wadati-Benioff zone, especially the slab tip. The trench position predicted by the model is about 75 km off, which is acceptable, considering that the Puysegur slab is subducting at a highly oblique angle relative to the trench [Lamarche & Lebrun, 2000]. Moreover, the Wadati-Benioff zone is projected into a profile along the same oblique angle, whereas the 2D model represents a cross-section of the subduction zone perpendicular to the trench. Additionally, the trench position mismatch would also be minimized by implementing an arcuate initial slab in experiment S1.

All experiments exhibit trench retreat, which is the most common style of trench behaviour amongst subduction zones in nature [Schellart et al., 2008]. Fast trench retreat results in horizontal deflection of the slab at the transition zone and slow trench retreat results in slab piling and/or slab penetration through the transition zone [e.g., Schellart, 2005]. The trailing edge condition seems to be more important to the way the slab tip impinges on the bottom boundary than the initial slab geometry. In the Free case experiments, slabs developed a sub-vertical geometry, whereas in the Fixed case experiments, slabs are strongly tilted. The trailing edge condition induces large variations in slab sinking and trench migration velocity. On average the trench velocity is 50 km/Ma and 5 km/Ma in the deep and the shallow mantle experiments, respectively, and slower when the plate is free to move, which explains the sub-vertical slab geometries observed.

Trenches retreat rapidly close to the slab lateral edges in nature (< 1500 km), at about $60 - 170$ km/Ma. Far from the edges (> 2000 km) trench retreat is slow, with trench retreating rates < 20 km/Ma [Schellart et al., 2008]. Based on the results presented here, the Fixed case experiments represent slabs sinking close to the slab lateral edge, while the Free case experiments represent slabs sinking away from the slab lateral edge. However, the 2D configuration of the experiments limits the comparison between the results and nature to the centre of wide slabs, where poloidal mantle flow is best developed. Consequently, the results represent 2D cross-sections across the centre of intrinsically 3D wide subduction zones, in which the sub-horizontal component of the mantle flow is minimized [Schellart et al., 2007]. The Fixed case configuration can be interpreted as a subducting plate in which there is no ridge at the plate trailing edge. This suggests that subducting plates in the Fixed case may never mature because the plate will be rapidly consumed within the first ~ 70 Ma after subduction initiation. Thus, if no new oceanic lithosphere is created at the plate trailing edge, subduction may not reach a steady-state stage.

Additional factors that may impact the way the slab impinges on the mantle transition zone include the upper-mantle rheology. In this study, both plate and the mantle were simulated with a constant viscosity, however, in nature, the way materials deform depends on temperature and stress, which translates to a variable viscosity. Indeed, if the upper-mantle deforms non-linearly with temperature and stress, the viscosity will be reduced and the way the slab interacts with the bottom boundary will vary [Holt & Becker, 2017].

5. Conclusions

Subduction is a complex process that is controlled by many different parameters, such as plate age and viscosity. In this study, subduction always starts with an initial slab bending stage. During this stage, both the slab tip and the trench move little and slowly, and if the trailing plate is free it also moves slowly. At the end of the bending stage, when the slab has lengthened sufficiently to accelerate sinking, the velocities increase. When the slab trailing edge is free, trench motion remains slow, indicating that subduction occurs mostly through trenchward subducting plate motion. When the slab trailing edge is fixed, subduction occurs mostly by trench retreat, while trenchward subducting plate motion is slow and occurs by plate stretching.

‘Fixed’ and ‘Free’ plates are affected differently by changes in initial slab length and dip angle, especially with respect to the amount of stretching the plate undergoes. The thickness of the mantle plays a fundamental role, as it constrains the subduction induced mantle poloidal flow and forces the slab to slow down as it approaches the bottom. In the Fixed case, the maximum sinking and trench velocities reached for the Deep mantle experiments are 68 % and 65 % greater than in the Shallow mantle experiments, respectively. In the Free case, the maximum sinking and trench velocities reached for the Deep mantle experiments are 73 % and 19 % greater than in the Shallow mantle experiments, respectively. The maximum trailing edge velocity (Free case) reached in the Deep mantle experiments is, on average 70 % greater than in Shallow mantle experiments.

Generally, the initial dip angle has a larger impact on the maximum velocities reached than the initial slab length. The main observations from the experiments presented here are:

1. When initial slab length is increased, the system evolves faster (i.e., the slab reaches the bottom earlier). However, the increase does not significantly impact the maximum absolute slab sinking velocity. Increasing the initial slab length from 125 km to 250 km leads to a 10 % decrease of the maximum sinking velocity, except in the Fixed Deep mantle experiments, where there is an increase.
2. Variations in the initial slab dip angle have a greater impact on the maximum sinking and trench velocities. Increasing the initial slab dip angle from 15 to 90° leads to increases of the maximum sinking velocity of $< 9\%$ in the Deep mantle models, but by $\sim 40\%$ in the shallow mantle models. The maximum trench velocity is the most affected by these variations in initial slab dip angle. In the Fixed cases, increasing the initial slab dip leads to a decrease of the maximum trench velocity of 26% in the Deep mantle and 8% in the Shallow mantle experiments. In the Free cases, it leads to an increase the maximum trench

velocity of 12 % in the Deep mantle and 56 % in the Shallow mantle experiments.

3. Changes in the initial slab geometry result in variations of the trailing edge maximum velocity of less than 9 %.
4. Increasing the mantle thickness H leads to longer subduction times as the slab interacts with the bottom later, thus reaching higher maximum absolute sinking velocities. This indicates that in deep mantle settings the viscosity of the mantle controls subduction for longer time periods.

The 2D results presented in this study also validate the adopted numerical methodology chosen – implementation of a harmonic averaging scheme has allowed for the development of models in which free-surface is well approximated, overcoming numerical instabilities related to the high viscosity ratios at the material boundaries in the experiments.

6. References

Bellahsen, N., Faccenna, C. & Funiciello, F. (2005), Dynamics of subduction and plate motion in laboratory experiments: Insights into the "plate tectonics" behavior of the Earth. *J. Geophys. Res.*, 110(B1), B01401, doi: 10.1029/2004jb002999.

Capitanio, F. A., Stegman, D. R., Moresi, L. N. & Sharples, W. (2010), Upper plate controls on deep subduction, trench migrations and deformations at convergent margins. *Tectonophysics*, 483(1-2), 80-92, doi: 10.1016/j.tecto.2009.08.020.

Cawood, P. A., Kröner, A. & Pisarevsky, S. (2006), Precambrian plate tectonics: Criteria and evidence. *GSA Today*, 16(7), 4, doi: 10.1130/gsat01607.1.

Conrad, C. P. & Lithgow-Bertelloni, C. (2002), How mantle slabs drive plate tectonics. *Science*, 298(5591), 207-209, doi: 10.1126/science.1074161.

Crameri, F., Schmeling, H., Golabek, G. J., Duretz, T., Orendt, R., Buiter, S. J. H., May, D. A., Kaus, B. J. P., Gerya, T. V. & Tackley, P. J. (2012), A comparison of numerical surface topography calculations in geodynamic modelling: an evaluation of the 'sticky air' method. *Geophys. J. Int.*, 189(1), 38-54, doi: 10.1111/j.1365-246X.2012.05388.x.

Davies, G. F. & Richards, M. A. (1992), Mantle Convection. *Journal of Geology*, 100(2), 151-206, doi: 10.1086/629582.

Faccenna, C., Funiciello, F., Giardini, D. & Lucente, P. (2001), Episodic back-arc extension during restricted mantle convection in the Central Mediterranean. *Earth Planet. Sci. Lett.*, 187(1-2), 105-116, doi: 10.1016/S0012-821x(01)00280-1.

Forsyth, D. & Uyeda, S. (1975), On the Relative Importance of the Driving Forces of Plate Motion. *Geophys. J. Int.*, 43(1), 163-200, doi: 10.1111/j.1365-246X.1975.tb00631.x.

Funiciello, F., Faccenna, C., Giardini, D. & Regenauer-Lieb, K. (2003a), Dynamics of retreating slabs: 2. Insights from three-dimensional laboratory experiments. *J. Geophys. Res.*, 108(B4), 2207, doi: 10.1029/2001jb000896.

Funiciello, F., Moroni, M., Piromallo, C., Faccenna, C., Cenedese, A. & Bui, H. A. (2006), Mapping mantle flow during retreating subduction: Laboratory models analyzed by feature tracking. *J. Geophys. Res.*, 111, B03402, doi: 10.1029/2005jb003792.

Funiciello, F., Morra, G., Regenauer-Lieb, K. & Giardini, D. (2003b), Dynamics of retreating slabs: 1. Insights from two-dimensional numerical experiments. *J. Geophys. Res.*, 108(B4), 2206, doi: 10.1029/2001jb000898.

Hayes, G. P. & Furlong, K. P. (2010), Quantifying potential tsunami hazard in the Puysegur subduction zone, south of New Zealand. *Geophys. J. Int.*, 183(3), 1512-1524, doi: 10.1111/j.1365-246X.2010.04808.x.

Holt, A. F. & Becker, T. W. (2017), The effect of a power-law mantle viscosity on trench retreat rate. *Geophys. J. Int.*, 208(1), 491-507, doi: 10.1093/gji/ggw392.

Houseman, G. A. & Gubbins, D. (1997), Deformation of subducted oceanic lithosphere. *Geophys. J. Int.*, 131(3), 535-551, doi: 10.1111/j.1365-246X.1997.tb06598.x.

Lamarche, G. & Lebrun, J.-F. (2000), Transition from strike-slip faulting to oblique subduction: active tectonics at the Puysegur Margin, South New Zealand. *Tectonophysics*, 316(1-2), 67-89, doi: 10.1016/s0040-1951(99)00232-2.

Lebrun, J.-F., Lamarche, G. & Collot, J.-Y. (2003), Subduction initiation at a strike-slip plate boundary: The Cenozoic Pacific-Australian plate boundary, south of New Zealand. *J. Geophys. Res. Solid Earth*, 108(B9), 2453, doi: 10.1029/2002jb002041.

Lebrun, J.-F., Lamarche, G., Collot, J.-Y. & Delteil, J. (2000), Abrupt strike-slip fault to subduction transition: The Alpine Fault-Puysegur Trench connection, New Zealand. *Tectonics*, 19(4), 688-706, doi: 10.1029/2000tc900008.

Li, Z. H. & Ribe, N. M. (2012), Dynamics of free subduction from 3-D boundary element modeling. *J. Geophys. Res.*, 117, B06408, doi: 10.1029/2012jb009165.

Mao, X., Gurnis, M. & May, D. A. (2017), Subduction Initiation With Vertical Lithospheric Heterogeneities and New Fault Formation. *Geophys. Res. Lett.*, 44(22), 11,349-11,356, doi: 10.1002/2017gl075389.

Marques, F. O., Cabral, F. R., Gerya, T. V., Zhu, G. & May, D. A. (2014), Subduction initiates at straight passive margins. *Geology*, 42(4), 331-334, doi: 10.1130/G35246.1.

Moresi, L., Dufour, F. & Mühlhaus, H. B. (2003), A Lagrangian integration point finite element method for large deformation modeling of viscoelastic geomaterials. *J. Comput. Phys.*, 184(2), 476-497, doi: 10.1016/S0021-9991(02)00031-1.

Moresi, L. & Gurnis, M. (1996), Constraints on the lateral strength of slabs from three-dimensional dynamic flow models. *Earth Planet. Sci. Lett.*, 138(1-4), 15-28, doi: 10.1016/0012-821x(95)00221-W.

Moresi, L., Quenette, S., Lemiale, V., Mériaux, C., Appelbe, B. & Mühlhaus, H. B. (2007), Computational approaches to studying non-linear dynamics of the crust and mantle. *Phys. Earth Planet. Inter.*, 163(1-4), 69-82, doi: 10.1016/j.pepi.2007.06.009.

Nikolaeva, K., Gerya, T. V. & Marques, F. O. (2010), Subduction initiation at passive margins: Numerical modeling. *J. Geophys. Res.*, 115, B03406, doi: 10.1029/2009jb006549.

OzBench, M., Regenauer-Lieb, K., Stegman, D. R., Morra, G., Farrington, R., Hale, A., May, D. A., Freeman, J., Bourgouin, L., Mühlhaus, H. & Moresi, L. (2008), A model comparison study of large-scale mantle-lithosphere dynamics driven by subduction. *Phys. Earth Planet. Inter.*, 171(1-4), 224-234, doi: 10.1016/j.pepi.2008.08.011.

Quinquis, M. E. T., Buiter, S. J. H. & Ellis, S. (2011), The role of boundary conditions in numerical models of subduction zone dynamics. *Tectonophysics*, 497(1-4), 57-70, doi: 10.1016/j.tecto.2010.11.001.

Ribe, N. M. (2010), Bending mechanics and mode selection in free subduction: a thin-sheet analysis. *Geophys. J. Int.*, 180(2), 559-576, doi: 10.1111/j.1365-246X.2009.04460.x.

Ringwood, A. E. (1956), The Olivine–Spinel Transition in the Earth's Mantle. *Nature*, 178(4545), 1303-1304, doi: 10.1038/1781303a0.

Ringwood, A. E. & Major, A. (1966), Synthesis of Mg_2SiO_4-Fe_2SiO_4 spinel solid solutions. *Earth Planet. Sci. Lett.*, 1(4), 241-245, doi: 10.1016/0012-821x(66)90077-x.

Schellart, W. P. (2004a), Kinematics of subduction and subduction-induced flow in the upper mantle. *J. Geophys. Res.*, 109, B07401, doi: 10.1029/2004jb002970.

Schellart, W. P. (2004b), Quantifying the net slab pull force as a driving mechanism for plate tectonics. *Geophys. Res. Lett.*, 31(7), L07611, doi: 10.1029/2004gl019528.

Schellart, W. P. (2005), Influence of the subducting plate velocity on the geometry of the slab and migration of the subduction hinge. *Earth Planet. Sci. Lett.*, 231(3-4), 197-219, doi: 10.1016/j.epsl.2004.12.019.

Schellart, W. P. (2008), Kinematics and flow patterns in deep mantle and upper mantle subduction models: Influence of the mantle depth and slab to mantle viscosity ratio. *Geochem. Geophys. Geosyst.*, 9, Q03014, doi: 10.1029/2007gc001656.

Schellart, W. P. (2010), Evolution of Subduction Zone Curvature and its Dependence on the Trench Velocity and the Slab to Upper Mantle Viscosity Ratio. *J. Geophys. Res.*, 115, B11406, doi: 10.1029/2009jb006643.

Schellart, W. P., Freeman, J., Stegman, D. R., Moresi, L. & May, D. (2007), Evolution and diversity of subduction zones controlled by slab width. *Nature*, 446(7133), 308-311, doi: 10.1038/nature05615.

Schellart, W. P., Stegman, D. R. & Freeman, J. (2008), Global trench migration velocities and slab migration induced upper mantle volume fluxes: Constraints to find an Earth reference frame based on minimizing viscous dissipation. *Earth Sci. Rev.*, 88(1-2), 118-144, doi: 10.1016/j.earscirev.2008.01.005.

Schmeling, H., Babeyko, A. Y., Enns, A., Faccenna, C., Funiciello, F., Gerya, T., Golabek, G. J., Grigull, S., Kaus, B. J. P., Morra, G., Schmalholz, S. M. & van Hunen, J. (2008), A benchmark comparison of spontaneous subduction models – Towards a free surface. *Phys. Earth Planet. Inter.*, 171(1-4), 198-223, doi: 10.1016/j.pepi.2008.06.028.

Shirey, S. B. & Richardson, S. H. (2011), Start of the Wilson cycle at 3 Ga shown by diamonds from subcontinental mantle. *Science*, 333(6041), 434-6, doi: 10.1126/science.1206275.

Stegman, D. R., Freeman, J., Schellart, W. P., Moresi, L. & May, D. (2006), Influence of trench width on subduction hinge retreat rates in 3-D models of slab rollback. *Geochem. Geophys. Geosyst.*, 7, Q03012, doi: 10.1029/2005gc001056.

Stegman, D. R., Schellart, W. P. & Freeman, J. (2010), Competing influences of plate width and far-field boundary conditions on trench migration and morphology of subducted slabs in the upper mantle. *Tectonophysics*, 483(1-2), 46-57, doi: 10.1016/j.tecto.2009.08.026.

Stern, R. J. (2004), Subduction initiation: spontaneous and induced. *Earth Planet. Sci. Lett.*, 226(3-4), 275-292, doi: 10.1016/j.epsl.2004.08.007.

Stern, R. J. & Gerya, T. (2018), Subduction initiation in nature and models: A review. *Tectonophysics*, 746, 173-198, doi: 10.1016/j.tecto.2017.10.014.

Toth, J. & Gurnis, M. (1998), Dynamics of subduction initiation at preexisting fault zones. *J. Geophys. Res. Solid Earth*, 103(B8), 18053-18067, doi: 10.1029/98jb01076.

Wilson, J. T. (1965), A New Class of Faults and Their Bearing on Continental Drift. *Nature*, 207(4995), 343-347, doi: 10.1038/207343a0.

Appendices

Appendix I – Table A1

Table A1. Different instants and corresponding slab tip depth during the subduction process for all experiments. Also summarised are the trench position and the trailing edge of the plate position (for the Free cases).

Fixed	t_0 [Ma]	y_0 [km]	x_0 [km]	t_1 [Ma]	y_1 [km]	x_1 [km]	t_2 [Ma]	y_2 [km]	x_2 [km]	t_3 [Ma]	y_3 [km]	x_3 [km]
D1	0	127	2787	29	684	2230	38	1165	1837	71	2215	663
D2	0	140	2787	25	738	2207	33	1182	1817	64	2207	1082
D3	0	152	2787	22	725	2263	31	1210	1841	59	2188	1734
D4	0	167	2787	20	708	2334	28	1148	1982	59	2208	884
D5	0	191	2787	17	694	2115	26	1188	1456	55	2213	89
D6	0	138	2787	23	705	2312	31	1181	1918	60	2200	561
D7	0	231	2787	17	690	2318	25	1162	2016	53	2197	1346
D8	0	256	2787	15	674	2331	24	1197	1611	54	2214	118
D9	0	262	2787	17	712	2264	25	1181	1826	55	2207	748
D10	0	253	2787	20	681	2243	28	1211	1863	57	2205	707
S1	0	127	2828	17	292	2613	29	511	2396	63	643	2172
S2	0	140	2828	16	332	2589	28	522	2360	56	643	2129
S3	0	152	2828	13	312	2643	25	518	2379	55	644	2126
S4	0	164	2828	9	280	2704	24	523	2399	49	643	2170
S5	0	191	2828	9	330	2706	20	511	2482	46	643	2232
S6	0	136	2842	13	328	2692	25	512	2438	51	643	2244
S7	0	231	2830	5	301	2743	20	527	2433	47	644	2193
S8	0	255	2836	5	314	2746	17	517	2499	45	644	2270
S9	0	261	2847	5	306	2757	17	530	2499	45	644	2204
S10	0	252	2862	8	321	2707	18	534	2481	41	642	2216
H11	0	190	2787	31	395	2575	–	–	–	–	–	–
H13	0	192	2787	15	500	2512	21	692	2334	58	1096	1854
H14	0	192	2787	19	704	2313	37	1335	1633	61	1699	1140

Free	t_0 [Ma]	y_0 [km]	x_0 [km]	x_{te_0} [km]	t_1 [Ma]	y_1 [km]	x_1 [km]	x_{te_1} [km]	t_2 [Ma]	y_2 [km]	x_2 [km]	x_{te_2} [km]	t_3 [Ma]	y_3 [km]	x_3 [km]	x_{te_3} [km]
DF1	0	128	3293	253	36	712	2912	612	43	1235	2756	957	52	2228	2668	1846
DF2	0	141	3293	253	31	727	2983	545	37	1165	2845	836	47	2191	2748	1721
DF3	0	154	3293	253	27	715	2872	477	32	1118	2728	755	43	2220	2627	1725
DF4	0	165	3293	253	24	733	2943	469	30	1236	2769	780	39	2223	2637	1659
DF5	0	191	3293	253	17	720	2986	445	25	1244	2818	791	37	2247	2738	1954
DF6	0	139	3293	253	22	706	2997	436	29	1252	2809	790	39	2223	2719	1669
DF7	0	231	3293	253	17	684	3028	453	25	1245	2822	803	35	2262	2751	1747
DF8	0	256	3293	253	18	701	2959	424	24	1176	2809	716	34	2197	2699	1580
DF9	0	263	3293	253	20	729	2928	444	26	1154	2767	688	35	2189	2659	1565
DF10	0	253	3293	253	25	708	2856	407	32	1253	2678	752	40	2184	2595	1562
SF1	0	127	3081	254	17	313	2881	407	23	483	2788	509	29	628	2727	661
SF2	0	140	3081	254	13	294	2925	368	21	480	2798	489	26	628	2717	630
SF3	0	152	3081	254	13	345	2915	389	20	540	2798	516	25	639	2757	661
SF4	0	164	3081	254	10	302	2974	310	16	469	2880	454	22	622	2792	599
SF5	0	190	3081	254	6	287	3024	291	16	535	2901	480	23	631	2821	701
SF6	0	136	3094	254	10	281	3022	307	20	551	2856	535	33	639	2796	906
SF7	0	231	3084	254	5	315	3012	289	12	472	2914	400	18	620	2811	555
SF8	0	254	3091	254	5	320	3010	287	12	480	2908	400	18	640	2810	546
SF9	0	262	3101	254	5	309	3011	279	15	571	2863	454	18	647	2796	531
SF10	0	252	3116	254	9	327	2968	296	15	517	2872	441	18	620	2866	507
HF11	0	190	3293	253	19	389	3215	354	–	–	–	–	–	–	–	–
HF13	0	192	3293	253	14	491	3143	356	20	718	3029	482	28	1094	2939	785
HF14	0	192	3293	253	19	694	3011	473	28	1346	2871	931	34	1712	2830	1357

Appendix II – Table A2

Table A2. Instants at which the slab tip reaches the bottom of the mantle $t(y = H)$ and half of the mantle height $t(y = H/2)$. Absolute maximum sinking, trench and trailing edge (in Free case) velocities, $|v_t|_{max}$, $|v_t|_{max}$ and $|v_{te}|_{max}$, reached and the instants these occur, $t(|v_t|_{max})$, $t(|v_t|_{max})$ and $t(|v_{te}|_{max})$, for all experiments.

Fixed	$t(y=H)$ [Ma]	$t(y=H/2)$ [Ma]	$\|v_s\|_{max}$ [km/Ma]	$t(\|v_s\|_{max})$ [Ma]	$\|v_t\|_{max}$ [km/Ma]	$t(\|v_t\|_{max})$ [Ma]	Free	$t(y=H)$ [Ma]	$t(y=H/2)$ [Ma]	$\|v_s\|_{max}$ [km/Ma]	$t(\|v_s\|_{max})$ [Ma]	$\|v_t\|_{max}$ [km/Ma]	$t(\|v_t\|_{max})$ [Ma]	$\|v_{te}\|_{max}$ [km/Ma]	$t(\|v_{te}\|_{max})$ [Ma]
D1	71	37	60	35	67	33	**DF1**	52	42	126	49	25	30	119	52
D2	64	32	65	31	83	40	**DF2**	47	37	123	43	22	34	119	47
D3	59	29	58	29	69	22	**DF3**	43	33	113	40	26	29	104	43
D4	59	28	63	24	64	27	**DF4**	39	29	120	36	26	28	105	39
D5	55	25	65	21	79	21	**DF5**	37	24	120	29	24	17	110	31
D6	60	30	64	30	85	33	**DF6**	39	28	121	35	26	29	107	31
D7	53	24	69	22	68	30	**DF7**	35	24	113	31	29	21	102	32
D8	54	23	70	19	94	22	**DF8**	34	24	128	31	26	13	107	34
D9	55	24	70	22	67	21	**DF9**	35	26	124	32	30	24	116	35
D10	57	27	70	22	63	20	**DF10**	40	31	122	38	29	27	111	40
S1	63	19	20	23	21	19	**SF1**	29	18	31	24	18	17	37	29
S2	56	16	20	19	22	27	**SF2**	26	15	32	21	21	16	28	26
S3	55	14	20	16	28	23	**SF3**	25	13	31	19	20	15	31	25
S4	49	12	20	14	30	18	**SF4**	22	11	31	18	25	18	33	22
S5	46	9	18	11	21	16	**SF5**	23	8	28	14	15	17	36	21
S6	51	13	19	13	26	20	**SF6**	33	12	29	17	18	13	33	21
S7	47	7	19	10	25	14	**SF7**	18	6	30	13	20	16	37	13
S8	45	6	20	11	24	15	**SF8**	18	5	33	13	23	1	30	18
S9	45	7	23	12	25	13	**SF9**	18	6	36	13	27	1	26	18
S10	41	9	27	14	28	15	**SF10**	18	9	39	15	28	1	30	15
H11	32	1	11	0.06	11	22	**HF11**	19	1	11	5	6	23	21	38
H13	58	17	34	17	68	23	**HF13**	28	16	54	24	21	17	41	27
H14	61	23	47	20	53	26	**HF14**	34	21	82	30	26	16	74	30

Appendix III – Figure A1

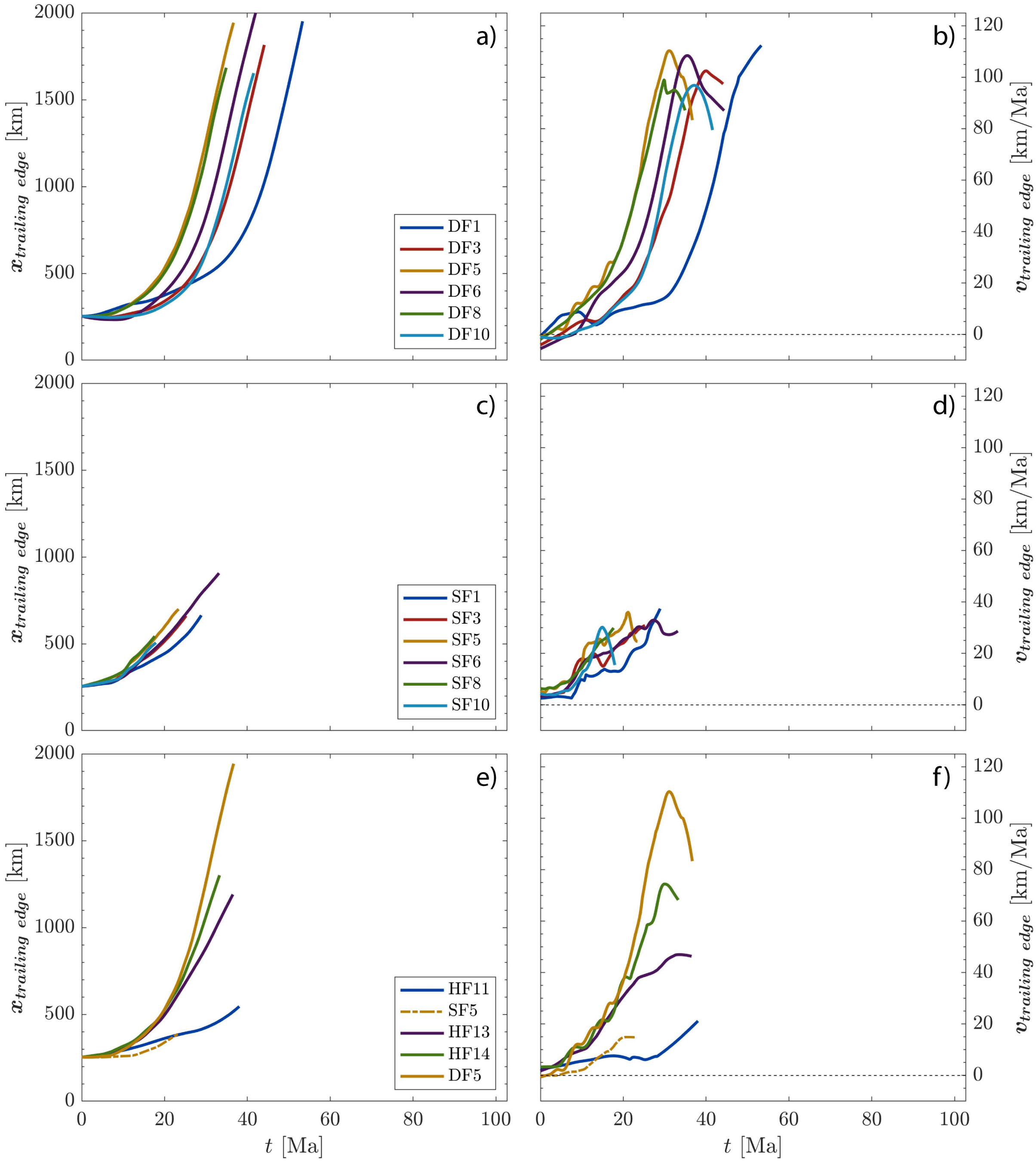

Figure A1. Slab tip vertical position y_{slab} plotted against time for a) Deep mantle experiments, c) Shallow mantle experiments and e) changing H experiments. Trench horizontal position x_{trench} plotted against time for b) Deep mantle experiments, d) Shallow mantle experiments and f) changing H experiments. Solid lines refer to Fixed setting experiments and dashed lines refer to Free setting experiments.

Chapter 3

Exploring power-law rheology in the upper and lower mantle during subduction

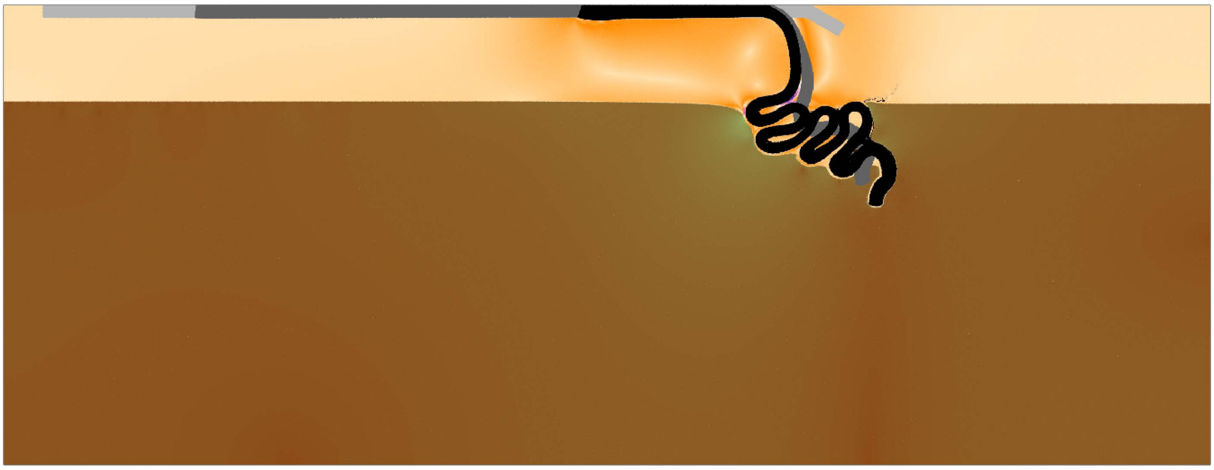

Cover image: Slab geometric configuration of experiment LM7-D2 at three time steps. Both upper and lower mantle have a non-linear viscosity component. The background colours indicate the effective viscosity field in the upper and lower mantle for the slab during the final time step, shown in black.

Abstract

Geodynamic models of subduction underpin reconstructions of past, current and future tectonic settings. These models usually implement a linear viscous mantle rheology, where the viscosity is constant and the strain rate varies linearly with stress. While this is a reasonable assumption for low stress conditions in the mantle, it likely breaks down in the regions surrounding subducting slabs, where high stress can trigger power-law creep flow. In the case of a power-law rheology, the strain rate varies with the stress to a power $n > 1$ for typical mantle compositions. Power-law rheology can reduce the effective viscosity in the mantle around the slab, thereby impacting the interaction between the slab and the mantle during sinking. Mantle properties are usually derived from laboratory experiments and seismological observations. However, the rheological properties of the lower mantle remain poorly constrained due to the uncertainties associated with both of these sources. Previous numerical subduction models have included a power-law rheology in the upper-mantle but have typically assumed a linear viscous lower mantle. Nevertheless, subducting slabs are capable of localising domains of power-law viscous flow even in the lower mantle.

In this study, 2D numerical models are used to explore mantle rheology parameters by analysing the interaction between a subducting plate and the upper-lower mantle discontinuity at 660 km. The results confirm that the rheology of the mantle plays a key role in controlling the slab geometry and how subduction evolves. Adding a power-law component to the mantle viscosity promotes a subduction mode in which, upon reaching the mantle discontinuity, the slab initially sinks straight into the lower mantle and over time accumulates below the mantle discontinuity by folding. This subduction mode differs from the previously proposed slab-avalanche mode, in which the slab only sinks into the lower mantle after accumulating at the transition zone. It is also proposed that changes in slab configuration along arcs, as shown by tomography, can be explained by the differential activation of the power-law rheology in the mantle, which could be caused by lateral variations in water content in the mantle.

Keywords: Subduction models, geodynamics, numerical modelling, slab penetration mode, stress-dependent rheology

1. Introduction

Geodynamic models of subduction are widely used to reconstruct and understand the past, current and future evolution of tectonic settings. The reconstructions result from the detailed analysis of the plate tectonics driving forces and the processes that are only accessible by either direct geological or geophysical observation or from the limited geological record. One of the main drivers of mantle convection and plate motions at the Earth's surface is subduction [Forsyth & Uyeda, 1975; Davies & Richards, 1992; Conrad & Lithgow-Bertelloni, 2002]. Subduction is the process by which old and cold, and therefore denser, oceanic lithosphere sinks into the mantle and is recycled. Subduction processes have been extensively studied over the last few decades, and the role of parameters such as plate length and width, plate-mantle viscosity and density ratios has been widely quantified and related to subduction sinking velocity and trench migration [e.g., Bellahsen et al., 2005; Funiciello et al., 2006; Stegman et al., 2006; Schellart, 2008a; Li & Ribe, 2012]. Trench migration and trench-ward motion of subducting plates are a consequence of subduction evolution [e.g., Elsasser, 1971; Molnar & Atwater, 1978; Lallemand et al., 2005; Schellart et al., 2008] and motivated the commonly used terminology of 'trench retreat', which designates trench motion towards the subducting plate, and 'trench advance', which designates trench motion away from the subducting plate. Trench migration is controlled by parameters such as the boundary conditions of the subducting plate trailing edge (i.e., if the plate itself moves fast or slow compared to the trench) [Funiciello et al., 2004; Schellart, 2005; Stegman et al., 2010], plate width [Stegman et al., 2006; Schellart et al., 2007], plate stiffness [Capitanio et al., 2007; Di Giuseppe et al., 2008; Schellart, 2008a; Ribe, 2010] and proximity to the lateral borders of the subducting plate [Schellart et al., 2011]. These studies focus mainly on the dynamics of a single plate sinking into a linear viscous mantle, either considering only the upper mantle, a deep homogeneous mantle or only the uppermost part of the lower mantle. However, the dynamic evolution of a subducting plate also depends on the rheology of the surrounding mantle.

The rheology of viscous materials describes the relation between stress (applied forces per unit area) and strain rate (rate of change of deformation), describing the way rocks deform, and is generally written as:

$$\dot{\varepsilon}_{II} = 2\eta_{eff}(\sigma_{II})^n, \tag{1}$$

where $\dot{\varepsilon}_{II}$ is the second invariant of the strain rate, η_{eff} is the effective viscosity, σ_{II} is the second invariant of the deviatoric stress and n is the flow law exponent [e.g., Turcotte &

Schubert, 2014]. At low stress levels, rocks deform by diffusion creep (also referred to as linear viscous flow and Newtonian flow), the exponent n is 1 and the second invariant of the strain rate increases linearly with stress [Ashby, 1972]. At high stress, rocks deform by dislocation creep (also referred to as non-linear viscous flow, power-law creep and non-Newtonian flow), the exponent n is > 1 and the strain rate increases nonlinearly with stress [Ashby, 1972]. Flow laws vary for each mineral and under different conditions (e.g., pressure, temperature, grain size), different deformation mechanisms dominate [Ashby, 1972]. If power-law flow dominates, the effective viscosity of the material is proportional to ${\sigma_{II}}^{-n}$ and is reduced in areas where the stresses are higher, resulting in higher flow velocities.

The properties of materials in Earth's interior, such as viscosity, density, structure and composition are constrained through indirect studies such as seismological observations, gravity and gravitational potential anomalies, surface heat flow measurements, geochemical and petrological data and experimental petrology [e.g., Wada & King, 2015]. For example, seismic discontinuities reflect mineral phase transitions, changes in composition or changes in microstructures. Additionally, seismic wave velocities have directional dependence, known as seismic anisotropy, which reflects rock deformation processes. Thus, seismological observations provide information on the geometry, composition and structure of the deep Earth. The flow laws of deep Earth minerals are determined experimentally. However, laboratory studies of mineral deformation are limited to strain rates as low as $\gtrsim 10^{-8}$ s^{-1}, which are $5-7$ orders of magnitude higher than the strain rates in the mantle ($\lesssim 10^{-13}$ s^{-1}), requiring the extrapolation of test results to mantle values. Geochemical and petrological data are limited to natural samples retrieved from depths < 200 km, and therefore are not representative of the entire mantle. Additionally, grain size and water content, which are not constrained in the deep mantle, have a strong influence on the effective viscosity: if the grain size is reduced during mineral phase transitions, or if there is an increase in water content, the strength of the material will be locally reduced. Consequently, the rheological parameters of the mantle, particularly the lowermost upper mantle and the lower mantle remain poorly constrained.

The rheological properties of olivine are usually taken as a proxy for the upper mantle, as it is the most abundant component [Karato & Wu, 1993]. However, other mineral components should not be neglected, as they may have compensating effects. It is usually assumed that power-law flow dominates in the upper mantle, which favours subducting plate motion and results in reduced trench retreat rates, compared to linear viscous mantle rheology [Holt & Becker, 2017]. The lower mantle is assumed to deform by linear flow, based on its general absence of seismic anisotropy. However, if subduction evolves quickly it may induce large high stress regions in the mantle, and the presence of water, can soften the material, reducing mantle viscosity. Thus, even in the linear flow dominated lower mantle, subducting slabs may localise power-law flow around them [McNamara et al., 2001], which results from the lattice preferred orientation of bridgmanite (calcium-silicate perovskite) in regions where stresses are higher [Ferreira et al., 2019].

The stratification of the mantle results from mineral phase changes, caused by temperature and pressure changes, or changes of composition. The most studied mantle discontinuities are at 410 km, below which olivine transitions to wadsleyite [Katsura & Ito, 1989; Ita & Stixrude, 1992; Vidale et al., 1995]; at 520 km, below which wadsleyite transitions to ringwoodite [Akaogi et al., 1989; Shearer, 1990]; and at 660 km, separating the upper mantle from lower mantle, and below which ringwoodite transitions to bridgmanite, ferropericlase and a calcium ferrite-type phase [Anderson, 1967; Ito & Takahashi, 1989; Mitrovica & Forte, 1997].

As a plate subducts, the slab will inevitably interact with these mantle discontinuities. Seismic tomography and both analogue and numerical experiments have shown that the slab will either: (1) not penetrate the discontinuity, spreading along the interface; (2) partially penetrate it; or (3) sink through it with little deformation [Kincaid & Olson, 1987; Christensen, 1996; Olbertz et al., 1997]. Seismicity and seismic tomography data show a wide range of slab morphologies, from slabs trapped in the transition zone to slabs sinking deeply into the lower mantle, in some cases even along the same arc [Fukao & Obayashi, 2013]. This variety of configurations results from processes that affect the relative strength of plate, such as yielding, grain size reduction, changes in water content, and relative motion of the slab and surrounding mantle. It has been shown that slab penetration into the lower mantle is best promoted by relatively stationary trenches, sub-vertical slabs and a low upper-lower mantle density contrast ($< 3\%$) [Kincaid & Olson, 1987; Enns et al., 2005; Čížková et al., 2007]. However, given that the relative strength of the slab depends on the mantle viscosity, it is important to evaluate to what degree mantle deformation mechanisms influence the interaction between slabs and mantle discontinuities.

Given the uncertainties associated with mantle rheological parameters, this study aims to investigate the influence of mantle flow laws on subduction dynamics. Mantle rheology parameters are explored using a simplified isothermal numerical modelling approach (i.e., temperature effects are not included) where subduction is driven by density contrasts alone, considering the full extent of the mantle and mantle discontinuity at 660 km. Previous studies have limited the lower mantle to a depth of ~1300 km, assuming that the plate loses all negative buoyancy at ~ 1000 km [e.g., Olbertz et al., 1997; Schellart et al., 2007; Quinteros et al., 2010].

However, tomography studies show slabs may sink below this depth [e.g., Fukao & Obayashi, 2013]. The novelty of this study is the exploration of the parameter space for mantle power-law flow and relate mantle rheology parameters to slab geometry, maximum depths of sinking and interactions between slabs and mantle discontinuities. The main advantage of this approach is that it isolates the effects of a stress dependent mantle rheology on a subducting plate.

2. Methodology

2.1. Model setup

The general model domain is a two-dimensional Cartesian coordinate system with the origin at the lower-left corner (Figure 1). The mantle has dimensions $L \times H$ and is divided into an upper mantle, with thickness H_{UM}, and a lower mantle, with thickness H_{LM}. The upper mantle has density ρ_{UM} and dynamic viscosity η_{UM}, and the lower mantle has density ρ_{LM} and dynamic viscosity η_{LM}. A single homogenous plate of length L_{sp}, thickness h_{sp}, density ρ_{sp} and viscosity η_{sp} overlies the upper mantle with a kinked tip of initial length l_0 dipping into the mantle at an angle θ_0. The top the plate comprises a thin, low viscosity crust, which is included as part of the subducting plate, of thickness h_c, density $\rho_c = \rho_{sp}$ and viscosity $\eta_c = \eta_{UM}$ that decouples the plate from the top boundary. The edge of the plate is initially located at a distance ${x^0}_{sp}$ from the left domain boundary.

The experiments start with a very long trailing plate ($L_{sp}(0) = 4810$ km) to ensure that, as

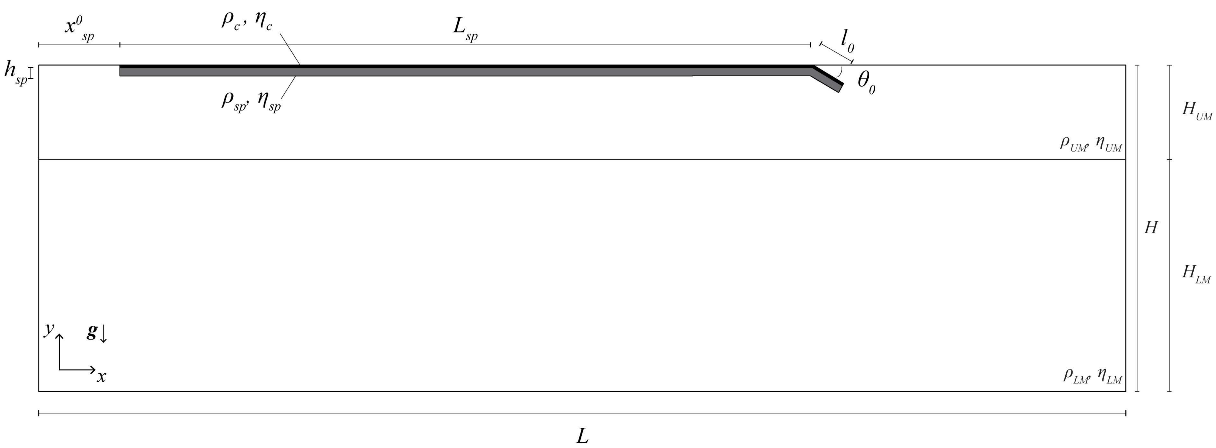

Figure 1. 2D model setup: a plate of length L_{sp} and thickness h_{sp}, with an initial slab length l_0, dipping at θ_0, and density ρ_{sp} and viscosity η_{sp}, is initially lying on top of the mantle. The top layer of the lithosphere is a crust of thickness h_c, density ρ_c and viscosity η_c. The mantle has length L, total thickness H, and is divided into upper mantle and lower mantle, with respective densities ρ_{UM} and ρ_{LM} and viscosities η_{UM} and η_{LM}. The gravitational acceleration is represented by **g**.

subduction evolves, the slab is able to reach the lower mantle, even if it develops folds upon interaction with the mantle discontinuity, without consuming the entire subducting plate. The natural consequence of a very long subducting plate is an increased drag force exerted on the bottom of the plate is higher, limiting the plate velocity [Ribe, 2010].

This study focuses on the first order effects of power-law mantle rheology on slab behaviour and plate motion at the surface. To achieve this, the system is simplified assuming:

1. Linear viscous rheology in the lithospheric plate, because over geological timescales, to a first approximation subducting slabs behave like a fluid [Houseman & Gubbins, 1997].

2. The plate represents oceanic lithosphere, which is compositionally homogeneous. The negative buoyancy of the slab is the only force driving subduction and there are no external forces acting on the plate, such as ridge-push or pre-existing mantle convection.

3. Heat transfer in the mantle occurs primarily by convection, since in nature the Rayleigh number is high ($5 \times 10^5 - 5 \times 10^7$). It is also assumed that temperature dependent effects are confined to the top and bottom layers (the lithosphere and the core-mantle boundary, respectively). Thus, thermal effects are not included in the system.

4. The overriding plate is passive. Interactions between subducting slabs and overriding plates are complex and beyond the scope of this study. Hence, the system includes a single subducting plate.

5. The subducting plate is infinitely wide and the 2D geometry corresponds to a cross-section at the centre of the subduction zone, where subduction induced mantle flow occurs mainly through poloidal flow.

6. The 660 km mantle discontinuity is the only mantle discontinuity. This discontinuity resists sinking of a slab due to the negative Clapeyron slope of the ringwoodite phase transition, which causes the transition boundary to be depressed, lowering the density contrast between slab and the surrounding mantle.

2.2. Numerical description

The subduction system is governed by the equations of conservation of momentum, equation (2), and conservation of mass, equation (3), for an incompressible fluid with negligible inertia:

$$\nabla \cdot \boldsymbol{\tau} - \nabla p = \Delta\rho \boldsymbol{g}, \tag{2}$$

$$\nabla \cdot \boldsymbol{u} = 0, \tag{3}$$

where p is the dynamic pressure, $\Delta\rho$ is the density contrast between plate and ambient mantle,

$\boldsymbol{g}$ is the gravitational acceleration, $\boldsymbol{u}$ is the velocity and τ is the deviatoric stress tensor,

$$\tau_{ij} = \eta \left(\frac{\partial u_i}{\partial x_j} + \frac{\partial u_j}{\partial x_i} \right), \tag{4}$$

and η is the dynamic shear viscosity.

The model domain is used to construct and execute numerical experiments of dynamic subduction with the code Underworld 2.0[1] [Moresi et al., 2003; Moresi et al., 2007]. Underworld is a hybrid parallel particle-in-cell finite element code that solves the governing conservation equations on an Eulerian Finite Element mesh. Material properties, such as density and viscosity are carried by Lagrangian particles inside each mesh element. In this study, the models were solved with a multigrid solver, with a total of 20 particles per element.

2.3. Composite viscosity

A power-law mantle rheology is implemented following the approach used by Capitanio & Faccenda [2012], Holt & Becker [2017] and Király et al. [2017]. The power-law viscosity is computed by imposing a limit on the strain rate:

$$\eta_p = \eta_0 \left(\frac{\dot{\varepsilon}_{II}}{\dot{\varepsilon}_{II}^{T}} \right)^{\frac{1-n}{n}}, \tag{5}$$

where η_p is the power-law viscosity, η_0 is the linear viscosity, $\dot{\varepsilon}_{II}$ is the second invariant of the strain rate, $\dot{\varepsilon}_{II}^{T}$ is the transition strain rate (i.e., the second invariant of strain rate at which the power-law viscosity is equal to the linear viscosity), and n is the power-law exponent. In this approach, the number of parameters to evaluate is reduced to two: the power-law exponent, which is material dependent, and the transition strain rate. The transition strain rate defines a threshold for the activation of the power-law component in the regions of the mantle where the strain rate is higher than the transition strain rate.

The effective viscosity η_{eff} of each layer of the mantle is the harmonic average between the linear viscosity, which is a reference value, and the computed power-law viscosity:

$$\eta_{eff} = \left(\frac{1}{\eta_0} + \frac{1}{\eta_p} \right)^{-1}. \tag{6}$$

The experiments in this study add to the 2D models of Holt & Becker [2017] by including the lower mantle in the model setup.

[1] http://www.underworldcode.org/

3. Results

Experiments in which a power-law component is included in the mantle viscosity are referred to as composite. The experiments are divided into four sets: 1) experiments in which only the upper mantle is composite and the transition strain rate and power law exponent are varied (UM1 to UM5); 2) experiments in which both the upper and lower mantle are composite and the transition strain rate and power law exponent are varied in both layers (LM1 to LM8); 3) experiments in which the mantle is linear viscous and the mantle density contrast and viscosity ratio are varied; and 4) and experiments in which both the upper and the lower mantle are composite and the mantle density contrast is varied.

Table 1. Model parameters common to all experiments.

Parameter	Symbol	Value	Units
Gravity acceleration	g	9.8	m/s^2
Domain length	L	7600 x 10^3	m
Domain height	H	2900 x10^3	m
Upper mantle thickness	H_{UM}	660 x10^3	m
Lower mantle thickness	H_{LM}	2240 x10^3	m
Trailing plate length at $t = 0$ s	$L_{sp}(0)$	4810 x 10^3	m
Distance of plate trailing edge to boundary	$x^0{}_{sp}$	250×10^3	m
Lithospheric mantle thickness	h_{sp}	65 x 10^3	m
Crust thickness	h_c	15 x 10^3	m
Initial slab length	l_0	250×10^3	m
Initial slab dipping angle	θ_0	30	°
Upper mantle density	ρ_{UM}	3200	kg/m^3
Lithospheric mantle density	ρ_{sp}	3300	kg/m^3
Crust density	ρ_c	3300	kg/m^3
Plate to upper mantle density contrast	$\Delta\rho = \rho_{sp} - \rho_m$	100	kg/m^3
Upper mantle reference viscosity	η_{UM}	10^{21}	Pa·s
Lithospheric mantle viscosity	η_{sp}	5 x 10^{23}	Pa·s
Crust viscosity	η_c	10^{21}	Pa·s
Lithospheric mantle-upper mantle reference viscosity ratio	$\gamma = \eta_{sp}/\eta_m$	500	–

The mantle density contrast is defined as:

$$D_M = \frac{\Delta\rho_M}{\rho_{UM}} = \frac{\rho_{LM} - \rho_{UM}}{\rho_{UM}}, \tag{7}$$

where $\Delta\rho_M = \rho_{LM} - \rho_{UM}$ is the density contrast between upper and lower mantle, ρ_{UM} is the density of the upper mantle and ρ_{LM} is the density of the lower mantle. The mantle viscosity ratio is the ratio between the reference viscosity of the upper mantle η_{UM} and the reference viscosity of the lower mantle η_{LM}:

$$\gamma_M = \frac{\eta_{LM}}{\eta_{UM}}. \tag{8}$$

The parameters that are kept constant between experiments are summarised in Table 1, whereas the parameters that are varied are summarised in Table 2. All experiments were executed with a mesh of 768×384 elements, corresponding to a resolution of $\sim 10 \times 9$ km over the entire domain.

Table 2. Model parameters varied between the experiments: mantle viscosity ratio γ_M, mantle density contrast D_M and upper and lower mantle transition strain rate, $(\dot{\varepsilon}_{II}^{T})_{UM}$ and $(\dot{\varepsilon}_{II}^{T})_{LM}$, and power-law exponent, n_{UM} and n_{LM}.

<table>
<tr><th>Experiment</th><th>γ_M</th><th>D_M</th><th>$(\dot{\varepsilon}_{II}^{T})_{UM}$ [s^{-1}]</th><th>n_{UM}</th><th>$(\dot{\varepsilon}_{II}^{T})_{LM}$ [s^{-1}]</th><th>n_{LM}</th></tr>
<tr><td>Linear</td><td rowspan="20">25</td><td rowspan="14">0.78 %</td><td>-</td><td>-</td><td>-</td><td>-</td></tr>
<tr><td>UM1</td><td>3×10^{-11}</td><td>3.5</td><td>-</td><td>-</td></tr>
<tr><td>UM2</td><td>1×10^{-12}</td><td>3.5</td><td>-</td><td>-</td></tr>
<tr><td>UM3</td><td rowspan="3">3×10^{-13}</td><td>1.5</td><td>-</td><td>-</td></tr>
<tr><td>UM4</td><td>3.5</td><td>-</td><td>-</td></tr>
<tr><td>UM5</td><td>5</td><td>-</td><td>-</td></tr>
<tr><td>LM1</td><td rowspan="2">3×10^{-11}</td><td>3.5</td><td>3×10^{-11}</td><td>3.5</td></tr>
<tr><td>LM2</td><td>3.5</td><td>1.5×10^{-11}</td><td>3.5</td></tr>
<tr><td>LM3</td><td rowspan="6">3×10^{-13}</td><td>1.5</td><td>5×10^{-12}</td><td>1.5</td></tr>
<tr><td>LM4</td><td>1.5</td><td>5×10^{-12}</td><td>3.5</td></tr>
<tr><td>LM5</td><td>3.5</td><td>3×10^{-11}</td><td>3.5</td></tr>
<tr><td>LM6</td><td>3.5</td><td>1.5×10^{-11}</td><td>3.5</td></tr>
<tr><td>LM7</td><td>3.5</td><td>5×10^{-12}</td><td>1.5</td></tr>
<tr><td>LM8</td><td>3.5</td><td>5×10^{-12}</td><td>3.5</td></tr>
<tr><td>Linear-DC1</td><td rowspan="3">1.6 %</td><td>-</td><td>-</td><td>-</td><td>-</td></tr>
<tr><td>UM4-DC1</td><td rowspan="2">3×10^{-13}</td><td rowspan="2">3.5</td><td>-</td><td>-</td></tr>
<tr><td>LM7-DC1</td><td>5×10^{-12}</td><td>1.5</td></tr>
<tr><td>Linear-DC2</td><td rowspan="3">2.5 %</td><td>-</td><td>-</td><td>-</td><td>-</td></tr>
<tr><td>UM4-DC2</td><td rowspan="2">3×10^{-13}</td><td rowspan="2">3.5</td><td>-</td><td>-</td></tr>
<tr><td>LM7-DC2</td><td>5×10^{-12}</td><td>1.5</td></tr>
<tr><td>Linear-V1-D0</td><td rowspan="4">1</td><td>0 %</td><td>-</td><td>-</td><td>-</td><td>-</td></tr>
<tr><td>Linear-V1</td><td>0.78 %</td><td>-</td><td>-</td><td>-</td><td>-</td></tr>
<tr><td>Linear-V1-D1</td><td>1.6 %</td><td>-</td><td>-</td><td>-</td><td>-</td></tr>
<tr><td>Linear-V1-D2</td><td>2.5 %</td><td>-</td><td>-</td><td>-</td><td>-</td></tr>
<tr><td>Linear-D0</td><td>25</td><td>0 %</td><td>-</td><td>-</td><td>-</td><td>-</td></tr>
<tr><td>Linear-V50-D0</td><td rowspan="4">50</td><td>0 %</td><td>-</td><td>-</td><td>-</td><td>-</td></tr>
<tr><td>Linear-V50-D1</td><td>0.78 %</td><td>-</td><td>-</td><td>-</td><td>-</td></tr>
<tr><td>Linear-V50</td><td>1.6 %</td><td>-</td><td>-</td><td>-</td><td>-</td></tr>
<tr><td>Linear-V50-D2</td><td>2.5 %</td><td>-</td><td>-</td><td>-</td><td>-</td></tr>
</table>

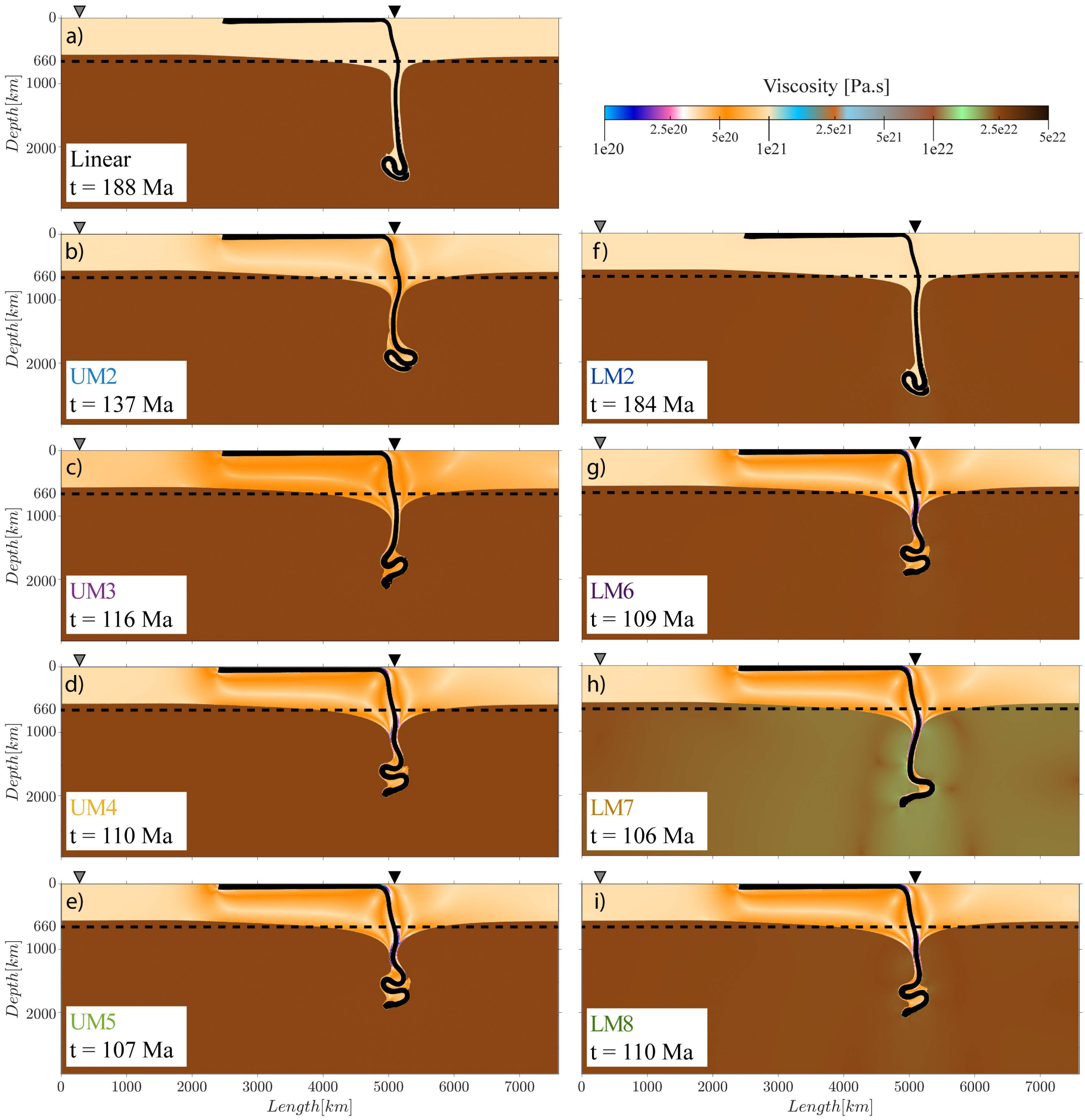

Figure 2. Viscosity field and slab geometry of experiments varying upper and lower mantle power-law parameters at times in which ~50 % of the plate has been consumed by subduction. a) Linear case, b-e) only upper mantle is composite and f-i) both upper and lower mantle are composite. The colour of the plate, black, is excluded from the viscosity colour bar ($\eta_{sp} = 5 \times 10^{23}$ Pa s). Inverted triangles indicate the initial position of the trench (black) and the plate trailing edge (grey). Dashed lines represent the 660 km depth mantle discontinuity.

3.1. Power-law upper mantle parameters

The transition strain rate and power-law exponent in the upper mantle are varied in a suite of five experiments, denoted 'UM' in Table 2, and compared to the linear viscosity mantle case, referred to as 'Linear' in Table 2. In this set of experiments, the lower mantle is linear viscous, the mantle density contrast $D_M = 0.78$ % and the mantle viscosity ratio $\gamma_M = 25$.

Table 3. Summary of results for all experiments. Times at which the slab tip reaches 660 km depth, t^{660}, and respectives plate consumption C_{plate}^{660} and trench position x_{trench}^{660}. Times at which C_{plate}~50 % and the respective slab tip depth y_{slab}^{C50} and the trench position x_{trench}^{C50}. The superscripts $C50$ refers to the time at which C_{plate}~50 %. The maximum subduction velocity reached while the slab sinks through the upper mantle (during $t < t^{660}$) and the overall subduction velocity maximum during each experiment are listed.

Experiment	C_{plate}^{660} %	t^{660} [Ma]	x_{trench}^{660} [km]	t^{C50} [Ma]	y_{slab}^{C50} [km]	x_{trench}^{C50} [km]	$v_{subduction}^{max}$ $(t < t^{660})$ [km/Ma]	$v_{subduction}^{max}$ [km/Ma]
Linear	9.16	26	4980	188	2481	5007	6.9	14.8
UM1	8.20	26	4976	184	2477	5007	7.0	15.2
UM2	8.17	21	4970	137	2093	5014	8.9	22.3
UM3	8.27	18	4983	116	2115	4984	13.4	27.5
UM4	8.23	16	4963	110	1986	4958	13.6	31.8
UM5	8.23	16	4960	107	1915	4956	13.9	34.2
LM1	8.21	26	4976	184	2482	5003	7.1	14.9
LM2	8.21	26	4977	184	2485	5001	7.0	17.1
LM3	8.22	18	4984	111	2276	4988	13.7	27.4
LM4	8.20	18	4986	115	2146	4985	13.3	28.6
LM5	8.13	16	4968	110	1994	4955	13.2	32.1
LM6	8.17	16	4965	109	1935	4962	13.8	32.5
LM7	8.15	16	4967	106	2165	4973	13.4	30.1
LM8	8.18	16	4965	110	2038	4952	12.7	33.2
Linear-D1	8.09	28	4984	228	1468	4955	6.9	13.8
UM4-D1	8.10	17	4969	140	1550	4902	12.4	29.5
LM7-D1	8.05	17	4972	137	1646	4913	12.4	29.5
Linear-D2	8.08	29	4986	267	922	4870	6.1	10.4
UM4-D2	8.03	17	4972	171	1176	4885	12.1	28.0
LM7-D2	8.06	17	4970	168	1225	4864	11.8	30.1
Linear-V1-D0	9.17	21	4909	52	2864	4618	−1.4	91.4
Linear-V1	8.20	24	4964	130	2891	4986	8.4	26.9
Linear-V1-D1	8.08	25	4978	164	2892	4908	9.0	18.0
Linear-V1-D2	8.17	26	4978	201	890	4853	9.2	14.9
Linear-D0	8.40	24	4968	92	2299	4910	7.5	54.1
Linear-V50-D0	8.24	26	4976	113	1973	4920	6.8	45.9
Linear-V50-D1	8.15	28	4981	203	1958	5000	6.2	15.9
Linear-V50	8.14	29	4982	255	1457	4961	5.8	12.9
Linear-V50-D2	8.17	29	4983	272	1020	4924	5.6	11.9

3.1.1. Plate geometry

The percentage of the plate at the surface that has been consumed by subduction C_{plate} is calculated as the ratio between the distance from the trench to the free edge of the plate at any given time and the plate length at the beginning of each experiment. In Figure 2, the slab geometric configuration is compared for times, t^{C50}, when C_{plate}~50 %. Black downward pointing triangles on top of each snapshot represent the initial position of the trench, while grey ones represent the initial plate trailing edge. The t^{C50} times and the respective slab tip depth, and trench position are summarised in Table 3 for all experiments.

In the linear case (Figure 2a), the slab takes 188 Ma to reach t^{C50} and the slab tip depth is 2481 km. The trailing plate is thickened on the edge and thinned close to the trench and at the mantle discontinuity. The slab tip folded upon interaction with the 600 km discontinuity, with the slab tip pointing towards the mantle wedge (to the right), and it continued sinking into the lower mantle, while the plate and slab ensemble stretched. The upper mantle composite experiments (Figure 2b-e and Table 3) reach t^{C50} earlier and the slab tip reaches a shallower depth. Experiments UM1 and UM5 are 4 and 81 Ma earlier and the slab is 4 and 566 km shallower, respectively. However, both the transition strain rate and power-law exponent were varied between composite experiments and the effects of each of these parameters are described separately.

Between experiments UM2 (Figure 2b) and UM4 (Figure 2d), the power-law exponent is constant ($n_{UM} = 3.5$) and the transition strain rate varies from 1×10^{-12} s^{-1} to 3×10^{-13} s^{-1}. The slab configuration in experiment UM2 is very similar to the linear case, with a more accentuated fold on the slab tip. The viscosity of the upper mantle is reduced at the trench, around the slab close to the mantle discontinuity and around the trailing edge of the plate. In experiment UM4 the slab tip folded in the opposite direction upon interaction with the mantle discontinuity and the viscosity of the upper mantle is reduced on a broader area, including the regions of the upper mantle directly above the mantle discontinuity. Thus, a lower transition strain rate results in a broader area of the reduced upper mantle viscosity.

Between experiments UM3 (Figure 2c), UM4 (Figure 2d and Movie 1) and UM5 (Figure 2e), the transition strain rate is constant ($(\dot{\varepsilon}_{II}^{T})_{UM} = 3 \times 10^{-13}$ s^{-1}) and the power-law exponent varies from 1.5 to 3.5 to 5. In the three cases, the slab folded oceanwards (the slab tip points to the left) upon interaction with the mantle discontinuity, and with increasing power-law exponent the slab recumbent folds are vertically stacked. In experiment UM3 most of the upper mantle viscosity is reduced to $\sim 5 \times 10^{20}$ Pa.s. In experiment UM4, the area where the upper mantle viscosity is reduced to $\sim 5 \times 10^{20}$ Pa.s is smaller, but in the regions around the trench and on the contact between the slab and the mantle discontinuity, the upper mantle viscosity is reduced to $\sim 2 - 2.5 \times 10^{20}$ Pa s. In experiment UM5, the viscosity of the upper mantle in the same regions is further reduced to $\sim 1 \times 10^{20}$ Pa.s. Thus, a higher power-law exponent localises and intensifies regions of reduced mantle viscosity.

Both decreasing $(\dot{\varepsilon}_{II}^{T})_{UM}$ and increasing n_{UM} results in the plate to reach t^{C50}progressively earlier and the slab tip to reach a progressively shallower depth (Table 2).

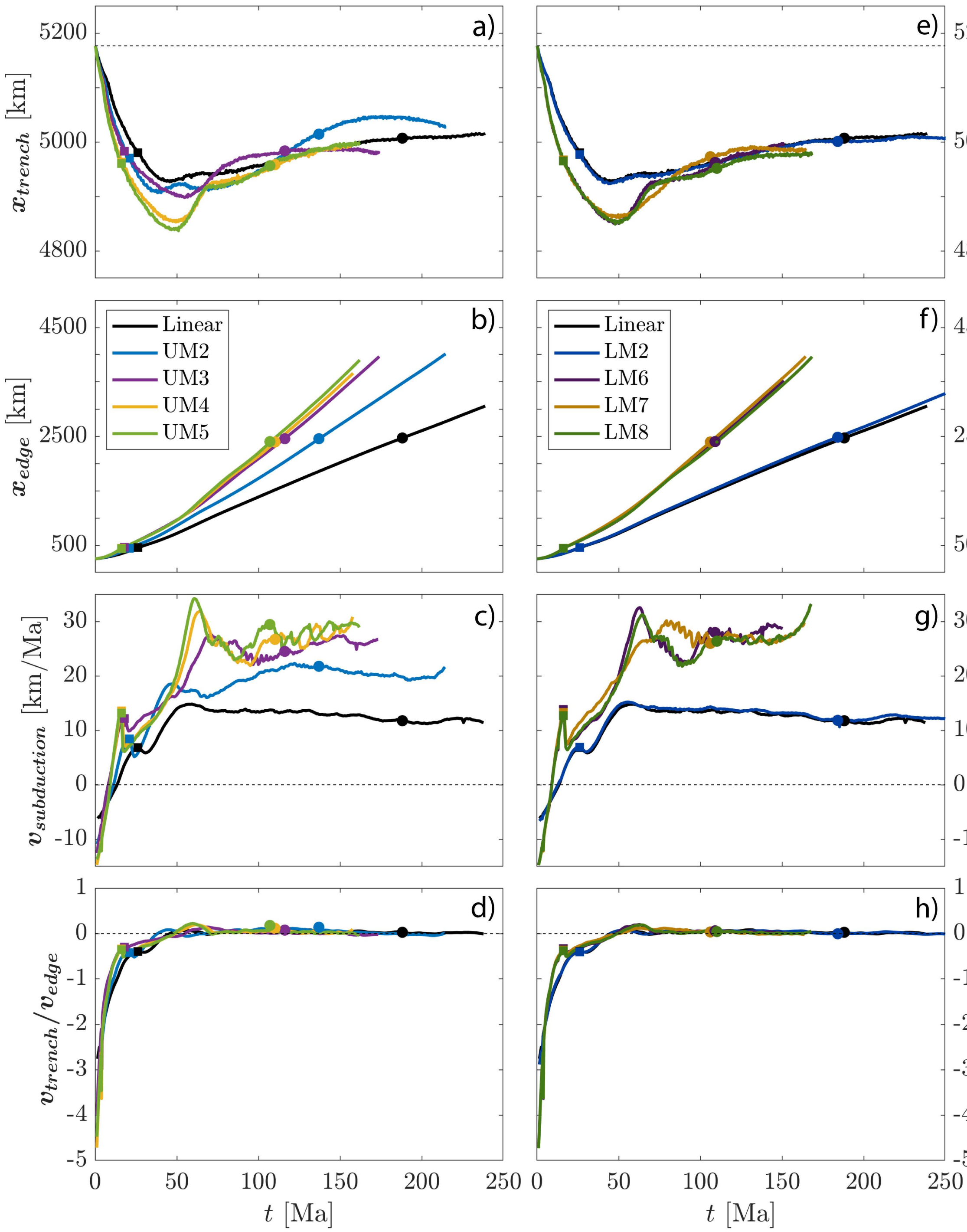

Figure 3. Trench position x_{trench} over time for a) UM experiments and e) LM experiments. The dotted line represents the trench initial position. Surface plate trailing edge position x_{edge} over time for b) UM experiment and f) LM experiments. Subduction velocity $v_{subduction}$ calculated as the difference between the trailing edge velocity and the trench velocity ($v_{edge} + v_{trench}$) over time for c) UM experiment and g) LM experiments. Ratio between v_{trench} and v_{edge} over time for d) UM experiment and h) LM experiments. Square symbols refer to the time at which the slab tip reaches a depth of 660 km and the circle symbols refer to the times at which the plate consumption is C_{Plate}~50 %.

3.1.2. Trench and trailing edge motion

The positions of the trench and trailing edge are plotted against time in Figure 3a and 3b for the upper mantle composite experiments. The square symbols indicate the times at which the slab tip reaches 660 km depth and the circle symbols marks t^{C50}, corresponding to the subduction states illustrated in Figure 2. The time when the slab tip reaches 660 km (t^{660}) and t^{C50} occur earlier with both lower transition strain rate and higher power-law exponent and the trench retreats further from its initial position (Figure 3a). The trench position at t^{660}, x_{trench}^{660}, varies ~ 9.4 km between experiments and x_{trench}^{C50} varies ~ 27.4 km between experiments (Table 3). In all cases, the trench retreats in the first 50 Ma of subduction and, after this stage, the but does not return to its initial position. At the end of the experiments, the trench is positioned between ~ 150 to ~ 200 km away from its initial position.

A change in the power law exponent n_{UM} from 1.5 – 5 (UM3, UM4 and UM5) results in 32 – 90 km more initial trench retreat than in the Linear case, as well as faster trailing edge motions (Figure 3b). Decreasing the transition strain rate from 1×10^{-12} to 3×10^{-13} s^{-1} (UM2 and UM4) also results in 21 and 76 km more initial trench retreat than in the Linear case, and more accentuated differences in the plate trailing edge motion. A higher transition strain rate (UM2) results in a lower rate of trailing edge displacement, closer to the linear case.

The trench velocity v_{trench} (Figure A1a) and the trailing plate edge velocity v_{edge} (Figure A1b) were calculated over time from centered differences of the trench position and the trailing edge position, respectively. The trench velocity is taken negative during trench retreat and the trailing edge velocity, which used as a proxy for the plate velocity, is positive when the plate moves towards the trench. The subduction velocity $v_{subduction}$ was calculated as $v_{edge} + v_{trench}$ and is plotted against time in Figure 3c. In Figure 3d, the ratio v_{trench}/v_{edge} is plotted against time. At the start of the experiments the subduction velocity is negative because the trench velocity is negative, around -20 to -10 km/Ma, as the slab bends downwards to initiate subduction and the trailing edge velocity is only ~ 5 km/Ma. As subduction evolves the trailing edge velocity increases resulting in an increase of the subduction velocity towards zero, which occurs between $\sim 8 - 13$ Ma. After this stage, the ratio $|v_{trench}/v_{edge}| < 1$, indicates the trailing edge velocity is higher than the trench velocity and the subduction velocity is mostly due to trenchward plate motion.

In Figure 3c, there is a local maximum of the subduction velocity (Table 3) just before the slab reaches the mantle discontinuity (marked by the squared symbols), after which it decreases. After a further 5 to 10 Ma, the velocity increases again. In the Linear case, the subduction velocity tends to a constant value of ~ 11 km/Ma, and in experiment UM2 tends to ~ 20 km/Ma. However, in experiments UM3, UM4 and UM5 the velocity continues to increase, with mean subduction velocities, after 100 Ma, of 25, 26.4 and 26.2 km/Ma, respectively. Between ~ 40

and $\sim$80 Ma all experiments exhibit a local maximum, which is higher for lower transition strain rate and higher power-law exponent (in experiment UM5, $v_{subduction}^{max} = 34.2$ km/Ma). This maximum is related to a change in the trench velocity, which during this period is advancing, as demonstrated by the positive ratio v_{trench}/v_{edge} at this time (Figure 3d), and is caused by forward folding of the slab at depth. After $\sim$80 Ma there is a decrease of the trench velocity due to backward folding. In experiments UM4 and UM5, the slab develops another fold which is marked by another local maximum is the subduction velocity at $\sim$110 and $\sim$120 Ma.

3.2. Power-law upper and lower mantle parameters

The transition strain rate and power-law exponent in both the upper and lower mantle are varied in a suite of eight experiments, denoted with ‘LM’ in Table 2, and compared to the Linear case. The mantle density contrast $D_M = 0.78$ % and the mantle viscosity ratio $\gamma_M = 25$.

3.2.1. Plate geometry

In Figure 2f-i, the slab geometric configuration is compared at t^{C50} times (Table 3). The lower mantle composite experiments reach t^{C50} between 4 and 82 Ma earlier and the slab tip reaches varying depths, between 4 km deeper and 316 km shallower, compared with in the Linear case (Table 2). The transition strain rate and power-law exponent in both upper and lower mantle were varied between experiments, and the effects of each of these parameters are described below.

Between experiments LM2 (Figure 2f) and LM6 (Figure 2g) the upper mantle power-law exponent, the lower mantle power-law exponent and the lower mantle transition strain rate are constant ($n_{UM} = n_{LM} = 3.5$ and $(\dot{\varepsilon}_{II}^{T})_{LM} = 1.5 \times 10^{-11}$ s^{-1}). The transition strain rate of the upper mantle $(\dot{\varepsilon}_{II}^{T})_{UM}$ is varied, from 3×10^{-11} s^{-1} to 3×10^{-13} s^{-1}. Experiment LM2 shows a slab geometry very similar to the Linear case, but it evolved 4 Ma faster and the power-law component lowering effects of mantle viscosity are too small to be manifested in changes of the colouring in Figure 2f. In experiment LM6, the slab tip folded in the opposite direction upon interaction with the mantle discontinuity (folded oceanwards) twice during sinking. The viscosity of the upper mantle is reduced around the plate and the slab, and on top of the mantle discontinuity. However, in the lower mantle, the viscosity lowering effects of the power-law component are too small to be manifested in changes of the viscosity colour. In these two experiments, the transition strain rate in the lower mantle is high, indicating that the power-law component is activated in a small area, resulting in an unnoticeable viscosity reduction in the mantle. The slab geometric configuration in experiment LM6 resembles experiments UM4 and UM5, in which the lower mantle is entirely linear viscous.

Between experiments LM5 (not shown), LM6 (Figure 2g) and LM8 (Figure 2i), the upper mantle power-law exponent, the upper mantle transition strain rate and the lower mantle power-law exponent are constant ($n_{UM} = n_{LM} = 3.5$ and $(\dot{\varepsilon}_{II}^{T})_{UM} = 3 \times 10^{-13}$ s^{-1}). Only the transition strain rate of the lower mantle $(\dot{\varepsilon}_{II}^{T})_{LM}$ is varied from 3×10^{-11} s^{-1} to 1.5×10^{-11} s^{-1} to 5×10^{-12} s^{-1}. The slab geometric configuration in experiments LM5 and LM6 is indistinguishable. However, in experiment LM8, the slab is straighter in the mantle discontinuity area. In these three experiments, the slab tip folded oceanwards upon interaction with the mantle discontinuity. Moreover, in experiments LM5 and LM6 the viscosity lowering effects of the power-law component in the lower mantle are too small to be manifested in changes of the viscosity colouring. In experiment LM8, the lower mantle region surrounding the slab displays a faded light greenish colour, indicating lower viscosity in that region.

Between experiments LM7 (Figure 2h and Movie 1) and LM8 (Figure 2i) the upper mantle power-law exponent, the upper mantle transition strain rate and the lower mantle transition strain rate are constant ($n_{UM} = 3.5$, $(\dot{\varepsilon}_{II}^{T})_{UM} = 3 \times 10^{-13}$ s^{-1} and $(\dot{\varepsilon}_{II}^{T})_{LM} = 5 \times 10^{-12}$ s^{-1}). Only the power-law exponent of the lower mantle n_{LM} is varied, from 1.5 s^{-1} to 3.5. In experiments LM7 the slab tip folded only once upon interaction with the mantle discontinuity (oceanwards), whereas in all other experiments the tip folded at least twice. The viscosity lowering effects of the power-law component in the lower mantle are marked by the light green shadings around the slab, which indicate viscosity values of $\sim 1.8 \times 10^{22}$ Pa s.

3.2.2. Trench and trailing edge motion

The curves of the trench and trailing edge positions (Figure 3e and 3f) are very similar to those of the upper mantle composite experiments (cf. Figure 3a and 3b) and the time at which the slab tip reaches 660 km (t^{660}) and t^{C50} are not affected by variations in the power-law parameters of the lower mantle (Table 3). In all cases, the trench retreats during the first 50 Ma of subduction. After this stage, the trench advances to a position between ~ 160 to ~ 200 km away from its initial position.

A change in the transition strain rate of the upper mantle from 3×10^{-11} s^{-1} in experiment LM2, to 3×10^{-13} s^{-1} in experiments LM6, LM7 and LM8, results in a higher initial trench retreat of up to $67 - 78$ km more than in both the Linear case and experiment LM2. However, variations in the power-law exponent and the transition strain rate of the lower mantle (experiments LM6, LM7 and LM8) do not induce significant changes in the trench and trailing edge motion over time, as the position curves for these three experiments overlap for the most of the duration of the experiments.

The variation in subduction velocity $v_{subduction}$ and in the ratio v_{trench}/v_{edge} (Figure 3g and 3h) are similar to the upper mantle composite experiments (cf. Figure 3c and 3d). At the start of the experiments the subduction velocity is negative because the trench velocity is negative, around -20 to -10 km/Ma (Figure A1c), as the slab bends downwards to initiate subduction and the trailing edge velocity is ~ 5 km/Ma (Figure A1d). As subduction evolves, the trailing edge velocity increases, resulting in an increase of the subduction velocity towards zero, which occurs between $\sim 9-13$ Ma. After this stage, the ratio $\left|v_{trench}/v_{edge}\right| < 1$, indicating that the trailing edge velocity is higher than the trench velocity and the subduction velocity is mostly due to trenchward plate motion.

In Figure 3g, the subduction velocity reaches a local maximum (Table 3) before the slab reaches the mantle discontinuity (marked by the squared symbols), after which it decreases and after a further 5 to 10 Ma, the velocity increases again. In the Linear case and experiment LM2, the subduction velocity is approximately constant at $\sim 11-13$ km/Ma. However, in experiments LM6, LM7 and LM8 the velocity continues to increase, with mean subduction velocities, after 100 Ma, of 27.8, 28.6 and 30.1 km/Ma, respectively. Between ~ 55 and ~ 65 Ma all experiments, with the exception of LM7, exhibit a velocity maximum, which is higher for higher transition strain rate in the lower mantle (in LM6, $v_{subduction}^{max} = 32.5$ km/Ma). The subduction velocity maximum in LM7 occurs at ~ 65 Ma. This maximum is related to a change in the trench velocity, which is advancing at the indicated times. This is illustrated by the positive ratio v_{trench}/v_{edge} (Figure 3h) and is caused by the forward folding of the slab at depth. After ~ 80 Ma there is a decrease of the trench velocity due to backward folding. In experiments LM6 and LM8, the slab develops another fold which is marked by another local maximum in the subduction velocity at ~ 110 Ma. In experiment LM7 there is only one pronounced local maximum at $t > 50$ Ma and in Figure 2h the slab has folded only once.

3.3. Linear mantle viscosity: varying D_M and γ_M

An additional suite of twelve experiments was executed considering linear mantle viscosity and varying both the mantle density contrast and viscosity ratio, by increasing the density and viscosity of the lower mantle and keeping the density and viscosity of the upper mantle constant (Table 3). The values of the mantle density contrast used were 0 %, 0.78 %, 1.8 % and 2.5 % and the values of the mantle viscosity ratio used were $1, 25$ and 50.

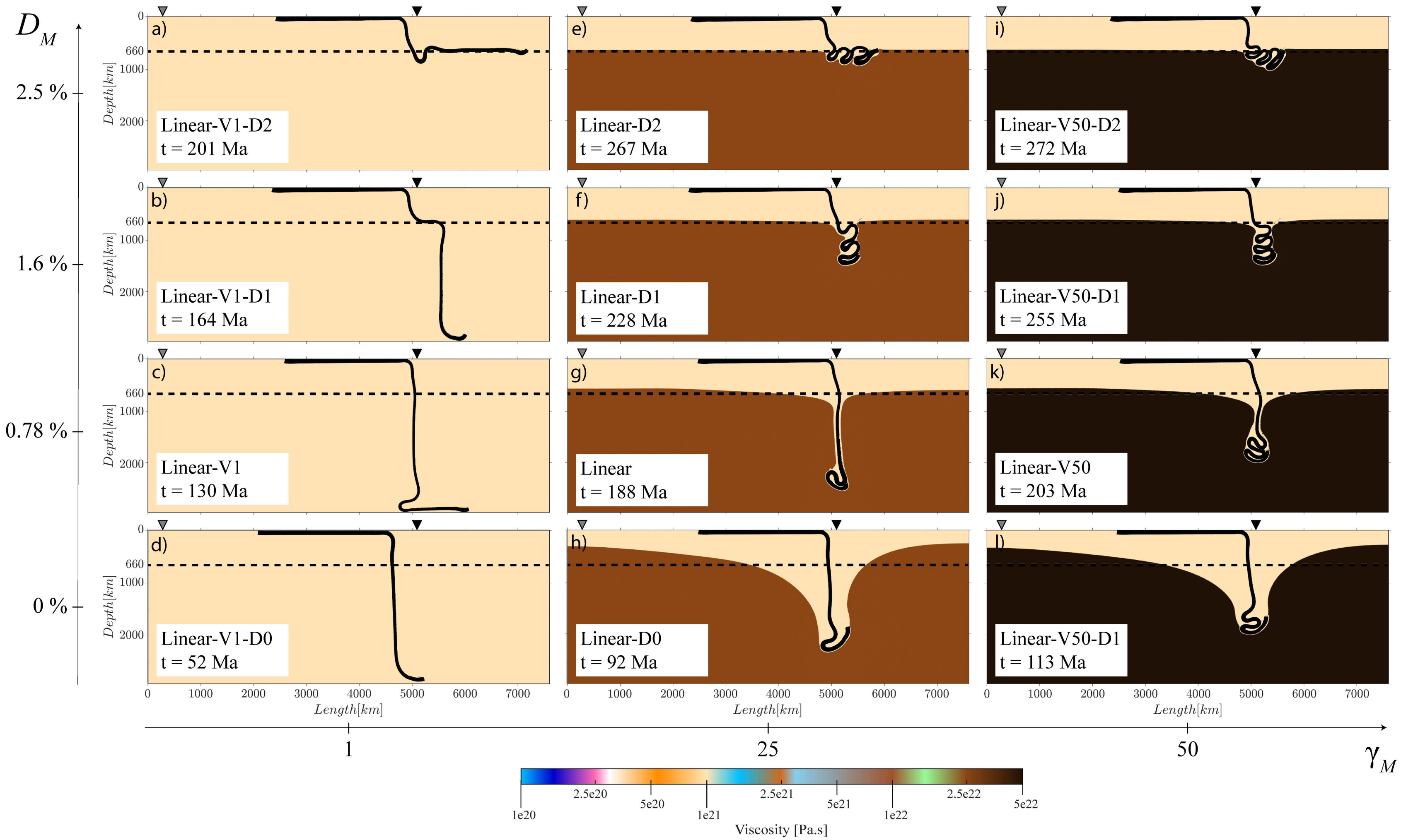

Figure 4. Viscosity field and slab geometry of experiments with linear mantle viscosity, varying the mantle density contrast and the mantle viscosity ratio at times in which ~50 % of the plate has been consumed by subduction. The mantle density contrast D_M increases between the bottom row panels and the top row panels, as indicated by the vertical arrow on the left. The mantle viscosity ratio increases for the left panels to the right panels, as indicated by the horizontal arrow on the bottom. The black colour of the plate is not included in the viscosity colour bar ($\eta_{sp} = 5 \times 10^{23}$ Pa s). Inverted triangles indicate the initial position of the trench (black) and the plate trailing edge (grey). Dashed lines represent the 660 km depth mantle discontinuity.

3.3.1. Plate geometry

In the experiments with a mantle viscosity ratio of 1 (Figure 4a-d), increasing D_M from 0 to 2.5 %, t^{C50} occurs progressively later, varying between 52 and 201 Ma. For $D_M = 0$ % and 0.78 % the slab reaches the bottom easily with a vertical shape and the slab thins in the lower mantle. For $D_M = 1.6$ % the slab was temporarily delayed at the mantle density discontinuity, but still reached the bottom with a vertical shape below a depth of 660 km. However, for $D_M = 2.5$ % the slab is stagnant above the mantle discontinuity, with only partial lower mantle penetration, reaching a maximum depth of 890 km.

In the experiments with a mantle viscosity ratio of 25 (Figure 4e-h), increasing D_M from 0 to 2.5 %, t^{C50} occurs progressively later, varying between 92 and 267 Ma. For $D_M = 0$ %, the slab tip folded once and sinks vertically. The mantle discontinuity is depressed where the slab is sinking and it is uplifted at the lateral domain boundaries, indicating that the sinking of the slab induces full mantle convection. Because there is no density contrast between upper and lower mantle, there is no buoyancy force that keeps the upper mantle closer to the surface and the lower mantle closer to the bottom in order to maintain the mantle layering, resulting in excessive mantle discontinuity depth variations. In Figure 4d, the mantle discontinuity is similarly disturbed. However, because there is no viscosity contrast either, the slab sinks into a homogenous mantle. For $D_M = 0.78$ % (Figure 4g), the slab tip folded twice, sinks vertically, reaching 2481 km depth and the mantle discontinuity is less uplifted at the lateral domain boundaries. For $D_M = 1.6$ % the slab is developing folds as it sinks into the lower mantle and the slab tip reaches a shallower depth, at 1468 km depth. For $D_M = 2.5$ % the slab is developing folds as it sinks but accumulates at the mantle discontinuity, spreading laterally and reaching a maximum depth of 922 km.

In the experiments with a mantle viscosity ratio of 50 (Figure 4i-l), increasing D_M from 0 to 2.5 %, t^{C50} also occurs progressively later, varying between $113 - 272$ Ma. For $D_M = 0$ %, the slab tip folded more than once and sinks vertically, reaching a depth of 1973 km and the mantle discontinuity is depressed similarly to Figure 4h, for the same reason. For $D_M = 0.78$ %, the slab tip folded four times, sinking vertically in a blob-like shape, reaching 1958 km depth and the mantle discontinuity is less uplifted at the lateral domain boundaries. For $D_M = 1.6$ % the slab is developing folds as it sinks into the lower mantle and the slab tip reaches of depth of 1457 km. The slab geometry configuration is visually similar to Figure 4f (where $\gamma_M = 25$). However, the slab develops a higher number of folds as it sinks. For $D_M = 2.5$ % the slab also develops folds as it sinks but it accumulates at the mantle discontinuity at $\sim 30°$, reaching a maximum depth of 1020 km, which is deeper than in Figures 4a and 4e.

In summary, increasing the mantle density contrast results in slower and shallower subduction and the mantle discontinuity is less disturbed (i.e., the mantle discontinuity is less elevated in the vicinity of the domain boundaries) and the mantle encases the slab more tightly. Moreover, increasing the mantle viscosity ratio results in the development of additional folds as the slab sinks.

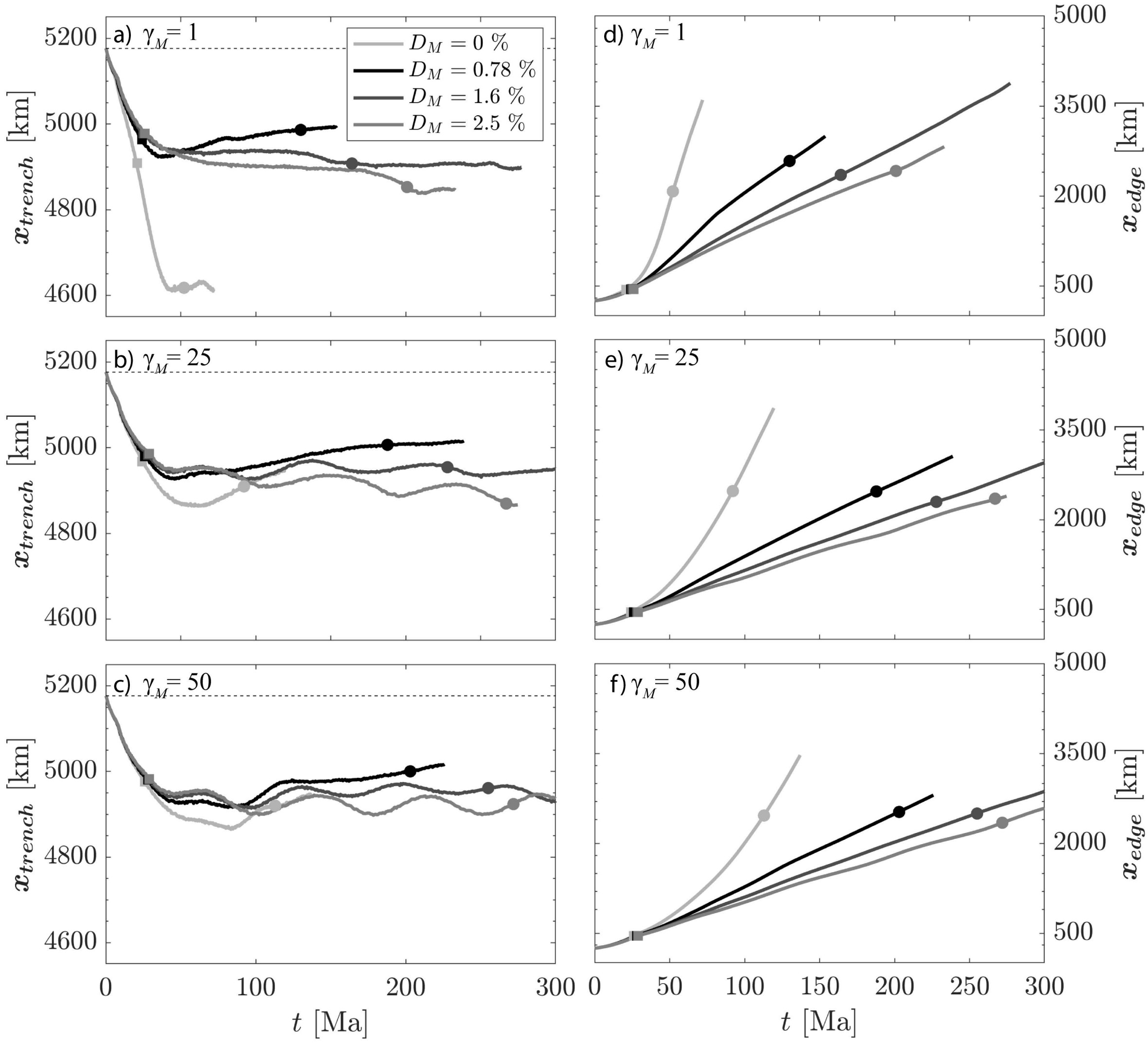

Figure 5. Trench and plate trailing edge position against time for the experiments varying the mantle density contrast D_M and the mantle viscosity ratio γ_M. a, d) $\gamma_M = 1$; b, e) $\gamma_M = 25$; and c, f) $\gamma_M = 50$. The squares refer to the times at which the slab tip reaches a depth of 660 km. The circles refer to the times at which the plate consumption is C_{Plate}~50 %. Dotted lines in a-c) represent the trench initial position.

3.3.2. Trench and trailing edge motion

The position of the trench and the position of the plate trailing edge are plotted against time in Figure 5, for the linear experiments varying D_M and γ_M. In all experiments, the trench retreats during the first 50 Ma of subduction and after this stage the trench advances, although it does not return to its initial position. If $D_M = 0$ %, the trench retreats the most in this initial stage,

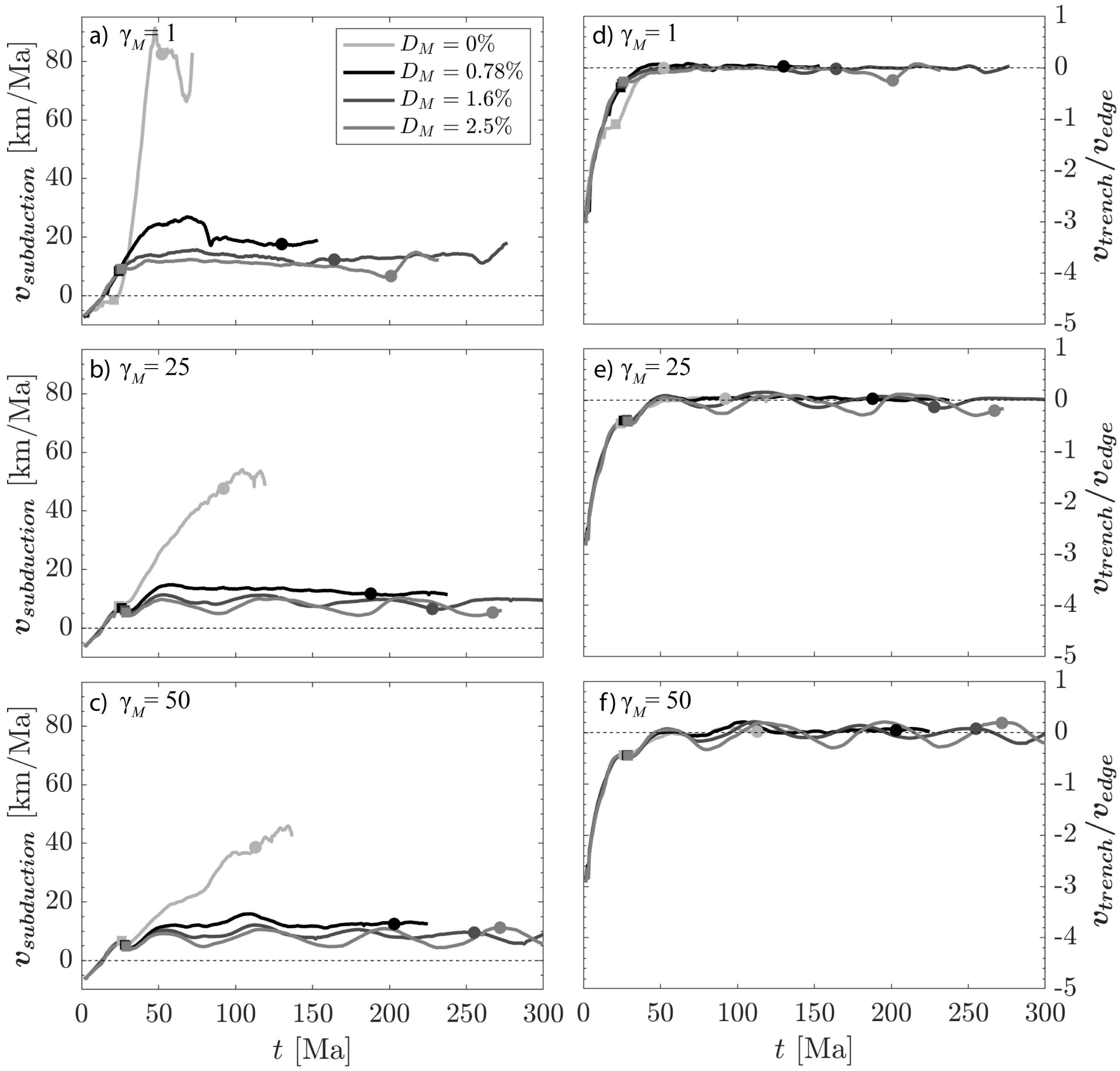

Figure 6. Subduction velocity and ratio between trench velocity and plate trailing edge velocity against time for the experiments varying the mantle density contrast D_M and the mantle viscosity ratio γ_M. a, d) $\gamma_M = 1$; b, e) $\gamma_M = 25$; and c, f) $\gamma_M = 50$. Subduction velocity $v_{subduction}$ was calculated as the difference between the trailing edge velocity and the trench velocity ($v_{edge} + v_{trench}$). The squares refer to the times at which the slab tip reaches a depth of 660 km. The circles refer to the times at which the plate consumption is C_{Plate}~50 %.

regardless of the mantle viscosity ratio. And if $D_M = 1.78$ %, the trench advances the most after this initial stage, also regardless of the mantle viscosity ratio. For $D_M \geq 1.6$ % and $\gamma_M \geq 25$ the trench motion is periodic after the first 50 Ma, alternating phases of trench retreat and trench advance, between ~$4915 - 4955$ km, with a longer wavelength of the periodicity for higher values of D_M.

Increasing the mantle density contrast D_M, for $\gamma_M = 1$ (Figures 5a and 5d), t^{660} (Table 3) occurs 1 to 3 Ma later (at 24 ± 2 Ma), the trench retreats between 59 and 73 km less (at 4957 ± 33 km) and the trailing edge position varies between $5 - 7$ km (at 445 ± 9 km). For $\gamma_M = 25$ (Figure 5b and e), t^{660} occurs 2 to 5 Ma later (at 27 ± 2 Ma), the trench retreats between 12 and 18 km less (at 4980 ± 8 km) and the trailing edge position varies between $0 - 3$ km (at

456 ± 2 km). For $\gamma_M = 50$ (Figure 5c and f), t^{660} occurs 2 to 3 Ma later (at 28 ± 1 Ma), the trench retreats between 5 and 7 km less (at 4981 ± 3 km) and the trailing edge position varies between $0 - 3$ km (at 457 ± 2 km).

The times t^{C50} vary more significantly with the mantle density contrast D_M (Table 3). Increasing D_M for $\gamma_M = 1$ (Figure 5a and 5d), t^{C50} occurs 78 to 149 Ma later (with $t^{C50} = 52$ Ma for $D_M = 0$ %), the trench retreats between 235 and 368 km less (with $x^{C50}_{trench} = 4618$ km for $D_M = 0$ %) and the trailing edge position varies between 273 and 510 km (with $x^{C50}_{edge} = 2074$ km for $D_M = 0$ %). For $\gamma_M = 25$ (Figures 5b and 5e), t^{C50} occurs 96 to 175 Ma later (with $t^{C50} = 92$ Ma for $D_M = 0$ %), the trench retreats between 40 more and 97 km less (with $x^{C50}_{trench} = 4910$ km for $D_M = 0$ %) and the trailing edge position varies between $10 - 183$ km (with $x^{C50}_{edge} = 2479$ km for $D_M = 0$ %). For $\gamma_M = 50$ (Figures 5c and 5f), t^{C50} occurs 90 to 159 Ma later (with $t^{C50} = 113$ Ma for $D_M = 0$ %), the trench retreats between 4 and 80 km less (with $x^{C50}_{trench} = 4920$ km for $D_M = 0$ %) and the trailing edge position varies -125 to 55 km (with $x^{C50}_{edge} = 2467$ km for $D_M = 0$ %).

At the start of the experiments the subduction velocity (Figure 6a-c) is negative because the trench initially retreats faster than the trailing edge moves trenchward. As subduction evolves the trailing edge velocity increases resulting in an increase of the subduction velocity towards zero, which occurs between $\sim 13 - 14$ Ma for all experiments. Except if $D_M = 0$ % and $\gamma_M = 1$, in which case, it occurs at 24 Ma. After this stage, the ratio $|v_{trench}/v_{edge}| < 1$ (Figure 6d-f), indicating that the trailing edge velocity is higher than the trench velocity and the subduction velocity occurs mostly due to trenchward plate motion.

In experiments where $\gamma_M > 1$, the subduction velocity maximum (Figure 6a-c and Table 3) occurs shortly before the slab reaches 660 km depth (indicated by the square symbols), and once the slab reaches the mantle discontinuity the velocity decreases. The subduction velocity in experiments with $D_M = 0.78$ % tends to a constant value that is lower with higher mantle viscosity ratio (between 12 and 17 km/Ma). In experiments with $D_M > 0.78$ % and $\gamma_M \geq 25$ the subduction velocity is periodic and related to the slab folding, which controls the trench advance/retreat phase alternation.

3.3.3. Surface velocity

The variations in mantle density contrast and viscosity ratio also affect the plate surface velocity. The horizontal velocity along the top of domain was extracted from the velocity field for the times presented in Figure 4, and is plotted in Figure 7 against the length of the domain.

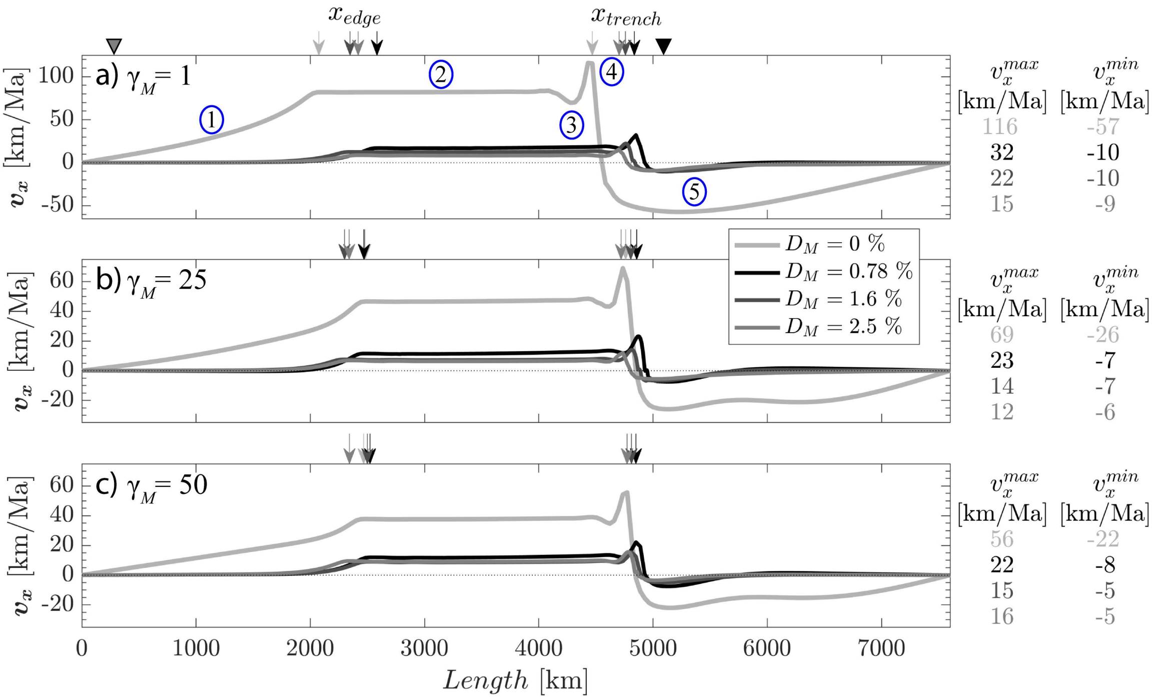

Figure 7. Surface horizontal velocity v_x against domain length for the experiments varying the mantle density contrast D_M and the mantle viscosity ratio. a) $\gamma_M = 1$, b) $\gamma_M = 25$ and c) $\gamma_M = 50$. The horizontal velocity profiles are plotted for the times at which the plate consumption is C_{Plate}~50 % and the corresponding positions of the trench and the plate trailing edge are indicated by the arrows and x_{trench} and x_{edge}. The triangles indicate the initial positions of the trench (black) and of the plate trailing edge (grey). The maximum and minimum values of the surface horizontal velocity are listed on the right for each experiment.

The horizontal velocity at the surface follows the same pattern in all cases, from left to right along the length of the domain: 1) the horizontal velocity increases from the boundary to the trailing edge vicinity, from 0 km/Ma to an approximately constant value that varies for each experiment, decreasing with both higher D_M and higher γ_M; 2) the constant value is maintained along most of the length, indicated by x_{edge} and x_{trench}; 3) before the trench, the horizontal velocity drops to a local minimum that also varies for each experiment, and is less pronounced for higher D_M; 4) at the trench, the horizontal velocity peaks to a maximum and drops to negative values after the trench; and 5) in the mantle wedge (in front of the trench) until the right boundary of the domain, the horizontal velocity increases again from negative values towards 0 km/Ma.

When the mantle density contrast, D_M, is increased, the horizontal velocity at the surface is reduced and its maximum value decreases between $61 - 87$ %. Stage 1 occurs closer to the plate edge (within 1000 km from the edge) and in stage 5, the horizontal velocity increases to 0 km/Ma closer to the trench position. Increasing the mantle viscosity ratio, the horizontal velocity at the surface is also reduced and the maximum value decreases between $25 - 52$ %, and the trench retreats $0.3 - 6.3$ % less (Table 3).

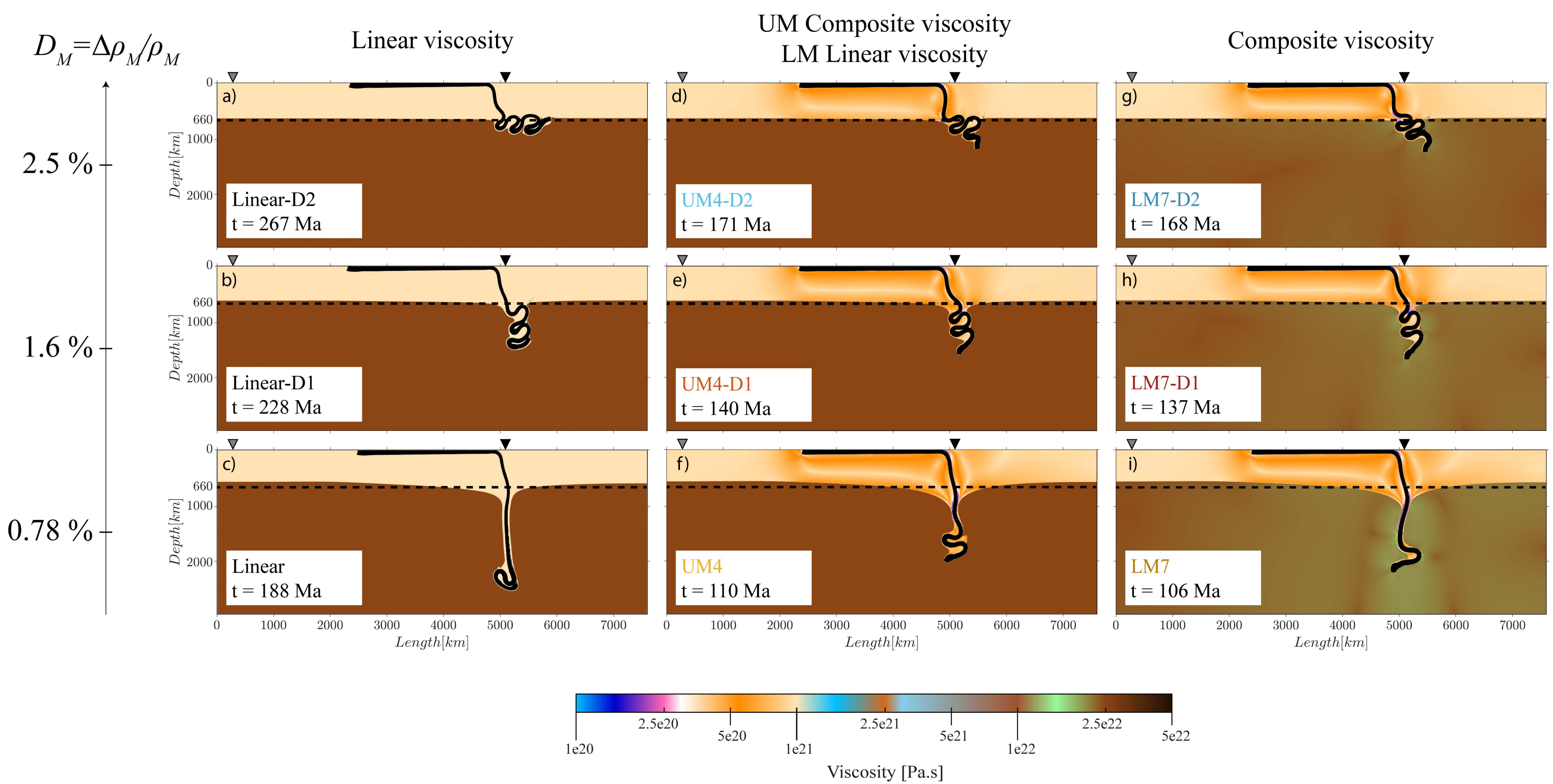

Figure 8. Viscosity field and slab geometry of experiments varying the mantle density contrast, comparing linear and non-linear experiments at times in which ~50 % of the plate has been consumed by subduction. a-c) the mantle viscosity is linear; d-f) the viscosity of the upper-mantle is composite and the viscosity of the lower-mantle is linear; and g-i) the viscosity of both upper and lower mantle is composite. The mantle density contrast D_M increases between the bottom row panels and the top row panel, as indicated by the vertical arrow on the left. In all experiments, the reference viscosity of the upper mantle is 1×10^{21} Pa.s, $n = 3.5$ and $\dot{\varepsilon}_{II}^{T} = 3 \times 10^{-13}$ s-1. The reference viscosity of the lower mantle is 2.5×10^{22} Pa.s, $n = 1.5$ and $\dot{\varepsilon}_{II}^{T} = 5 \times 10^{-12}$ s^{-1}. The black colour of the plate is not included in the viscosity colour bar ($\eta_{sp} = 5 \times 10^{23}$ Pa.s). Inverted triangles indicate the initial position of the trench (black) and the plate trailing edge (grey). Dashed lines represent the 660 km depth mantle discontinuity.

3.4. Power-law mantle viscosity: varying D_M

The mantle density contrast controls the slab sinking geometry and its ability to penetrate into the lower mantle [Kincaid & Olson, 1987; Christensen, 1996; Olbertz et al., 1997]. However, as reported in sections 3.1 and 3.2, the addition of a power-law rheology component in the mantle viscosity results in deeper and faster subduction. A fourth set of experiments was executed to evaluate if and how the power-law rheology component in the mantle counter-balances the hindrances to subduction caused by a higher mantle density contrast. In this set of nine experiments, the power-law parameters are kept constant ($(\dot{\varepsilon}_{II}^{T})_{UM} = 3 \times 10^{-13}$ s^{-1}, $n_{UM} = 3.5$, $(\dot{\varepsilon}_{II}^{T})_{LM} = 5 \times 10^{-12}$ s^{-1} and $n_{UM} = 1.5$) and D_M was varied. Experiments Linear, UM4 and LM7, in which the $D_M = 0.78$ %, are compared with experiments Linear-D1, UM4-D1 and LM7-D1, in which $D_M = 1.6$ %, and with experiments Linear-D2, UM4-D2 and LM7-D2, in which $D_M = 2.5$ %. The reference mantle viscosity ratio $\gamma_M = 25$ and the mantle density contrast was increased by increasing the density of the lower mantle and keeping the density of the upper mantle constant.

3.4.1. Plate geometry

In Figure 8 the slab geometric configuration for the nine experiments is compared at t^{C50} times (Table 3). The slab geometric configuration of experiments Linear, Linear-D1 and Linear-D2 (Figure 8a-c) have been described in the previous section. The experiments in which only the upper mantle is composite (UM4, UM4-D1 and UM4-D2, Figure 8d-f) reach t^{C50} 78, 88 and 96 Ma later for $D_M = 0.78\%$, 1.6 % and 2.5 % than their respective linear analogous cases. In the three experiments, the slab tip folded upon interaction with the mantle discontinuity, pointing oceanwards and the slab tip reaches varying depths. If $D_M = 0.78\%$, y_{slab}^{C50} is 945 km shallower that in the Linear case because, contrary to the Linear case, the slab keeps its thickness constant during subduction. If $D_M = 1.6$ %, y_{slab}^{C50} is 82 km deeper that in the Linear-D1 case, because the slab tip dips at $\sim 45°$ into the lower mantle, whereas in Linear-D1 case the slab tip is sub-horizontal. If $D_M = 2.5$ %, y_{slab}^{C50} is 254 km deeper that in the Linear-D2 case, because the slab tip anchored into the lower mantle upon interaction with the mantle discontinuity (in the Linear-D2 case, the slab slid along the discontinuity), causing the slab folds to accumulate at an angle between $30 - 50°$, which pushes the slab tip further into the lower mantle. The power-law component reduces the viscosity of the upper mantle around the slab, below the plate and above the mantle discontinuity underneath the plate, independently of the mantle density contrast.

The experiments in which the lower mantle is also composite (LM7, LM7-D1 and LM7-D2, Figure 8g-i) reach t^{C50} 82, 91 and 99 Ma later for $D_M = 0.78\%$, 1.6 % and 2.5 %, then their respective linear analogous case. In these three experiments, the slab tip also folded upon interaction with the mantle discontinuity, pointing oceanwards. The slab tip reaches varying depths: if $D_M = 0.78\%$, y_{slab}^{C50} is 316 km shallower that in the Linear case for the same reason as in experiment UM4, and the slab developed less folds; if $D_M = 1.6$ %, y_{slab}^{C50} is 178 km deeper than in the Linear-D1 case, for the same reason as in experiment UM4-D1; and if $D_M =$ 2.5 %, y_{slab}^{C50} is 303 km deeper than in the Linear-D2 case for the same reason as in experiment UM4-D2. The power-law component also reduces the viscosity of the upper mantle around the slab, below the plate and above the mantle discontinuity underneath the plate, independently of the mantle density contrast. However, the lowering of viscosity of the lower mantle viscosity varies with the mantle density contrast. At a higher D_M, the viscosity lowering effects of the power-law component in the lower mantle are concentrated around the slab and are weaker. This indicates that the slab, in a higher density contrast mantle induces lower stresses in the lower mantle as it sinks. However, there is still power-law rheology activation around the slab.

In summary, the power-law component in the upper mantle results in faster subduction, facilitates the slab to sink into the lower mantle without stretching, and promotes deeper slab penetration into the lower mantle at higher mantle density contrasts. Moreover, the power-law component in the lower mantle further enhances these effects.

3.4.2. Trench and trailing edge motion

The positions of the trench and the trailing edge for the linear and non-linear experiments varying D_M are plotted against time in Figures 9a and 9b. In the three linear experiments, $t^{660} \approx$ 28 Ma and the slab reaches t^{C50} at 188, 228 and 267 Ma, for a mantle density contrast of 0.78 %, 1.6 % and 2.5 %, respectively. In the non-linear experiments, the slab reaches t^{660} at ~ 17 Ma (~ 11 Ma earlier than the linear cases). The slab reaches t^{C50}, in upper mantle composite experiments (UM4, UM4-D1, and UM4-D2), at 110, 140 and 171 Ma, for a mantle density contrast of 0.78 %, 1.6 % and 2.5 %, respectively. In the lower mantle composite experiments (LM7, LM7-D1, and LM7-D2), the slab reaches t^{C50} at 106, 137 and 168 Ma, for mantle density contrasts of 0.78 %, 1.6 % and 2.5 %, respectively.

In all experiments, the trench retreats during the first $40 - 50$ Ma of subduction and after this stage the trench advances, although it does not return to its initial position (Figure 9a). When $D_M = 1.6$ %, the experiments Linear, UM4 and LM7, the trench continues to retreat and at the end of the experiments is at 164, 184 and 189 km away from its initial position,

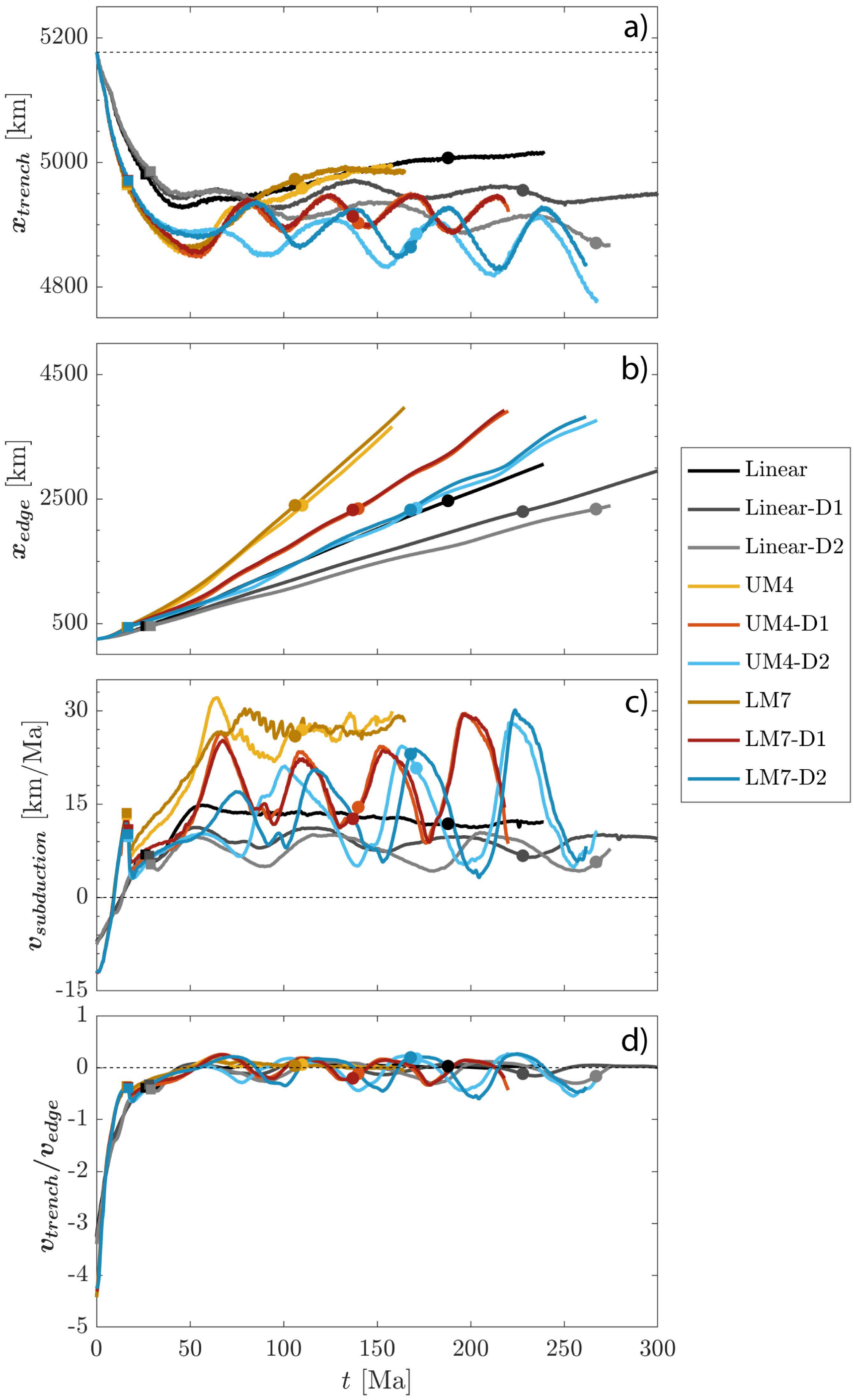

Figure 9. a) Trench position, b) trailing edge position and c) subduction velocity against time for the experiments varying the mantle density contrast, comparing linear and non-linear mantle viscosity. Subduction velocity $v_{subduction}$ was calculated as the difference between the trailing edge velocity and the trench velocity ($v_{edge} + v_{trench}$). Squares refer to the times at which the slab tip reaches a depth of 660 km and the circles refer to the times at which the plate consumption is C_{Plate}~50 %. Dotted line in a) represents the trench initial position.

respectively. In the other six experiments, after the first 50 Ma, the trench motion is periodic, alternating phases of trench retreat with trench advance. The trench position in experiments UM4-D1 and LM7-D1 almost overlap, oscillating around ~4925 km, however in the Linear-D1, the trench position motion has a longer wavelength and lower amplitude, oscillating around

~ 4950 km. The trench position in the experiments UM4-D2 and LM7-D2 does not overlap after the first 50 Ma, although the curves have similar wavelength and amplitude. In these experiments and the Linear-D2 case (with $D_M = 2.5$ %) the trench continues to retreat with an oscillatory motion. However, the oscillatory motion of the trench position in the Linear-D2 case has a longer wavelength and lower amplitude.

Experiments Linear-D1, UM4-D1, LM7-D1, Linear-D2, UM4-D2 and LM7-D2 show two full cycles of trench advance and retreat between 50 Ma and t^{C50} (Figure 9a). The trench motion periodicity can be directly attributed to the slab folding. The trench advances while the slab folds forwards towards the mantle wedge and retreats while the slab folds backwards. In all experiments, the slab has folded twice over the slab tip that initiated the subduction process (Figure 8). However, there is a difference in the shape of the first fold of the slab between the linear and the non-linear cases, which results from the slab tip bending oceanwards upon reaching the mantle discontinuity in the non-linear cases.

When considering experiments with the same mantle density contrast, the trailing edge (Figure 9b) moves at a higher rate in experiments where either the upper mantle only or both the upper and lower mantle have a composite viscosity. The plate trailing edge moves the fastest in Experiments UM4 and LM7 (yellow lines in Figure 9b), which have the lowest mantle density contrast $D_M = 0.78$ %. This results from the viscosity lowering effect of the power-law component in the mantle rheology. As the viscosity of the upper mantle region just below the plate is reduced, the plate motion is facilitated due to reduced drag forces. By contrast, the plate trailing edge moves the slowest in the linear experiments (black and grey lines in Figure 9b), especially for Linear-D2 which has $D_M = 2.5$ %. An increase in the mantle density contrast represents a hindrance to the plate sinking, therefore the overall subduction process evolves slower.

At the start of the experiments the subduction velocity (Figure 9c) is negative because the trench initially retreats faster than the trailing edge moves trenchward (Figure A2). As subduction evolves the trailing edge velocity increases resulting in an increase of the subduction velocity towards zero, which occurs between $\sim 13 - 14$ Ma for the linear experiments and at 9 Ma for the composite experiments (Figure A2a). After this stage, the ratio $\left|v_{trench}/v_{edge}\right| < 1$ (Figure 9d), indicating that the trailing edge velocity is higher than the trench velocity and the subduction velocity occurs mostly due to trenchward plate motion.

In all experiments, there is a local maximum of the subduction velocity shortly before the slab reaches 660 km depth (Table 3), varying between 6 and 7 km/Ma in the linear experiments, and between 12 to 14 km/Ma in the composite experiments with higher D_M. The interaction of

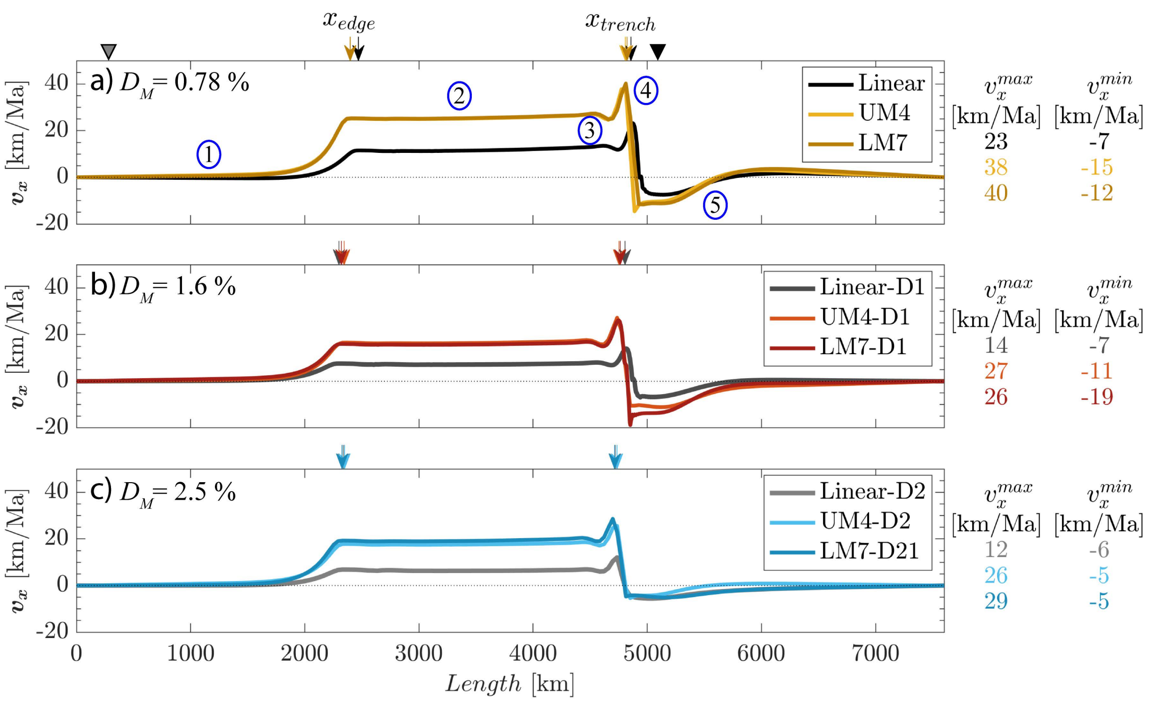

Figure 10. Surface horizontal velocity v_x against domain length for the experiments varying the mantle density contrast D_M, comparing linear and non-linear mantle viscosity. a) $D_M = 0.78$ %, b) $D_M = 1.6$ % and c) $D_M = 2.5$ %. The horizontal velocity profiles are plotted for the times at which the plate consumption is C_{Plate}~50 % and the corresponding positions of the trench and the plate trailing edge are indicated by the arrows and x_{trench} and x_{edge}. The triangles indicate the initial positions of the trench (black) and of the plate trailing edge (grey). The maximum and minimum values of the surface horizontal vel ocity are listed on the right for each experiment.

the slab tip with the mantle discontinuity results in a decrease of the subduction velocity. After $t \approx 30$ Ma in the linear experiments and $t \approx 18$ Ma in the composite experiments, the subduction velocity increases again. However, the subduction velocity in the Linear, UM4 and LM7 experiments ($D_M = 0.78$ %) tends to a constant value of ~12 km/Ma in the Linear case and to ~27 km/Ma in UM4 and LM7. In the other experiments (with $D_M > 0.78$ %), the subduction velocity is periodic, which is related to the slab folding, controlling the trench advance/retreat phase alternation. The subduction velocity in experiments Linear-D1 and Linear-D2 oscillates around $\sim 7 - 8$ km/Ma, and in experiments UM4-D1, LM7-D1, UM4-D2 and LM7-D2 oscillates around $\sim 14 - 16$ km/Ma.

The subduction velocity in the composite experiments show higher amplitudes of periodicity, as a result of the lowering of the sub-lithospheric mantle viscosity. Thus, weakening the mantle drag at the bottom of the plate, which allows the plate to move trenchward horizontally easily, compared to the linear cases. With higher mantle density contrast, the slab develops more folds, resulting in more cycles between the two phases of the subduction velocity increase/decrease. The experiments UM4 and LM7 ($D_M = 0.78$ %) developed only one full folding cycle (Figures 8c, 8f and 8i), thus the subduction velocity curves of these experiments show only one peak after 50 Ma (Figure 9c). Whereas the other experiments with multiple folds, show up to four peaks in the subduction velocity curves.

3.4.3. Surface velocity

The horizontal velocity at the surface (Figure 10) follows the same pattern in all cases, similarly to what has been previously described in section 3.3 for the linear experiments, where $D_M$and γ_M are varied. The maximum horizontal velocity occurs at the trench. When the mantle density contrast is increased, the overall horizontal velocity at the surface is reduced and the maximum value decreases by $28 - 48$ %. This velocity reduction is more accentuated in the linear cases. When D_M is increased, variation of the maximum velocity is higher between the linear and non-linear cases: for $D_M = 0.78$ % the maximum horizontal velocity in the non-linear experiments is $65 - 73$% higher; for $D_M = 1.6$ % the maximum horizontal velocity in the non-linear experiments is $86 - 92$ % higher; and for $D_M = 2.5$ % the maximum horizontal velocity in the non-linear experiments is $117 - 142$ % higher. The increase of the maximum horizontal velocity is due to weakening the mantle drag at the bottom of the plate, mentioned above.

4. Discussion

Subduction is a large-scale geodynamic process, both in time and space, that takes place mostly at inaccessible depths below the surface. It is also the main driver of plate tectonics and global mantle convection and as such it is important to understand its processes. Investigations on subduction processes have been greatly facilitated by geodynamic models. However, modelling work requires simplifications of nature and there are very limited constraints on the material properties in the Earth, especially of the deep mantle. Hence, most models do not consider the possibility of a more complex stress-dependent rheology in the lower mantle, except for the D” layer at the bottom ~ 200 km of the lower mantle [e.g., Lay et al., 1998; Garnero, 2004]. The purpose of this study was to implement a stress-dependent rheology into both the upper and lower mantle and to evaluate how variations of the power-law parameters potentially influence subduction evolution. In addition, such implementation was evaluated under varying mantle density contrast conditions to determine how the mantle density contrast may impact the way stress-dependent rheology affects subduction dynamics.

4.1. Effect of upper and lower mantle power-law parameters

The slab geometry and subduction times were investigated using 2D isothermal numerical models with a linear viscous subducting plate, in a two-layer mantle. The parameters varied were the transition strain rate and the power-law exponent in both the upper and lower mantle. Results show that while a composite viscosity in the upper mantle accelerates subduction processes, the composite viscosity in the lower mantle mainly impacts the slab folding geometry.

The mineralogical significance of the strain rates tested are beyond the scope of this study, as the goal was to explore the implications of varying the strain rates at which the flow transitions from diffusion to dislocation creep. The transition strain rates were chosen based on the distribution of strain rate in the linear case over the model domain, which due to the boundary conditions also depends on the domain size. The transition strain rate values were chosen by limiting the area of the upper mantle that enters the power-law regime (Equation 5) to a maximum of 80%; and by limiting the area of lower mantle that enters the power-law regime to a maximum of 60%. It should be noted that the transition strain rates tested here in the upper mantle, between $3 \times 10^{-11} - 3 \times 10^{-13}$ s^{-1}, are higher than those used in previous studies, between $10^{-13} - 10^{-15}$ s^{-1} [e.g., Billen & Hirth, 2007; Holt & Becker, 2017]. Typical tectonic strain rates are 10^{-12} to 10^{-16} s^{-1} [e.g., Karato, 2010].

The effects of varying the transition strain rate were assessed by comparing the slab geometry at t^{C50} times, when ~ 50 % of the plate had been consumed by subduction. If the mantle viscosity is composite, considering either the upper mantle only or both the upper and lower mantle, t^{C50} occurs earlier, the slab penetration depth is shallower and the subduction velocity is higher compared to the case when mantle viscosity is linear. The composite viscosity in the upper mantle causes a reduced viscosity lubricating layer to form around the plate and slab, which facilitates plate motion and slab sinking. As a result, the combined plate and slab stretch less during subduction (Figure 2), as indicated by experiments UM4, UM5, LM7 and LM8, which have thicker slabs at the trench and at the mantle discontinuity compared to the Linear case.

The periodicity observed in the subduction velocity curves (Figures 3c, 3f and 7c) can be directly related to slab folding behaviour at the 660 km discontinuity, which involves two phases: 1) the slab rolls over, folding forward and the trench advances; and 2) the slab rolls back, folding backwards and the trench retreats. It has been documented that slab folding is linked periodic plate trench velocities [Schellart, 2005; Čížková & Bina, 2013], periodic subducting plate velocities [Čížková & Bina, 2013; Schellart, 2017a] and periodic convergence velocities [Lee & King, 2011]. This study shows how this behaviour depends on the mantle rheology.

In Figure 2, experiments UM3 (with $n_{UM} = 1.5$) and LM7 (with $n_{LM} = 1.5$) exhibit less folding at the slab tip. The low power-law exponent results in a broader area of mantle that is affected by the power-law viscosity, which in turn promotes faster slab sinking. However, it also results in a more moderate mantle viscosity reduction (Section 4.3), indicating that in regions of high stress, such as in the vicinity of where the slab is bending/unbending, the viscosity of the mantle is less reduced, compared to experiments in which the power-law exponent is 3.5, which hinders further buckling of the slab. Furthermore, because the slab does not develop more folds, the subduction velocity maximum, after ~ 75 Ma, is lower and less pronounced compared to experiments in which the power-law exponent is 3.5. Additionally, the subduction velocity local maximum, at ~75 Ma (Figure 3c), results from the combined effects of a decrease in the trench velocity and an increase in plate edge velocity, when the first slab fold develops at the mantle discontinuity (Movies 1, 2 and 3 in digital appendix).

4.2. Effects of mantle density contrast

Subduction dynamics has been extensively investigated in two-layer mantle configurations, however there have been no systematic studies in which both the mantle density contrast and the mantle viscosity ratio are varied. Some studies consider a homogenous mantle density and a viscosity ratio between upper and lower mantle that ranges between $10 - 100$ [Faccenna et al., 2001; Enns et al., 2005; OzBench et al., 2008; Capitanio et al., 2011; Quinquis et al., 2011; Faccenda & Capitanio, 2013; Schellart, 2017b]. Other studies impose a density contrast by defining depth dependent mineral transitions [Agrusta et al., 2017], which is complex to translate into variations of the upper-lower mantle density contrast.

Kincaid & Olson [1987] reported that the mode of slab penetration into the lower mantle depends on the 'slab density anomaly' defined as:

$$R = \frac{\rho_{sp} - \rho_{LM}}{\rho_{sp} - \rho_{UM}}, \tag{9}$$

where ρ_{sp} is the subducting plate density, ρ_{LM} is the lower mantle density and ρ_{UM} is the upper mantle density. They found that the slab either penetrates the lower mantle with little deformation ($R \gtrsim 0.5$), partially penetrates the lower mantle ($-0.2 \lesssim R \lesssim 0.5$), or does not penetrate the lower mantle, deflecting on top of the mantle discontinuity ($R < -0.2$). However, the range of mantle density contrasts and mantle viscosity ratios explored by Kincaid & Olson [1987] was very limited: $2.12\ \% < D_M < 2.91\ \%$ and $5.61 < \gamma_M < 11.53$; the density and viscosity of the subducting plate were also varied.

By comparison, the experiments reported here are characterised by $0.2 < R < 1$, $0\ \% < D_M < 2.5\ \%$ and $1 < \gamma_M < 50$, and the density and viscosity of the subducting plate is kept constant, reducing the number of variable parameters in equation 9. Hence, the results of linear viscosity experiments here expand on Kincaid & Olson's [1987] classification, considering a wider range of mantle density contrasts and viscosity ratios. When $R \leq 0.5$ (or $D_M \leq 1.6\ \%$) the slab penetrates into the lower mantle, but if $\gamma_M > 25$ the slab deforms significantly, developing multiple folds. When $R = 0.2$ (or $D_M = 2.5\ \%$), if $\gamma_M = 1$ the slab does not penetrate the lower mantle, if $\gamma_M = 25$ the slab folds and is stagnant just below the mantle discontinuity, and if $\gamma_M = 50$ the slab partially penetrates the lower mantle. It seems counterintuitive that the slab reaches greater depths when the mantle viscosity contrast is higher, since it represents an increased hindrance to slab sinking. However, horizontal spreading of the slab along the mantle discontinuity is resisted by a stronger drag from the lower mantle, which hinders the horizontal motion. Consequently, the slab folds accumulate at a sub-horizontal angle, which results in a more compacted slab pile under the trench, increasing the negative buoyancy and promoting ~ 100 km deeper slab sinking.

The mantle discontinuity at 660 km depth was implemented to freely adjust under the weight of the sinking slab. Consequently, the discontinuity is depressed where the slab is sinking and elevated close to the lateral domain boundaries, which is also facilitated by the free-slip lateral boundary conditions. For low mantle density contrast, the distortion of the mantle discontinuity is greater. In the most extreme example, with $D_M = 0\%$ and $\rho_{LM} = \rho_{UM}$ (Figures 4h and 4l), the discontinuity is severely depressed after ~ 100 Ma, favouring the upper mantle material to descend to ~ 2000 km depth (through a ~$500 - 1000$ km wide downwelling) and the lower mantle material is at ~ 300 km depth at the sides of the domain. Although the 410 and 660 km depth mantle discontinuities vary regionally in nature [Shearer & Masters, 1992], the observed distortion in these experiments is unrealistic, which highlights the role of the mantle density contrast in maintaining the mantle stratification and to minimise flow entrainment of upper mantle into lower mantle [Silver et al., 1988].

The dependence of modes of slab penetration on mantle composite viscosity were also evaluated. The composite viscosity decreases the mantle viscosity in areas of high stress, particularly around the slab (Figures 4e, 4f and 4g and Figures 8a, 8b and 8c). If the mantle is composite, upon reaching the mantle discontinuity, the slab sinks into the lower mantle almost without deformation before folding (Movies 1, 2 and 3 in Appendix III). When $R = 0.2$ (or $D_M = 2.5$ %), the mode of penetration changes from stagnant just below the mantle discontinuity to partial slab penetration into the lower mantle. The composite mantle viscosity results in faster subduction and the slab is able to penetrate deeper into the lower mantle, facilitated by the lubricating effect of the lower mantle composite rheology.

In Figure 9, the trenches in experiments with $D_M = 2.5$ % (light grey and blue lines) have a periodic motion after ~50 Ma, which is related to slab folding. When the slab folds forwards towards the mantle wedge, the trench advances, and when the slab folds backwards the trench retreats. Despite this oscillatory motion, the trench generally tends to retreat, because the slab accumulates at the mantle discontinuity and the folded slab pile does not flow easily along the discontinuity, forcing the trench to retreat in order for subduction to proceed. The composite experiments with $D_M = 1.6$ % (red lines in Figure 9) overlap. However, the composite experiments with $D_M = 2.5$ % (blue lines in Figure 9) are out of phase, indicating that the lower-mantle rheology has a stronger effect on subduction when the mantle density contrast is higher.

4.3. Mantle viscosity reduction

For higher values of the transition strain rate in the upper mantle, the composite rheology generally has a weaker effect on slab dynamics because the viscosity of the surrounding mantle is less reduced, approaching the behaviour of the linear case. Increasing the power-law exponent in the upper mantle localises and intensifies the reduction in mantle viscosity around the slab, developing a lubricating channel of lower viscosity around the slab. This facilitates an increase in the plate velocity and the slab sinking velocity, as well as less stretching of the plate and slab as subduction evolves.

The upper mantle has a lower reference viscosity than the lower mantle in all composite experiments ($\eta_{LM} = 25\eta_{UM}$), and the transition strain rates used for the upper and the lower mantle are different ($(\dot{\varepsilon}_{II}^T)_{UM} < (\dot{\varepsilon}_{II}^T)_{LM}$). Consequently, the transition from linear to power-law flow occurs at lower stresses in the upper mantle, resulting in a greater reduction of the effective viscosity in the upper. The ratio between the minimum viscosity in each mantle layer recorded during the experiments and the reference viscosity of the layer is summarised in Table 4. If only the upper mantle is composite, decreasing the upper mantle transition strain rate from 3×10^{-11} to 3×10^{-13} s^{-1} results in a decrease of the minimum viscosity of the upper mantle from 80 % to 25 % of the reference upper mantle viscosity (UM1 to UM3). Increasing the upper mantle power-law exponent also results in a lower minimum viscosity of the upper mantle from 25 % to 3 % of the reference upper mantle viscosity (UM3 to UM5).

The composite experiments UM4, LM6, LM7 and LM8 have the same upper mantle power-law parameters ($(\dot{\varepsilon}_{II}^{T})_{UM} = 3 \times 10^{-13}$ s^{-1} and $n_{UM} = 3.5$). However, the lower mantle power-law parameters vary between experiments LM6, LM7 and LM8 (Table 2). The minimum viscosity in the upper mantle increases when the lower mantle is also composite, from 5 % in UM4 to $10 - 11$ % in LM6, LM7 and LM8. Decreasing $(\dot{\varepsilon}_{II}^{T})_{LM}$ from 1.5×10^{-11} to 5×10^{-12} s^{-1} (LM6 to LM8) results in a lower minimum viscosity of the lower mantle from 87 % to 73 % of the reference lower mantle viscosity. Increasing n_{LM} from 1.5 to 3.5 (LM7 to LM8) results in a higher minimum viscosity of the lower mantle from 60 % to 73 % of the reference lower mantle viscosity. A lower power-law exponent in the lower mantle is therefore more effective in reducing the lower mantle viscosity, which facilitates slab sinking and explains why experiment LM7 is the fastest experiment to reach t^{C50} and why the slab geometry develops

Table 4. Ratio between minimum viscosity recorded and the reference viscosity in the upper and lower mantle in the composite experiments $(\eta)_{min}/\eta$. The subscripts UM and LM refer to the upper mantle and the lower mantle, respectively.

Experiment	$(\eta_{UM})_{min}/\eta_{UM}$	$(\eta_{LM})_{min}/\eta_{LM}$
Linear	1.00	1.00
UM1	0.80	1.00
UM2	0.21	1.00
UM3	0.25	1.00
UM4	0.05	1.00
UM5	0.03	1.00
LM1	0.83	0.94
LM2	0.83	0.91
LM3	0.28	0.62
LM4	0.29	0.76
LM5	0.10	0.90
LM6	0.10	0.87
LM7	0.10	0.60
LM8	0.11	0.73
Linear-DC1	1.00	1.00
UM4-DC1	0.05	1.00
LM7-DC1	0.05	0.50
Linear-DC2	1.00	1.00
UM4-DC2	0.05	1.00
LM7-DC2	0.05	0.52

fewer folds. Moreover, if the lower mantle is also composite, the stresses induced by the slab in the upper mantle are lower and the upper mantle viscosity is less reduced.

Variations of the mantle density contrast do not impact the minimum upper mantle viscosity recorded in experiments UM4, UM4-D1 and UM4-D2, which is 5 % of the reference upper mantle viscosity in all three cases. However, in experiments LM7, LM7-D1 and LM7-D2, increasing the mantle density contrast from 0.78 to 2.5 %, decreases the minimum upper mantle viscosity from 10 % to 5 % of the reference value, and the minimum lower mantle viscosity from 60 % to 50 % of the reference value. The composite viscosity of the upper mantle facilitates plate sinking, because the slab encounters the mantle discontinuity at a higher velocity than it would if the mantle was linear viscous. The mantle density contrast is increased by increasing the lower mantle density, which means that the plate is less negatively buoyant relative to the lower mantle. Upon reaching a more strongly stratified boundary, the slab therefore induces higher stresses in both the upper and lower mantle, leading to a more localised and more pronounced reduction of the mantle viscosity.

4.4. Comparison with previous models

Both trench motion and velocity have been previously explored in composite rheology models [e.g., Čížková & Bina, 2013; Holt & Becker, 2017]. Using a thermomechanical approach, Čížková & Bina [2013] evaluated the effects of slab yield strength, subducting plate age, crustal viscosity and the Clausius-Clapeyron slope of the mineral phase transition at 410 km on trench motion and slab buckling and stagnation. The trench retreats regardless of the age or strength of the subducting plate in most of their models. Čížková & Bina [2013] report that trench velocities are generally lower than plate velocities and both trench and plate velocities are periodic reflecting slab buckling, with dominant periodicities on the order of 20 Ma, which is also in agreement with the results of Lee & King [2011]. Additionally, an increase on the lower mantle viscosity, results in both reduced plate and trench velocities [Čížková & Bina, 2013].

In all experiments reported here the trench velocity is also lower than the plate velocity after the slab tip interacts with the mantle discontinuity. The dominant periodicities associated to the slab buckling are between $\sim 40 - 45$ Ma, and only the experiments with $\gamma_M = 25$ and $\gamma_M = 50$ exhibit periodic buckling, which can be explained by the high upper-lower mantle viscosity ratio [Čížková & Bina, 2013].

One major difference between the experiments in this study and the models of Čížková & Bina [2013] is the absence of an overriding plate. In this study, the trench motion is solely prescribed by the motion of the subducting hinge, controlled by lateral migration of the slab. However, in nature subducting plates are accompanied by overriding and neighbouring plates. Thus, the motion of the subducting plate alone is not sufficient to completely assess the evolution of the convergent margins. It is well documented that an overriding plate modifies the subduction induced poloidal flow, resulting in reduced trench retreats rates and increased slab tip dip angles at depth [Yamato et al., 2009; Meyer & Schellart, 2013; Holt et al., 2015]. The rheology and thickness of the overriding plate also play an important role in the deformation and motion of the subducting plate [Kincaid & Olson, 1987; Griffiths et al., 1995; Guillou-Frottier et al., 1995; Stegman et al., 2006; Capitanio et al., 2010]. The interplay between subducting and overriding plates is complex and beyond the scope of this study. Nevertheless, if an overriding plate were to be included, the experiments in this study can be expected to exhibit reduced trench retreat, especially during the initial slab descent through the upper mantle.

The second major difference between this and previous studies is the choice here not to include plastic yielding of the slab in this study. Plastic yielding weakens the strength of the slab during subduction, and combined with the upper mantle composite rheology, can induce the separation between the sinking slab and the plate once the slab has stalled, also known as slab detachment (or slab break-off) [Andrews & Billen, 2009]. Čížková & Bina [2013] do not report any slab detachments in their experiment, but also show that the effects of the yield stress in young slabs (between 70 to 100 Ma) on trench retreat are almost negligible, and very small in older slabs (~ 170 Ma) relative to other parameters, such as the crustal viscosity, justifying the simplification made in this study.

It is important to note that in this study all experiments are isothermal, whereas the models of Čížková & Bina [2013] are thermomechanical, which limits the comparisons of results. However, the results reported here can be compared to other studies of subduction that used an isothermal approach. For example, Holt & Becker [2017] used an upper mantle model setup-up that included an overriding plate, and varied the transition strain rate in the upper mantle, the depth of the initial slab and the length of the subducting plate. This study builds on the results of Holt & Becker [2017] by including a lower mantle.

The power-law deformation observed is localised in regions close to the slab and below the plates is also reported in other studies [Billen & Hirth, 2007; Garel et al., 2014]. When the power-law becomes more dominant by lowering the transition strain rate, the trench velocity is reduced relatively to the plate velocity, which in turn increases the slab dip angle [Holt & Becker, 2017].

Considering longer subducting plates, the plate motion resisting forces (i.e., the sub-lithospheric drag force acting on the bottom of the plate) increases with the slab length, reducing the plate velocity [Ribe, 2010] and resulting in an increase of the trench motion contribution to convergence [Holt & Becker, 2017]. The experiments reported here actually show generally lower trench and subduction velocities (between $1 - 3$ cm/yr, see Figures 3, 5d-f and 6c) and generally steeper slab dip angles in both the upper mantle and in the lower mantle ($\sim 70 - 90$ degrees, Figures 2, 4 and 8) than is reported in nature [Lallemand et al., 2005; Li et al., 2008; Schellart, 2008b]. These differences can be explained by the considerably long subducting plate ($L_{sp} = 4810$ km at the start of the experiments), which until the slab reaches the mantle discontinuity moves very slowly, resulting in subduction occurring by trench retreat during this period.

The parameter $log_{10}(v_{trench}/v_{edge})$ indicates if subduction occurs preferentially by plate motion (if it is < 0, $v_{trench} < v_{edge}$) or by trench motion (if it is > 0, $v_{trench} > v_{edge}$), assuming the plate velocity is represented by the plate trailing edge velocity. In Holt & Becker's [2017] 2D models, $log_{10}(v_{trench}/v_{edge}) < 0$ and is further reduced when transition strain rates are low. Comparing the linear model and the non-linear model with a transition strain rate of 1×10^{-14} s^{-1}, shortly after the slab reached the bottom of the upper mantle, $log_{10}(v_{trench}/v_{edge})$ is reduced by ~ 1.25 if the plate is 2000 km long and reduced by ~ 0.75 if the plate is 4000 km long [Holt & Becker, 2017]. In this study, the plate is longer ($L_{sp} = 4810$ km) and, at times when the slab tip is at a depth of 660 km, $log_{10}(v_{trench}/v_{edge})$ is reduced by ~ 0.7 between the linear case and the non-linear model with transition strain rate of 3×10^{-13} s^{-1}. This is in agreement with the results of Holt & Becker [2017], since a plate longer than 4000 km should yield a lower variation of $log_{10}(v_{trench}/v_{edge})$ between linear and non-linear models than that these authors report.

The composite rheology of the mantle also impacts the dip of the subducting slab. If the transition strain rate is low enough (1×10^{-15} s^{-1}) and the initial slab is shallow (150 km), the slab can impinge on the bottom of the upper mantle at an angle higher than $90°$ causing the plate to rollover itself [Holt & Becker, 2017]. In this study, the initial slab depth is 125 km, however slab rollover is not observed because the transition strain rate values tested are higher ($\geq 3 \times 10^{-13}$ s^{-1}), resulting in high slab dip angles between $70 - 90°$ in the upper mantle.

4.5. Implications for nature

Tomography studies provide present-day snapshots of slab geometries [e.g., Li et al., 2008; Fukao & Obayashi, 2013], which can be divided into three types: 1) slabs that stagnate in the upper mantle, lying flat on top of the ~ 660 km mantle discontinuity, such as the Izu, Honshu and Calabria slabs; 2) slabs sinking deep into the lower mantle reaching depths of ~ 1700 km, which show significant thickening due to thermal diffusion or folding, such as the Cocos, Tonga and Kamchatka slabs; and 3) slabs that sink steeply into the lower mantle with very little deformation, reaching between $800-1000$ km depth, such as the Marianas, Antilles and Hellenic slabs [e.g., Li et al., 2008; Fukao & Obayashi, 2013]. Type 1 slabs are explained by plate buoyancy and trench motions [Christensen, 1996]. Type 2 slabs are thought to result from the slab accumulation at the mantle discontinuity that leads to 'slab avalanches' [Machetel & Weber, 1991; Tackley et al., 1993]. However, explaining Type 3 slabs is more complex because of their well-preserved tabular shape and vertical dip.

The experiments in this study reproduced almost all slab configurations imaged by tomography studies by changing only the mantle density contrast and mantle viscosity ratio (Figure 4). However, not all density contrasts and mantle viscosity ratios are viable in nature. In order for a slab to sink straight into the lower mantle without deforming and thickening, it requires a very low mantle density contrast and low viscosity ratio, which in turn would imply large and unrealistic lateral variations in mantle conditions. The results presented here show that the addition of a power-law component in the mantle rheology can induce similar geometries at higher and more realistic density contrasts.

Subduction is an intrinsically three-dimensional process that drives mantle flow around the slab, comprising a poloidal component (vertically oriented two-cell pattern, with one cell under the plate and the other in the mantle wedge, without mass transport around the slab [Schellart, 2008a; Li & Ribe, 2012]) and a toroidal component (mainly sub-horizontal and the flow occurs around the lateral edges of the slab [Kincaid & Griffiths, 2003; Schellart, 2004; Stegman et al., 2006; Schellart, 2008a; Strak & Schellart, 2014]). In this study, the experiments are 2D, prohibiting toroidal flow. Consequently, trench velocities in the experiments are expected to be reduced [Schellart et al., 2010; 2011], which leads to steeper slab dip angles [Griffiths et al., 1995; Schellart, 2004]. The 2D geometry also limits comparison of the experiments to subduction segments in nature located at the centre of wide subduction zones, which are significantly less impacted by the toroidal component of the subduction induced mantle flow [Schellart et al., 2007]. Thus, the experiments can only be interpreted as trench-perpendicular cross sections of areas such as the Honshu segment of the Kamchatka-Kuril-Honshu-Izu-Bonin-Mariana subduction zone or the southern Peru-northern Chile segment of the South America subduction zone.

Additionally, the geometry of the domain used is rectangular and very wide (~ 2900 km $\times$ ~ 7500 km) neglecting Earth's curvature. However, it is assumed that the effects of such geometry are not significant, since the focus of the study is on the region where the slab is sinking. The wide domain and long plate were adopted to minimise boundary effects and ensure continuity of subduction.

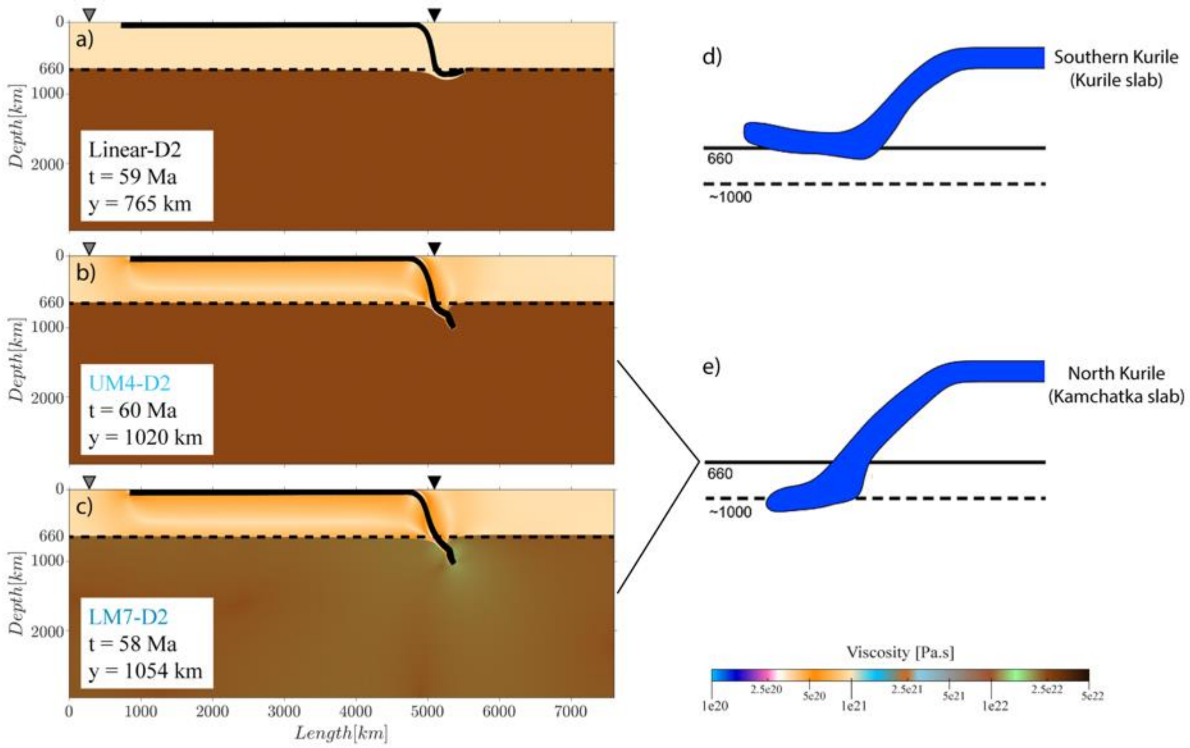

Figure 11. Viscosity field and slab geometry of experiments with $D_M = 2.5$ %, comparing linear and non-linear mantle viscosity at t~60 Ma. a) Linear case, b) upper mantle has a power-law component in the viscosity and c) both upper and lower mantle have a power-law component in the viscosity. The black colour of the plate is not included in the viscosity colour bar ($\eta_{sp} = 5 \times 10^{23}$ Pa s). The triangles indicate the initial position of the trench (black) and the plate trailing edge (grey). Dashed lines represent the 660 km depth mantle discontinuity. e-d) Sketches of slab configurations of Kurile (stagnant) and Kamchatka (penetrating ~1000 km depth) slabs [e.g., Li et al., 2008; Fukao & Obayashi, 2013], interpreted from tomography by Fukao & Obayashi [2013].

The following comparison of results with nature therefore focuses on slabs located at the centre of wide subduction zones that show a variation in geometry, such as the Kurile and Kamchatka slabs. The Kurile slab is stagnant at the bottom of the mantle transition zone and the Kamchatka slab penetrates into the lower mantle, reaching ~1000 km depth [Li et al., 2008; Fukao & Obayashi, 2013]. In Section 3, all experiments were presented at the same subduction stage, when half of the initial surface plate has sunk into the mantle. Thus, all snapshots show slabs at different depths and different at times after subduction initiation. In Figure 11, the experiments in which $D_M = 2.5$ %, Linear-D2, UM4-D2 and LM7-D2 are compared at t~60 Ma after subduction started with the slab geometries interpreted from tomography by Fukao & Obayashi [2013]. The slab in the Linear-D2 experiment (Figure 11a) is stagnant at ~660 km with a bulge that reaches a maximum depth of 765 km, matching the shape of the Kurile slab (Figure 11d). Whereas in the composite experiments (Figures 11b and 11c) the slab sinks through the mantle discontinuity with little deformation, reaching a depth of $1020 - 1054$ km, which matches the configuration of the Kamchatka slab (Figure 11e). The snapshots of two composite experiments differ by only 2 Ma and the slab tip depths vary by 34 km. The difference in depth is explained by the non-linear component in the lower mantle rheology, which enhances slab penetration and lessens slab deformation due to interaction with the mantle discontinuity.

Following continued subduction, the slabs in experiments Linear-D2, UM4-D2 and LM7-D2 develop a series of folds (Figure 8), which in Linear-D2 remain stagnant at the mantle discontinuity, and in the composite experiments (UM4-D2 and LM7-D2) sink deeper into the lower mantle. The future behaviour of the Kurile and the Kamchatka slabs may not include this folding behaviour, because variables such as plate age, composition and overriding plate characteristics also play an important role in the dynamics of subduction. However, the experiments show that a lateral change in the mantle rheology would be capable of controlling differences in slab geometry along an arc. Such lateral changes could be explained by variations in water distribution in the upper mantle as a consequence of past subduction events, which are reported under the western USA and China [e.g., Dixon et al., 2004; Hao et al., 2016], or variations in composition due to earlier formed mantle heterogeneity.

The apparent stagnation of some slabs may represent a transient stage that transitions to slab penetration over timescales of tens of millions of years [Mao et al., 2017]. Moreover, slabs that reach greater depths and have also thickened (Tonga, Kermandec, Cocos) might have started by sinking straight into the lower mantle without significant deformation and then thickened by slab folding in time.

It is proposed that the range of slab configurations observed in nature is partially a consequence of the activation of a power-law rheology (or dislocation creep) in both the upper and lower mantle. When slabs sink into the upper mantle with a trench motion $> 2 - 4$ cm/yr ($20 - 40$ km/Ma) [Christensen, 1996], they flatten along the mantle discontinuity, and therefore do not induce high enough stresses for the power-law component to be activated. However, when the trench motion is reduced and the slab is able to sink faster, due to higher plate velocity, the subduction induced stresses in the mantle are greater and the power-law component is activated, facilitating slab penetration into the lower mantle without slab deformation, or with reduced deformation. After penetration, the slab material accumulates by folding in the lower mantle, which continuously increases its negative buoyancy and promotes further slab sinking as a blob-like shape. Thus, the geometry of a slab depends firstly on the trench motion and secondly on the slab's ability to activate the power-law component in the mantle rheology, especially in the lower mantle.

5. Conclusions

The rheology of the mantle is an important parameter that controls the geometry of slabs and the evolution of subduction. The results presented here show that a lower transition strain rate in the upper mantle (considering a linear viscous lower mantle) leads to faster subduction, observed in terms of higher surface plate velocity. Conversely, power law viscosity parameters of the lower mantle seem to have a secondary effect, affecting mainly the shape of the subducting slab. Considering a composite rheology in the upper mantle only or in both upper and lower mantle, results in only a 4 Ma difference in the time for the subducting plate to reach a comparable state of consumption.

The density contrast between the upper and lower mantle controls the slab penetration mode, how deep the slab sinks, and how the mantle discontinuity deflects under the weight of the slab. The viscosity ratio between upper and lower mantle controls the number of folds of the slab that develop, which can also contribute to the slab penetration mode, provided enough material has accumulated in order to enhance negative buoyancy.

The results presented here also show that the implementation of a composite mantle rheology results in variations in slab geometry. A composite mantle rheology also affects how the mantle density contrast impacts how slabs interact with the mantle discontinuity. When the mantle rheology is composite, the slab penetrates the mantle discontinuity with very little deformation before developing folds.

A power-law component in to the mantle rheology also promotes a new subduction mode in which the slab penetrates the upper-lower mantle boundary without deforming, where it then accumulates by folding in the lower mantle. This mode is best developed when the lower mantle also has a composite rheology. The variations in slab geometries along arcs imaged by seismic tomography can be explained by lateral changes in the mantle rheology, which may be caused by lateral variations in water content or composition.

6. References

Agrusta, R., Goes, S. & van Hunen, J. (2017), Subducting-slab transition-zone interaction: Stagnation, penetration and mode switches. *Earth Planet. Sci. Lett.*, 464, 10-23, doi: 10.1016/j.epsl.2017.02.005.

Akaogi, M., Ito, E. & Navrotsky, A. (1989), Olivine-modified spinel-spinel transitions in the system Mg_2SiO_4-Fe_2SiO_4: calorimetric measurements, thermochemical calculation, and geophysical application. *J. Geophys. Res. Solid Earth*, 94(B11), 15671-15685, doi: 10.1029/JB094iB11p15671.

Anderson, D. L. (1967), Phase changes in the upper mantle. *Science*, 157(3793), 1165-73, doi: 10.1126/science.157.3793.1165.

Andrews, E. R. & Billen, M. I. (2009), Rheologic controls on the dynamics of slab detachment. *Tectonophysics*, 464(1-4), 60-69, doi: 10.1016/j.tecto.2007.09.004.

Ashby, M. F. (1972), A first report on deformation-mechanism maps. *Acta Metallurgica*, 20(7), 887-897, doi: 10.1016/0001-6160(72)90082-x.

Bellahsen, N., Faccenna, C. & Funiciello, F. (2005), Dynamics of subduction and plate motion in laboratory experiments: Insights into the "plate tectonics" behavior of the Earth. *J. Geophys. Res.*, 110(B1), B01401, doi: 10.1029/2004jb002999.

Billen, M. I. & Hirth, G. (2007), Rheologic controls on slab dynamics. *Geochem. Geophys. Geosyst.*, 8, Q08012, doi: 10.1029/2007gc001597.

Capitanio, F. A. & Faccenda, M. (2012), Complex mantle flow around heterogeneous subducting oceanic plates. *Earth Planet. Sci. Lett.*, 353-354, 29-37, doi: 10.1016/j.epsl.2012.07.042.

Capitanio, F. A., Faccenna, C., Zlotnik, S. & Stegman, D. R. (2011), Subduction dynamics and the origin of Andean orogeny and the Bolivian orocline. *Nature*, 480(7375), 83-6, doi: 10.1038/nature10596.

Capitanio, F. A., Morra, G. & Goes, S. (2007), Dynamic models of downgoing plate-buoyancy driven subduction: Subduction motions and energy dissipation. *Earth Planet. Sci. Lett.*, 262(1-2), 284-297, doi: 10.1016/j.epsl.2007.07.039.

Capitanio, F. A., Stegman, D. R., Moresi, L. N. & Sharples, W. (2010), Upper plate controls on deep subduction, trench migrations and deformations at convergent margins. *Tectonophysics*, 483(1-2), 80-92, doi: 10.1016/j.tecto.2009.08.020.

Christensen, U. R. (1996), The influence of trench migration on slab penetration into the lower mantle. *Earth Planet. Sci. Lett.*, 140(1-4), 27-39, doi: 10.1016/0012-821x(96)00023-4.

Čížková, H. & Bina, C. R. (2013), Effects of mantle and subduction-interface rheologies on slab stagnation and trench rollback. *Earth Planet. Sci. Lett.*, 379, 95-103, doi: 10.1016/j.epsl.2013.08.011.

Čížková, H., van Hunen, J. & van den Berg, A. (2007), Stress distribution within subducting slabs and their deformation in the transition zone. *Phys. Earth Planet. Int.*, 161(3-4), 202-214, doi: 10.1016/j.pepi.2007.02.002.

Conrad, C. P. & Lithgow-Bertelloni, C. (2002), How mantle slabs drive plate tectonics. *Science*, 298(5591), 207-209, doi: 10.1126/science.1074161.

Davies, G. F. & Richards, M. A. (1992), Mantle Convection. *Journal of Geology*, 100(2), 151-206, doi: 10.1086/629582.

Di Giuseppe, E., van Hunen, J., Funiciello, F., Faccenna, C. & Giardini, D. (2008), Slab stiffness control of trench motion: Insights from numerical models. *Geochem. Geophys. Geosyst.*, 9(2), Q02014, doi: 10.1029/2007gc001776.

Dixon, J. E., Dixon, T. H., Bell, D. R. & Malservisi, R. (2004), Lateral variation in upper mantle viscosity: role of water. *Earth Planet. Sci. Lett.*, 222(2), 451-467, doi: 10.1016/j.epsl.2004.03.022.

Elsasser, W. M. (1971), Sea-Floor Spreading as Thermal Convection. *J. Geophys. Res.*, 76(5), 1101-1112, doi: 10.1029/JB076i005p01101.

Enns, A., Becker, T. W. & Schmeling, H. (2005), The dynamics of subduction and trench migration for viscosity stratification. *Geophys. J. Int.*, 160(2), 761-775, doi: 10.1111/j.1365-246X.2005.02519.x.

Faccenda, M. & Capitanio, F. A. (2013), Seismic anisotropy around subduction zones: Insights from three-dimensional modeling of upper mantle deformation and SKS splitting calculations. *Geochem. Geophys. Geosyst.*, 14(1), 243-262, doi: 10.1029/2012gc004451.

Faccenna, C., Funiciello, F., Giardini, D. & Lucente, P. (2001), Episodic back-arc extension during restricted mantle convection in the Central Mediterranean. *Earth Planet. Sci. Lett.*, 187(1-2), 105-116, doi: 10.1016/S0012-821x(01)00280-1.

Ferreira, A. M. G., Faccenda, M., Sturgeon, W., Chang, S. J. & Schardong, L. (2019), Ubiquitous lower-mantle anisotropy beneath subduction zones. *Nat. Geosci.*, 12(4), 301, doi: 10.1038/s41561-019-0325-7.

Forsyth, D. & Uyeda, S. (1975), On the Relative Importance of the Driving Forces of Plate Motion. *Geophys. J. Int.*, 43(1), 163-200, doi: 10.1111/j.1365-246X.1975.tb00631.x.

Fukao, Y. & Obayashi, M. (2013), Subducted slabs stagnant above, penetrating through, and trapped below the 660 km discontinuity. *J. Geophys. Res. Solid Earth*, 118(11), 5920-5938, doi: 10.1002/2013jb010466.

Funiciello, F., Faccenna, C. & Giardini, D. (2004), Role of lateral mantle flow in the evolution of subduction systems: insights from laboratory experiments. *Geophys. J. Int.*, 157(3), 1393-1406, doi: 10.1111/j.1365-246X.2004.02313.x.

Funiciello, F., Moroni, M., Piromallo, C., Faccenna, C., Cenedese, A. & Bui, H. A. (2006), Mapping mantle flow during retreating subduction: Laboratory models analyzed by feature tracking. *J. Geophys. Res.*, 111, B03402, doi: 10.1029/2005jb003792.

Garel, F., Goes, S., Davies, D. R., Davies, J. H., Kramer, S. C. & Wilson, C. R. (2014), Interaction of subducted slabs with the mantle transition-zone: A regime diagram from 2-D thermo-mechanical models with a mobile trench and an overriding plate. *Geochem. Geophys. Geosyst.*, 15(5), 1739-1765, doi: 10.1002/2014gc005257.

Garnero, E. J. (2004), A new paradigm for Earth's core-mantle boundary. *Science*, 304(5672), 834-6, doi: 10.1126/science.1097849.

Griffiths, R. W., Hackney, R. I. & van der Hilst, R. D. (1995), A laboratory investigation of effects of trench migration on the descent of subducted slabs. *Earth Planet. Sci. Lett.*, 133(1-2), 1-17, doi: 10.1016/0012-821x(95)00027-a.

Guillou-Frottier, L., Buttles, J. & Olson, P. (1995), Laboratory Experiments on the Structure of Subducted Lithosphere. *Earth Planet. Sci. Lett.*, 133(1-2), 19-34, doi: 10.1016/0012-821x(95)00045-E.

Hao, Y. T., Xia, Q. K., Jia, Z. B., Zhao, Q. C., Li, P., Feng, M. & Liu, S. C. (2016), Regional heterogeneity in the water content of the Cenozoic lithospheric mantle of Eastern China. *J. Geophys. Res. Solid Earth*, 121(2), 517-537, doi: 10.1002/2015jb012105.

Holt, A. F. & Becker, T. W. (2017), The effect of a power-law mantle viscosity on trench retreat rate. *Geophys. J. Int.*, 208(1), 491-507, doi: 10.1093/gji/ggw392.

Holt, A. F., Becker, T. W. & Buffett, B. A. (2015), Trench migration and overriding plate stress in dynamic subduction models. *Geophys. J. Int.*, 201(1), 172-192, doi: 10.1093/gji/ggv011.

Houseman, G. A. & Gubbins, D. (1997), Deformation of subducted oceanic lithosphere. *Geophys. J. Int.*, 131(3), 535-551, doi: 10.1111/j.1365-246X.1997.tb06598.x.

Ita, J. & Stixrude, L. (1992), Petrology, Elasticity, and Composition of the Mantle Transition Zone. *J. Geophys. Res. Solid Earth*, 97(B5), 6849-6866, doi: 10.1029/92jb00068.

Ito, E. & Takahashi, E. (1989), Postspinel transformations in the system Mg_2SiO_4-$Fe_2SiO_4$and some geophysical implications. *J. Geophys. Res. Solid Earth*, 94(B8), 10637-10646, doi: 10.1029/JB094iB08p10637.

Karato, S. (2010), Rheology of the Earth's mantle: A historical review. *Gondwana Research*, 18(1), 17-45, doi: 10.1016/j.gr.2010.03.004.

Karato, S. & Wu, P. (1993), Rheology of the upper mantle: a synthesis. *Science*, 260, 771-778, doi: 10.1126/science.260.5109.771.

Katsura, T. & Ito, E. (1989), The system Mg_2SiO_4-Fe_2SiO_4 at high pressures and temperatures: Precise determination of stabilities of olivine, modified spinel, and spinel. *J. Geophys. Res. Solid Earth*, 94(B11), 15663-15670, doi: 10.1029/JB094iB11p15663.

Kincaid, C. & Griffiths, R. W. (2003), Laboratory models of the thermal evolution of the mantle during rollback subduction. *Nature*, 425(6953), 58-62, doi: 10.1038/nature01923.

Kincaid, C. & Olson, P. (1987), An Experimental Study of Subduction and Slab Migration. *J. Geophys. Res.*, 92(B13), 13832-13840, doi: 10.1029/JB092iB13p13832.

Király, Á., Capitanio, F. A., Funiciello, F. & Faccenna, C. (2017), Subduction induced mantle flow: Length-scales and orientation of the toroidal cell. *Earth Planet. Sci. Lett.*, 479, 284-297, doi: 10.1016/j.epsl.2017.09.017.

Lallemand, S., Heuret, A. & Boutelier, D. (2005), On the relationships between slab dip, back-arc stress, upper plate absolute motion, and crustal nature in subduction zones. *Geochem. Geophys. Geosyst.*, 6, Q09006, doi: 10.1029/2005gc000917.

Lay, T., Williams, Q. & Garnero, E. J. (1998), The core–mantle boundary layer and deep Earth dynamics. *Nature*, 392(6675), 461-468, doi: 10.1038/33083.

Lee, C. & King, S. D. (2011), Dynamic buckling of subducting slabs reconciles geological and geophysical observations. *Earth Planet. Sci. Lett.*, 312(3-4), 360-370, doi: 10.1016/j.epsl.2011.10.033.

Li, C., van der Hilst, R. D., Engdahl, E. R. & Burdick, S. (2008), A new global model for P wave speed variations in Earth's mantle. *Geochem. Geophys. Geosyst.*, 9(5), Q05018, doi: 10.1029/2007gc001806.

Li, Z. H. & Ribe, N. M. (2012), Dynamics of free subduction from 3-D boundary element modeling. *J. Geophys. Res.*, 117, B06408, doi: 10.1029/2012jb009165.

Machetel, P. & Weber, P. (1991), Intermittent layered convection in a model mantle with an endothermic phase change at 670 km. *Nature*, 350(6313), 55-57, doi: 10.1038/350055a0.

Mao, X., Gurnis, M. & May, D. A. (2017), Subduction Initiation With Vertical Lithospheric Heterogeneities and New Fault Formation. *Geophys. Res. Lett.*, 44(22), 11,349-11,356, doi: 10.1002/2017gl075389.

McNamara, A. K., Karato, S.-I. & van Keken, P. E. (2001), Localization of dislocation creep in the lower mantle: implications for the origin of seismic anisotropy. *Earth Planet. Sci. Lett.*, 191(1-2), 85-99, doi: 10.1016/s0012-821x(01)00405-8.

Meyer, C. & Schellart, W. P. (2013), Three-dimensional dynamic models of subducting plate-overriding plate-upper mantle interaction. *J. Geophys. Res. Solid Earth*, 118(2), 775-790, doi: 10.1002/jgrb.50078.

Mitrovica, J. X. & Forte, A. M. (1997), Radial profile of mantle viscosity: Results from the joint inversion of convection and postglacial rebound observables. *J. Geophys. Res. Solid Earth*, 102(B2), 2751-2769, doi: 10.1029/96jb03175.

Molnar, P. & Atwater, T. (1978), Interarc spreading and Cordilleran tectonics as alternates related to the age of subducted oceanic lithosphere. *Earth Planet. Sci. Lett.*, 41(3), 330-340, doi: 10.1016/0012-821x(78)90187-5.

Moresi, L., Dufour, F. & Mühlhaus, H. B. (2003), A Lagrangian integration point finite element method for large deformation modeling of viscoelastic geomaterials. *J. Comput. Phys.*, 184(2), 476-497, doi: 10.1016/S0021-9991(02)00031-1.

Moresi, L., Quenette, S., Lemiale, V., Mériaux, C., Appelbe, B. & Mühlhaus, H. B. (2007), Computational approaches to studying non-linear dynamics of the crust and mantle. *Phys. Earth Planet. Inter.*, 163(1-4), 69-82, doi: 10.1016/j.pepi.2007.06.009.

Olbertz, D., Wortel, M. J. R. & Hansen, U. (1997), Trench migration and subduction zone geometry. *Geophys. Res. Lett.*, 24(3), 221-224, doi: 10.1029/96gl03971.

OzBench, M., Regenauer-Lieb, K., Stegman, D. R., Morra, G., Farrington, R., Hale, A., May, D. A., Freeman, J., Bourgouin, L., Mühlhaus, H. & Moresi, L. (2008), A model comparison study of large-scale mantle-lithosphere dynamics driven by subduction. *Phys. Earth Planet. Inter.*, 171(1-4), 224-234, doi: 10.1016/j.pepi.2008.08.011.

Quinquis, M. E. T., Buiter, S. J. H. & Ellis, S. (2011), The role of boundary conditions in numerical models of subduction zone dynamics. *Tectonophysics*, 497(1-4), 57-70, doi: 10.1016/j.tecto.2010.11.001.

Quinteros, J., Sobolev, S. V. & Popov, A. A. (2010), Viscosity in transition zone and lower mantle: Implications for slab penetration. *Geophys. Res. Lett.*, 37, L09307, doi: 10.1029/2010gl043140.

Ribe, N. M. (2010), Bending mechanics and mode selection in free subduction: a thin-sheet analysis. *Geophys. J. Int.*, 180(2), 559-576, doi: 10.1111/j.1365-246X.2009.04460.x.

Schellart, W. P. (2004), Kinematics of subduction and subduction-induced flow in the upper mantle. *J. Geophys. Res.*, 109, B07401, doi: 10.1029/2004jb002970.

Schellart, W. P. (2005), Influence of the subducting plate velocity on the geometry of the slab and migration of the subduction hinge. *Earth Planet. Sci. Lett.*, 231(3-4), 197-219, doi: 10.1016/j.epsl.2004.12.019.

Schellart, W. P. (2008a), Kinematics and flow patterns in deep mantle and upper mantle subduction models: Influence of the mantle depth and slab to mantle viscosity ratio. *Geochem. Geophys. Geosyst.*, 9, Q03014, doi: 10.1029/2007gc001656.

Schellart, W. P. (2008b), Overriding plate shortening and extension above subduction zones: A parametric study to explain formation of the Andes Mountains. *Geol. Soc. Am. Bull.*, 120(11-12), 1441-1454, doi: 10.1130/B26360.1.

Schellart, W. P. (2017a), Andean mountain building and magmatic arc migration driven by subduction-induced whole mantle flow. *Nat. Commun.*, 8(1), 2010, doi: 10.1038/s41467-017-01847-z.

Schellart, W. P. (2017b), A geodynamic model of subduction evolution and slab detachment to explain Australian plate acceleration and deceleration during the latest Cretaceous–early Cenozoic. *Lithosphere*, 9(6), 976-986, doi: 10.1130/l675.1.

Schellart, W. P., Freeman, J., Stegman, D. R., Moresi, L. & May, D. (2007), Evolution and diversity of subduction zones controlled by slab width. *Nature*, 446(7133), 308-311, doi: 10.1038/nature05615.

Schellart, W. P., Stegman, D. R., Farrington, R. J., Freeman, J. & Moresi, L. (2010), Cenozoic tectonics of western North America controlled by evolving width of Farallon slab. *Science*, 329(5989), 316-9, doi: 10.1126/science.1190366.

Schellart, W. P., Stegman, D. R., Farrington, R. J. & Moresi, L. (2011), Influence of lateral slab edge distance on plate velocity, trench velocity, and subduction partitioning. *J. Geophys. Res.*, 116, B10408, doi: 10.1029/2011jb008535.

Schellart, W. P., Stegman, D. R. & Freeman, J. (2008), Global trench migration velocities and slab migration induced upper mantle volume fluxes: Constraints to find an Earth reference frame based on minimizing viscous dissipation. *Earth Sci. Rev.*, 88(1-2), 118-144, doi: 10.1016/j.earscirev.2008.01.005.

Shearer, P. M. (1990), Seismic imaging of upper-mantle structure with new evidence for a 520-km discontinuity. *Nature*, 344(6262), 121-126, doi: 10.1038/344121a0.

Shearer, P. M. & Masters, T. G. (1992), Global Mapping of Topography on the 660-Km Discontinuity. *Nature*, 355(6363), 791-796, doi: 10.1038/355791a0.

Silver, P. G., Carlson, R. W. & Olson, P. (1988), Deep slabs, geochemical heterogeneity, and the large-scale structure of mantle convection: investigation of an enduring paradox. *Annu. Rev. Earth Planet Sci.*, 16(1), 477-541, doi: 10.1146/annurev.ea.16.050188.002401.

Stegman, D. R., Freeman, J., Schellart, W. P., Moresi, L. & May, D. (2006), Influence of trench width on subduction hinge retreat rates in 3-D models of slab rollback. *Geochem. Geophys. Geosyst.*, 7, Q03012, doi: 10.1029/2005gc001056.

Stegman, D. R., Schellart, W. P. & Freeman, J. (2010), Competing influences of plate width and far-field boundary conditions on trench migration and morphology of subducted slabs in the upper mantle. *Tectonophysics*, 483(1-2), 46-57, doi: 10.1016/j.tecto.2009.08.026.

Strak, V. & Schellart, W. P. (2014), Evolution of 3-D subduction-induced mantle flow around lateral slab edges in analogue models of free subduction analysed by stereoscopic particle image velocimetry technique. *Earth Planet. Sci. Lett.*, 403, 368-379, doi: 10.1016/j.epsl.2014.07.007.

Tackley, P. J., Stevenson, D. J., Glatzmaier, G. A. & Schubert, G. (1993), Effects of an endothermic phase transition at 670 km depth in a spherical model of convection in the Earth's mantle. *Nature*, 361(6414), 699-704, doi: 10.1038/361699a0.

Turcotte, D. L. & Schubert, G. (2014) *Geodynamics*. Cambridge: Cambridge University Press. doi: 10.1017/CBO9780511843877

Vidale, J. E., Ding, X.-Y. & Grand, S. P. (1995), The 410-km-depth discontinuity: A sharpness estimate from near-critical reflections. *Geophys. Res. Lett.*, 22(19), 2557-2560, doi: 10.1029/95gl02663.

Wada, I. & King, S. (2015) Dynamics of Subducting Slabs: Numerical Modeling and Constraints from Seismology, Geoid, Topography, Geochemistry, and Petrology, *Treatise on Geophysics (Second Edition)*, 339-391. doi: 10.1016/B978-0-444-53802-4.00132-9

Yamato, P., Husson, L., Braun, J., Loiselet, C. & Thieulot, C. (2009), Influence of surrounding plates on 3D subduction dynamics. *Geophys. Res. Lett.*, 36(7), L07303, doi: 10.1029/2008gl036942.

Chapter 3

Appendices

Appendix I – Figure A1

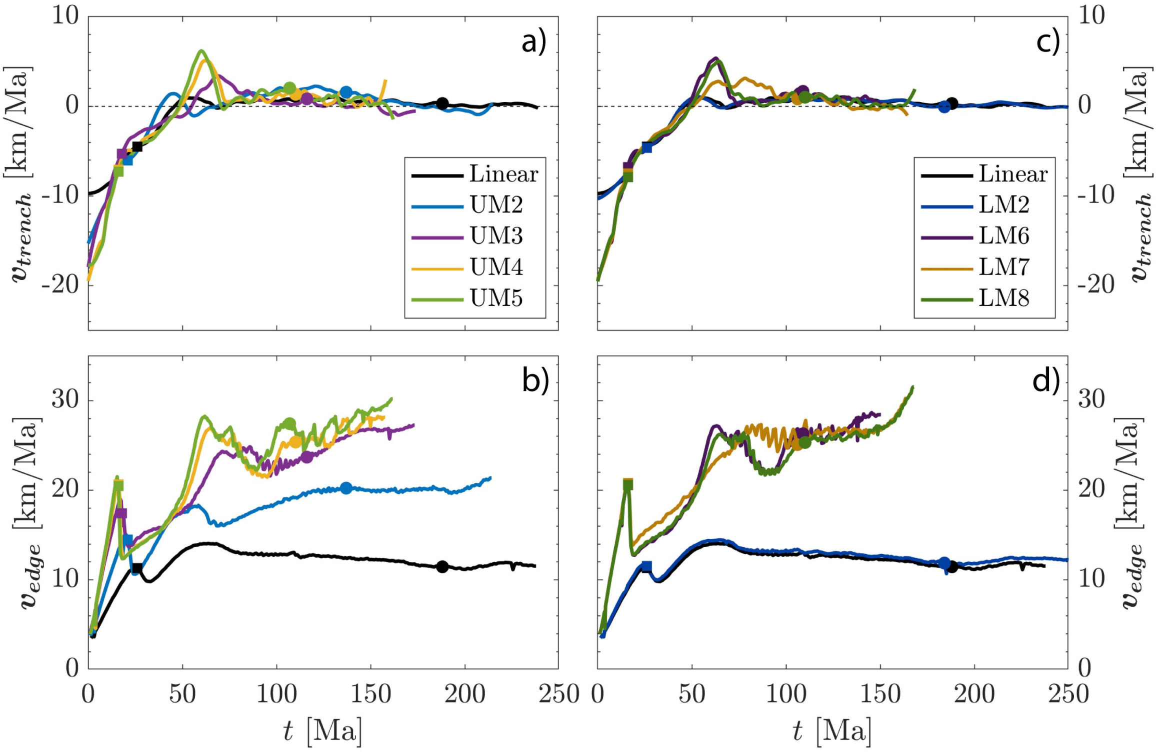

Figure A1. Trench velocity v_{trench} over time for a) UM experiments and b) LM experiments and trailing plate edge velocity v_{edge} over time for b) UM experiment and d) LM experiments. Squares refer to the time at which the slab tip reaches a depth of 660 km and circles refer to the times at which the plate consumption is C_{Plate}~50 %.

Appendix II – Figure A2

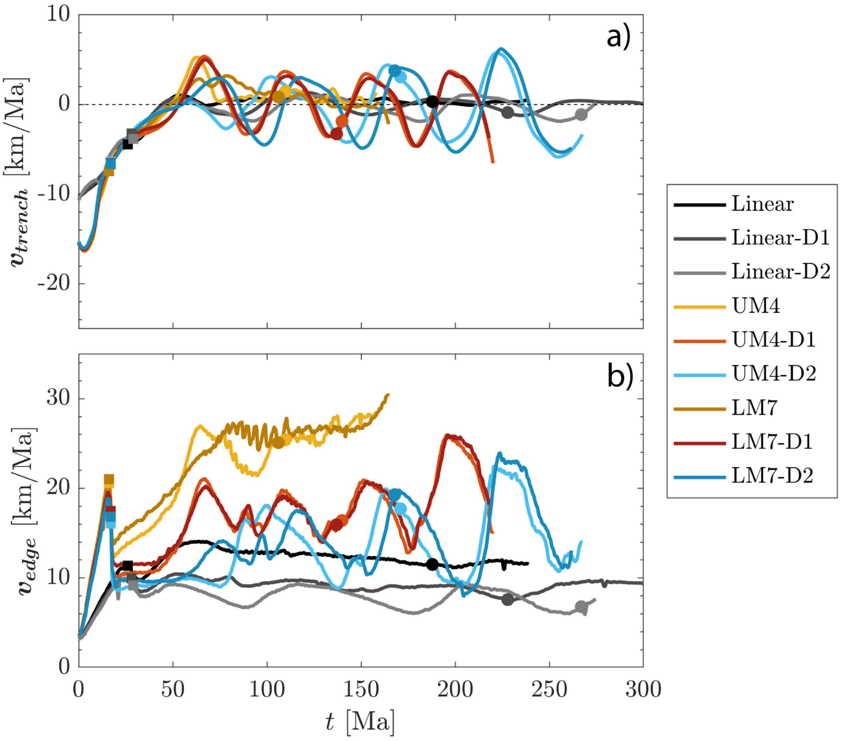

Figure A2. a) Trench velocity and b) trailing edge velocity against time for the experiments varying the mantle density contrast, comparing linear and non-linear mantle viscosity. Squares refer to the time at which the slab tip reaches a depth of 660 km and circles refer to the times at which the plate consumption is C_{Plate}~50 %.

Appendix III – Digital content

The digital appendix for Chapter 3 includes three movie clips:

- **Movie 1**: time evolution of experiments Linear, UM4 and LM7, in which $D_M = 0.78$ %, from 0 to ~160 Ma (duration 8 s).
- **Movie 2**: time evolution of experiments Linear-DC1, UM4-DC1 and LM7-DC1, in which $D_M = 1.6$ %, from 0 to 260 Ma (duration 13 s).
- **Movie 3**: time evolution of experiments Linear-DC2, UM4-DC2 and LM7-DC2, in which $D_M = 2.5$ %, from 0 to 270 Ma (duration 13 s).

The movie clips can be found at https://monash.figshare.com/s/a98d5185ab76deb1f639.

Chapter 4

Entrainment of upper mantle by subducted slabs

Cover image: The geometry of a slab in an experiment in which both upper and lower mantle have a composite rheology, and the viscosity ratio between upper and lower mantle is initially 50. The background colours reflect variations in the viscosity field ~ 200 Ma after subduction initiation.

Abstract

Mantle plumes transport heat from the bottom of the mantle towards the surface and subducting plates bring cold material to depth. Plumes are responsible for bringing previously subducted material back to the surface, entraining heterogeneous components of different mantle sources during their ascent. These sources are revealed by radiogenic isotope studies of young basalts derived by partial melting of the mantle. The composition of the isotopically enriched components of Ocean Island Basalts (OIB) are globally diverse. However, it is not known if the material recycled by mantle plumes originates exclusively from the subducted lithosphere. This study explores a potential extra source that originates by dragging upper mantle material by subducting slabs to depths well below the mantle transition zone. Two dimensional numerical models of subduction are used to quantify the contribution of a subducting slab to entrainment of upper mantle material into the deep lower mantle. Different scenarios are tested by varying the upper-lower mantle density contrast and by including a power-law component in the mantle rheology. Results show that as the slab subducts it folds on itself and part of the upper mantle becomes trapped inside 'slab pockets'. It is proposed that variations in the volume of upper mantle trapped by folding subducting slabs can help explaining the global diversity of OIB. If dehydration melting of both serpentinites and pelagic sediments produces ambient reaction zone pyroxenites inside the slab pockets during subduction, these may represent the main part, if not the entire part, of the enriched components in OIB.

Keywords: subduction, geodynamics, numerical modelling, non-linear rheology, recycling of subducted components

1. Introduction

Heat transfer inside Earth occurs dominantly through convection, as manifested by downwellings and upwellings between the base of the lower mantle and the surface. Mantle convection is primarily driven by the negative buoyancy of subducting plates, which is also the primary driving force of plate tectonics, [e.g., Forsyth & Uyeda, 1975; Davies & Richards, 1992; Conrad & Lithgow-Bertelloni, 2002]. Subduction is the process by which oceanic lithosphere is recycled. The oceanic lithosphere comprises the oceanic crust and the oceanic lithospheric mantle. Oceanic crust is ~7 km thick and composed of three layers: 1) deep sea and continental sediments; 2) underlying basaltic pillow lavas and sheeted dikes of predominantly basaltic composition; and 3) layered cumulate gabbro, all of which to a large degree are hydrated during serpentinisation [Dilek et al., 1998]. The oceanic lithospheric mantle corresponds to the uppermost non-convecting part of the upper mantle, comprising partly melt-depleted harzburgite.

Seismic tomography imaging provides observations of present-day subducting slabs, which show variable geometric configurations at the mantle transition zone (MTZ) [e.g., Fukao & Obayashi, 2013]. While some slabs penetrate into the lower mantle with little to no deformation (e.g., Marianas, Northern Kurile and Cocos slabs), others stagnate at the 660 km mantle discontinuity (e.g., Izu-Bonin, Southern Kurile and Calabria slabs). Furthermore, some slabs appear to be temporarily stalled either above or below the mantle discontinuity, penetrating partially into the lower mantle (e.g., Tonga and Kermadec slabs) [e.g. Kincaid & Olson, 1987; Christensen, 1996; Olbertz et al., 1997]. Slabs configuration depends on multiple processes that affect the relative strength of plates such as yielding, grain size reduction and changes in water content. However, the proclivity of a slab to enter the lower mantle seems to be dominantly determined by the trench motion, which is required to be almost stationary in order to promote slab penetration [e.g., Kincaid & Olson, 1987; Enns et al., 2005; Čížková et al., 2007].

The mode of slab-mantle discontinuity interaction may shift from penetrating to stagnant or vice-versa. This shift can occur as a result of changes in the kinematics of trench migration. The ageing of the subducting plate or a decrease in the overriding plate forcing can easily lead to the stagnation of penetrating slabs [Guillou-Frottier et al., 1995; Christensen, 1996]. Conversely, a stagnant slab can start penetrating into the lower mantle if a large-scale plate reorganisation induces strong changes in the overriding plate forcing applied to the trench [Agrusta et al., 2017]. Thus, subducted lithosphere is capable of sinking deeply and potentially reach the core mantle boundary (CMB), either if a slab has already penetrated into the lower mantle or if there is a change of mode in the stagnated slab.

The bottom ~200 km of the lower mantle, just above the CMB, referred to as the D'' layer, is highly heterogeneous [e.g., Lay et al., 1998; Garnero, 2004]. This tomographically imaged region [Courtillot et al., 2003] is typically associated with the origin of long-term mantle plumes [Morgan, 1971] (e.g., sourcing the Hawaiian Islands). Mantle plumes are considered to entrain heterogeneous components of crustal origin during their ascent [Hoffmann, 2014; Hofmann & White, 1982]. However, the timescales for recycled plume recycled components to reach the surface have varied vary from the Archean [Cabral et al., 2013; Nebel et al., 2013; Delavault et al., 2016] to the Phanerozoic [Sobolev et al., 2011].

Radiogenic isotope studies of young basalts derived from the mantle reveal the presence of diverse mantle sources within single plume localities [Hart et al., 1992l; Hofmann, 1997]. The isotopic composition of these mantle sources is often grouped into four end-member categories [Hart et al., 1992; White, 2010; Hoffmann, 2014]: 1) High U/Pb mantle (HIMU), a rare mantle source associated with a mixture of subducted oceanic crust and ambient upper mantle, predominantly found at St. Helena and the Cook-Austral Islands; 2) Enriched mantle I (EM-I), the most common component, associated with either recycled old oceanic mantle lithosphere or sediments; 3) Enriched mantle II (EMU-II), associated with subducted sediments derived from upper continental crust; and 4) The focal zone (FOZO), which is common to all ocean island basalts (OIB) [Hart et al., 1992; White, 2010; Hoffmann, 2014], and possibly represents the plume matrix [Stracke et al., 2005; Jackson et al., 2014] associated with material that has ascended from the CMB. A potential fifth component is the depleted upper mantle (DM), associated with a mid-ocean ridge basalt (MORB) isotopic signature. This component has also been identified in plumes with high volume fluxes (e.g., Hawaii and Samoa), and is referred to as rejuvenated melt [DeFelice et al., 2019].

Plumes originating from the lowermost mantle entrain ambient material, some of which have a crustal isotopic character [Hart et al., 1992; Hauri et al., 1994; Farnetani & Hofmann, 2009]. Moreover, the isotopic character of these components is diverse, and can vary spatially along a double volcanic chain, as demonstrated by Hawaii [Abouchami et al., 2005; Weis et al., 2011]. Although the petrological nature of these components remains unclear, they are either composed of peridotite, including subducted oceanic crust [Niu et al., 2011; Matzen et al., 2017], or the reaction products of melts derived thereof with ambient peridotite – pyroxenites [Sobolev et al., 2005; Herzberg, 2011]. The latter case implies that pyroxenites could form during subduction and be transported to depth, mixing with deeper plume sources. It may therefore unnecessary to invoke the ascent of dense eclogite in rising plumes to explain the ocean island basalts (OIB) isotopic compositions. However, this scenario requires a mechanism to transport sections of soft buoyant upper mantle into the deep Earth.

While it is clear from seismic tomography that slabs sink deep into the lower mantle, potentially reaching the CMB, one question remains: is the deep subducted material composed exclusively of oceanic lithosphere, or is upper mantle material also dragged to depth by the slab? This study addresses this question by quantifying the volume of upper mantle material that can be potentially entrained by a sinking slab and dragged into the deep lower mantle. The entrainment of upper mantle material is quantified under different upper-lower mantle density contrast scenarios. A comparison is also made between cases where the mantle is linear viscous (i.e., the deformation in the mantle occurs only through diffusion creep) and where there is a power-law component in the mantle rheology (i.e., the deformation in the mantle occurs by dislocation creep).

2. Methods

Numerical experiments of dynamic and isothermal subduction were built and executed in a 2D Cartesian geometry using the code Underworld2[1] [e.g., Moresi et al., 2003; Moresi et al., 2007]. The experiments follow the same model setup and parameters described in Chapter 3. Each experiment starts with a single linear viscous oceanic plate, composed of a thin crust and its underlying and non-convecting lithospheric mantle, lying on top of a two-layer mantle without pre-existing mantle convection. The plate has an initially kinked tip dipping into the mantle. This initial slab acts as the instability that starts subduction, which is solely driven and maintained by the plate-mantle density contrast.

The viscosity of both upper and lower mantle is defined as either 1) linear viscous, or 2) with a power-law component. In case 1), the mantle viscosity is constant. In case 2), the viscosity is stress-dependent, the power-law component is activated by the high stresses the subducting slab induces on the surrounding mantle, which results in an effective lowering of the mantle viscosity in the vicinity of the plate and slab. The power-law component is computed by imposing a limit on the strain rate using an approach that has been previously implemented [e.g., Capitanio & Faccenda, 2012; Holt & Becker, 2017; Király et al., 2017]:

$$\eta_p = \eta_0 \left(\frac{\dot{\varepsilon}_{II}}{\dot{\varepsilon}_{II}^T}\right)^{\frac{1-n}{n}}, \tag{1}$$

where η_p is the power-law viscosity, η_0 is the linear reference viscosity, $\dot{\varepsilon}_{II}$ is the second

[1] http://www.underworldcode.org/

invariant of the strain rate, $\dot{\varepsilon}_{II}^{T}$ is the transition strain rate (i.e., the second invariant of strain rate at which the power-law viscosity is equal to the linear viscosity), and n is the power-law exponent. In this approach, the number of parameters to evaluate is reduced to only two: the power-law exponent, which is material dependent, and the transition strain rate. The composite viscosity is the harmonic average between the linear reference viscosity and a stress-dependent component in the mantle viscosity, also referred to as power-law. The upper mantle material entrainment is evaluated for three cases: 1) both upper and lower mantle are linear viscous; 2) the upper mantle rheology is composite and the lower mantle is linear viscous; and 3) both upper and lower mantle rheology are composite. Based on the results of Chapter 3, in the upper mantle $\dot{\varepsilon}_{II}^{T} = 3 \times 10^{-13}$ s^{-1}, $n = 3.5$, and in the lower mantle $\dot{\varepsilon}_{II}^{T} = 5 \times 10^{-12}$ s^{-1}, $n = 1.5$.

The density contrast between upper and lower mantle (hereinafter ‘mantle density contrast’) is defined as:

$$D_M = \frac{\Delta\rho_M}{\rho_{UM}} = \frac{\rho_{LM} - \rho_{UM}}{\rho_{UM}}, \tag{2}$$

where $\Delta\rho_M = \rho_{LM} - \rho_{UM}$ is the density contrast between upper and lower mantle, ρ_{UM} is the density of the upper mantle and ρ_{LM} is the density of the lower mantle. Additionally, three values of D_M were tested (0.78 %, 1.6 % and 2.5%) by increasing the density of the lower mantle and keeping the density of the upper mantle constant. A total of nine experiments are presented and discussed in this study.

3. Results

3.1. Subducted plate geometry

Depending on the mantle density contrast, three different types of interaction between slab and mantle discontinuity are observed. If $D_M = 0.78$ % (Figures 1a-c), the slab penetrates the mantle discontinuity and the folded slab tip reaches deep into the lower mantle. If $D_M = 1.6$ % (Figures 1d-f), the slab penetrates the mantle discontinuity whilst folding continuously and the slab tip takes longer to reach deep into the lower mantle. If $D_M = 2.5$ % (Figures 1g-i), the slab folds continuously at the mantle discontinuity, accumulating sub-horizontally.

During the first $\sim$50 Ma of subduction, the shape the slab acquires depends only on the mantle rheology condition. If the mantle is linear viscous (left panels in Figures 1a, 1d and 1g) the slab tip deflects horizontally upon interaction with the mantle discontinuity. If the viscosity of the mantle is composite, the slab penetrates into the lower mantle with little to no deformation, reaching a greater depth for lower mantle density contrast.

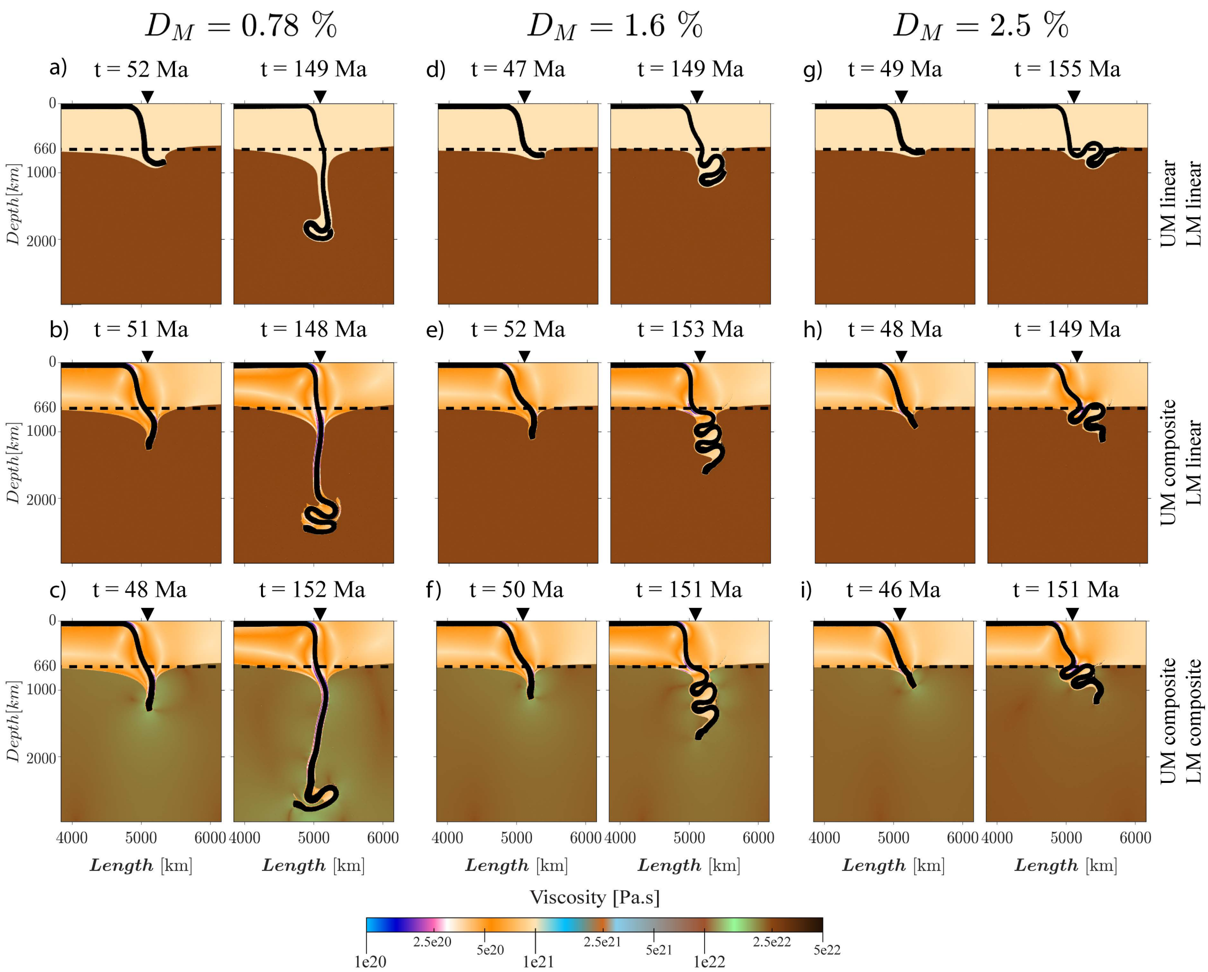

Figure 1. Viscosity field and slab geometry configuration of experiments at $t{\sim}50$ Ma and $t{\sim}150$ Ma. a-c) $D_M = 0.78$ %, d-f) $D_M = 1.6$ %, g-i) $D_M = 2.5$ %. The mantle is linear viscous in the top row panels, only the upper mantle is composite in the middle row panels and both the upper and lower mantle are composite in the bottom row panels. Time is indicated above each snapshot and the inverted triangles indicate the initial position of the trench. The dashed lines represent mantle discontinuity at 660 km depth. The black colour of the plate is not included in the viscosity colour bar ($\eta_{sp} = 5 \times 10^{23}$ Pa.s). Only the area of the domain around the subducting slab is shown in the panels.

About 150 Ma into subduction, the effects of the mantle rheology condition on the shape of the slab are weaker. At $D_M \geq 1.6$ %, (right panels in Figures 1d-i), the slab develops more folds trapping upper mantle material in between the fold limbs. The composite viscosity in the mantle allows the slab to sink deeper. When $D_M = 2.5$ % (right panels in Figures 1h and 1i), the slab folds and accumulates just below the mantle discontinuity. However, in all experiments, irrespective of the mantle conditions, the slab develops recumbent folds with pinched limbs, as it sinks forming pockets of trapped upper mantle material that are ultimately entrained into the lower mantle. The pockets developed above the top surface of the slab trap less upper mantle material than pockets below the bottom of the slab surface because the more buoyant upper mantle material escapes upwards through gaps between fold limbs.

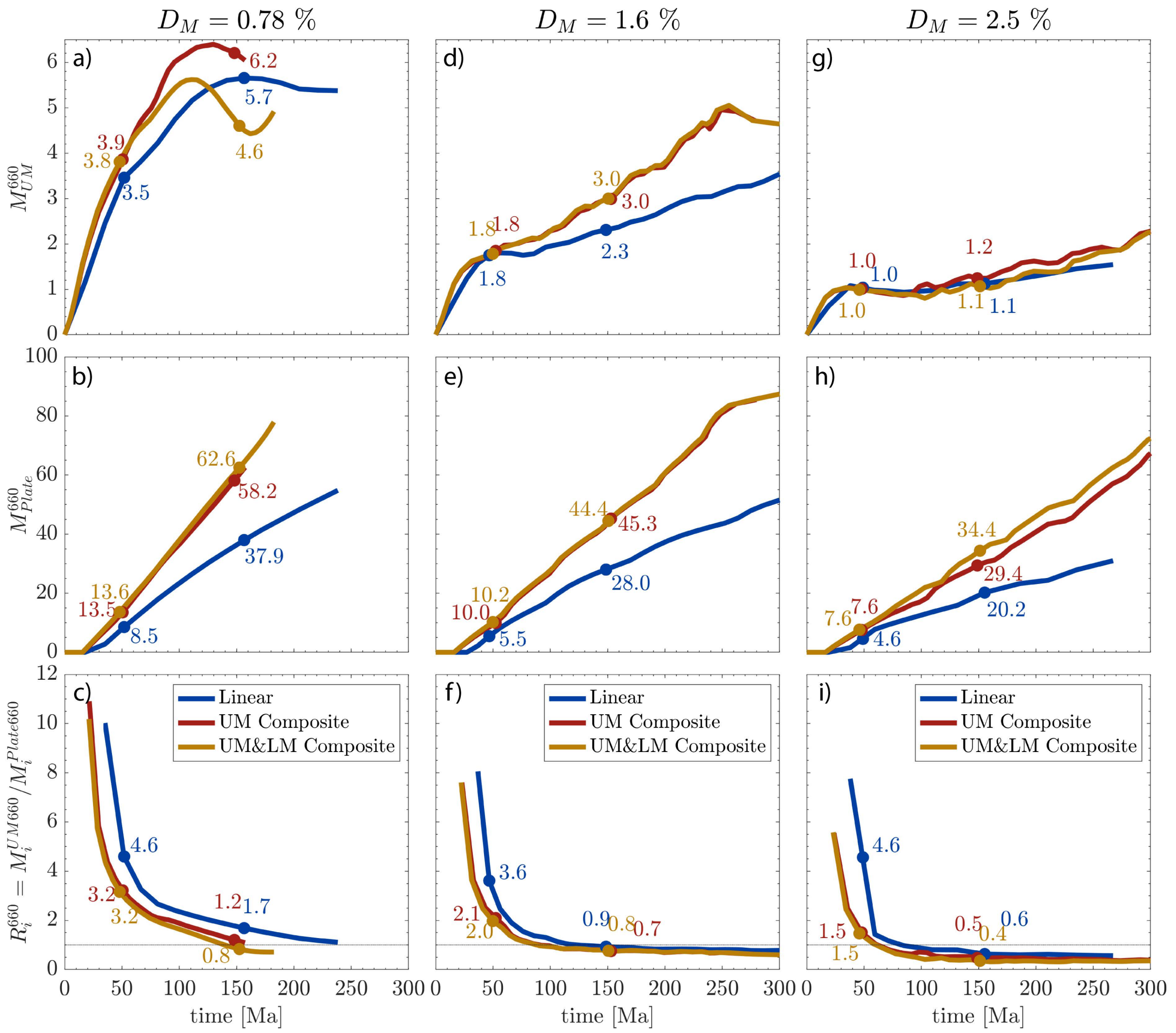

Figure 2. Plate and upper mantle entrainment into the lower mantle over time. Percentage of material that has sunk below 660 km depth of a-c) Upper mantle – M_{UM}^{660}, and d-f) Plate – M_{Plate}^{660}. g-i) ratio between the surface area of upper mantle at a given time below 660 km depth and the surface area of plate at the same time below the same depth – R_i^{660}. Circles indicate the times presented in the snapshots of Figure 1, for each experiment, with the annotated value of the quantity represented in the y-axis.

3.2. Plate and upper mantle entrainment into the lower mantle

The surface area corresponding to the downgoing plate and upper mantle below 660 km depth were calculated over time, during the experiments. The surface area of plate material (considering both slab and surface plate) that has sunk below 660 km depth is calculated as $M_{Plate}^{660} = M_i^{Plate660}/M_{tot}^{Plate} \times 100$, where $M_i^{Plate660}$ is the surface area of plate material at a given time below that depth and M_{tot}^{Plate} is the total area of plate material inside of the domain. Similarly, the surface area of upper mantle material that has sunk below 660 km depth is $M_{UM}^{660} = M_i^{UM660}/M_{tot}^{UM} \times 100$. Similarly, the surface area of upper mantle material that has sunk below 660 km depth is $M_{UM}^{660} = M_i^{UM660}/M_{tot}^{UM} \times 100$. Both M_{Plate}^{660} and M_{UM}^{660} start at zero at the beginning of the experiments (Figure 2).

The downward motion of the slab induces poloidal flow [e.g., Kincaid & Griffiths, 2003; Schellart, 2004; Stegman et al., 2006; Li & Ribe, 2012] in the upper mantle, which displaces the mantle discontinuity vertically in front of and adjacent to where the slab tip is sinking. Consequently, parts of the upper mantle material sink below 660 km and the quantity M_{UM}^{660} increases from the beginning of the experiments (Figures 2a, 2d and 2g). When $D_M = 0.78$ % (Figure 2a), a maximum of M_{UM}^{660} is reached, indicating an upper limit on the amount of upper mantle material the slab can transport to depth. This maximum is lower and occurs later if the mantle is linear viscous, compared to the cases where the upper mantle is composite. When both the upper and lower mantle have a composite rheology, the ${M_{UM}^{660}}_{max}$ is the same as in the linear case, although it occurs ~ 50 Ma earlier. In the composite experiments, M_{UM}^{660} decreases because the upper mantle material around the slab is softened by the power-law rheology. Additionally, due to the positive buoyancy of the upper mantle relative to the lower mantle, a part of it rises back to depths above 660 km. When $D_M = 1.6$ % (Figure 2d), M_{UM}^{660} continually increases for 250 Ma, regardless of the mantle rheology conditions, because the slab continues to develop folds as it sinks deeper into the lower mantle, trapping upper mantle material in each recumbent fold.

When both the upper mantle and the lower mantle rheology is linear, the amount of upper mantle captured is lower, because subduction evolves slower and at $t \approx 50$ Ma the slab has only folded twice, whereas in the composite experiments in the same amount of time the slab folded around five times. Moreover, when $D_M = 2.5$ %, M_{UM}^{660} continually increases in comparable amount for 250 Ma, regardless of the mantle rheology conditions (Figure 2g).

In Figures 2b, 2e and 2h, after the time when slab first reaches 660 km (Table 1), M_{Plate}^{660} increases continuously and independently of the mantle density contrast. However, it increases more rapidly with lower D_M and in the composite experiments. The surface area of plate material is higher at low D_M since the plate negative buoyancy relative to the lower mantle is reduced, resulting in faster sinking of the slab. M_{Plate}^{660} is also higher in the composite rheology experiments because the viscosity of the mantle around the slab is reduced, facilitating faster slab sinking.

Table 1. Times at which the slab tip first reaches 660 km in Ma.

	$D_M = 0.78$ %	$D_M = 1.6$ %	$D_M = 2.5$ %
Linear	26	28	29
UM composite	16	17	17
UM & LM composite	16	17	17

The contribution of the upper mantle to the total surface area of material that sinks into the lower mantle is quantified by the ratio $R_i^{660} = M_i^{UM660}/M_i^{Plate660}$ (Figures 2c, 2f and 2i). Between the start of the experiments and the time when the slab tip sinks below 660 km, $R_i^{660} \to \infty$ and only upper mantle crosses the mantle discontinuity. Once the slab reaches 660 km, $R_i^{660} \sim 10$ when $D_M = 0.78$ % (Figure 2c), R_i^{660}~8 when $D_M = 1.6$ % (Figure 2f), and $R_i^{660} \sim 8$ (linear case) and ~ 6 (composite cases) when $D_M = 2.5$ % (Figure 2i). For low mantle density contrast, R_i^{660} starts at a higher value because the mantle discontinuity is more disturbed. After the slab impinges on the lower mantle, the mantle discontinuity is lowered over a wider lateral extent on both sides of the slab. All experiments show that as subduction evolves and the further the slab sinks across the mantle discontinuity, R_i^{660} decreases, tending to values between $0 - 1$.

When $R_i^{660} = 1$, the amount of plate material in the lower mantle equals the amount of upper mantle material, however the time at which this occurs depends not only on the mantle density contrast but also on the rheological conditions of the mantle. When $D_M = 0.78$ % (Figure 2c), the linear case and upper mantle composite rheology case do not reach $R_i^{660} = 1$ for the duration of the experiments. When both the upper and lower mantle have composite rheology, $R_i^{660} = 1$ occurs at 138 Ma since subduction evolves faster and the slab sinks deeper into the lower mantle in the same time interval. When $D_M = 1.6$ % (Figure 2f), $R_i^{660} = 1$ at ~ 121, ~ 92 and ~ 87 Ma for the linear, the upper mantle composite rheology and the both upper and lower mantle composite rheology experiments, respectively. When $D_M = 2.5$ % (Figure 2i), $R_i^{660} = 1$ at ~ 85, ~ 60 and ~ 58 Ma for the linear, upper mantle composite rheology and both upper and lower mantle composite rheology experiments, respectively. In these six experiments the slab folds while it sinks. Thus, more plate material accumulates in the lower mantle and the composite rheology facilitates faster and deeper subduction.

In summary, for low mantle density contrast more upper mantle is dragged to depths below the mantle transition zone during subduction. However, most of the upper mantle material is between $660 - 1000$ km because the mantle discontinuity is depressed around the slab. Only when $D_M = 1.6$ % is a greater amount of upper mantle material dragged to greater depths. In all experiments, R_i^{660} converges to values between 0 and 1, indicating that, as long as the slab penetrates the mantle discontinuity, even if only partially, a part of the upper mantle material is entrained into the lower mantle.

4. Discussion

The experiments presented here imply that part of the upper mantle material may be dragged by the subducting slab to lower mantle depths, independently of the mantle rheology or the mantle density contrast. The entrained upper mantle potentially represents an additional source of material that is brought back to surface by mantle plumes. Considering the simplifications of the experiments, the limitations of the results are discussed first, followed by their implications for mantle recycling processes.

4.1. Experimental limitations

The experiments were designed to focus on the mass transport of material across the 660 km mantle discontinuity and did not include thermal or mineral phase changes effects. Thermal diffusion in the mantle is inefficient [e.g., Kohlstedt & Mackwell, 1998] and the slab thermally equilibrates with the mantle on a time-scale of 100 million years or more. The timescale of the experiments (< 200 Ma) is therefore assumed to be short enough to neglect these thermal diffusion effects. Moreover, even if mineral phase changes occur, the isotopic signature of the entrained upper mantle material would be conserved, as phase changes are isochemical. The subducting plate was modelled as linear viscous and neglected plastic yielding, which, together with the upper mantle composite rheology, is likely to induce the separation between the sinking slab and the plate once the slab has stalled (i.e., slab detachment or break-off) [Andrews & Billen, 2009]. Despite the omission of plastic yielding of the slab, it is assumed that even if slab break-off occurred, subducted material would continue to sink deeper into the lower mantle due to its negative buoyancy, dragging entrained buoyant upper mantle material with it.

The experiments show a limited subduction style: the slab sinks initially almost vertically, develops folds as it sinks through the 660 km mantle discontinuity and exhibits overall reduced trench retreat rates. In nature, the catalogue of subduction styles is far more varied [Schellart, 2008; Schellart et al., 2008 (and references therein)]. However, the subduction style observed is comparable to subduction segments located at the centre of wide subduction zones, and the 2D experiments can be seen as trench-perpendicular cross sections of such areas (e.g., the Honshu segment of the Kamchatka-Kuril-Honshu-Izu-Bonin-Mariana subduction zone, or the southern Peru-northern Chile segment of the South America subduction zone).

The experiments demonstrate that during subduction more than just the oceanic lithosphere may sink into the lower mantle. Regardless of their limitations, the experiments show that subducting plates are capable of dragging parts of the upper mantle material into the lower mantle.

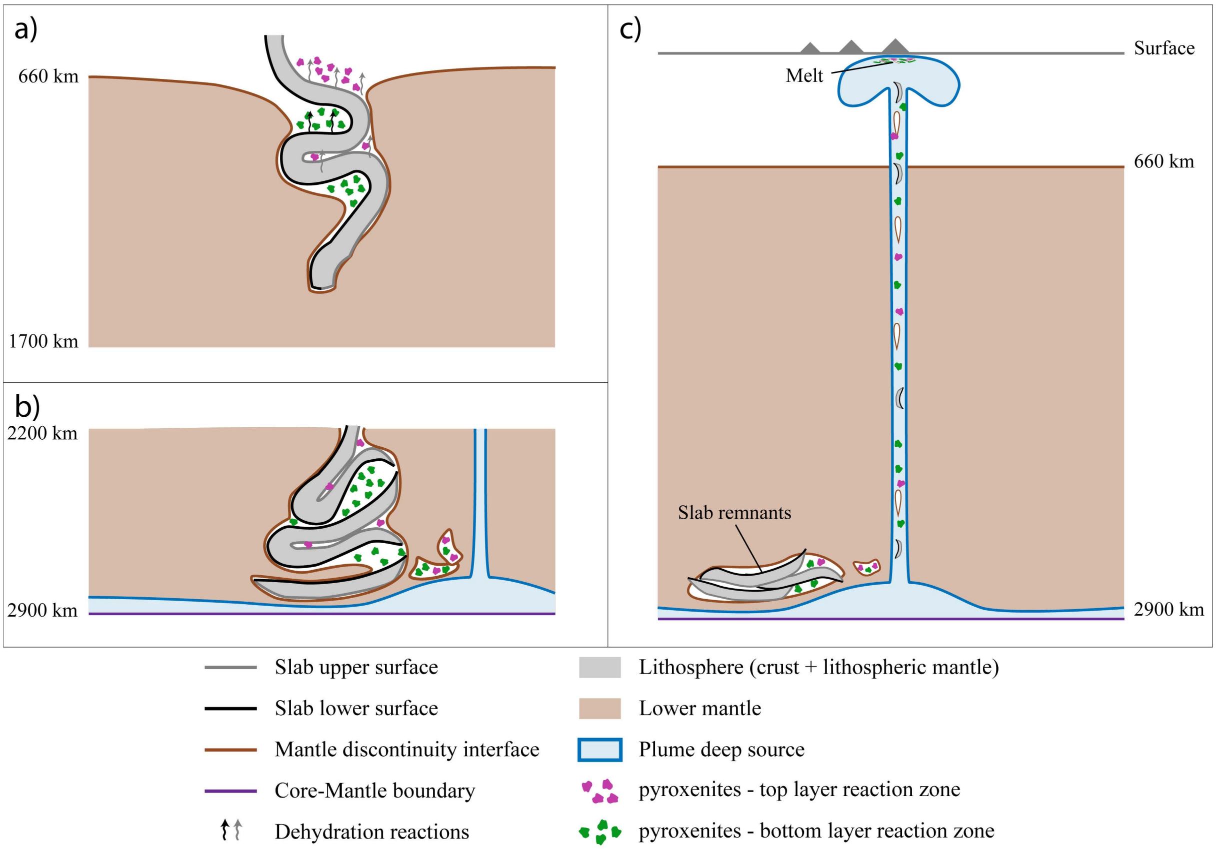

Figure 3. Conceptual model of the subducted upper mantle. a) the subducting slab penetrates through the upper-mantle discontinuity, trapping upper mantle material as it folds. b) the slab drags the upper mantle pockets to the core-mantle boundary, along with the dehydrations products (pyroxenites). c) a mantle plume entrains old subducted materials, which rise and melt once they are close to the surface.

4.2. Implications for mantle recycling

Intra-oceanic island lavas, such as the Hawaiian Islands, indicate that selective parts of the subducted lithosphere return to the surface via mantle plumes [Kendrick et al., 2011]. The predominantly enriched components in Hawaiian lavas are represented by EM-I, tentatively linked to either subducted sediments or lithospheric mantle, with all enriched components sharing a high volatile constituent [Kendrick et al., 2011].

Most dehydration reactions in the slab occur at depths < 200 depth, which fertilises the overlying mantle wedge and produces arc volcanism [Schmidt & Poli, 2014 (and references therein)]. However, water can be transported to lower-mantle depths within hydrous magnesium-silicate mineral phases [e.g., Ohtani et al., 2004]. Infusion of fluids into slabs may occur as a result of plate bending, which produces sub-hydrostatic (and even negative) pressure gradients [Faccenda et al., 2009]. Therefore, if subducting slabs are able to retain part of their hydrous cargo into the mantle transition zone and possibly beyond, serpentinised lithospheric mantle and sediments will be the likely reservoirs for EM-I precursors.

Slabs can lose up to 48 % of their water content by chemical diffusion while crossing the mantle transition zone over a transit time of 50 Ma [Richard et al., 2006]. In the numerical experiments reported here, the slab geometry exhibits segments of “inverted” lithosphere, in which the lithospheric mantle overlies the crust. Considering the fluid content of the slab preferably move upwards, these would transit through the subducted lithospheric mantle. It is therefore plausible for dehydration melting of both serpentinites and pelagic sediments to occur across these inverted sections, producing reaction zone pyroxenites within the slab folds (Figure 3a). Consequently, pyroxenite may become concentrated in the slab pockets that trap depleted upper mantle. As subduction proceeds, the slab will reach the CMB where depletes upper mantle material may leak into the adjacent lower mantle (Figure 3b). The leaked subducted material would then be available to be entrained into mantle plumes and ascend back to the surface. However, melting of pyroxenite and subsequent mixing with plume matrix will only occur shortly prior to eruption [Nebel et al., 2019](Figure 3c).

Entrainment of the various components of subducted material, either in the form of pyroxenites or eclogites will occur at the mantle plume source, which for plumes with high volume fluxes (e.g., Hawaii) is thought to be in the lowermost mantle [Courtillot et al., 2003]. The distribution of subduction-related components is random and seemingly isolated within the ascending plume matrix [Jackson et al., 2014]. Eclogite is much denser than pyroxenite, which has a mantle-like density. Thus, it is plausible that the initially entrained slab pockets, now converted to a certain degree to pyroxenite, represent the main part, if not the entire part, of the enriched components in OIB. At the same time, depleted parts of the lithosphere may have also been entrained by plumes. Trace element signatures of either pelagic sediment (low Ba/Th) or serpentinite derived melts can be expected to infused the depleted mantle surrounding the slab, creating a geochemical mirror image of subducted oceanic crust. This implies that the crustal component that returns to the surface is limited in volume. Thus, the global diversity of OIB may be explained by variations in volume of upper mantle material trapped in slab folds, due to the range of slab subduction styles around the planet.

5. Conclusions

The upper-lower mantle density contrast is a key parameter in determining the interaction mode between subducting slabs and the mantle transition zone [Kincaid & Olson, 1987]. Furthermore, the rheology of the mantle controls how fast subduction evolves. Results of numerical experiments presented here show some upper mantle material becomes entrained into the lower mantle, independent of the mantle density contrast or rheology. All experiments exhibit folding of the slab tip upon interaction with the transition zone. When the mantle density contrast is greater than 1.6 %, which represents a minimum increase of 50 kg/m^3 of the lower mantle density, the slab continues to fold recumbently as it penetrates into the lower mantle. Consequently, the slab traps a larger volume of upper mantle material. If the mantle rheology is composite, entrainments occurs more rapidly, retaining larger amounts hydrous mineral phases [Richard et al., 2006]. This will promote dehydration reactions within slab pockets at a later stage in the subduction process. The pyroxenites that result from these reactions may be entrained into ascending plumes, providing an additional component to the global diversity of OIB.

6. References

Abouchami, W., Hofmann, A. W., Galer, S. J. G., Frey, F. A., Eisele, J. & Feigenson, M. (2005), Lead isotopes reveal bilateral asymmetry and vertical continuity in the Hawaiian mantle plume. *Nature*, 434(7035), 851-856, doi: 10.1038/nature03402.

Agrusta, R., Goes, S. & van Hunen, J. (2017), Subducting-slab transition-zone interaction: Stagnation, penetration and mode switches. *Earth Planet. Sci. Lett.*, 464, 10-23, doi: 10.1016/j.epsl.2017.02.005.

Andrews, E. R. & Billen, M. I. (2009), Rheologic controls on the dynamics of slab detachment. *Tectonophysics*, 464(1-4), 60-69, doi: 10.1016/j.tecto.2007.09.004.

Cabral, R. A., Jackson, M. G., Rose-Koga, E. F., Koga, K. T., Whitehouse, M. J., Antonelli, M. A., Farquhar, J., Day, J. M. & Hauri, E. H. (2013), Anomalous sulphur isotopes in plume lavas reveal deep mantle storage of Archaean crust. *Nature*, 496(7446), 490-3, doi: 10.1038/nature12020.

Capitanio, F. A. & Faccenda, M. (2012), Complex mantle flow around heterogeneous subducting oceanic plates. *Earth Planet. Sci. Lett.*, 353-354, 29-37, doi: 10.1016/j.epsl.2012.07.042.

Christensen, U. R. (1996), The influence of trench migration on slab penetration into the lower mantle. *Earth Planet. Sci. Lett.*, 140(1-4), 27-39, doi: 10.1016/0012-821x(96)00023-4.

Čížková, H., van Hunen, J. & van den Berg, A. (2007), Stress distribution within subducting slabs and their deformation in the transition zone. *Phys. Earth Planet. Int.*, 161(3-4), 202-214, doi: 10.1016/j.pepi.2007.02.002.

Conrad, C. P. & Lithgow-Bertelloni, C. (2002), How mantle slabs drive plate tectonics. *Science*, 298(5591), 207-209, doi: 10.1126/science.1074161.

Courtillot, V., Davaille, A., Besse, J. & Stock, J. (2003), Three distinct types of hotspots in the Earth's mantle. *Earth Planet. Sci. Lett.*, 205(3-4), 295-308, doi: 10.1016/S0012-821x(02)01048-8.

Davies, G. F. & Richards, M. A. (1992), Mantle Convection. *Journal of Geology*, 100(2), 151-206, doi: 10.1086/629582.

DeFelice, C., Mallick, S., Saal, A. E. & Huang, S. (2019), An isotopically depleted lower mantle component is intrinsic to the Hawaiian mantle plume. *Nature Geoscience*, 12(6), 487-492, doi: 10.1038/s41561-019-0348-0.

Delavault, H., Chauvel, C., Thomassot, E., Devey, C. W. & Dazas, B. (2016), Sulfur and lead isotopic evidence of relic Archean sediments in the Pitcairn mantle plume. *Proc Natl Acad Sci U S A*, 113(46), 12952-12956, doi: 10.1073/pnas.1523805113.

Dilek, Y., Moores, E. M., Elthon, D. & Nicolas, A. (1998) Ophiolites and oceanic crust: new indights from field studies and oceanic drilling, *Penrose Conference*. Marshall, california, USA: The Geological Society of America.

Enns, A., Becker, T. W. & Schmeling, H. (2005), The dynamics of subduction and trench migration for viscosity stratification. *Geophys. J. Int.*, 160(2), 761-775, doi: 10.1111/j.1365-246X.2005.02519.x.

Faccenda, M., Gerya, T. V. & Burlini, L. (2009), Deep slab hydration induced by bending-related variations in tectonic pressure. *Nature Geoscience*, 2(11), 790-793, doi: 10.1038/Ngeo656.

Farnetani, C. G. & Hofmann, A. W. (2009), Dynamics and internal structure of a lower mantle plume conduit. *Earth Planet. Sci. Lett.*, 282(1-4), 314-322, doi: 10.1016/j.epsl.2009.03.035.

Forsyth, D. & Uyeda, S. (1975), On the Relative Importance of the Driving Forces of Plate Motion. *Geophys. J. Int.*, 43(1), 163-200, doi: 10.1111/j.1365-246X.1975.tb00631.x.

Fukao, Y. & Obayashi, M. (2013), Subducted slabs stagnant above, penetrating through, and trapped below the 660 km discontinuity. *J. Geophys. Res. Solid Earth*, 118(11), 5920-5938, doi: 10.1002/2013jb010466.

Garnero, E. J. (2004), A new paradigm for Earth's core-mantle boundary. *Science*, 304(5672), 834-6, doi: 10.1126/science.1097849.

Guillou-Frottier, L., Buttles, J. & Olson, P. (1995), Laboratory Experiments on the Structure of Subducted Lithosphere. *Earth Planet. Sci. Lett.*, 133(1-2), 19-34, doi: 10.1016/0012-821x(95)00045-E.

Hart, S. R., Hauri, E. H., Oschmann, L. A. & Whitehead, J. A. (1992), Mantle plumes and entrainment: isotopic evidence. *Science*, 256(5056), 517-20, doi: 10.1126/science.256.5056.517.

Hauri, E. H., Whitehead, J. A. & Hart, S. R. (1994), Fluid dynamics and geochemical aspects of entrainment in mantle plumes. *J. Geophys. Res.*, 99(B12), 24275-24300, doi: 10.1029/94jb01257.

Herzberg, C. (2011), Identification of Source Lithology in the Hawaiian and Canary Islands: Implications for Origins. *J. Petrol.*, 52(1), 113-146, doi: 10.1093/petrology/egq075.

Hoffmann, A. W. (2014), Sampling mantle heterogeneity though oceanic basalts: isotopes and trace elements. *Treatise on Geochemistry*, 3, 67-101, doi: 10.1016/B978-0-08-095975-7.00203-5.

Hofmann, A. W. (1997), Mantle geochemistry: the message from oceanic volcanism. *Nature*, 385, 219-229, doi: 10.1038/385219a0.

Hofmann, A. W. & White, W. M. (1982), Mantle Plumes from Ancient Oceanic-Crust. *Earth Planet. Sci. Lett.*, 57(2), 421-436, doi: 10.1016/0012-821x(82)90161-3.

Holt, A. F. & Becker, T. W. (2017), The effect of a power-law mantle viscosity on trench retreat rate. *Geophys. J. Int.*, 208(1), 491-507, doi: 10.1093/gji/ggw392.

Jackson, M. G., Hart, S. R., Konter, J. G., Kurz, M. D., Blusztajn, J. & Farley, K. A. (2014), Helium and lead isotopes reveal the geochemical geometry of the Samoan plume. *Nature*, 514(7522), 355-8, doi: 10.1038/nature13794.

Kincaid, C. & Griffiths, R. W. (2003), Laboratory models of the thermal evolution of the mantle during rollback subduction. *Nature*, 425(6953), 58-62, doi: 10.1038/nature01923.

Kincaid, C. & Olson, P. (1987), An Experimental Study of Subduction and Slab Migration. *J. Geophys. Res.*, 92(B13), 13832-13840, doi: 10.1029/JB092iB13p13832.

Király, Á., Capitanio, F. A., Funiciello, F. & Faccenna, C. (2017), Subduction induced mantle flow: Length-scales and orientation of the toroidal cell. *Earth Planet. Sci. Lett.*, 479, 284-297, doi: 10.1016/j.epsl.2017.09.017.

Kohlstedt, D. L. & Mackwell, S. J. (1998), Diffusion of hydrogen and intrinsic point defects in olivine. *Z. Phys. Chem.*, 207(1-2), 147-162, doi: DOI 10.1524/zpch.1998.207.Part_1_2.147.

Lay, T., Williams, Q. & Garnero, E. J. (1998), The core–mantle boundary layer and deep Earth dynamics. *Nature*, 392(6675), 461-468, doi: 10.1038/33083.

Li, Z. H. & Ribe, N. M. (2012), Dynamics of free subduction from 3-D boundary element modeling. *J. Geophys. Res.*, 117, B06408, doi: 10.1029/2012jb009165.

Matzen, A. K., Wood, B. J., Baker, M. B. & Stolper, E. M. (2017), The roles of pyroxenite and peridotite in the mantle sources of oceanic basalts. *Nat. Geosci.*, 10(7), 530-535, doi: 10.1038/Ngeo2968.

Moresi, L., Dufour, F. & Mühlhaus, H. B. (2003), A Lagrangian integration point finite element method for large deformation modeling of viscoelastic geomaterials. *J. Comput. Phys.*, 184(2), 476-497, doi: 10.1016/S0021-9991(02)00031-1.

Moresi, L., Quenette, S., Lemiale, V., Mériaux, C., Appelbe, B. & Mühlhaus, H. B. (2007), Computational approaches to studying non-linear dynamics of the crust and mantle. *Phys. Earth Planet. Inter.*, 163(1-4), 69-82, doi: 10.1016/j.pepi.2007.06.009.

Morgan, W. J. (1971), Convection plumes in the lower mantle. *Nature*, 230, 42-43, doi: 10.1038/230042a0.

Nebel, O., Arculus, R. J., van Westrenen, W., Woodhead, J. D., Jenner, F. E., Nebel-Jacobsen, Y. J., Wille, M. & Eggins, S. M. (2013), Coupled Hf-Nd-Pb isotope co-variations of HIMU oceanic island basalts from Mangaia, Cook-Austral islands, suggest an Archean source component in the mantle transition zone. *Geochim. Cosmochim. Acta*, 112(87-101), 87-101, doi: 10.1016/j.gca.2013.03.005.

Nebel, O., Sossi, P. A., Bénard, A., Arculus, R. J., Yaxley, G. M., Woodhead, J. D., Rhodri Davies, D. & Ruttor, S. (2019), Reconciling petrological and isotopic mixing mechanisms in the Pitcairn mantle plume using stable Fe isotopes. *Earth Planet. Sci. Lett.*, 521, 60-67, doi: 10.1016/j.epsl.2019.05.037.

Niu, Y. L., Wilson, M., Humphreys, E. R. & O'Hara, M. J. (2011), The Origin of Intra-plate Ocean Island Basalts (OIB): the Lid Effect and its Geodynamic Implications. *J. Petrol.*, 52(7-8), 1443-1468, doi: 10.1093/petrology/egr030.

Ohtani, E., Litasov, K., Hosoya, T., Kubo, T. & Kondo, T. (2004), Water transport into the deep mantle and formation of a hydrous transition zone. *Phys. Earth Planet. Inter.*, 143, 255-269, doi: 10.1016/j.pepi.2003.09.015.

Olbertz, D., Wortel, M. J. R. & Hansen, U. (1997), Trench migration and subduction zone geometry. *Geophys. Res. Lett.*, 24(3), 221-224, doi: 10.1029/96gl03971.

Richard, G., Bercovici, D. & Karato, S. I. (2006), Slab dehydration in the Earth's mantle transition zone. *Earth Planet. Sci. Lett.*, 251(1-2), 156-167, doi: 10.1016/j.epsl.2006.09.006.

Schellart, W. P. (2004), Kinematics of subduction and subduction-induced flow in the upper mantle. *J. Geophys. Res.*, 109, B07401, doi: 10.1029/2004jb002970.

Schellart, W. P. (2008), Kinematics and flow patterns in deep mantle and upper mantle subduction models: Influence of the mantle depth and slab to mantle viscosity ratio. *Geochem. Geophys. Geosyst.*, 9, Q03014, doi: 10.1029/2007gc001656.

Schellart, W. P., Stegman, D. R. & Freeman, J. (2008), Global trench migration velocities and slab migration induced upper mantle volume fluxes: Constraints to find an Earth reference frame based on minimizing viscous dissipation. *Earth Sci. Rev.*, 88(1-2), 118-144, doi: 10.1016/j.earscirev.2008.01.005.

Schmidt, M. W. & Poli, S. (2014) Devolatilization During Subduction, *Treatise on Geochemistry*, 669-701. doi: 10.1016/b978-0-08-095975-7.00321-1

Sobolev, A. V., Hofmann, A. W., Jochum, K. P., Kuzmin, D. V. & Stoll, B. (2011), A young source for the Hawaiian plume. *Nature*, 476(7361), 434-7, doi: 10.1038/nature10321.

Sobolev, A. V., Hofmann, A. W., Sobolev, S. V. & Nikogosian, I. K. (2005), An olivine-free mantle source of Hawaiian shield basalts. *Nature*, 434(7033), 590-7, doi: 10.1038/nature03411.

Stegman, D. R., Freeman, J., Schellart, W. P., Moresi, L. & May, D. (2006), Influence of trench width on subduction hinge retreat rates in 3-D models of slab rollback. *Geochem. Geophys. Geosyst.*, 7, Q03012, doi: 10.1029/2005gc001056.

Stracke, A., Hofmann, A. W. & Hart, S. R. (2005), FOZO, HIMU, and the rest of the mantle zoo. *Geochem. Geophys. Geosyst.*, 6(5), Q05007, doi: 10.1029/2004gc000824.

Weis, D., Garcia, M. O., Rhodes, J. M., Jellinek, M. & Scoates, J. S. (2011), Role of the deep mantle in generating the compositional asymmetry of the Hawaiian mantle plume. *Nature Geoscience*, 4(12), 831-838, doi: 10.1038/Ngeo1328.

White, W. M. (2010), Oceanic Island Basalts and Mantle Plumes: The Geochemical Perspective. *Annu. Rev. Earth Planet Sci.*, 38, 133-160, doi: 10.1146/annurev-earth-040809-152450.

Chapter 5

Conclusions

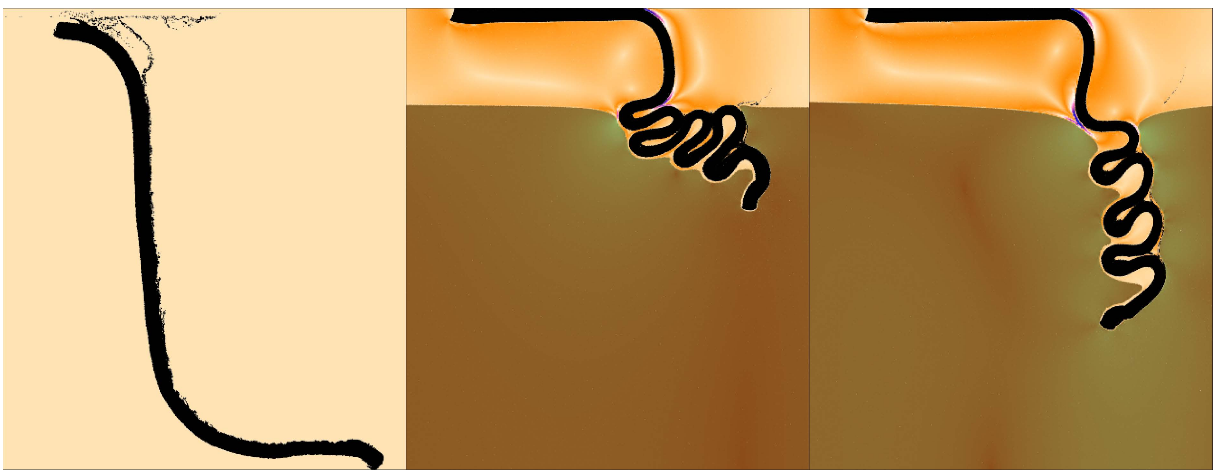

Cover image: Geometric configuration of the slab after reaching the CMB in experiment DF1 (Chapter 2). Final stage of experiment LM7-D2 (Chapter 3). Slab geometric configuration of the experiment with an initial upper-lower mantle viscosity ratio of 50 (Chapter 4).

1. Research outcomes

The overarching aim of this thesis was to analyse and quantify how specific modelling parameters influence subduction dynamics. These included the initial slab length and dipping angle, the mantle power law rheology parameters (power-law exponent and transition strain rate), as well as the upper-lower mantle density contrasts and viscosity ratios. The mode of subduction depends on the initial slab geometry and the angle at which the slab impinges on the bottom boundary [Ribe, 2010; Li & Ribe, 2012]. However, geodynamic models of subduction mostly focus either on 'self-sustained' subduction evolution or on subduction initiation processes, not considering the link between the two. Consequently, the instability that initiates subduction is imposed with little consideration on the full extent of its impacts. Moreover, the evolution of a subducting plate depends on the rheology of the mantle as well as the upper to lower mantle density and viscosity contrasts. If subduction evolves quickly, it may induce high stresses in the surrounding mantle. Thus, even in the linear flow dominated lower mantle, subducting slabs may localise power-law flow around them [McNamara et al., 2001]. In subduction models, the whole mantle is usually assumed to be linear viscous or non-linear, but only in the upper mantle. Recent studies have shown that a power-law component in the upper mantle rheology results in a reduced trench motion contribution to the subduction velocity [Holt & Becker, 2017]. Hence, it was essential to analyse how these parameters are limiting the applicability of modelling results to nature.

This thesis addressed the following key objectives into three self-contained chapters (Chapters 2, 3 and 4):

- Examine how variations of the initial slab geometry (length and angle) affect incipient subduction dynamics.
- Evaluate the effects of the power-law parameters of both upper and lower mantle rheology on the interaction mode between slab and mantle discontinuity under different upper-lower mantle density and viscosity contrasts.
- Estimate the volume of upper mantle material trapped by a subducting plate that potentially sinks into the lower mantle.

The objectives of this thesis were accomplished using simplified numerical models. The complexity of models increased from a homogenous linear mantle configuration (Chapter 2) to a two-layer mantle configuration with both viscosity and density contrast and a power-law component in the viscosity (Chapters 3 and 4). However, the general model set-up was kept simple, which allowed to interpret precisely the effects of the parameters under investigation.

This concluding chapter concisely summarises and highlights the implications of the results for the modelling community and their significance for nature. In addition, recommendations for future research based on the findings of the thesis are briefly outlined.

2. Research implications

2.1. Effects of the initial slab geometry

Results from Chapter 2 highlight the importance of the initial slab geometry on the evolution of incipient subduction zones. The focus was on the stage after subduction initiation until the time the slab reaches a bottom boundary, which was defined as either an impenetrable upper-lower mantle discontinuity (shallow mantle models) or deep discontinuity in the lower mantle (deep mantle models). In both types of models, the mantle was assumed linear viscous and homogeneous. The effects of varying either the initial slab length or the initial slab dipping angle are largely manifested by changes in the sinking and trench velocity. The deep mantle setup resulted in higher maximum sinking velocities, as well as maximum trench velocities. However, such scenario is unlikely in nature, given the layered structure of the mantle [Mitrovica & Forte, 1997; Fowler, 2004].

The plate trailing edge also conditions the subduction velocity partitioning: if the plate is fixed, subduction occurs predominantly through trench retreat; and if the plate is free to move, the trench motion is reduced (although the retreating mode continues to dominate) and subduction results mostly from the plate motion towards the trench. This contrast significantly impacts the stretching of the plate and slab ensemble, which is extensive in fixed plates. The lengthening of the plate and slab, in turn, results in a lowering of the slab stiffness and the sinking velocity is controlled mostly by the slab viscosity [Ribe, 2010; Li & Ribe, 2012].

The initial slab geometry determines the duration of the initial bending stage during the first stage after the subduction starts. A 125 km increase of the initial slab length resulted in up to ~ 17 Ma shorter subduction duration. However, the maximum velocities (both sinking and trench migration) are not significantly affected. Conversely, variations of the slab initial dipping angle impact the maximum velocities reached. Higher velocities are reached for initial angles between $30-60°$ and resulted in faster subduction overall.

2.2. Effects of mantle stress-dependent rheology

Chapter 3 focused on the slab interaction with the mantle transition zone. Results emphasise how the interaction not only depends on upper-lower mantle density contrasts and viscosity ratios, but also on the activation of a power-law component in the mantle rheology. The power-law rheology was fully described by two parameters: the transition strain rate and the power-law exponent, both of which are dependent on mineral composition [Ashby, 1972; Karato & Wu, 1993]. The transition strain rate represents the strain rate at which the power-law (dislocation) viscosity equals the linear (diffusion) viscosity. Results show that variations of the transition strain rate determine the breadth of the mantle in which the effective viscosity is lowered: a lower transition strain rate results in a larger affected region. Variations of the power-law exponent control the degree to which the effective viscosity can be lowered: a higher power-law exponent results in lower mantle viscosity values, when under large stresses.

Thus, the primary consequence of the power-law component is lowering the effective viscosity of the mantle in regions of high stress (i.e., regions around a subduction slab). As a result, a lubricating layer of low viscosity mantle develops around the slab, promoting faster sinking of the slab and faster motion of the surface trailing plate (i.e., higher plate velocity).

The variations of the upper mantle power-law rheology parameters considerably affect the trench motion and subduction rates. However, variations of the lower mantle power-law rheology parameters mantle mainly impact the shape of the subducting slab. When the mantle rheology is composite, the slab initially penetrates the mantle discontinuity with very little deformation before developing folds. Additionally, the composite rheology promotes deeper subduction, over the same time interval, even at high upper-lower mantle density contrasts.

By adding a power-law component to the mantle rheology, a new subduction mode was identified. This mode is characterised by initial slab straight penetration of the upper-lower mantle transition, followed by accumulation of the slab as a result of buckling inside the lower mantle.

2.3. Effects of upper mantle entrapment

Results from the numerical experiments conducted as part of Chapter 3 revealed that part of the upper mantle material gets entrained into the lower mantle during subduction, trapped in ‘slab pockets’. This occurs independently of the upper-lower mantle density contrast or mantle rheology. However, the mantle rheology controls the volume of trapped material and the rate of the entrainment. If the mantle rheology is composite, the volume of entrained material is higher and the entrainment occurs faster. Therefore, the slab possibly retains larger amounts hydrous mineral phases during upper mantle transit [Richard et al., 2006]. This is likely to induce dehydration reactions inside the slab pockets at a later stage in the subduction process. Consequently, the reactions products (pyroxenites), may represent an additional component to the global diversity of ocean island basalts (OIB), following their entrainment by an ascending plume.

2.4. Significance of research for nature

Tomography shows a wide range of slab morphologies around the planet, from slabs trapped in the transition zone (e.g., Izu-Bonin slab, North Japan slab) to slabs sinking deeply into the lower mantle (e.g., Mariana slab, Kermadec slab, Central America slab) [Fukao & Obayashi, 2013]. The mode of slab-mantle discontinuity interaction is intimately related to features such as plate length, width, thickness, plate-mantle viscosity ratios and density contrasts [Funiciello et al., 2003; 2006; Schellart, 2004, 2008, 2010; Bellahsen et al., 2005; Li & Ribe, 2012]. Moreover, the interaction mode is closely related to the trench motion, which in turn, is linked to the ability of the trailing plate at the surface to move [Schellart, 2004]. If subduction occurs via trench-ward motion of the plate, the trench motion is reduced, promoting sub-vertical slabs. This, associated with an upper-lower mantle density contrast below 3%, leads to slab penetration across the mantle discontinuity into the lower mantle [Kincaid & Olson, 1987; Enns et al., 2005; Čížková et al., 2007].

By contrast, if subduction occurs mostly by trench retreat, the trench velocity is high ($> 2-4$ cm/yr), inducing the slab to lie flat on top of the mantle discontinuity [Christensen, 1996]. In this situation, slabs appear to be stagnant at the bottom of the upper mantle. In addition to the trench mobility, the apparent stagnation results from the combination of the viscosity increase between upper and lower mantle and the endothermic mineral phase transition at 660 km (ringwoodite to bridgmanite and ferropericlase transition [e.g., Anderson, 1967; Ito & Takahashi, 1989; Mitrovica & Forte, 1997]). However, most subducted slabs eventually sink into the lower mantle on times scales of $100-200$ Ma [Goes et al., 2017 (and references therein)].

The results of this thesis showed that variations of the initial slab geometry can lead to changes in the slab sinking and trench motion velocities. If a slab sinks through the upper mantle at higher velocities, it may induce higher stresses in the surrounding mantle. This can activate the power-law component in the rheology of the mantle and promote faster sinking, in a positive feedback loop. Moreover, the interaction between slab and mantle discontinuity is affected. As the slab approaches the bottom of the upper mantle, the slab sinking velocity does not decrease, due to the decrease of the mantle viscosity following the activation of the power-law rheology. Thus, the slab impinges on the mantle discontinuity at a higher velocity and is able to initially penetrate the discontinuity. Consequently, the slab is ‘anchored’ to the top of the lower mantle and folding is promoted, with continued subduction. Hence, plates that stagnated on top of the mantle transition zone may have initiated with initial geometries that lead to lower sinking velocities, resulting in the non-activation of the power-law rheology of the mantle, and the upper-lower mantle discontinuity acts as an impenetrable barrier.

3. Future research

Over the last few decades the subduction processes have been extensively studied and our understanding of the long-term evolution of slab has greatly improved. It is important to continue to study the drivers and the consequences of subduction processes because they shape Earth's surface and correspond to the places where the strongest and most damaging earthquakes take place.

Steady advances in computational performance allows for continuous improvement of the efficiency and accuracy of numerical models. Experiments presented in this thesis were executed with a simple setup in a 2D Cartesian domain. The main limitations of the models developed in this thesis have been discussed throughout Chapters 2, 3 and 4. In order to improve and further develop the findings, the complexity of the models' setup should increase gradually. Every step towards increasing model complexity adds more variables into the system. Hence, it is recommended that future research builds on the already studied models. Recommendations for future research include the following topics:

- Effects of the slab initial geometry on subduction dynamics, considering a composite mantle rheology. Chapter 2 explored the effects of varying the slab initial geometry in a linear viscous homogeneous mantle, however, the upper mantle behaves non-linearly. Thus, adding the power-law component to the mantle rheology constitutes a more realistic scenario. If the mantle rheology is composite, it is expected that variations of the slab initial geometry yield more pronounced effects. For instance, longer initial slabs, which have an increased negative buoyancy, will induce higher stress on the mantle. This will result in enhanced lowering of the mantle viscosity and subduction should evolve faster than if the mantle is linear viscous.

- Effects of the slab initial geometry and mantle power-law rheology in 3D models of subduction. The 3D geometry includes the intrinsic subduction induced toroidal mantle flow. The results of Chapters 2, 3 and 4 would be much improved by adding the third space dimension, which would also expand the comparison between model results and nature. It is expected that, in a 3D model setup, the role of the mantle rheology in the changes of slab configuration along arc (e.g. the Kamchatka-Kuril-Honshu-Izu-Bonin-Mariana subduction zone) becomes more evident. Additionally, the 3D geometry enables to explore the role of plate width and lateral variations of plate age.

- Effects of the overriding and neighbouring plates on subduction. The addition of the overriding plate will likely reduce the trench velocity. It may also reduce the stresses induced by the subducting plate on the surrounding mantle. As a consequence, the power-law activation can be limited to a smaller region of the mantle.

- Effects of mantle stratification on subduction. The mantle was assumed to be homogeneous in Chapter 2 and composed of two layers in Chapters 3 and 4. However, mantle stratification is more complex than the 'upper-lower' mantle configuration. The addition of the transitions at 410 km, associated with the olivine to wadsleyite mineral phase transition, and at 1000 km, associated with a viscosity jump [Rudolph et al., 2015], would likely affect sinking and trench retreat velocities. Additional mantle transition boundaries are likely to promote greater buckling of the plate, which in turn is likely to entrain greater amounts of sub-lithospheric mantle to depth. Multiple mantle transition boundaries, in addition to the power-law rheology in the mantle, could explain the wide variety of slab geometries imaged by tomography.

4. References

Anderson, D. L. (1967), Phase changes in the upper mantle. *Science*, 157(3793), 1165-73, doi: 10.1126/science.157.3793.1165.

Ashby, M. F. (1972), A first report on deformation-mechanism maps. *Acta Metallurgica*, 20(7), 887-897, doi: 10.1016/0001-6160(72)90082-x.

Bellahsen, N., Faccenna, C. & Funiciello, F. (2005), Dynamics of subduction and plate motion in laboratory experiments: Insights into the "plate tectonics" behavior of the Earth. *J. Geophys. Res.*, 110(B1), B01401, doi: 10.1029/2004jb002999.

Christensen, U. R. (1996), The influence of trench migration on slab penetration into the lower mantle. *Earth Planet. Sci. Lett.*, 140(1-4), 27-39, doi: 10.1016/0012-821x(96)00023-4.

Čížková, H., van Hunen, J. & van den Berg, A. (2007), Stress distribution within subducting slabs and their deformation in the transition zone. *Phys. Earth Planet. Int.*, 161(3-4), 202-214, doi: 10.1016/j.pepi.2007.02.002.

Enns, A., Becker, T. W. & Schmeling, H. (2005), The dynamics of subduction and trench migration for viscosity stratification. *Geophys. J. Int.*, 160(2), 761-775, doi: 10.1111/j.1365-246X.2005.02519.x.

Fowler, C. M. R. (2004) *The Solid Earth: An Introduction to Global Geophysics*. 2nd edition. Cambridge: Cambridge University Press. doi: 10.1017/CBO9780511819643

Fukao, Y. & Obayashi, M. (2013), Subducted slabs stagnant above, penetrating through, and trapped below the 660 km discontinuity. *J. Geophys. Res. Solid Earth*, 118(11), 5920-5938, doi: 10.1002/2013jb010466.

Funiciello, F., Moroni, M., Piromallo, C., Faccenna, C., Cenedese, A. & Bui, H. A. (2006), Mapping mantle flow during retreating subduction: Laboratory models analyzed by feature tracking. *J. Geophys. Res.*, 111, B03402, doi: 10.1029/2005jb003792.

Funiciello, F., Morra, G., Regenauer-Lieb, K. & Giardini, D. (2003), Dynamics of retreating slabs: 1. Insights from two-dimensional numerical experiments. *J. Geophys. Res.*, 108(B4), 2206, doi: 10.1029/2001jb000898.

Goes, S., Agrusta, R., van Hunen, J. & Garel, F. (2017), Subduction-transition zone interaction: A review. *Geosphere*, 13(3), 644-664, doi: 10.1130/Ges01476.1.

Holt, A. F. & Becker, T. W. (2017), The effect of a power-law mantle viscosity on trench retreat rate. *Geophys. J. Int.*, 208(1), 491-507, doi: 10.1093/gji/ggw392.

Ito, E. & Takahashi, E. (1989), Postspinel transformations in the system Mg_2SiO_4-$Fe_2SiO_4$and some geophysical implications. *J. Geophys. Res. Solid Earth*, 94(B8), 10637-10646, doi: 10.1029/JB094iB08p10637.

Karato, S. & Wu, P. (1993), Rheology of the upper mantle: a synthesis. *Science*, 260, 771-778, doi: 10.1126/science.260.5109.771.

Kincaid, C. & Olson, P. (1987), An Experimental Study of Subduction and Slab Migration. *J. Geophys. Res.*, 92(B13), 13832-13840, doi: 10.1029/JB092iB13p13832.

Li, Z. H. & Ribe, N. M. (2012), Dynamics of free subduction from 3-D boundary element modeling. *J. Geophys. Res.*, 117, B06408, doi: 10.1029/2012jb009165.

McNamara, A. K., Karato, S.-I. & van Keken, P. E. (2001), Localization of dislocation creep in the lower mantle: implications for the origin of seismic anisotropy. *Earth Planet. Sci. Lett.*, 191(1-2), 85-99, doi: 10.1016/s0012-821x(01)00405-8.

Mitrovica, J. X. & Forte, A. M. (1997), Radial profile of mantle viscosity: Results from the joint inversion of convection and postglacial rebound observables. *J. Geophys. Res. Solid Earth*, 102(B2), 2751-2769, doi: 10.1029/96jb03175.

Ribe, N. M. (2010), Bending mechanics and mode selection in free subduction: a thin-sheet analysis. *Geophys. J. Int.*, 180(2), 559-576, doi: 10.1111/j.1365-246X.2009.04460.x.

Richard, G., Bercovici, D. & Karato, S. I. (2006), Slab dehydration in the Earth's mantle transition zone. *Earth Planet. Sci. Lett.*, 251(1-2), 156-167, doi: 10.1016/j.epsl.2006.09.006.

Rudolph, M. L., Lekic, V. & Lithgow-Bertelloni, C. (2015), Viscosity jump in Earth's mid-mantle. *Science*, 350(6266), 1349-1352, doi: 10.1126/science.aad1929.

Schellart, W. P. (2004), Kinematics of subduction and subduction-induced flow in the upper mantle. *J. Geophys. Res.*, 109, B07401, doi: 10.1029/2004jb002970.

Schellart, W. P. (2008), Kinematics and flow patterns in deep mantle and upper mantle subduction models: Influence of the mantle depth and slab to mantle viscosity ratio. *Geochem. Geophys. Geosyst.*, 9, Q03014, doi: 10.1029/2007gc001656.

Schellart, W. P. (2010), Evolution of Subduction Zone Curvature and its Dependence on the Trench Velocity and the Slab to Upper Mantle Viscosity Ratio. *J. Geophys. Res.*, 115, B11406, doi: 10.1029/2009jb006643.